

# Moderating the Photogenerated Exciton Dynamics in Molecular Aggregates

*A thesis submitted for the degree of*

**Doctor of Philosophy**

*in*

**Chemistry**

*by*

**Abbey M. Philip**



Indian Institute of Science Education and Research  
Thiruvananthapuram (IISER-TVM),  
Thiruvananthapuram - 695551  
Vithura, Kerala, India

October 2018



# Declaration

I hereby declare that the Ph. D. thesis entitled "*Moderating the Photogenerated Exciton Dynamics in Molecular Aggregates*" is an independent work carried out by me at School of Chemistry, Indian Institute of Science Education and Research Thiruvananthapuram (IISER-TVM), under the supervision of **Dr. Mahesh Hariharan** and it has not been submitted anywhere else for any other degree, diploma or title. In keeping with the general practice of reporting the scientific observations, due acknowledgements have been made wherever the work described is based on the findings of other investigators.

Place: IISER Thiruvananthapuram

**Abbey M. Philip**

Date: 22-10-2018

This is to certify that the work embodied in the thesis entitled "*Moderating the Photogenerated Exciton Dynamics in Molecular Aggregates*" has been carried out by **Abbey M. Philip (PHD131001)** under my supervision at the School of Chemistry, Indian Institute of Science Education and Research Thiruvananthapuram (IISER-TVM) and the same has not been submitted elsewhere for a degree.

Place: IISER Thiruvananthapuram

**Dr. Mahesh Hariharan**

Date: 22-10-2018

(Thesis Supervisor)



*Dedicated To My*

*Beloved Family ...*



*“The way to get started is to quit talking and begin doing”*

**- Walt Disney**

*“On the arid lands there will spring up industrial colonies without smoke and without smokestacks; forests of glass tubes will extend over the plains and glass buildings will rise everywhere; inside of these will take place the photochemical processes that hitherto have been the guarded secret of the plants, but that will have been mastered by human industry which will know how to make them bear even more abundant fruit than nature, for nature is not in a hurry and mankind is”*

**- Giacomo Ciamician**  
(*Science*, 1912, 36, 385)



# Acknowledgements

Time certainly flies, and all that left behind is a long exciting journey that have guided me towards the end of my path here at IISER-TVM. The current thesis dissertation would not have been possible without the support of many people that I would like to acknowledge for their help along the way.

First and foremost, I owe a deep sense of gratitude and sincere thanks to my mentor and supervisor, Dr. Mahesh Hariharan, for his constant support, guidance, and for providing excellent research environment during my doctoral study. I am extremely thankful to him for giving me the freedom to pursue my interests and encouraging independent scientific thinking and rationale while simultaneously keeping me on the right track. I will always be grateful to him for being available round the clock whenever necessary and for the lengthy scientific discussions and debates throughout my Ph. D. work. He has constantly encouraged me to push my limits farther and it has indeed been a rare privilege to work under his guidance.

I would like to express my sincere thanks to Prof. V. Ramakrishnan and Prof. E. D. Jemmis, present and former Directors of IISER-TVM, for the providing excellent infrastructure and research facilities at IISER-TVM. I am grateful to my doctoral committee members, Dr. Reji Varghese and Dr. R. S. Swathi for their support, guidance and helpful suggestions. I extend my sincere gratitude to Prof. K. George Thomas for providing extensive help and support during my Ph. D. program. I would like to thank all my Ph. D. course instructors and the faculty members of School of Chemistry, IISER-TVM for their support and motivation.

I will take this opportunity to thank Dr. Anil Shaji (School of Physics, IISER-TVM), Prof. Bern Kohler (Ohio State University) and Prof. Qiquan Qiao (South Dakota State University) for the extensive collaborative support during the tenure of my Ph. D. program. I would like to thank Dr. K. R. Gopidas (NIIST-TVM) and Prof. Frederick D. Lewis (Northwestern University) for providing critical comments and suggestions on my research work.

I would like to acknowledge IISER-TVM for the research fellowship and thank them for ensuring a continuous funding during my doctoral study. I am indebted to Bhaskara Advanced Solar Energy (BASE) fellowship supported by the Indo-US Science and Technology Forum (IUSSTF) and the Department of Science and

Technology (DST), Government of India for providing an opportunity and funding me to visit Prof. Qiquan Qiao's lab, South Dakota State University, Brookings, US for a five month (August-December 2017) collaborative research internship on organic photovoltaics.

I am deeply indebted to all my past and present group members: Dr. Rijo T. C., Dr. Shinaj K. R., Dr. Ajith R. M., Dr. Kalaivanan N., Mrs. Somadrita D., Dr. Hitesh K., Mr. Jimmy J., Dr. Salini P. S., Ms. Gopika G., Dr. Nanditha G. N., Ms. Shubhasmin R., Ms. Amalu M., Mr. Vinayak B., Ms. Remya R., Mr. Nagaraj K., Mr. Ebin S., Ms. Devika S., Ms. Athira T., and Ms. Lijina M. P. for their help and support during my Ph. D. work. I would like to give my sincere thanks to all the project students directly or indirectly worked along with me, Mr. Murugan, Mr. Vidymanand V., Mr. Febin K., Mr. Abin V., Ms. Arya A., Ms. S. L. Vaishnavi, Mr. Amit L., Mr. Shubham S., Mr. Philip M., and Mr. Niyas M. A. for being patient with me and providing utmost support and help. A special thanks to Dr. Shinaj for being an incredible mentor and Mr. Febin K. and Mr. Sreenath K. M. for providing critical contributions to some of work in the present thesis. I'm indebted to Dr. Ajith R. M., Mr. Ebin S. and Mr. Nagaraj K. for their efforts towards acquiring femtosecond transient absorption data. All the BS-MS/visiting students associated with the Hariharan group are duly acknowledged for their support during my tenure at IISER-TVM.

I would like to thank several people who made this work possible, and who have made my stay at IISER-TVM enjoyable, especially, Dr. Rijo T. Cheriya, Dr. Shinaj K. Rajagopal, and Dr. Baiju P. Krishnan for their unconditional care and support. A special thanks to Dr. Anoop T., Dr. Shine K. A., Dr. Sandeep K., Dr. Reshmi T., Mr. Sanoop S., Dr. Sabnam K., Dr. Subila K., Dr. Hari V. P. T., Mr. Murali G., Mr. Nithiyandandan K., Mr. Libin, Dr. Atchuth Rao, Mr. Mohan Rao, Dr. Jiji A. C., Mr. Shine A., Dr. Vidyasagar A., Mr. Soumik M., Dr. Amol V., Ms. Hema S., Dr. Pratap Z., Mr. Selvakumar, Ms. Jobha J., Dr. S. Chandra Shekar, Mr. Perumal D., Mr. Vignesh A., Mr. Prathap A., Ms. Arthi, Mr. Atchimnaidu, Dr. Pradeep D., Mr. Noufal J., Dr. Sankaran N., Mr. Rafeeqe P. P., Mr. Purnachandra R., Mr. Rajesh G., Ms. Anjana P. K., Dr. Asha K. S., Ms. Anu G., Mr. Ramkumar K., Ms. Hemna, Mr. Sujith M., Mr. Ajaykumar, Mr. Vishnu and for their acquaintance, help and support.

My wholehearted thanks goes to Mr. Alex P. Andrews for single crystal X-ray diffraction measurements and structure solving, Mr. Adarsh for NMR experiments,

Mr. Nibith K. and Mr. Shiju for the GC-MS, elemental and IR analyses, and Mr. Aneesh A. for the SEM analysis. I also thank Dr. Gireesh K. K. for his timely help with the confocal microscopy. It is my pleasure to express my sincere thanks to Dr. Suresh Das and Dr. A. Ajayaghosh, present and former Directors, NIIST Trivandrum for allowing the use of instrumental facilities at NIIST. I express my sincere gratitude to Dr. M. L. P. Reddy, Dr. Bejoy, Mrs. Viji, Mr. Kiran, Mr. Robert at NIIST Trivandrum for their timely help. I thank Mr. Anu, M. G. University for the help with the HR-TEM image acquisition. I would like to acknowledge Mrs. Vrindha V. and SAIF- IIT Bombay for providing an outstanding support with the EPR analyses. I also thank the technical support from the Laser Spectra Services, Bangalore for the assistance and judicious help.

I take this opportunity to express my immense gratitude towards all my teachers in School for the motivation to keep high standard in my life and studies. I would like to thank all the teachers at V. P. and R. P. T. P. Science College (S. P. University) and Department of Chemistry (M. S. University), especially Dr. P. M. Patel, Dr. V. K. Sinha and Prof. A. V. Bedekar for the motivation to pursue my passion. I'm highly indebted to Dr. R. Ramajayam for the motivation and his guidance for pursuing academic (Ph. D.) research. I would also like to thank all my friends at V. P. Science College (S. P. University), Department of Chemistry (M. S. University), and Apicore Pharmaceuticals for their help and support. I would also like to thank all the teaching and nonteaching (library, IT, purchase, finance and mess) staff of IISER-TVM for their timely help and support.

I am extremely thankful to my brother, Mr. Baiju, for solely taking the responsibility of my family and supporting me to pursue my research. I also thank my sister-in-law and nephew, Mrs. Jisha Baiju and Dennis for extending their care and support throughout my Ph. D. program.

Above all, I would like to acknowledge the tremendous sacrifices from my parents, who ensured that I had an excellent education. For this and much more, I am forever in their debt.

- **Abbey M. Philip**



# Preface

Nature has always been at the forefront of developing innovative, proficient, immensely complex molecular machineries for the persistence of life on planet earth. Light harvesting in photosynthetic bacteria, algae and plants is one of the marvels of nature which not only is incredibly complex, but also extremely efficient in terms of light-to-chemical energy conversion. Light harvesting in plants involves a primary solar light absorption step and efficient coherent exciton energy funnelling to the distant reaction centre, wherein long-range sequential electron transfer render a near-unity quantum efficiency. Key to the extraordinary efficacy of the natural light harvesting system originates from the adept location of the redox-active, electronically complementary chromophores and the directional nature of the energy and electron migration processes in the incredibly complex chromophore-protein network.

Mankind's pursuit to acquire independence from fossil fuels have invigorated the quest to harness the incessant, clean, renewable energy from the sun. Though, modern organic solar cells have made colossal leaps in terms of harnessing the solar energy since its inception, it still lags far-behind in terms of matching the stunning efficiency of the natural light harvesting system. A thorough understanding of the critical factors of the natural light harvesting process, i.e., (i) coherent exciton migration and (ii) effective long-range charge transfer (CT) and separation (CS) can help better emulate the natural light harvesting system for real-world applications. Insights into the electronic communication between the proximate chromophores is one of the keys to designing functional photosynthetic mimics and simultaneously novel photonic/semiconducting devices. Additionally, several supramolecular donor-acceptor (D-A) assemblies have emerged to mimic the long-range CT and efficient CS for emergent photofunctional applications. Chapter 1 in the thesis, accommodates a brief account of the natural light harvesting process and the complex molecular and photoexcited-state processes involved in the same. Mimicking the natural photosynthesis in laboratory necessitates the creation of adept assemblies of redox-active, electronically complementary  $\pi$ -chromophores with the capability to deliver versatile coherent exciton migration and charge separation at long distances. A review of the several artificial multichromophoric architectures and assemblies aimed to mimic the natural light harvesting would be discussed subsequently at a greater length in the chapter.

Unraveling the fate of excitons in  $\pi$ -chromophoric aggregates is imperative for the evolution of novel organic electronic materials. Organization of the chromophores in supramolecular/crystalline assembly play a crucial role in dictating the interchromophoric electronic communication and the effective  $\pi$ -orbital overlap.

Consequently, the structure-property correlation in molecular aggregates can provide a versatile description of exciton migration and/or the delocalization of the charges (hole/electron) in multichromophoric assemblies. In regard to the efficient exciton migration, interplay between the long-range (Coulomb/dipole coupling) and short-range ( $\pi$ -overlap mediated excimer formation) interactions command the optoelectronic output in molecular aggregates crystals. Majority of the work on the chromophoric dye aggregates have described the optical properties in terms of either (i) Coulomb coupling mediated exciton splitting or (ii)  $\pi$ -overlap mediated excimer formation. Investigation of the collective influence of Coulomb coupling and the excimer states on the optical properties of chromophoric aggregates remains sparse. In Chapter 2, we try to deconvolute the effective contributions of the exciton coupling and the excimer interactions on the photoexcited state properties of six crystalline acetylanthracene (1-3) derivatives. Friedel-Crafts acylation of anthracene rendered crystalline mono-, di- and triacetylanthracenes with discrete close-packing (stacking), varied orbital overlap, and a resultant distinct emission (blue-green-yellow). A conjoint theoretical and experimental investigation on the concerted role of long- (Coulomb/dipole coupling) and short-range (orbital overlap mediated excimer) electronic interactions in modulating the excited-state emission of six crystalline acetylanthracenes (1-3) would be discussed in detail.

Long-range photoinduced electron transfer is ubiquitous in nature and plays a crucial role in light harvesting in green plants and respiration in animals. Simulating natural photosynthesis in laboratory necessitates a precise control over the dynamics of the photogenerated excitons in artificial donor-acceptor motifs. Moderating the CT and CS efficiencies of D-A ensemble demands subtle balance between the forward and back (geminate) electron transfer dynamics. The forward electron transfer characteristics ( $k_{cs}$ ) of a D-A hybrid can be partially regulated via modulating the (i) distances and/or (ii) enhancing the electronic coupling among the D and A components. However, photogenerated excitons at D-A interface can instantaneously annihilate due to the Coulomb interactions and further improvement in CS efficiency demand attention toward delaying the geminate charge recombination. Bioinspired self-assembly approach of constructing segregated paths for the delocalization of the complementary charges in covalently linked D-A conjugates has resulted in improving the CS efficiency. Concurrently, seminal supramolecular strategies demonstrated by several groups have proved fruitful in decelerating the instantaneous recombination of radical ion-pair intermediates.

Towards this direction, in Chapter 3, we have utilized the exceptional self-sorting capability of the DNA nucleobases for organizing a hierarchical D-A architecture to achieve long-lived charge separated state. Nucleobases with strong self-sorted base-

pairing and the propensity to transport holes over nanometer lengths are an ideal candidate to provide nanoscale molecular architectures for light-harvesting applications. Herein, we explore the influence of D-A assembly on the ultrafast photoexcited-state processes in AdNp mixed D-A and AdAn alternate distichous supramolecular motifs. Photoexcitation of the mixed D-A AdNp assembly reveals the presence of only a triplet excited state ( $^3\text{Np}^*$ ), whereas the alternate distichous AdAn assembly reveals the formation of long-lived radical ion-pair intermediates. Lack of the RIP intermediates in the mixed D-A assembly suggest the ultrafast charge recombination in AdNp. Contrarily, segregated trajectories of the charge carriers in the alternate distichous assembly offers delocalization of the electron through the columnar  $\pi$ -channels of anthracenes and the diffusion of the holes across hydrogen bonded adenines, resulting in persistent radical ion-pair intermediates. "Emergence-upon-assembly" mediated long-lived charge-separated state in the alternate distichous D-A stack proposes an elegant self-assembly strategy for retarding the rates of the charge recombination in multichromophoric D-A architectures.

In chapter 4, we discuss the self-assembly mediated long-lived charge separation in an all-carbon donor-bridge-acceptor ( $\text{D-B}_n\text{-A}$ ,  $n = 0, 1, 2$ ) motifs wherein aceanthrylene, a functional analog of fullerene ( $\text{C}_{70}$ ) acts an efficient electron acceptor. Planar aceanthrylene act as a versatile electron acceptor owing to the possibility to form hierarchical stacked assemblies, while at the same time possessing high electron affinity, visible light absorption and the structural resemblance to  $\text{C}_{70}$ . Preliminary spectroscopic investigation suggests a shallow distance dependent ( $\beta = 0.11 \text{ \AA}^{-1}$ ) fluorescence quenching in  $\text{P}_n\text{A}$  ( $n = 0, 1, 2$ ) dyads. Interestingly, the all-carbon pyren-1-ylaceanthrylene ( $\text{P}_0\text{A}$ ) dyad forms a self-assembled donor-on-donor and acceptor-on-acceptor bicontinuous assembly which results in extended survival time of the photoinduced radical ion-pair intermediates. Additionally, the semi-classical Marcus theory of charge transfer rates predicts an ambipolar charge transport characteristic in crystalline  $\text{P}_0\text{A}$ , thereby endorsing  $\text{P}_0\text{A}$  as an all-carbon D-A hybrid for nonfullerene photovoltaic applications.



# Contents

---

List of Figures

List of Tables

List of Schemes

List of Abbreviations

<b>1. Lessons from Nature: Photoexcited State Processes in Molecular Aggregates</b>	
1.1. Introduction.....	2
1.2. Natural Light Harvesting.....	3
1.3. Fates of the Excited State.....	8
1.3.1. Intramolecular Excited State Decay.....	8
1.3.1.1. Electronic Absorption .....	9
1.3.1.2. Vibrational Relaxation .....	9
1.3.1.3. Internal Conversion (IC).....	10
1.3.1.4. Fluorescence .....	10
1.3.1.5. Intersystem Crossing (ISC).....	11
1.3.1.6. Phosphorescence .....	11
1.3.1.7. Delayed Fluorescence (DF) .....	11
1.3.2. Intermolecular Electronic Interactions and the Photoexcited State Properties of Chromophoric Ensembles .....	12
1.3.2.1. Photoinduced Electron Transfer .....	12
1.3.2.2. Photoinduced Energy Transfer .....	16
1.3.2.3. Exciton Interactions .....	18
1.3.2.4. Excimer/Exciplex Formation .....	21
1.3.2.5. Singlet Exciton Fission .....	21
1.3.2.6. Singlet-Singlet Annihilation (SSA) .....	22
1.3.2.7. Triplet-Triplet Annihilation (TTA) .....	23
1.4. Artificial Photosynthesis and Light Harvesting.....	23
1.4.1. Water Splitting.....	24
1.4.2. Organic Photovoltaics.....	24
1.5. Emergence Upon Assembly Approach for Light Harvesting.....	26
1.6. Aim and Objective of the Thesis .....	33
<b>2. Concerted Interplay of Excimer and Dipole Coupling Governs the Exciton Relaxation Dynamics in Crystalline Anthracenes</b>	
2.1. Introduction.....	35
2.2. Results and Discussion .....	39
2.2.1. Syntheses and Structure.....	39

---

---

2.2.2. Close-Packing Analyses.....	40
2.2.3. Quantum Theory of Atoms in Molecules (QTAIM) and Hirshfeld Analyses	45
2.2.4. Pitch and Roll Analyses.....	48
2.2.5. Excited-State Properties in Isotropic Solution.....	49
2.2.6. Excited-State Properties in Crystalline Assembly.....	53
2.2.7. Estimating the Dipole Coupling (Mean Field Approximation).....	60
2.2.8. Time-Resolved Emission Spectral (TRES) Analysis.....	65
2.3. Conclusions.....	70
2.4. Experimental section.....	71
2.4.1. Syntheses and Characterization .....	71
2.5. Additional Figures and Tables.....	74
2.6. Appendix.....	80
<b>3. Nucleobase-Arene Assembly for Long-Lived Charge Separation</b>	
3.1. Introduction.....	89
3.2. Synthesis and Structure of N-Arylated Adenines .....	91
3.3. Results and Discussion .....	98
3.3.1. Steady-State Photophysical and Aggregation Studies .....	98
3.3.2. Frontier Molecular Orbital and Weller Analysis .....	102
3.3.3. Characterization of the Transient Radical Ion-Pair Intermediates.....	104
3.3.3.1. Femtosecond Transient Absorption (fTA) Measurements.....	104
3.3.3.2. Nanosecond Transient Absorption (nTA) Measurements.....	106
3.3.3.3. Spectroelectrochemistry and Simulation of RIP Intermediates....	110
3.3.3.4. Concentration Dependent Cyclic Voltammetry and FMO analyses.....	111
3.4. Conclusions.....	117
3.5. Experimental Section.....	119
3.5.1. Syntheses and Characterization .....	119
3.6. Additional Figures and Tables.....	120
3.7. Appendix.....	126
<b>4. Prolonged Charge Separated States in Twisted Stacks of All-Carbon Donor and Acceptor Stacks</b>	
4.1. Introduction.....	135
4.2. Results and Discussion .....	138
4.2.1. Synthesis and Structure of All-Carbon Donor-bridge-Acceptor Dyads .....	138
4.2.2. Steady-State Photophysical Studies .....	145
4.2.3. Concentration Dependence and Aggregation Studies .....	149
4.2.4. Cyclic Voltammetry, FMO and Rehm-Weller Analysis .....	151
4.2.5. Characterization of the Transient Radical Ion-Pair Intermediates.....	154
4.3. Conclusions.....	158
4.4. Experimental Section.....	160

---

4.5.	Additional Figures and Tables.....	169
4.6.	Appendix.....	177
<b>5.</b>	<b>Bibliography.....</b>	<b>186</b>
<b>6.</b>	<b>List of Publications.....</b>	<b>204</b>
<b>7.</b>	<b>Internship, Workshop and Conferences.....</b>	<b>206</b>
<b>8.</b>	<b>Copyrights and Permission.....</b>	<b>208</b>

## List of Figures

Figure	Title	Page
1.1.	a) Cross section of a leaf and b) primary sites of photosynthesis (chloroplasts) showing thylakoid membranes and stroma.	3
1.2.	Schematic illustration of a) funnel analogy of a photosynthetic antenna; b) spherical chromatophore from Rhodobacter sphaeroides showing proteins (left) and bacteriochlorophylls (right); c) One LH1-RC complex with three LH2 complexes nearby; and d) simplified scheme in charge separation and electron transfer events in the purple bacterial reaction centre.	4
1.3.	a) Fates of the excited state of a molecule (monomer) after photoexcitation; and b) Perrin-Jablonski diagram depicting the various excited state transitions.	9
1.4.	Schematic depiction of reductive electron and oxidative hole transfer in D/A systems.	13
1.5.	Schematic depiction of a) potential energy description of electron-transfer process; b) Marcus theory prediction of the dependence of the electron transfer rate on the thermodynamic driving force.	15
1.6.	Schematic depiction of intermolecular excitation energy (homo and hetero molecular) transfer in donor (D) and (acceptor) systems.	16
1.7.	Schematic depiction of a) intermolecular excitation energy migration in donor (D) and (acceptor) systems via dipole-dipole coupling and b) spectral overlap among the donor emission and the acceptor absorption spectra for resonance energy transfer.	17
1.8.	Schematic depiction of exciton coupling in a) parallel cofacial (H-aggregate); b) staggered cofacial (J-aggregate); and c) oblique (Davydov splitting) transition dipoles.	20
1.9.	Mechanism of the excimer formation; b) fluorescence emission spectra depicting the signature corresponding to pyrene excimer and c) schematic depiction of pyrene excimer formation.	21
1.10.	a) Mechanism of exciplex formation; and b) fluorescence emission spectra depicting the signature corresponding to anthracene and dimethyl aniline exciplex.	22
1.11.	Mechanism of the singlet exciton fission.	22
1.12.	Mechanism of the singlet-singlet annihilation.	22
1.13.	Mechanism of the triplet-triplet annihilation.	23

1.14.	Schematic depiction of a) device structures of bilayer/bulk heterojunction; and b) the light induced processes occurring after the photoexcitation.	25
1.15.	Schematic depiction of a) Monomeric PMI-Ph <sub>2</sub> -D dyad and the self-sorted stacked assembly; fTA spectra of b) monomeric PMI-Ph <sub>2</sub> -D in THF; and c) self-assembled PMI-Ph <sub>2</sub> -D in MCH; d) H-bonded DPP (donor, red) and PDI (acceptor, purple) assembly; e) superstructure formation upon annealing; and f) fTA spectra of the 2:1 (DPP:PDI) mixture in toluene with absorption vs. time profiles at $\lambda = 622$ nm (upper inset) and $\lambda = 722$ nm (lower inset).	28
1.16.	Schematic depiction of a) self-assembled donor-acceptor $\pi$ -peptide hybrid; fTA spectral dynamics of b) unassembled; and c) self-assembled D-A hybrid in aqueous solutions.	29
1.17.	Schematic depiction of a) donor-bridge-acceptor dyad based on guanine (G)/PDI and the core-shell columnar assembly of GPDI; b) fTA spectra of self-assembled GPDI quadruplex ( $3 \times 10^{-3}$ M + 0.25 eq. of KPF <sub>6</sub> ) in THF. Inset shows the principal kinetic components and decay-associated spectra of GPDI-quadruplex.	30
1.18.	Molecular structure and Schematic depiction of tubularly assembled a) segregated D-A stack assembly in 2 and b) mixed D-A stack in 3; and c) log I-V profiles at 25 °C of cast films of tubularly assembled 2 (red) and 3 (blue) in PV devices.	32
2.1.	Close-packing arrangement in the acetylanthracene derivatives a) 1A; b) 1B; c) 2A; d) 2B; e) 2C and f) 3 indicating the values of $q[(\%C\bullet\bullet\bullet H)/(\%C\bullet\bullet\bullet C)]$ . Herringbone ( $q > 4.5$ ), sandwich herringbone ( $3.2 < q < 4.0$ ), $\gamma$ ( $1.2 < q < 2.7$ ) and $\beta$ ( $0.46 < q < 1.0$ ).	40
2.2.	Close-packing arrangement in acetylanthracene derivatives guided by weak intermolecular interactions (C-H $\bullet\bullet\bullet$ H-C, C-H $\bullet\bullet\bullet$ O, C $\bullet\bullet\bullet$ C, and C-H $\bullet\bullet\bullet$ $\pi$ ) in a) 1A; b) 1B; c) 2A; d) 2B; e) 2C; and f) 3.	42
2.3.	Angle between the mean planes of adjacent molecules in the crystal packing of a) 1A; b) 1B; c) 2A; d) 2B; e) 2C; and f).	43
2.4.	QTAIM electron density map of a) 2B; and b) 3.	45
2.5.	a) Percentage contribution of intermolecular interactions in crystalline acetylanthracenes (1-3); b) Hirshfeld surface mapped with $d_{norm}$ depicting hydrogen (C-H $\bullet\bullet\bullet$ O) bonding and c) 2D fingerprint plot obtained from Hirshfeld surface analysis of 2A.	47
2.6.	a) Pitch and b) roll displacement analysis and c) co-facial stacking motif and the definition of pitch (P) and roll (R) angles and associated distances among nearest co-facial anthracene units in 2A. The acetyl group and the hydrogen atoms are omitted for clarity. The sphere at the center of the ring denotes the centroid of the molecule.	48
2.7.	Normalized fluorescence excitation (solid) and emission (dashed) spectra of a) 1A; b) 1B; c) 2A; d) 2B; e) 2C and f) 3 in CHCl <sub>3</sub> (shaded blue, $\lambda_{ex} = 350$ nm) and crystalline (shaded red, $\lambda_{ex} = 360$ nm) state. Excitation spectra were monitored at 474 and 490 nm (1A); 450 and 513 nm (1B); 450 and 555 nm (2A); 461 and 487 nm (2B); 451 and 538 nm (2C); and 460 and 550 nm (3) for solution and crystalline state, respectively.	50

2.8.	Fluorescence excitation spectra of a) 1A; b) 1B; c) 2A; d) 2B; e) 2C and f) 3 in CHCl <sub>3</sub> as compared to absorption spectrum (black).	54
2.9.	Picosecond time-resolved fluorescence decay profiles of a) 1A (474 nm); b) 1B (450 nm); c) 2A (460 nm); d) 2B (461 nm); e) 2C (450 nm) and f) 3 (450 nm) in CHCl <sub>3</sub> . Excitation wavelength, $\lambda_{ex} = 377$ nm (pulsewidth = 100 ps). The fluorescence decay of the derivative 3 could not be fitted as the decay was fast compared to the pulsewidth of the excitation source.	55
2.10.	Fluorescence excitation spectra of crystalline a) 1A; b) 1B; c) 2A; d) 2B; e) 2C; and f) 3 as compared to the absorption spectra. Absorption spectra of crystalline 1-3 derivative are reproduced for comparison. Emission maxima, where the excitation spectra are monitored, are indicated in the bracket.	56
2.11.	Picosecond time-resolved fluorescence decay profiles of crystalline a) 1A; b) 1B; c) 2A; d) 2B; e) 2C and f) 3 monitored at different wavelengths. Excitation wavelength, $\lambda_{ex} = 377$ nm (pulsewidth = 100 ps).	57
2.12.	a) Characteristic excited-state transitions illustrating concerted excimer and dipole couplings in monomer vs. crystalline state and b) monomer, dimer (nearest-neighbour) and molecular ensemble (mean-field approximation) used for exciton coupling calculations in crystalline 1-3 [133]. For clarity the central molecule of the assembly in Figure 2.12b is depicted in purple.	62
2.13.	Time-resolved emission spectrum (TRES) (a, b, c); normalized evolution associated spectra (EAS; d, e, f) and the relative population profiles (g, h, i) of crystalline 2A, 2C and 3 respectively; excitation wavelength is 377 nm (pulse width $\leq 100$ ps). The emission spectra of 2A, 2C and 3 in CHCl <sub>3</sub> (shaded grey) solution are depicted for comparison in Figure 2.12d, e and f.	66
3.1.	(a) Molecular structure, (b) mixed D-A stack and (c) close-packing analysis depicting the intermolecular interactions in crystalline AdNp.	93
3.2.	(a) Molecular structure; (b) alternate distichous stacks; (c) the percentage of An-An overlap in $\pi$ -stacked anthracenes; and (d) close-packing analysis depicting the intermolecular interactions in crystalline AdAn.	94
3.3.	QTAIM electron density map depicting intermolecular interactions among the stacked dimers (a,c) and self-sorted adenines (b,d) in AdNp (a,b) and AdAn (c, d).	96
3.4.	Hirshfeld surface mapped with $d_{norm}$ (left) and 2D fingerprint plots (right) for crystalline AdNp (a,b) and AdAn (c, d).	97
3.5.	UV-vis absorption (blue), emission (maroon, $\lambda_{ex} = 300$ [AdNp] and 350 [AdAn] nm) and time-resolved fluorescence decay spectra of the nucleobase-arene conjugates AdNp (a, b) and AdAn (c, d) in dilute chloroform solution. For comparison the UV-vis absorption and emission spectra of the model arene derivatives Np and An are shown in Figure 3.5 a, c (dashed lines).	99
3.6.	Concentration dependent a) absorption; b) Beer-Lambert's plot depicting the deviation from linearity while monitoring at 388 nm; c) SEM (silicon wafer); d) TEM (carbon coated Cu grid); e) confocal image and f) SAED pattern for AdAn (1 mM) in CHCl <sub>3</sub> .	101
3.7.	Frontier molecular orbital (FMO) analysis of AdNp (left) and AdAn (right) calculated from B3LYP-D3/6-31G+(d,p) level of theory in Schrödinger	103

---

	Materials Science Suite using Jaguar DFT engine.	
3.8.	fTA spectra of AdAn ( $\lambda_{\text{ex}} = 360$ nm, pulsewidth = 110 fs, 1 mM in $\text{CHCl}_3$ ) conjugates depicting the 2D intensity plot (top), spectra (middle) and evolution associated spectra (EAS, bottom).	104
3.9.	nTA spectra of AdNp ( $\lambda_{\text{ex}} = 266$ nm, pulsewidth = 7 ns, 1 mM in $\text{CHCl}_3$ ) assembly depicting the 2D intensity plot (top), spectra (middle) and evolution associated spectra (EAS, bottom) in a) nitrogen and b) oxygen purged solutions.	106
3.10.	nTA spectra of AdAn ( $\lambda_{\text{ex}} = 355$ nm, pulsewidth = 7 ns, 0.12 mM) assembly depicting the 2D intensity plot (top), spectra (middle) and evolution associated spectra (EAS, bottom) in a) diethylether (100 ns $\rightarrow$ 20 $\mu\text{s}$ ) and b) chloroform (100 ns $\rightarrow$ 45 $\mu\text{s}$ ) solution.	107
3.11.	nTA spectra (100 ns $\rightarrow$ 45 $\mu\text{s}$ ) of AdAn assembly depicting the 2D intensity plot (top), spectra (middle) and evolution associated spectra (EAS, bottom) in a) methanol ( $\lambda_{\text{ex}} = 355$ nm, 0.12 mM) and b) chloroform ( $\lambda_{\text{ex}} = 266$ nm, 0.12 mM) solutions.	109
3.12.	Absorption spectra of a) $\text{Ad}^{\bullet+}$ (shift = -0.55 eV) and b) $\text{An}^{\bullet-}$ (shift = -0.21 eV) computed at PCM/TD-M06-2X/6-311G+(d,p) level of theory.	111
3.13.	a) Cyclic voltammetric (CV) analysis of AdAn (1 mM in $\text{CH}_2\text{Cl}_2$ ); b) concentration dependent (0.5 - 2 mM) CV measurements and c) decrease in reduction potential of AdAn with increasing concentration. Scan rate = 50-100 $\text{mV s}^{-1}$ with 0.1 M $\text{nBu}_4\text{NPF}_6$ as supporting electrolyte in $\text{CH}_2\text{Cl}_2$ .	112
3.14.	Frontier molecular orbital (FMO) analysis of AdAn (mono, dimer, tetramer and octamer) calculated from B3LYP-D3/6-31G+(d,p) level of theory in Schrödinger Materials Science Suite using Jaguar DFT engine.	113
3.15.	a) TLC analysis of the AdAn (in $\text{CHCl}_3$ ) before and after nTA analysis; B) high resolution mass spectrum of precipitate (AdAn dimer) obtained after nTA analysis in $\text{CHCl}_3$ ( $\lambda_{\text{ex}} = 355$ nm).	114
3.16.	Photoexcited state processes and kinetic pathways adopted by a) AdNp ( $\lambda_{\text{ex}} = 266$ nm) and b) AdAn ( $\lambda_{\text{ex}} = 266$ or 355 nm) assembly upon photoexcitation.	115
4.1.	a) Potential energy surfaces for the change in the torsional angle along C1-C2-C17-C18 (inset shows the expanded view for the potential energy surface) and b) pictorial representation of the torsion angle variation (0 to 180°) along C1-C2-C17-C18 in the dyad $\text{P}_0\text{A}$ .	141
4.2.	a) Packing motif; b) packing view along a-axis; c) the $\text{C}\cdots\text{Br}$ interaction propagating along c-axis and d) the $\pi$ - $\pi$ interaction propagating along a-axis in the derivative A-Br.	142
4.3.	QTAIM electron density map depicting intermolecular a) $\text{C}\cdots\text{Br}$ interaction in crystalline A-Br; b) $\text{C-H}\cdots\pi$ interaction in crystalline $\text{P}_0\text{A}$ and c) $\text{C-H}\cdots\text{H-C}$ and $\text{C-H}\cdots\text{C}$ interactions in $\text{P}_1\text{A}$ .	142
4.4.	Hirshfeld surface mapped with $\text{dnorm}$ (a, d, g); 2D fingerprint plots with the region corresponding to $\text{C-H}\cdots\pi$ (b, e, h) and $\pi$ - $\pi$ (c, f, i) interaction in A-Br, $\text{P}_0\text{A}$ and $\text{P}_1\text{A}$ , respectively.	144
4.5.	a) Schematic depiction of resemblance among crystalline $\text{P}_0\text{A}$ and $\text{P}_0\text{C}_{60}$ (proposed structure) dyads; b, c) bicontinuous D-on-D and A-on-A packing	145

---

	motif in P <sub>0</sub> A; d) packing motif depicting the $\pi$ - $\pi$ stacking; e) the intermolecular C-H... $\pi$ interaction propagating along c-axis and f) the stacking mediated D-on-D (50%) and A-on-A (45%) overlap in P <sub>0</sub> A.	
4.6.	a) Packing motif; b) tilted D-on-D and A-on-A stacks and c) packing view (top view) along bc-plane in P <sub>1</sub> A crystalline motif.	146
4.7.	a) UV-vis absorbance; fluorescence b) emission and c) lifetime of model derivatives (A-Br, P <sub>0-2</sub> ) and D-B-A (P <sub>0-2</sub> A) motifs in toluene.	147
4.8.	Exponential distance dependence of $\ln(k_{CS})$ versus $R_{(D-A)}$ for D-B-A (P <sub>0-2</sub> A) motifs in toluene.	149
4.9.	a) Concentration dependent absorption; b) DLS particle size distribution; c) 3D AFM (silicon wafer); d) SEM (silicon wafer); e) TEM (carbon coated Cu grid) images and f) SAED pattern of P <sub>0</sub> A (0.6 mM) in THF.	150
4.10.	Particle size distribution of P <sub>0</sub> A obtained from a) AFM; b) SEM; and c) TEM analyses in THF.	151
4.11.	a) Cyclic voltammetric analyses of A-Br and P <sub>0</sub> A in CHCl <sub>3</sub> vs. Ag/AgCl and b) FMO analysis of P <sub>0</sub> A monomer calculated using Jaguar DFT engine (B3LYP-D3/6-31G+(d,p)) in Schrödinger Materials Science Suite.	152
4.12.	a) fTA spectra; b) DAS of 0.6 mM P <sub>0</sub> A in THF. c) UV-vis SEC (0 to -1.5 V) analysis of P <sub>0</sub> A in THF using 0.1 M n-Bu <sub>4</sub> NPF <sub>6</sub> ; d) differential absorption spectrum of reduced A (A <sup>-</sup> ) attained by subtracting the absorption plots obtained before and after applying reduction potentials for the UV-vis spectroelectrochemistry data shown in Figures 4.12c; e) CW-EPR spectrum of P <sub>0</sub> A (2 mM in THF) at 77 K; Smooth curve (red) is computer simulation for experimental spectra (black).	154

## List of Tables

Table	Title	Page
2.1.	Crystallographic data and refinement parameters for crystalline 1-3 derivatives.	41
2.2.	Shows the various packing arrangements, $\pi$ -stacking distances and % $\pi$ -overlap in crystalline 2A-C, and 3 derivatives.	43
2.3.	Calculated topological properties of the electron density for the intra- and intermolecular interaction in 2B and 3 crystal derivatives.	46
2.4.	Percentage of intermolecular contacts of a single molecule in 1-3 crystal derivatives.	47
2.5.	Pitch and roll displacement angles and distances for the crystalline 1-3.	49
2.6.	Photophysical properties of 1-3 derivatives in solution and crystalline state.	51
2.7.	Excimer and dipole coupling (mean field approximation) mediated spectral shifts and the optical properties of acetylanthracene derivatives (1-3) in solution/crystalline.	64
3.1.	Crystallographic data and refinement parameters for AdNp and AdAn crystal derivatives.	92
3.2.	Calculated topological properties of the electron density for the intermolecular interaction in crystalline AdNp and AdAn.	95

3.3.	The percentage intermolecular interactions obtained from Hirshfeld surface analysis in crystalline AdNp and AdAn.	96
3.4.	Photophysical properties of AdNp and AdAn in CHCl <sub>3</sub> .	99
3.5.	Electrochemical redox potential and free energy of electron transfer ( $\Delta G_{CS}$ ) calculated for nucleobase-arene conjugates (AdNp and AdAn) in CHCl <sub>3</sub> .	103
4.1.	Crystallographic data and refinement parameters for crystalline A-Br, P <sub>0</sub> A and P <sub>1</sub> A.	140
4.2.	Calculated topological properties of the electron density for the intermolecular interaction in crystalline A-Br and P <sub>0</sub> A.	143
4.3.	Percentage intermolecular interactions in crystalline A-Br, P <sub>0</sub> A and P <sub>1</sub> A.	143
4.4.	Photophysical properties of all-carbon P <sub>0-2</sub> A dyads and the model derivatives (A-Br, P <sub>0-2</sub> ) in toluene.	148
4.5.	Electrochemical redox properties vs. Ag/AgCl and geometry optimized optoelectronic calculations of P <sub>0</sub> A [B3LYP/6-31G+(d,p)] and A-Br using Jaguar DFT engine [B3LYP/LACVP+(d,p)] in Schrödinger Materials Science Suite.	153
4.6.	Calculated hole/electron mobilities and reorganization energies for P <sub>0</sub> A using Jaguar DFT engine in Schrödinger Materials Science Suite.	158

### List of Schemes

Scheme	Title	Page
2.1.	Simplified schematic depiction of exciton band energy diagram for molecular H-type, J-type and oblique dimers.	36
2.2.	Chemical and molecular structure, structure formula, stacking, %overlap and the distance (d) between the nearest $\pi$ -stacked anthracenes in a) 1A; b) 1B; c) 2A; d) 2B; e) 2C and f) 3 with the crystal images of the derivatives under ambient (left) and under UV illumination (354 nm, right). <sup>a</sup> d= distance between the nearest-neighbors; n.d.= not determinable due to oblique stacking.	38
3.1.	Molecular structures of the N-arylated adenine (AdNp, and AdAn) conjugates under discussion.	90
3.2.	General synthesis scheme for the nucleobase-arene (AdNp, and AdAn) conjugates.	91
4.1.	Molecular structures of the all-carbon D-A dyads (bottom) and the model D and A components (top) under discussion.	137

## List of Abbreviations

ET	Electron Transfer
D-A	Donor-Acceptor
CS	Charge Separation
TW	Tera Watt
1D/2D/3D	One/Two/Three Dimensional
RC	Reaction Centre
LH1/LH2	Light Harvesting Complex 1/Light Harvesting Complex 2
SP	Special Pair
BChl	Bacteriochlorophyll
PSII	Photosystem II
ADP/ATP	Adenosine Diphosphate/Adenosine Triphosphate
IC	Internal Conversion
ISC	Intersystem Crossing
DF	Delayed Fluorescence
D	Donor
A	Acceptor
SF	Singlet Fission
SSA	Singlet-Singlet Annihilation
TTA	Triplet-Triplet Annihilation
OPV	Organic Photovoltaics
PMI	Perylene-3,4-dicarboxamide
MCH	Methylcyclohexane
RIP	Radical Ion-Pair
fTA	Femtosecond Transient Absorption
THF	Tetrahydrofuran
PDI	Perylenediimide
DPP	Diketopyrrolopyrrole

DNA	Deoxyribonucleic Acid
P <sub>Zn</sub>	Zinc Porphyrin
C <sub>60</sub>	C <sub>60</sub> Fullerene
TRES	Time Resolved Emission Spectrum
AA	Acetylanthracene
CS <sub>2</sub>	Carbon Disulphide
QTAIM	Quantum Theory of Atoms in Molecules
CHCl <sub>3</sub>	Chloroform
EAS	Evolution Associated Spectra
CIE	Commission Internationale de l'Eclairage
Alq <sub>3</sub>	Tris(8-hydroxyquinolate)aluminium
IRF	Instrument Response Function
TDDFT	Time Dependent Density Functional Theory
HOMO	Highest Occupied Molecular Orbital
LUMO	Lowest Unoccupied Molecular Orbital
TDC	Transition Density Cube
Ad	Adenine
Np	Naphthalene
An	Anthracene
AdNp	9-(adenine-9-yl)naphthalene
AdAn	9-(adenine-9-yl)anthracene
UV-vis	Ultraviolet-visible
SEM	Scanning Electron Microscopy
TEM	Tunneling Electron Microscopy
AFM	Atomic Force Microscopy
SAED	Selected Area Electron Diffraction
FMO	Frontier Molecular Orbital
DFT	Density Functional Theory
nTA	Nanosecond Transient Absorption

CW-EPR	Continuous Wave Electron Paramagnetic Resonance
CT	Charge Transfer
HRMS	High Resolution Mass Spectrometry
BCP	Bond Critical Point
DE	Dissociation Energy
CD	Concentration Dependent
DEE	Diethyl Ether
SEC	Spectroelectrochemical
CV	Cyclic Voltammetry
TLC	Thin Layer Chromatography
CNT	Carbon Nanotube
G	Graphene
CND	Carbon Nanodots
DCM	Dichloromethane
NMR	Nuclear Magnetic Resonance
IR	Infrared
m. p.	Melting point
CPA	Cyclopenta[ <i>hi</i> ]aceanthrylene
CP-PAH	Cyclopentafused Polyaromatic hydrocarbons
D-B-A	Donor-Bridge-Acceptor
A-A	Acceptor-on-Acceptor
D-D	Donor-on-Donor
NBS	N-Bromosuccinimide
DLS	Dynamic Light Scattering
D <sub>H</sub>	Hydrodynamic Diameter
TMS	Trimethylsilyl
ORTEP	Oak Ridge Thermal Ellipsoid Plot
EA	Electron Affinity
DAS	Decay Associated Spectra



# Chapter 1

## Lessons from Nature: Photoexcited State Processes in Molecular Aggregates

### 1.1. Introduction

Photodriven electron transfer (ET) in natural and synthetic donor-acceptor (D-A) motifs has received immense attention due to its importance in complex biological processes akin respiration [1], solar light harvesting [2], and its implications in the construction of novel molecular machineries for efficient light-to-energy conversion [2-4]. Molecular mimicry of natural photosynthesis, where sequential energy and electron transfer cascades promote a long-lived charge separation (CS, ~100% efficiency), serves as a vital inspiration for the design of artificial photosynthetic architectures [5-7]. Herein, coherent funnelling of the excitation energy by the light harvesting antenna complexes and the relatively fast short-range electron transfer at the reaction centre delivers a large overall charge-separation distance and prevents the loss of the photoinduced redox potential by rapid back electron transfer (Figure 1.1-1.2.) [5, 8]. Nevertheless, the imitation of natural light harvesting system in laboratory is limited by the fundamental issues of having an ideal supramolecular assembly which can provide a controlled directional energy and electron transfer cascade for efficient solar energy harvesting. Progressive research towards tackling the bottlenecks in this direction can have potential impact on the state-of-the-art

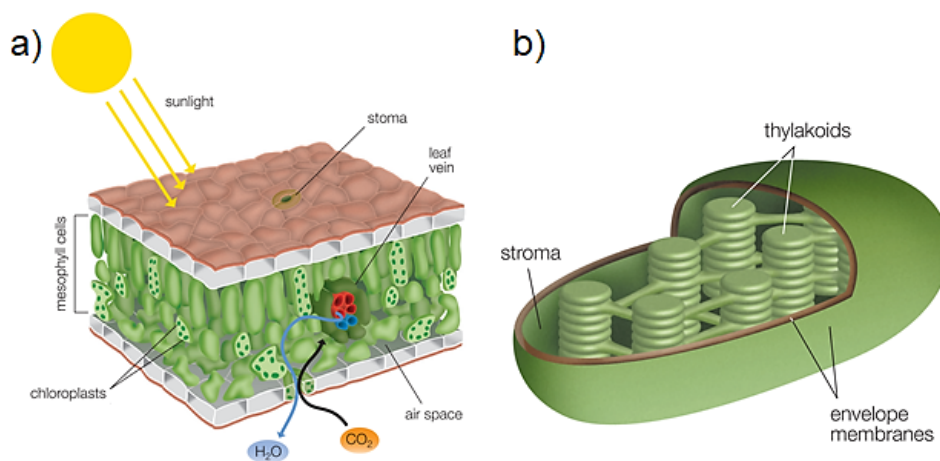


**Figure 1.1.** *a) Cross section of a leaf and b) primary sites of photosynthesis (chloroplasts) showing thylakoid membranes and stroma. (Adapted with permission from Ref. [8]. Copyrights © 2013, Pearson Education Ltd).*

molecular scale optoelectronics, photonics, and semiconducting applications.

## 1.2. Natural Light Harvesting

Light harvesting in photosynthetic bacteria, algae and plants is one of the perfect examples of the efficient utilization of solar energy in nature [9, 10]. Globally, the photosynthetic machinery converts solar energy into a proton gradient across the cellular membrane which propels a multitude of molecular processes responsible for the proficient transformation of light into biomass at a rate of  $1.2 \times 10^{11}$  terawatt (TW) each year (about 50 times the energy consumed by humans) [10, 11]. The impeccable efficiency of the natural light harvesting in green plant lies in the hierarchical three dimensional (3D) structure of the light harvesting apparatus (chromatophore) wherein the redox-active, electronically complementary chromophores are precisely embedded in the protein matrix (Figure 1.2.) [12].

The photosynthetic apparatus (chromatophore) of the purple bacterial consists

of a supramolecular assembly of membrane proteins wherein array of antenna pigment chromophores are strategically organized around the reaction centre (RC, Figure 1.2a-b) [11]. The structure of purple bacterial cell possess approximately 1000 spherical vesicles-like chromatophores [13] as shown in Figure 1.2b [11, 14, 15]. Each

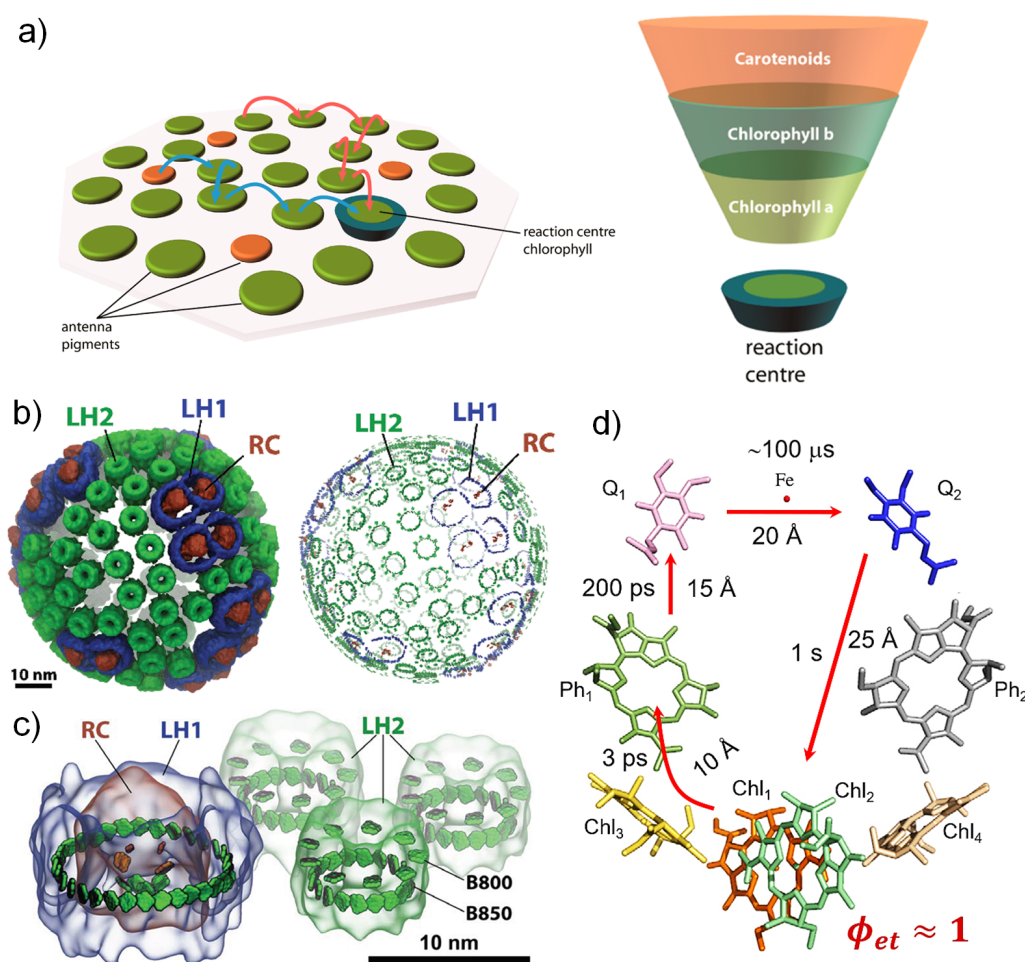


**Figure 1.2.** Schematic illustration of a) funnel analogy of a photosynthetic antenna (Adapted with permission from Ref. [12]. Copyrights © 2015, Springer Science Business Media New York); b) spherical chromatophore from *Rhodobacter sphaeroides* showing proteins (left) and bacteriochlorophylls (right); c) One LH1-RC complex with three LH2 complexes nearby (Adapted with permission from Ref. [11]. Copyrights © 2012, American Chemical Society); and d) simplified scheme in charge separation and electron transfer events in the purple bacterial reaction centre. (Adapted with permission from Ref. [16]. Copyrights © 2011, Elsevier B. V.)

chromatophore consists of a (i) secondary light harvesting complex (LH2); (ii) primary light harvesting complex (LH1) and (iii) RC comprising of the special pair (SP) of bacteriochlorophyll (BChl) which initiates the primary charge-separation in photosynthesis (Figure 1.2b) [11]. The chromatophore of purple bacteria consists of approximately 50-100 LH2, 10-20 LH1-RC complexes which drives together the charge-separation in photosynthesis [11, 14, 15]. The principal components of the chromatophore are precisely arranged in strategic positions to form a coherent ensemble structure and maximize the utility of individual chromophoric units.

The LH2 complex in the chromatophore are tactically arranged at the periphery and primarily functions to absorb and transfer the excitation energy to the LH1-RC complex located in the interior region (Figure 1.2c) [11]. The LH2 complex is smaller ring protein as compared to the LH1 complex and consists a framework of 27 BChls and 9 carotenoids [11, 17, 18]. The LH2 complex consist of two forms of BChl rings, i.e. B850 ring and a B800 ring, where 850 and 800 denotes their absorption maxima of the chromophores [11]. The B850 rings are tightly packed, whereas the B800 are loosely packed in a perpendicular direction to the B850 rings. The primary feature of B800 is to increase the absorption cross-section of the B850 ring and the ultrafast excitation energy transfer from B800 to B850 occurs in <1 ps [11, 19]. Subsequently, the coherent energy migration (within 20 ps) among the LH2 - LH2 complexes and LH2 - LH1 complex mediates the excitation migration to

the BChls in the LH1 complex [11, 20, 21].

The LH1 complex consists of 32 BChls (B875) rings and 16 carotenoids tightly arranged in a ring fashion around the RC and greatly enhances the absorption cross-section of the RC (Figure 1.2c) [22]. The tight packing of the B850s and the carotenoids render a strong exciton coupling mediated energy migration to the RC within 50 ps or less [11]. The most crucial segment of the chromatophore, the RC, consist of four BChl (Chl<sub>1-4</sub>); two bacteriopheophytin (Ph<sub>1</sub>, Ph<sub>2</sub>; similar to Chl<sub>1-4</sub>, but without Mg) and two quinone (Q<sub>1</sub> and Q<sub>2</sub>) moieties (Figure 1.2d) [11, 16]. The direct excitation and the downhill energy cascades, LH2→LH1→RC, lead to the coherent photoexcitation of the excitonically coupled (500-1000 cm<sup>-1</sup>) SP of BChls (Chl<sub>1</sub> and Chl<sub>2</sub>) in the RC [11, 23]. The SP then initiates the charge separation via transferring an electron to bacteriopheophytin (Ph<sub>1</sub>) mediated by the primary acceptor Chl<sub>3</sub> within 3 ps [11, 16]. Subsequent electron transfer to the permanently bound quinone Q<sub>1</sub> (within 200 ps) and then to the quinone (Q<sub>2</sub>) in approximately 100 μs render a charge separated state Q<sub>2</sub><sup>•-</sup> and Chl<sub>1</sub><sup>•+</sup> [16].

The quinone Q<sub>2</sub> is subsequently doubly reduced and protonated to form Q<sub>2</sub>H<sub>2</sub> which has a low affinity for the RC [16, 24]. Subsequently, Q<sub>2</sub>H<sub>2</sub> diffuses in the hydrophobic core of the bilayer which can be replaced by a quinone from the pool in the membrane [24, 25]. The Q<sub>2</sub>H<sub>2</sub> is transported across the membrane to the cytochrome c<sub>2</sub> (Cyt c<sub>2</sub>) via cytochrome bc<sub>1</sub> (Cyt bc<sub>1</sub>) and this drives the accumulation

of the electrochemical (proton) gradient in the periplasmic region of the membrane [24, 25]. The electron circuit is completed by transfer of low-energy electrons from Cyt  $bc_1$  to a soluble periplasmic protein, Cyt  $c_2$  which drives the consequent redox reactions for the ultimate conversion of ADP to ATP in the membrane [24, 25]. Electrons then move to the cytochrome subunit of the RC, which supplies SP with electrons for the photosynthetic reaction cycle [24, 25]. The reaction centre of photosystem II (PSII) in green plants is analogous to the purple bacteria RC, however is a bit complicated than RC in the purple bacteria [16]. Herein, the initially formed BChl<sub>1</sub> is stabilized by a tyrosine residue which subsequently oxidizes the Mn<sub>4</sub>Ca complex, the active site for water splitting, and which controls the subsequent redox reaction in the PSII [16]. Thus the main characteristic defining the unity quantum efficiency of the photosynthetic apparatus in purple bacteria, algae and green plants lies in (i) the way in which the light harvesting pigments tactically capture the light and coherently distribute the excitation energy to the reaction centre by the antenna complexes (ii) the fast short-range multiple electron transfer steps which provides an overall long-lived charge separated states at longer distances and (iii) minimizing the energy wasting pathways such as de-excitation via nonradiative process from single or triplet manifolds [5]. Thus mimicking the photosynthetic apparatus in laboratory necessitates the replication of the long-range coherent excitation energy migration and the creation of the long-lived charge separated states at the same time minimizing the energy-wasting reaction for

employing in organic photovoltaics or water splitting applications.

### 1.3. Fates of the Excited States

Depending on the geography and the seasonal changes, the plants on a daily basis can receive excess energy than that is required by the photosynthetic light harvesting apparatus [26]. In such situations, a subtle balance between the light absorption and utilization is necessary to limit the amount of photooxidative damage to the plants [26]. A status quo is achieved via releasing the excess excitation energy via alternative deexcitation pathways of BChl chromophore [26]. Consequently, exploration of the fates of an excited chromophore is vital from a fundamental perspective as well as the technological purview of light harvesting. The fates of an excited chromophore (monomer) after its initial electronic excitation depends on the various deexcitation paths akin (i) radiative decay; (ii) nonradiative decay; (iii) photochemical reactions; (iv) accessing triplet excited state etc. (Figure 1.3a). Photoexcited state properties of isolated molecules and organized chromophoric assemblies are dissimilar. Photoexcited state properties of a single chromophore can get modulated by the surrounding media (vacuum, gaseous, solvent or condensed state) or redox/electronically complementary chromophoric bodies.

#### 1.3.1. Intramolecular Excited State Decay

The Perrin-Jablonski diagram shown in Figure 1.3b represent the photoexcited state properties of a single molecule in isolated environment. Herein,  $S_0$  is the ground electronic state of the molecule, whereas the  $S_1/S_2$  and  $T_1/T_2$  represent the excited

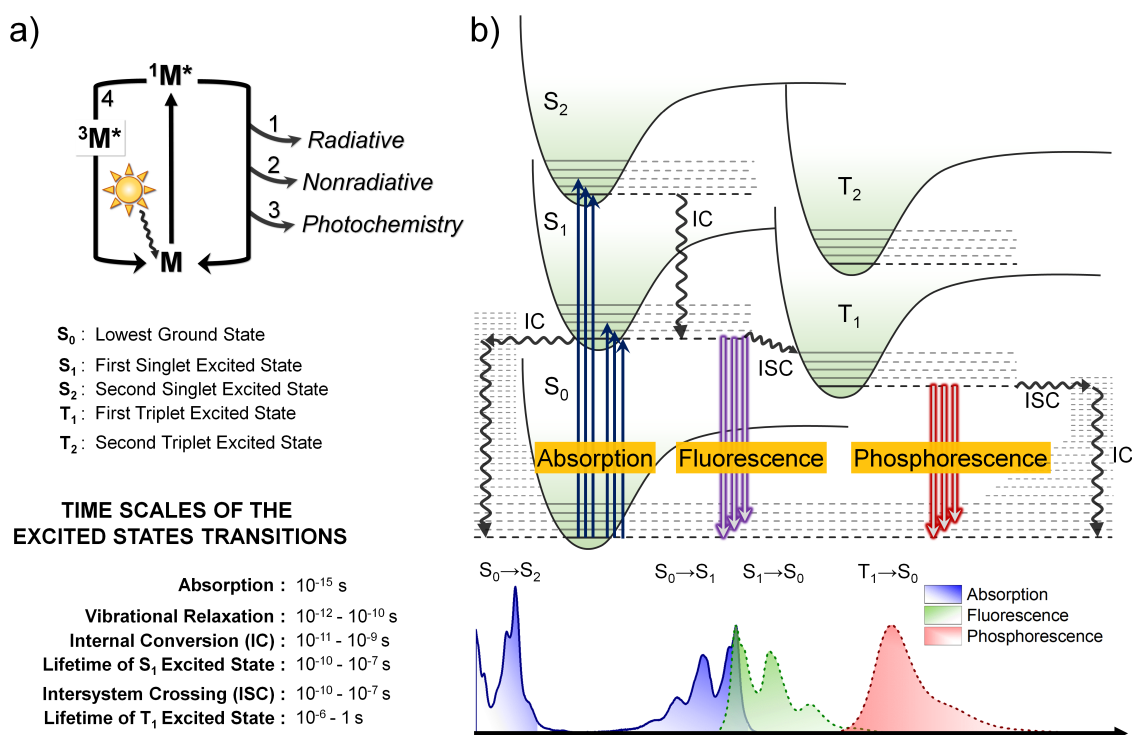


**Figure 1.3.** a) Fates of the excited state of a molecule (monomer) after photoexcitation; and b) Perrin-Jablonski diagram depicting the various excited state transitions.

singlet and triplet excited states [27].

### 1.3.1.1. Electronic Absorption

The electronic excitation via absorption (occurs within  $10^{-15}$  s) of photon can lead to the population of the higher vibrational levels of singlet ( $S_{1/2}$ ) excited state [27]. The condition necessary for the absorption is that the photon energy from the light should match the energy gap between the ground and the excited electronic states. Further radiative and nonradiative decay processes ensure the relaxation of the higher excited states via appropriate channels.

### 1.3.1.2. Vibrational Relaxation

The excitation of the ground electronic molecule follows the Franck-Condon principle and lead to the population of the vibrational levels of the higher excited

**Franck-Condon Principle:** *“An electronic (vertical) excitation is most likely to occur without the changes in the position of the nuclei in the molecular entity and its environment” or*

*“the most probable transition between the electronic states occur when the wave function of the initial vibrational state most closely resembles the wave function of the final vibrational state”*

state [27]. The newly populated state can be termed as ‘*hot excited state*’ compared to surrounding molecules present in their ground electronic state. The vibrationally excited entity will lose the excess energy via collision with the surrounding molecules or the solvent media in a few picoseconds ( $10^{-12}$ - $10^{-10}$  s) in a process called vibrational relaxation to reach the lowest vibrational level of a given electronic state [27].

#### 1.3.1.3. Internal Conversion (IC)

The vibronically relaxed excited states can then populate the lower electronic states via a process called internal conversion within  $10^{-11}$ - $10^{-9}$  s [27]. Internal conversion is a nonradiative transition between the electronic states of the same spin multiplicity [28]. The internal conversion from  $S_2 \rightarrow S_1$  is more efficient than  $S_1 \rightarrow S_0$  owing to the large energy difference between the  $S_1$  and  $S_0$  electronic levels. Since the internal conversion from  $S_1 \rightarrow S_0$  is weak, it is competed by radiative decay process like fluorescence or intersystem crossing (ISC) mediated population of the triplet excited state [27].

#### 1.3.1.4. Fluorescence

Radiative decay (via emission of photons) of the excited state from the lowest vibrational state of  $S_1$  is called fluorescence [27]. Barring a couple of exceptions, most

of the excited molecules typically emit from the lowest vibrational state of  $S_1$  as per the Kasha's rule [29]. The emission of photon can be as fast as the photon absorption

**Kasha's rule:** *"The emitting level of a given multiplicity is the lowest excited level of that multiplicity"*

( $\approx 10^{-15}$  s), however, considering that the molecule stay in the excited state for some time the fluorescence lifetime of a molecule can be within  $10^{-10}$ - $10^{-7}$  s [27].

### 1.3.1.5. Intersystem Crossing (ISC)

A possible decay path for the singlet excited state can be the intersystem crossing mediated population of the triplet excited state. *"Intersystem crossing is defined as the nonradiative transition between two isoenergetic vibrational levels belonging to the electronic states of different multiplicities"* [27, 28]. ISC is principally spin forbidden process, however, spin-orbit coupling can mediate the population of the triplet excited states ( $T_n$ ) via ISC. Alternatively, ISC can be efficient if the  $S_0 \rightarrow S_1$  transition have an  $n \rightarrow \pi^*$  character [27].

### 1.3.1.6. Phosphorescence

The populated triplet excited states return to the ground state via radiative or nonradiative relaxation [27]. Nonradiative relaxation is usually preferred over radiative relaxation as  $T_1 \rightarrow S_0$  transition is a spin forbidden process. The radiative relaxation from  $T_1 \rightarrow S_0$  is called phosphorescence and it usually appears at a longer wavelength than fluorescence emission [28].

### 1.3.1.7. Delayed Fluorescence (DF)

Alternatively, when the lifetime of the  $T_1$  state is long and the energy gap ( $\Delta E_{S-T}$ )

between  $T_1$  and  $S_1$  state is small, reverse intersystem crossing (rISC), i.e.,  $T_1 \rightarrow S_1$  transition can occur [27]. The consequent radiative decay from the  $S_1$  state, also called the delayed fluorescence (E-type DF since it was observed first in eosin), can then give a similar character to the fluorescence emission but with a longer fluorescence lifetime [27]. DF is thermally activated and can be enhanced with the increasing temperature [27].

### **1.3.2. Intermolecular Electronic Interactions and the Photoexcited State Properties of Chromophoric Ensembles**

Photoexcited state properties of chromophoric entities are very much sensitive to the surrounding electronic/redox and the solvent environment [27, 30]. The intermolecular electronic communications among the redox/electronically complementary chromophores in vicinity can modulate the photoexcited state properties of ensemble as compared to the isolated molecules [27]. Electron transfer, energy transfer, exciton interaction, excimer/exciplex formation, singlet fission, singlet-singlet annihilation and triplet-triplet annihilation are some of the outcomes of the interchromophoric electronic interactions.

#### **1.3.2.1. Photoinduced Electron Transfer**

Electron transfer is one of the ubiquitous and fundamental phenomena in nature and many biological processes such as respiration, photosynthesis, etc., utilize it for the running the essential molecular processes [1]. Electron transfer is initiated when an electron rich (donor) molecule transfers an electron to the electron deficient (acceptor) counterpart, facilitated by thermal or visible light

excitation [30]. Light induced electron transfer or photoinduced electron transfer reaction occurs when a quanta of light excites the donor and/or acceptor to its excited state and subsequently undergoes charge (hole/electron) transfer via either reductive electron transfer or oxidative hole transfer process (Figure 1.4.).

**(i) Rehm-Weller Analysis - Feasibility of Electron Transfer:** The change in free energy for the electron transfer ( $\Delta G_{et}$ ) when a donor and acceptor in vicinity undergoes photoexcitation can be estimated employing the Rehm-Weller relation [31] based on the Born dielectric continuum model (equation 1.1) [30, 32, 33].

$$\Delta G_{et} = E_{ox} - E_{red} - E_S - \frac{e^2}{r_{DA} \epsilon_s} + \frac{e^2}{2} \left( \frac{1}{r_D} + \frac{1}{r_A} \right) \times \left( \frac{1}{\epsilon_s} + \frac{1}{\epsilon_{sp}} \right) \quad (1.1)$$

where  $E_{ox}$  and  $E_{red}$  = oxidation and reduction potential of the donor and

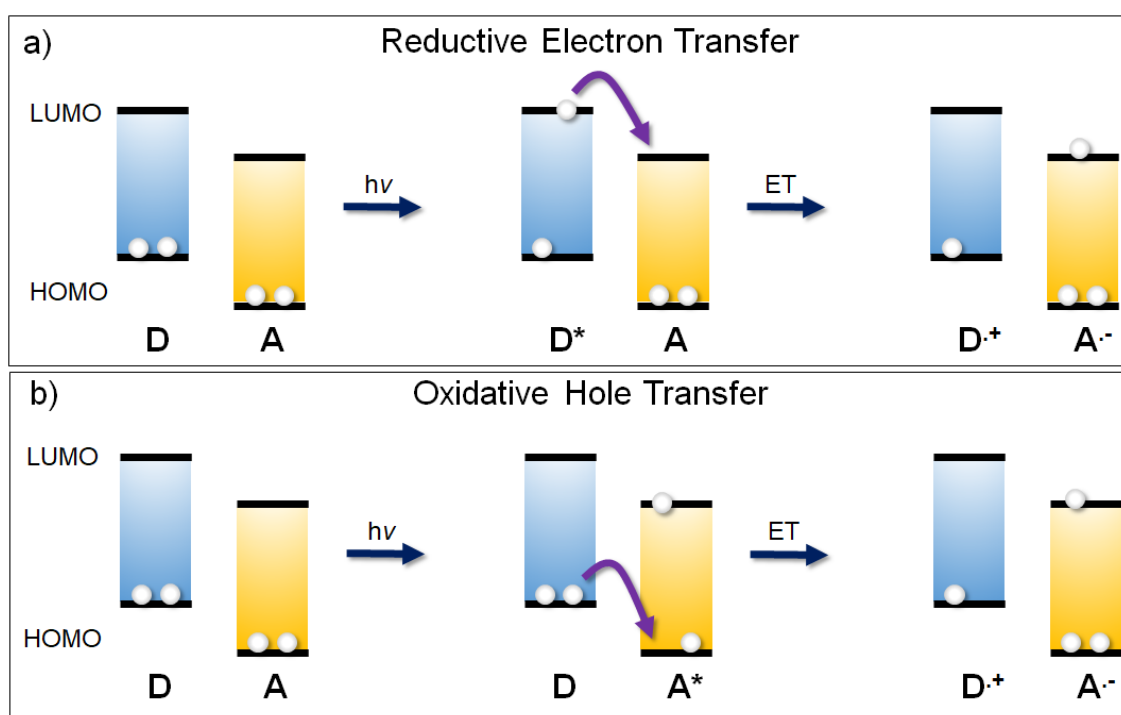


**Figure 1.4.** Schematic depiction of reductive electron and oxidative hole transfer in D/A systems.

acceptor respectively;  $e$  = the charge of an electron;  $r_{DA}$  = distance between the donor and the acceptor;  $r_D$  and  $r_A$  = ionic radii of the cation and anion respectively which can be approximated as  $r_{DA}/2$ ;  $\epsilon_s$  = static dielectric constant of the solvent used for electrochemistry;  $\epsilon_{sp}$  = static dielectric constant of the solvent used for the transient measurements. At finite distances, Coulombic attraction energy between the radical ion-pairs to a first approximation is given by a point-charge model as  $(\frac{e^2}{r_{DA} \epsilon_s})$ . Dielectric constant also influences the solvation free energy of the ions and should be corrected for different solvents.

**(ii) Marcus Theory of Electron Transfer:** Factors affecting the energetics and the thermodynamics/kinetics of electron transfer have been elaborated in the Marcus theory of electron transfer [30]. The basic assumption of the Marcus theory of electron transfer is that only a weak interaction among the donor and acceptor moieties is need for the electron transfer to occur [30]. The two-dimensional intersecting parabolic curves could very effectively presents the potential energy surfaces on which the electron transfer process occurs (Figure 1.5a). The schematic shown in Figure 1.5a could effectively represent the relation between the rate of the electron transfer (Figure 1.5b) to the reorganization energy ( $\lambda$ ) and the free energy for electron transfer process ( $\Delta G^0$ ) and activation energy ( $\Delta G^\ddagger$ ) [28, 30]. The relation between the  $\lambda$ ,  $\Delta G^0$  and  $\Delta G^\ddagger$  can be given by equation 1.2.,

$$\Delta G^\ddagger = \frac{(\Delta G^0 \pm \lambda)^2}{4\lambda} \quad (1.2)$$

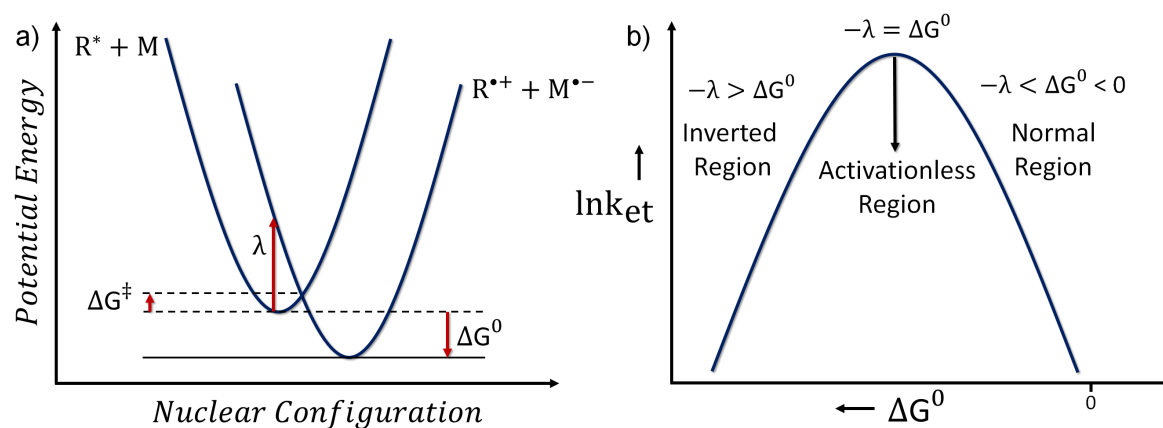


**Figure 1.5.** Schematic depiction of a) potential energy description of electron-transfer process; b) Marcus theory prediction of the dependence of the electron transfer rate on the thermodynamic driving force.

Furthermore, rate constant for the electron transfer can be given by (equation 1.3-1.5),

$$k_{et} = A e^{\left(-\frac{\Delta G^\ddagger}{RT}\right)} \quad (1.3)$$

$$k_{et} = A e^{\left[-\frac{(\Delta G^0 \pm \lambda)^2}{4\lambda}\right]/RT} \quad (1.4)$$

$$\ln k_{et} = \ln A + \left[-\frac{(\Delta G^0 \pm \lambda)^2}{4\lambda}\right]/RT \quad (1.5)$$

Above-mentioned equations provide a relationship between the kinetics and the thermodynamic driving force ( $\Delta G^0$ ) of the electron transfer reactions. A careful look in  $k_{et}$  versus ( $\Delta G^0$ ) plot suggests the presence of three distinct kinetic region as shown in Figure 1.5b [28, 30].

**(a) Normal Region ( $-\lambda < \Delta G^0 < 0$ ):** When the thermodynamics driving force are small, the electron-transfer process is thermally activated with its rate increasing as the driving force increases.

**(b) Activationless Region ( $-\lambda = \Delta G^0$ ):** Rate of electron transfer is maximum

and the change in driving force has negligible effect on the rate of electron transfer.

(c) **Inverted Region** ( $-\lambda > \Delta G^0$ ): Rate of electron transfer decreases with the increasing thermodynamic driving force.

### 1.3.2.2. Photoinduced Energy Transfer

Energy transfer is the process by which energy is relocated from one system to another. Photoinduced energy transfer from an excited molecule (energy donor) in an intermolecular process lends the photoexcitation of another molecule (energy acceptor) via excitation energy migration [27]. The energy transfer can effectively happen between two similar (homotransfer) or dissimilar (heterotransfer) molecular entities (Figure 1.6.) [27]. The excitation energy can be transferred via radiative or nonradiative excitation energy

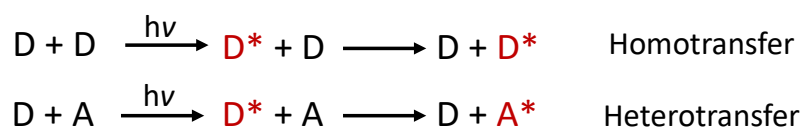


**Figure 1.6.** Schematic depiction of intermolecular excitation energy (homo and hetero molecular) transfer in donor (D) and (acceptor) systems.

transfer processes. Radiative energy transfer is a two step-process wherein the photon emitted by a donor molecule is absorbed by an acceptor molecule which lends the photoexcitation of the acceptor [27].

Nonradiative transfer of excitation energy occurs from an energy donor (D) to an energy acceptor (A) when there is a foreseeable interaction between the D and A components through intermolecular long-range dipole-dipole

(Coulombic) coupling and/or orbital overlap mediated interactions [5, 27]. The outcome of the excitation energy transfer is that the excitation of the donor, lends the emission from the acceptor via excitation energy transfer from the excited donor to the proximate acceptor via nonradiative energy transfer (Figure 1.7.) [34]. The intermolecular excitation energy transfer via dipole-dipole coupling has been well explained in the Förster's theory for resonance energy transfer [35]. The theory approximates the interaction as a electronic coupling between two chromophoric point-dipoles (equation 1.6-1.7) [5].

$$V_{D-A}^{d-d} = \frac{1}{4\pi\epsilon_0} \left[ \frac{\vec{\mu}_D \cdot \vec{\mu}_A}{R^3} - \frac{3(\vec{\mu}_D \cdot \vec{R})(\vec{\mu}_A \cdot \vec{R})}{R^5} \right] \equiv \frac{1}{4\pi\epsilon_0} \frac{\kappa |\vec{\mu}_D| |\vec{\mu}_A|}{R^3} \quad (1.6)$$

$$\kappa = \hat{\mu}_D \cdot \hat{\mu}_A - 3(\hat{\mu}_D \cdot \hat{R})(\hat{\mu}_A \cdot \hat{R}) \quad (1.7)$$

Förster proposed that the rate of the excitation energy transfer ( $k^{\text{Förster}}$ ) transfer between a donor and an acceptor chromophore to be dependent on several parameters as shown in the equation 1.8 [5, 36]. As the spectral line

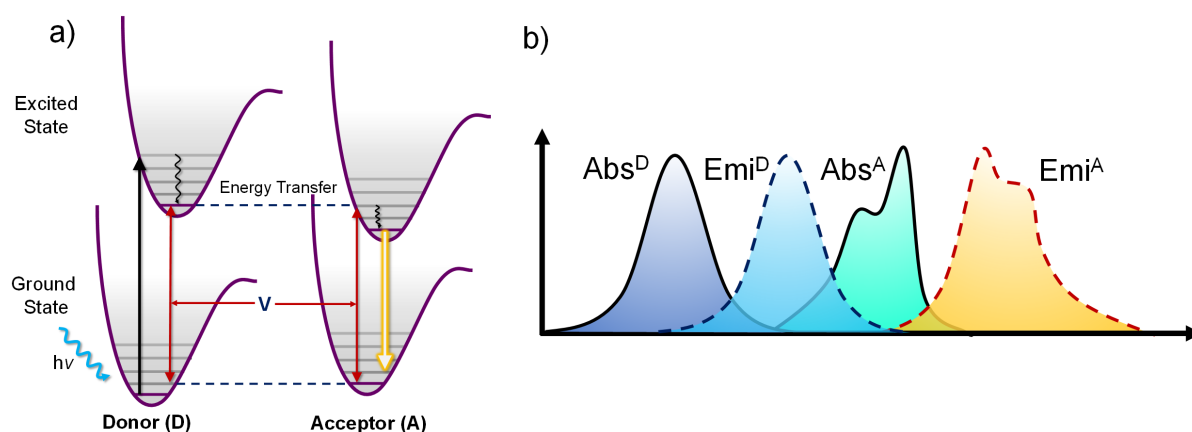


**Figure 1.7.** Schematic depiction of a) intermolecular excitation energy migration in donor (D) and (acceptor) systems via dipole-dipole coupling and b) spectral overlap among the donor emission and the acceptor absorption spectra for resonance energy transfer.

broadening of molecules in solution leads to phase decoherence before the excitation energy transfer, application of the Fermi's golden rule becomes quite important. In this model, the energy transfer rate scales as the square of the electronic coupling term (equation 1.8) [5, 36].

$$k^{\text{Förster}} = \frac{1}{\tau_D} \frac{9 (\ln 10) \kappa^2 \phi_D J_F}{128 \pi^5 N_A n^4} \frac{1}{R^6} \quad (1.8)$$

where  $n$  is the refractive index of medium;  $N_A$  is the Avagadro's number;  $\phi_D$  and  $\tau_D$  are the fluorescence quantum yield and the lifetime of the donor;  $\kappa$  is the orientation factor (see equation 1.7);  $J_F$  is the overlap integral of donor emission spectrum and the acceptor absorption spectrum (equation 1.9). The term  $J_F$  can be found by integrating the area-normalised spectrum of the donor emission ( $F_D(\lambda)$ ) and the extinction coefficient spectrum of the acceptor ( $\varepsilon_A(\lambda)$ ) [5].

$$J_F = \int_0^\infty F_D(\lambda) \varepsilon_A(\lambda) \lambda^4 d\lambda \quad (1.9)$$

To conserve the energy during the excitation energy transfer it is important to have a good overlap among the fluorescence emission and the extinction spectra of the acceptor and the rate of energy transfer exhibits a linear increase with the increasing overlap among the two parameters. The electronic interactions among the chromophoric dipoles in Förster's theory comes under the very weak coupling regime and hence can operate at larger distances (10-100 Å) with an inverse proportionality to the distance (i.e.  $R^{-6}$ ) between the two chromophores [5, 27].

### 1.3.2.3. Exciton Interactions

Spatially proximate chromophoric units in the molecular ensemble can

electronically couple (strong) via Coulomb coupling among the transition dipoles. (Figure 1.8) [5, 37]. Herein the excitation is distributed among the proximate chromophores instead of the being localised on the individual chromophores and this results in the formation of a molecular exciton [5]. Thus the strong Coulomb coupling among the chromophoric unit comprising the molecular exciton, lends a resonance splitting of the excited state into two non-degenerate states (an upper and a lower state) [5, 37]. The newly generated excited states are the result of the symmetric and the antisymmetric linear combination of the excitation of the two molecules (equations 1.10-1.11) [5].

$$\Psi_{\text{symm}} = \frac{1}{\sqrt{2}} (A'B + AB') \quad (1.10)$$

$$\Psi_{\text{antisymm}} = \frac{1}{\sqrt{2}} (A'B - AB') \quad (1.11)$$

where the prime indicates the excited molecule.

Transition to either the upper or lower state and the corresponding oscillator strengths depends on stacking (face-to-face/slip stacked) and the relative orientation (parallel/head-to-tail) of chromophore transition dipoles [37]. Exciton coupling among the parallel (head-to-tail) dipoles lend a net nonzero transition moment, allowing the transition to the upper (lower) state, whereas the transition to the lower (upper) state is forbidden due to the vanishing transition moment of the opposing dipoles [5, 38-40]. In contrast, the transition dipoles with oblique ( $\alpha \neq 0$ ) orientation lends a Davydov splitting of

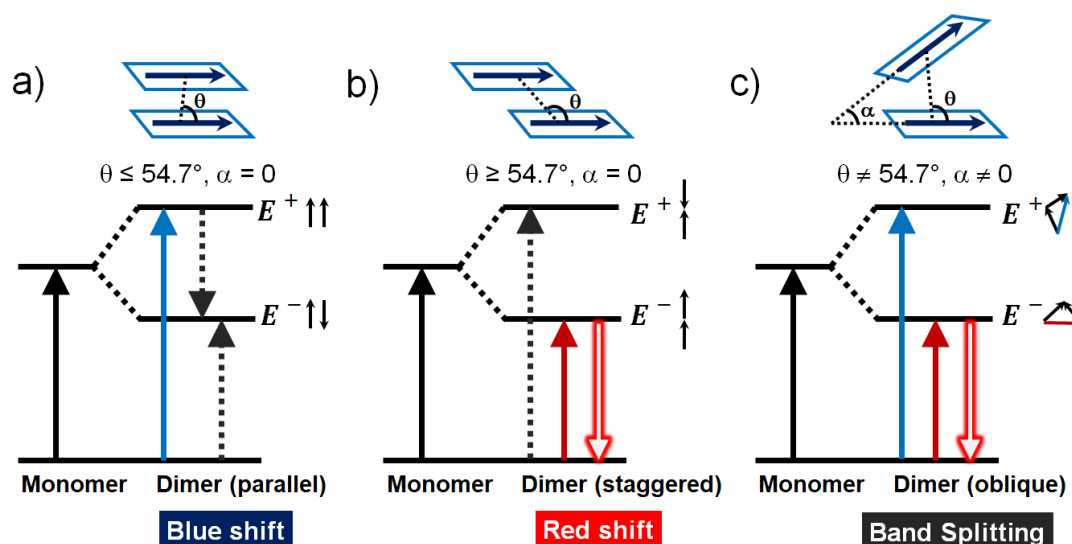


**Figure 1.8.** Schematic depiction of exciton coupling in a) parallel cofacial (H-aggregate); b) staggered cofacial (J-aggregate); and c) oblique (Davydov splitting) transition dipoles.

the excited state, allowing the transitions to both the upper and the lower states [40, 41]. Symmetry of the lowest exciton state dictates the radiative properties of the aggregate i.e. the fluorescence emission in parallel (head-to-tail) dipoles is suppressed (enhanced) as compared to the monomeric solution [29, 38]. Experimental assignment of the aggregate type purely on the basis of radiative/nonradiative lifetimes necessitates a precise accounting of (i) temperature dependent nonradiative decay channels (internal conversion, intersystem crossing, defect traps) and (ii) alternate channels of exciton relaxation such as excimer formation or singlet-singlet annihilation [38, 42]. Moreover, the geometric stacking and dipole orientations of the proximate chromophoric units in crystals possessing more than one molecule/unit cell can portray complex electronic transitions in the molecular ensemble as compared to the monomeric excited state properties [38, 41, 43].

### 1.3.2.4. Excimer/Exciplex Formation

Excimer are the dimers formed in the excited state when an excited singlet state interacts with a proximate neighbour present in its ground state (Figures 1.9.-1.10.) [44]. Identity of the two chromophoric entities involved in the excimer formation are identical.

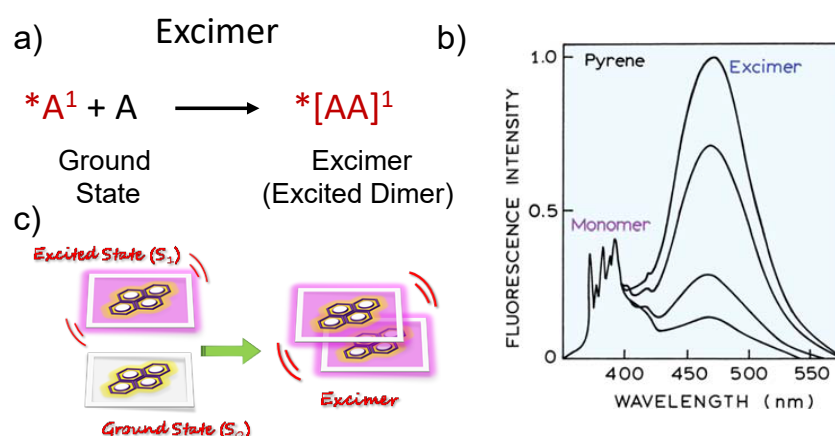


**Figure 1.9.** Mechanism of the excimer formation; b) fluorescence emission spectra depicting the signature corresponding to pyrene excimer (Adapted with permission from Ref. [44]. Copyrights © 2006, Springer Science Business Media, LLC) and c) schematic depiction of pyrene excimer formation.

Exciplexes are the excited complex formed between a donor (D) and acceptor (A) type molecules. The collision of an excited molecules (D or A) with a non-identical molecule (D or A) in ground state facilitates the exciplex formation [44].

### 1.3.2.5. Singlet Exciton Fission

Singlet fission (SF) is a spin allowed process in which a singlet excited molecule shares its energy with the neighboring ground state molecule to generate two triplet excitons (Figure 1.11.) [45]. This phenomenon has been observed in single crystal, polycrystalline, amorphous solids and concentrated

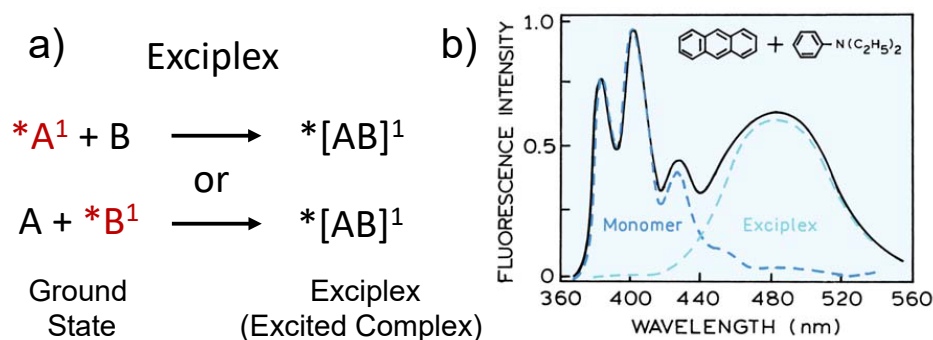


**Figure 1.10.** a) Mechanism of exciplex formation; and b) fluorescence emission spectra depicting the signature corresponding to anthracene and dimethyl aniline exciplex (Adapted with permission from Ref. [44]. Copyrights © 2006, Springer Science Business Media, LLC).

solutions, producing triplet yields as high as 200%. SF has been extensively studied in pentacene and its derivatives. SF mediated triplet generation has gained more attention due to its ability to enhance the Shockley-Queisser limit of solar cells from 32% to 45% [46].

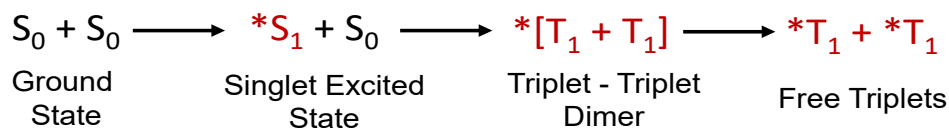


**Figure 1.11.** Mechanism of the singlet exciton fission.

### 1.3.2.6. Singlet-Singlet Annihilation (SSA)

Singlet-singlet annihilation originates from dipole interaction between two excited chromophoric entities in an assembly (probably nearest-neighbors) [47]. The dipole coupling between the two chromophoric entities enables a

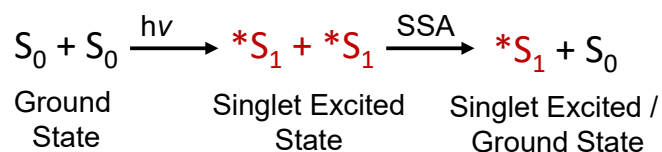


**Figure 1.12.** Mechanism of the singlet-singlet annihilation.

non-radiative transition, in which one of the two excited molecules relaxes to the ground state, while the other is excited to a higher energy state (Figure 1.12) [47]. The latter rapidly returns to the lowest excited state, thereby annihilating one of the two original excitons [48].

### 1.3.2.7. Triplet-Triplet Annihilation (TTA)

Collision among two proximate chromophoric units in present their  $T_1$  state can allow one of them to return to the  $S_1$  state and the other relaxes to the ground state (Figure 1.13) [27]. TTA can lead to delayed fluorescence, also known as the P-type DF as it was observed first time in pyrene [27].

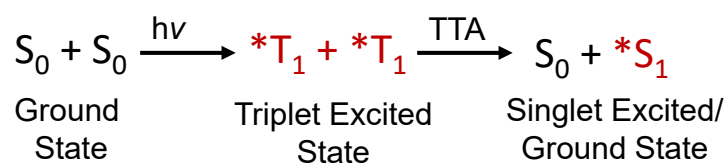


**Figure 1.13.** Mechanism of the triplet-triplet annihilation.

## 1.4. Artificial Photosynthesis and Light Harvesting

One of the first notions of utilizing the incessant power from the sun dates back to the early 1900s when Giacomo Ciamician suggested that mankind should shift from utilizing the fossil fuel to the sustainable energy in the form of solar light [49]. Artificial photosynthesis is an appealing strategy for producing and converting abundant solar light into useable form of sustainable fuel and viable energy [9]. Through efficient light harvesting the quanta of energy from the sun can be used to carry out redox reactions, i.e. photocatalytic water splitting akin to the natural photosynthesis, and/or for

creating a satiable electrical output via photovoltaic technology.

### 1.4.1. Water Splitting

The first experimental demonstration of the photocatalytic water splitting was provided by Honda and Fujishima in a process called '*Honda-Fujishima effect*' (equation 1.12) [50-52]. Herein they had utilized a photoelectrochemical cell comprising of a TiO<sub>2</sub> photoanode and a platinum cathode which upon photoexcitation lead to the photocatalytic splitting of water into O<sub>2</sub> and H<sub>2</sub> [52]. Later, similar efforts were put in by the same group for the photocatalytic



reduction of CO<sub>2</sub> using aqueous suspension of nanoparticles [52, 53]. Since the reports by Honda and Fujishima, the tremendous efforts have been directed towards the creation of sustainable fuels via photocatalytic water oxidation and CO<sub>2</sub> reduction which have led to the emergence of the solar light harvesting via the artificial leaf program. The artificial light harvesting via photocatalytic water splitting has been extensively documented in the literature, [54-59] and is not elaborated here.

### 1.4.2. Organic Photovoltaics

Organic photovoltaics (OPV) is one of the powerful tools to exploit the incessant quanta of energy from the sun and utilize it for developing a net electrical output as a clean and sustainable source of energy [60]. OPVs are particularly desired over the traditional silicon solar cells due to their low cost, low toxicity, large-area and the

possibility of large-scale production [60]. Consequently, enormous efforts has been applied in this direction and the field of OPVs has shown rapid progress over the last two decades and have led to the emergence of small solar cells with power conversion efficiencies of upto 13% [60]. In OPVs, the light harvesting material is an organic semiconductor which is embedded between two redox-active electrodes (Figure 1.14a) [60, 61]. The organic semiconductor in the OPVs absorbs the quanta of energy (photons) from the sun and generate an exciton, i.e., a bound electron-hole pair [60]. The photogenerated exciton can dissociate into free charge carrier at the D-A interface and get extracted by the electrodes to generate a net electrical power [60].

Though, OPVs, i.e. D-A bulk heterojunctions, have exhibited large strides in terms of optimizing the efficiency since its invention [61], they are yet to achieve the

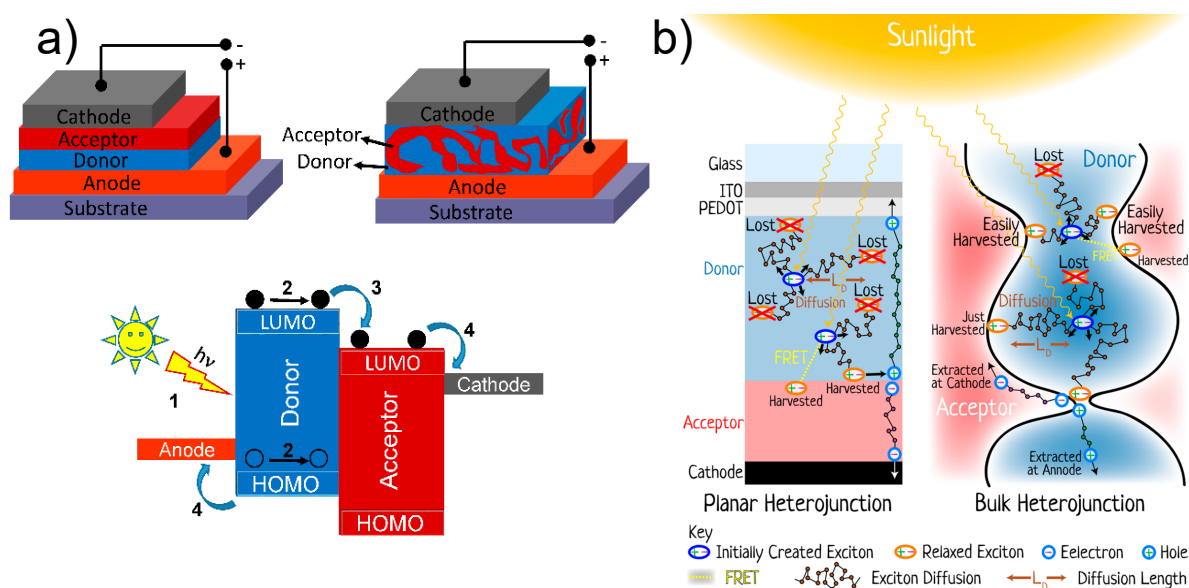


**Figure 1.14.** Schematic depiction of a) device structures of bilayer/bulk heterojunction (Adapted with permission from Ref. [62]. Copyrights © 2014, MDPI); and b) the light induced processes occurring after the photoexcitation (Adapted with permission from Ref. [60]. Copyrights © 2017, American Chemical Society).

stunning efficiency exhibited by the natural light harvesting apparatus in the green plants and photosynthetic bacteria. One of the reason for the low efficiency of the OPVs as compared to the light harvesting apparatus is the large recombination losses occurring from the annihilation of the excitons in the D-A blend [60]. The recombination losses can arise from a) inability of the photogenerated exciton to reach the D-A interface; b) geminate recombination of the electron-hole pair due to the inability to overcome the Coulomb attraction and c) inability of the free charge carriers to traverse through the labyrinth of the complex morphology before reaching the electrodes [60]. The above-mentioned factors essentially arises from the lack of the efficient charge percolation pathways in the D-A blend [60]. Further improvement in the efficiencies of the OPVs necessitate the improvement of the morphology of the D-A blend and the creation of the efficient charge percolation pathways for the efficient harvesting of the photogenerated charge carriers.

## **1.5. Emergence Upon Assembly Approach for Light Harvesting**

Self-assembly of organic chromophores into hierarchical structures can promote the creation of novel percolation pathways for the efficient transport of exciton and charges at longer distances in the D-A molecular aggregates [3, 63]. This provides an efficient method to avail nascent molecular properties that are absent in the monomeric units, however emerge when the monomeric units come together to form a self-assembly [63, 64]. Accordingly, '*emergence upon assembly*' [64] approach has been widely utilized to moderate the behavior

of the photogenerated exciton in artificial D-A hybrids [3]. The development of adaptable chromophore assembly and the exploration of energy and charge-transfer dynamics in such systems can provide vital understandings of how the factors such as geometry, organization, energetics and environment affect the photoconversion process [33].

As a result, exploration of the energy and charge-transfer dynamics in self-assembled chromophoric systems has attracted quite a lot attention from fundamental and technological perspective [3, 63, 65]. Several supramolecular D-A assemblies in the emerged to exploit the synergistically organized D and A conduits in the form of parallel [66], coaxial [67], contiguous [68, 69], cylindrical [70], slip-stacked [32], slipped-sandwich [71], double-helical [64, 72], or helix-wrapped [73] columnar stacks for efficient exciton and charge transport [33, 63, 74-77].

In one of the archetypal example, the effect of assembly on the photoexcited state properties was demonstrated by Wasielewski and co-workers (Figure 1.15a-c) [78]. Herein, they had explored the electron transfer dynamics in perylene-3,4-dicarboxamide (PMI, acceptor) covalently linked to *N,N'*-bis(3,4,5-tridodecyloxyphenyl)melamine (donor) attached via a biphenyl linker (PMI-Ph<sub>2</sub>-D) [78]. The D-A dyad forms a hierarchical hydrogen-bonded foldamers in methylcyclohexane (MCH), where a combination of the  $\pi$ - $\pi$  stacking ability of the PMI chromophore and the multipoint hydrogen

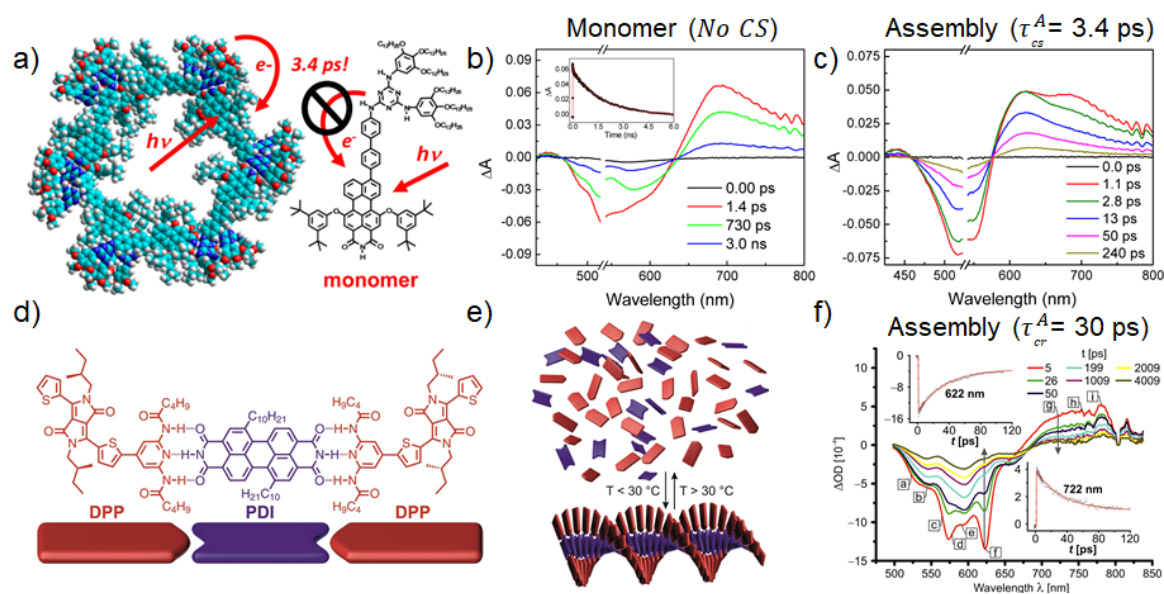


**Figure 1.15.** Schematic depiction of a) Monomeric PMI-Ph<sub>2</sub>-D dyad and the self-sorted stacked assembly; fTA spectra of b) monomeric PMI-Ph<sub>2</sub>-D in THF; and c) self-assembled PMI-Ph<sub>2</sub>-D in MCH (Adapted with permission from Ref. [78]. Copyrights © 2012, American Chemical Society); d) H-bonded DPP (donor, red) and PDI (acceptor, purple) assembly; e) superstructure formation upon annealing; and f) fTA spectra of the 2:1 (DPP:PDI) mixture in toluene with absorption vs. time profiles at  $\lambda = 622 \text{ nm}$  (upper inset) and  $\lambda = 722 \text{ nm}$  (lower inset, Adapted with permission from Ref. [64]. Copyrights © 2014, American Chemical Society).

bonding drives the assembly (Figure 1.15a). The photoexcitation of the PMI-Ph<sub>2</sub>-D assembly, reveals an emergent formation ( $k_{CS} = 3.4 \text{ p}$ ) of the radical ion-pair (RIP) intermediates due to the availability of a unique charge delocalisation pathway in the femtosecond transient absorption (fTA) measurements (Figure 1.15c). On the other hand, the photoexcitation of the monomeric PMI-Ph<sub>2</sub>-D in tetrahydrofuran (THF) reveals the formation of no charge transfer intermediates in the fTA measurements demonstrating the unique property rendered by the assembly (Figure 1.15b).

Along similar lines, Braunschweig and co-workers demonstrated a novel supramolecular assembly of diketopyrrolopyrrole (DPP) electron donor and perylene-3,4,9,10-tetracarboxylic diimide (PDI) electron acceptor exhibiting emergent photoexcited state properties upon self-assembly (Figure 1.15d-f) [64, 79]. The D and A components self-assemble (2:1) to form a helical supramolecular superstructure emanating from the triple H-bonding between the PDI/DPP and the  $\pi$ - $\pi$  stacking among the segregated D and A components [64, 79]. The fTA measurements of the helically assembled D-A components rendered emergent RIP intermediates ( $\tau_{CR}^A = 30$  ps) through photoinduced electron transfer whereas the disassembled D and A components exhibited no RIP intermediates (Figure 1.15f) [64]. In yet another example, Tovar and co-workers demonstrated the self-assembly and the electron transfer capabilities of peptide based electron D-A molecule in a supramolecular nanostructure (Figure 1.16.) [80, 81]. Herein, the peptides structure was modified with a  $\pi$ -

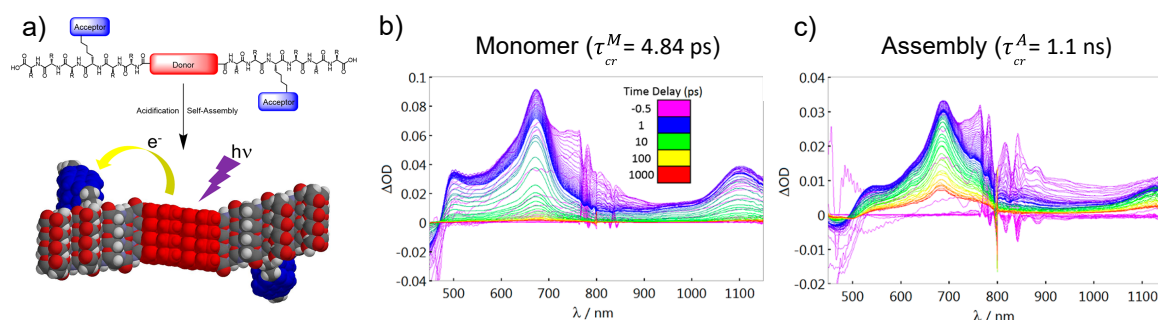


**Figure 1.16.** Schematic depiction of a) self-assembled donor–acceptor  $\pi$ -peptide hybrid; fTA spectral dynamics of b) unassembled; and c) self-assembled D-A hybrid in aqueous solutions (Adapted with permission from Ref. [81]. Copyrights © 2016, American Chemical Society).

conjugated oligothiophene (electron donor) core and was peripherally substituted with naphthalenediimide (electron acceptor) [81]. The peptide based D-A system self-assembled into a one-dimensional superstructure in aqueous media which exhibited an emergent ( $\tau_{CR}^A = 1.1 \text{ ns}$ ) photoinduced RIP intermediates as compared to the monomeric ( $\tau_{CR}^M = 4.84 \text{ ps}$ ) D-A peptide in aqueous solution (Figure 1.16 b-c) [81].

Wasielewski and co-workers utilized the biomimetic self-assembly properties of DNA nucleobases to create a core-shell type of D-A arrangement (Figure 1.17a) [33, 82-84]. Herein, the DNA nucleobase guanine (G, donor) was artificially modified by incorporating a perylenediimide (PDI) acceptor at the C-8 position via an ethynyl linker to form the D-A dyad GPDI [33]. The GPDI

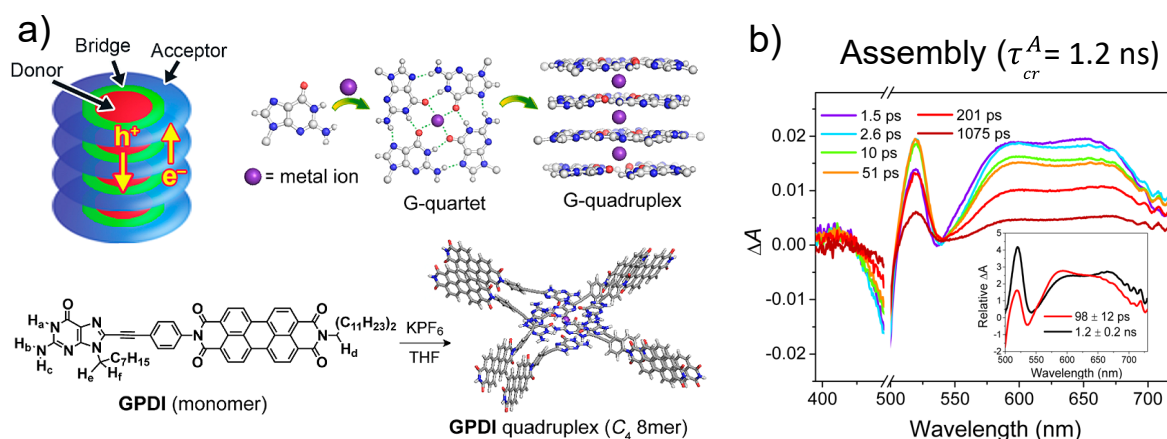


**Figure 1.17.** Schematic depiction of a) donor–bridge–acceptor dyad based on guanine (G)/PDI and the core–shell columnar assembly of GPDI; b) fTA spectra of self-assembled GPDI quadruplex ( $3 \times 10^{-3} \text{ M} + 0.25 \text{ eq. of } KPF_6$ ) in THF. Inset shows the principal kinetic components and decay-associated spectra of GPDI-quadruplex (Adapted with permission from Ref. [33]. Copyrights © 2013, American Chemical Society).

upon self-assembly formed a G-quartet structure wherein guanine acts as a donor core whereas PDI acts an acceptor shell around the core (Figure 1.17a) [33]. The photoexcitation of the PDI moiety rendered the charge separation in  $\tau_{CS} = 98 \pm 12$  ps to give  $G^{\bullet+} - PDI^{\bullet-}$  that recombined within  $\tau_{CR}^A = 1.2 \pm 0.2$  ns (Figure 1.17b) [33]. Thus the photoexcitation of the core-shell D-A assembly rendered a >100 times longer survival of the RIP intermediates as compared to that in the monomeric GPDI dyad because of the delocalization of the radical anion over the neighboring PDI units [33].

Aida and co-workers demonstrated the effect of the type of the assembly on the photoconductivity of the nanoassembly [67, 76, 85]. Herein, they utilized amphiphilic zinc porphyrin ( $P_{Zn}$ , electron donor)-fullerene ( $C_{60}$ , electron acceptor) dyads 2 and 3, which differ only in the linker connecting the two chromophoric units (Figure 1.18a-b) [76]. The self-assembly of the D-A dyads (2 and 3) render the formation of a nanotubular assembly [76]. The dyad 2 forms a favorable D-A assembly wherein the D and A units forms segregated 1D channels for the delocalisation of the charges whereas the dyad 3 forms an unfavorable mixed D-A stack wherein the D and A units are alternately stacked one on the another [76]. The exploration of the photoconductivity in the D-A dyad suggest a higher ambipolar photoconductivity in segregated path of the dyad 2 as compared to the mixed D-A dyad 3 (Figure 1.18c) [76]. Thus the effect of the type of the assembly on

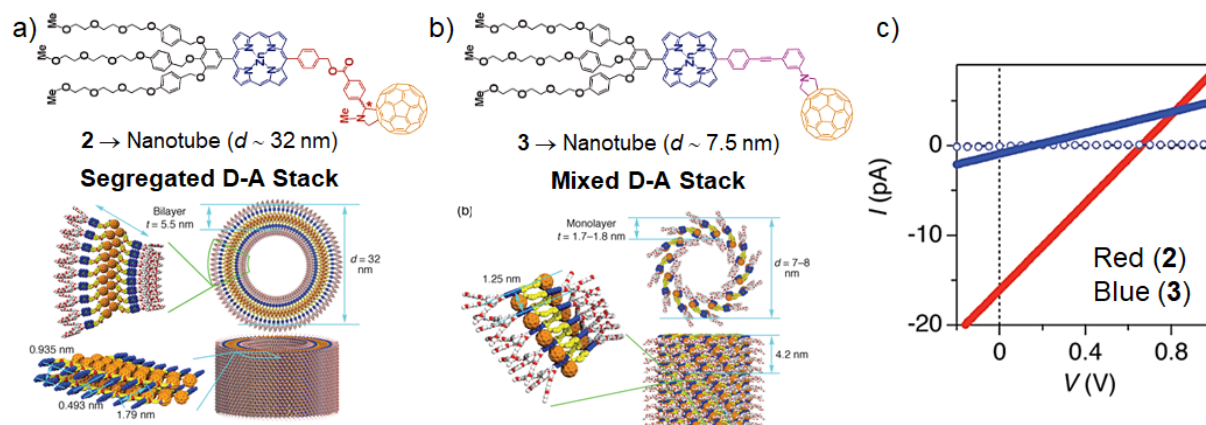


**Figure 1.18.** Molecular structure and Schematic depiction of tubularly assembled a) segregated D-A stack assembly in 2 and b) mixed D-A stack in 3; and c) log  $I$ - $V$  profiles at 25 °C of cast films of tubularly assembled 2 (red) and 3 (blue) in PV devices (Adapted with permission from Ref. [76]. Copyrights © 2012, American Chemical Society).

the photoexcited state properties of D-A hybrid was evidently demonstrated in the P<sub>Zn</sub>-C<sub>60</sub> D-A dyads 2 and 3, respectively [76].

Self-assembled chromophoric systems possess exceptional importance with respect to moderating the behaviour of the photogenerated exciton and the RIP intermediates in the natural photosynthetic apparatus. Similar self-assembly approaches can be extended to organize the artificial D-A chromophoric dyads and unearth the emergent photoexcited state properties upon self-assembly. Thus, with respect to the artificial light harvesting systems it is imperative to approach a self-assembly motifs which not only provides an emergent property but also a unique way to exploit the photoexcited state properties of a chromophoric systems upon self-assembly.

## 1.6. Aim and Objective of the Thesis

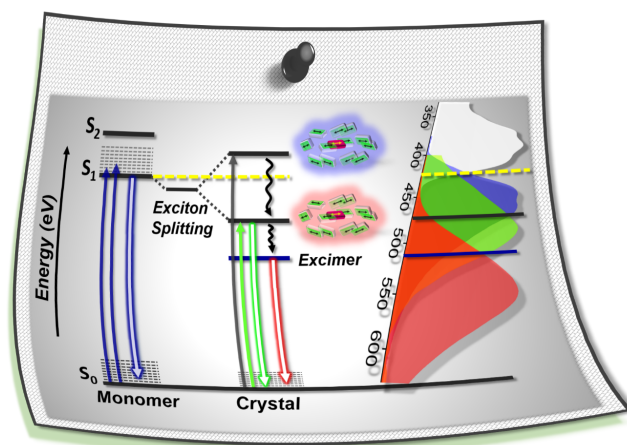
Unraveling the fate of the photogenerated excitons in  $\pi$ -chromophoric assemblies is one of the keys to designing functional photosynthetic mimics. Emulating the natural photosynthesis for artificial light harvesting necessitates a thorough understanding of the critical factors akin (i) coherent exciton migration and (ii) effective long-range migration of the radical ion-pair (RIP) intermediates. In this thesis, we attempt to explore the impact of the organization and the relative orientation of the  $\pi$ -chromophoric assembly on the photogenerated exciton relaxation and the survival of the RIP intermediates. Chapter 2, elaborates a conjoint experimental and theoretical investigation on the role of concerted dipole coupling and excimer interactions in modulating the exciton relaxation dynamics of crystalline arenes. Subsequently, Chapter 3 and 4, highlight the importance of the "emergence upon assembly" concept for the extending the survival of the RIP intermediates in hierarchical nonplanar D-A chromophoric assemblies.

## Chapter 2

# Concerted Interplay of Excimer and Dipole Coupling Governs the Exciton Relaxation Dynamics in Crystalline Anthracenes

### Abstract

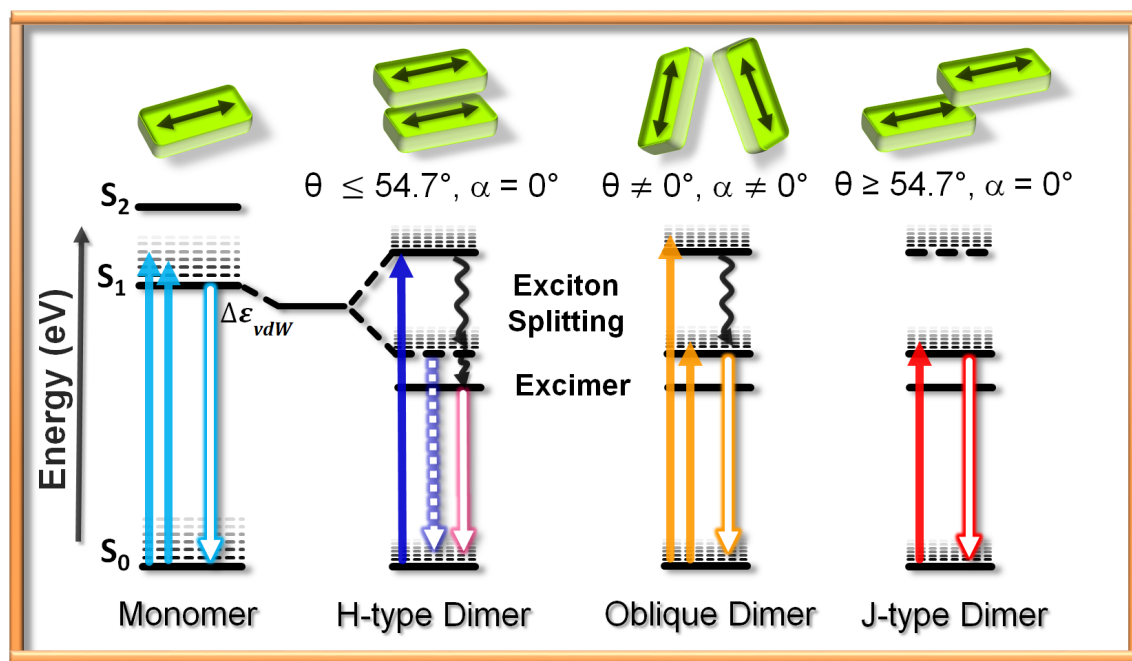
Unraveling the fate of excitons in  $\pi$ -chromophoric aggregates is imperative for the evolution of novel organic electronic materials. Herein, we report a conjoint theoretical and experimental investigation on the concerted role of long- (Coulomb/dipole coupling) and short-range (orbital overlap mediated excimer) electronic interactions in modulating the excited-state emission of six crystalline acetylanthracenes (1-3). Friedel-Crafts acylation of anthracene rendered crystalline mono-, di- and triacetylanthracenes with discrete close-packing (stacking), varied orbital overlap, and a resultant distinct emission (blue-green-yellow) from a cooperative excimer and dipole coupling. Time-resolved emission spectral (TRES) measurements and Kasha's exciton theory based quantitative estimation of the Coulomb coupling (mean field approximation), substantiates the concerted excimer and dipole shifts in crystalline 1-3. Extension of the Kasha's exciton model beyond the traditional nearest-neighbor approach, and the consistent agreement among the computed spectral shifts and the experimental TRES temporal components corroborate a holistic approach to decipher the exciton relaxation dynamics in molecular assembly of novel photonic materials.



## 2.1. Introduction

Burgeoning interest in organic luminescent crystals has intensified recently owing to its utility in optoelectronic and semiconducting device applications [86-88]. Photonic properties of the organic crystalline assemblies are archetypally dictated by the relative orientation and the 3D close-packing of the constituent chromophoric units [39, 89]. Consequently, investigation of the structure-optical property relationship in molecular aggregates have received great attention from a theoretical [40, 90-93], and experimental [39, 43, 89, 94-98] perspective. Hitherto, the origin of spectral shifts arising from the exciton dynamics [99] in bulk of supramolecular ensembles have predominantly been rationalized via Coulomb coupling among the transition dipoles of the nearest-neighbours (periodic dimer model) [100]. Depending on the relative dipole orientation of the adjacent chromophores, the excited-state of the monomer splits facilitating the transition to either upper (H-aggregate, parallel dipoles) and/or the lower excited (J-aggregate, head-to-tail) state (Scheme 2.1) [40, 42]. Though, the nearest-neighbour approach is highly pursued, it is implausible to neglect the contribution of the non-nearest neighbours towards the exciton splitting in the molecular aggregates. A comprehensive assessment of the exciton coupling in molecular aggregates, accounting the influence of all the nearest and non-nearest neighbours remains elusive.

Alternatively, co-facially stacked molecular assemblies with prominent  $\pi$ -

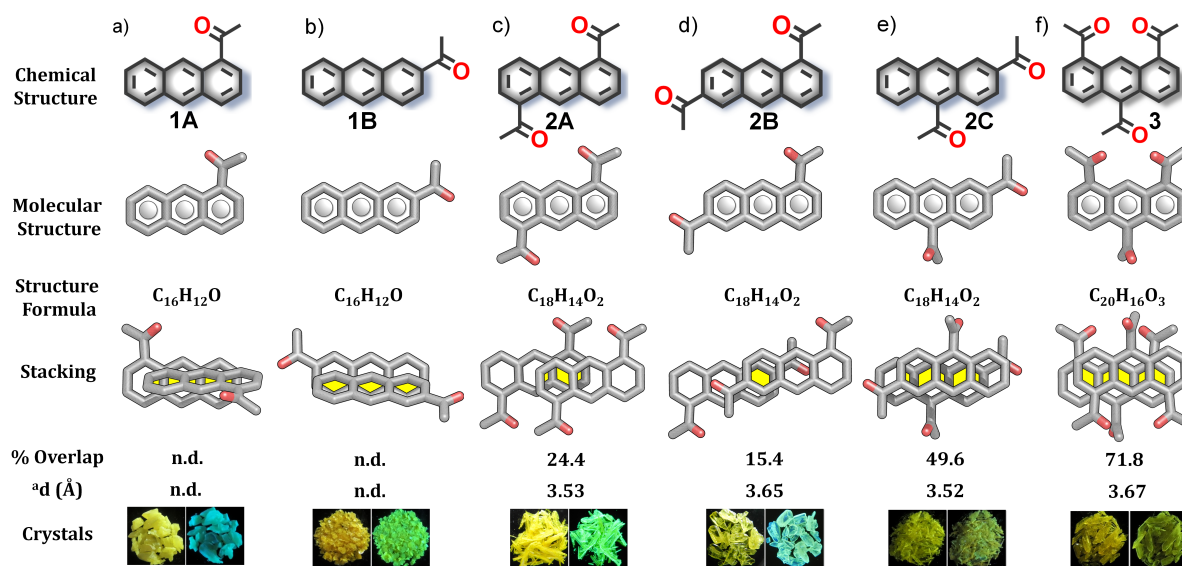


**Scheme 2.1.** Simplified schematic depiction of exciton band energy diagram for molecular H-type, J-type and oblique dimers.

orbital overlap can catalyze excited dimer/oligomer (excimer)[43, 101] and/or multimer formation (see Figure 1.9.) [102]. Concurrently, the fluorescence emission can be readily tuned depending on the extent of  $\pi$ -orbital overlap between the vicinal arene multimers [102-105]. Though, excimers are undesired due to the dramatic quenching of the excited states [106, 107], a thorough understanding of exciton relaxation dynamics between the Franck-Condon, Frenkel exciton and excimer trap states demands attention [108-110]. Anthracene is one of the simplest chromophores which has been utilised to explore the relation between the molecular organisation and the optical properties [43, 101, 111, 112]. Anthracene and its derivatives are well-known to form excimer in solution [106, 113], and crystalline states [43, 101, 114].

Depending on the geometrical orientation, anthracenes have been reported to exhibit three distinct types of excimers with unique excited-state characteristics [115-118]. Likewise, relying on the relative dipole orientation, the anthracenes can excitonically couple to exhibit H/J-type behaviour in the molecular ensemble [112, 119]. Though, the relationship between the molecular organisation and optical characteristics are rigorously explored, the precise assessment of orbital overlap (excimer) and long-range Coulomb (dipole) couplings mediated spectral changes in molecular ensemble remains sparse [112]. Herein we report a combined experimental/theoretical estimation of the excimer/dipole coupling mediated spectral shifts in the molecular ensemble of six crystalline anthracene derivatives (Scheme 2.2.).

Our continual efforts towards understanding the emergent optical[103, 104, 120] and photoexcited-state[63, 121, 122] properties in self-assembled molecular architectures encouraged us to explore the structure vs. optical property relation in a series of crystalline acetylanthracenes (1-3). Conventional Friedel-Crafts acylation of anthracene afforded crystalline mono-, di- and triacetylanthracene derivatives with discrete molecular structures and varied close-packing motifs. The crystalline 1-3 derivatives exhibited pale yellow-yellowish orange color with diverse solid-state fluorescence (blue-green-yellow) emission (Scheme 2.2.). Diverse excited-state character in crystalline 1-3 is a consequence of distinct (i)  $\pi$ -overlap and (ii)



**Scheme 2.2.** Chemical and molecular structure, structure formula, stacking, %overlap and the distance ( $d$ ) between the nearest  $\pi$ -stacked anthracenes in a) 1A; b) 1B; c) 2A; d) 2B; e) 2C and f) 3 with the crystal images of the derivatives under ambient (left) and under UV illumination (354 nm, right). <sup>a</sup> $d$  = distance between the nearest-neighbors; n.d. = not determinable due to oblique stacking.

stacking mediated concerted interplay of excimer and dipole couplings in the molecular ensemble. To deconvolute the contributions from the excimer and dipole coupling, quantitative evaluation of the dipole-dipole interaction between the nearest and non-nearest neighbours were carried out by extending the Kasha's exciton coupling formalism to a mean field approximation. Estimated mean values of the dipole interaction furnished a quantitative description of dipole and excimer shifts in crystalline 1-3. Additionally, the time-resolved emission spectral (TRES) measurement based temporal components of the fluorescence emission complement the numerically computed excimer shifts. Best agreement between the

theoretically computed spectral shifts and the experimentally evaluated TRES temporal components, reveal the importance of an all-inclusive approach to narrate the spectral shift in the molecular ensembles of polyaromatic hydrocarbons when compared to the monomeric analogues.

## 2.2. Results and Discussion

### 2.2.1. Syntheses and Structure

The syntheses of acetylanthracene (AA) derivatives 1-3 were carried out employing a simple and efficient Friedel-Crafts[123] acylation reaction (see experimental section, Scheme A2.1.). A mixture of anthracene and anhydrous  $\text{AlCl}_3$  in carbon disulphide ( $\text{CS}_2$ ) was reacted with stoichiometric quantity of acetyl chloride to provide the desired acetylanthracene derivative (1-3) with reasonable yields (see experimental section). The derivatives 1A, 1B and 2C were crystallized by slow evaporation of chloroform ( $\text{CHCl}_3$ )/*n*-hexane solvent mixture, whereas 2A, 2B, and 3 crystallized from ethyl acetate/*n*-hexane mixture (Figure 2.1., Table 2.1.). The AA derivative 1A crystallized in solvent-free orthorhombic crystal system with four molecules per unit cell ( $Z=4$ ). The derivative 1B ( $Z=4$ ), 2A ( $Z=2$ ) and 2C ( $Z=4$ ) crystallized in solvent-free monoclinic system, whereas 2B ( $Z=2$ ) and 3 ( $Z=4$ ) crystallized in solvent-free triclinic crystal system. Interestingly, the 1,8,10-triacetylanthracene (3) derivative exhibits two distinct monomers, differing in the relative orientation (in-phase/out-of-phase) of the 1, and 8-acetyl groups, lending an asymmetric

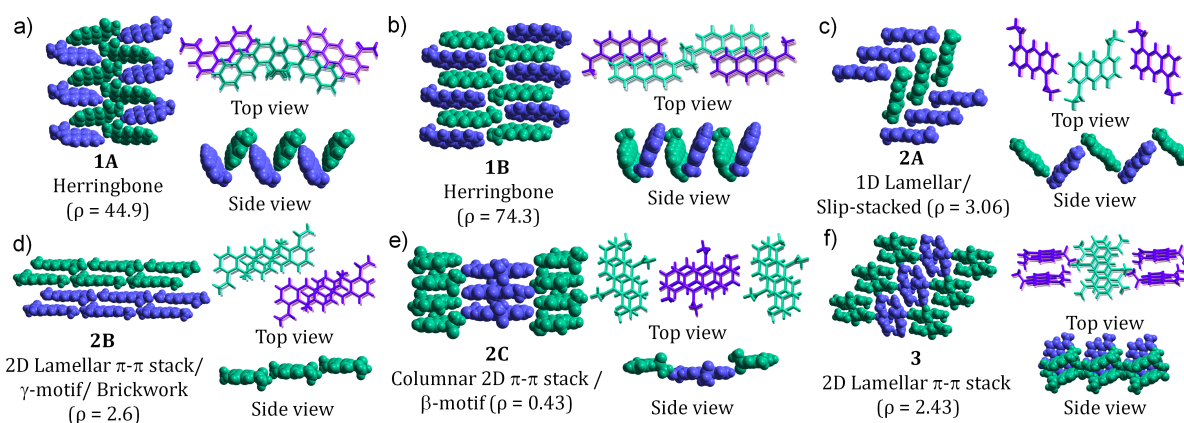


**Figure 2.1.** Close-packing arrangement in the acetylanthracene derivatives a) 1A; b) 1B; c) 2A; d) 2B; e) 2C and f) 3 indicating the values of  $\rho[(\%C\cdots H)/(\%C\cdots C)]$ . Herringbone ( $\rho > 4.5$ ), sandwich herringbone ( $3.2 < \rho < 4.0$ ), g ( $1.2 < \rho < 2.7$ ) and  $\beta$  ( $0.46 < \rho < 1.0$ ).

unit with two discrete molecules.

### 2.2.2. Close-Packing Analyses

To get insights into the structure-property relation and probe the weak intermolecular interactions driven assembly, the close-packing analyses of the crystalline 1-3 were performed (Figure 2.1.). Investigation of the close-packing in 1-3 crystalline derivatives revealed a diverse solid-state packing arising from an interplay of synergistic and/or competitive weak intermolecular interactions (Figure 2.1.-2.2.). The AA derivatives (1-3) displayed four distinct packing arrangements of the anthracene units in the crystal lattice (Figure 2.1-2.2., Table 2.2.). Compound 1A and 1B display a herringbone packing, typically observed in polyaromatic hydrocarbons, where the anthracene units are arranged in an edge-to-face manner aided by the  $C-H\cdots\pi$  interactions (Figure 2.1a, b). The  $C-H\cdots O$  interaction (distance,  $d = 2.36 \text{ \AA}$ , a-axis; Figure

**Table 2.1.** Crystallographic data and refinement parameters for crystalline 1-3 derivatives.

	1A	1B	2A	2B	2C	3
Formula	C <sub>16</sub> H <sub>12</sub> O	C <sub>16</sub> H <sub>12</sub> O	C <sub>18</sub> H <sub>14</sub> O <sub>2</sub>	C <sub>18</sub> H <sub>14</sub> O <sub>2</sub>	C <sub>18</sub> H <sub>14</sub> O <sub>2</sub>	C <sub>20</sub> H <sub>16</sub> O <sub>3</sub>
formula wt	220.26	220.26	262.29	262.29	262.29	304.10
colour, shape	Yellow	Yellow	Yellow	Yellow	Yellow	Yellow
dimens, mm	0.20 x 0.15 x 0.15	0.20 x 0.15 x 0.15	0.20 x 0.15 x 0.10	0.20 x 0.15 x 0.15	0.20 x 0.15 x 0.15	0.20 x 0.15 x 0.15
crystal system	Orthorhombic	Monoclinic	Monoclinic	Triclinic	Monoclinic	Triclinic
space group, <i>Z</i>	<i>Pca</i> 2 <sub>1</sub>	<i>P</i> 2 <sub>1</sub> / <i>n</i>	<i>P</i> 2 <sub>1</sub>	<i>P</i> -1	<i>P</i> 2 <sub>1</sub> / <i>n</i>	<i>P</i> -1
<i>a</i> , Å	21.2618 (1)	6.0736 (15)	5.5475 (14)	7.748	7.1178 (3)	9.3147 (3)
<i>b</i> , Å	6.6382 (3)	7.5411 (18)	14.254 (5)	8.968	17.4499 (8)	10.9672 (3)
<i>c</i> , Å	8.2680 (3)	25.055 (7)	8.486 (3)	10.204	11.2043 (5)	14.8603 (5)
$\alpha$ , deg	90.00	90.00	90.00	92.73	90.00	96.7110
$\beta$ , deg	90.00	90.458	102.441	90.78	106.111 (2)	91.2540
$\gamma$ , deg	90.00	90.00	90.00	111.59	90.00	90.8230
<i>V</i> , Å <sup>3</sup>	1166.95 (8)	1147.5 (5)	655.2 (3)	658.1	1336.97 (10)	1507.09 (8)
temp, K	296 (2)	296 (2)	296 (2)	296 (2)	296 (2)	296 (2)
<i>d</i> <sub>calcd</sub> , g/cm <sup>-3</sup>	1.254	1.275	1.329	1.324	1.303	1.341
no. of reflections collected	4890	7938	3735	9824	9978	21983
no. of unique reflections	1968	2006	1962	2316	2288	5131
2 $\theta$ <sub>max</sub> , deg	50	50	50	50	50	50
no. of parameters	154	155	181	181	183	415
<i>R</i> 1, <i>wR</i> 2 ( <i>I</i> > 2 $\sigma$ ( <i>I</i> ))	0.0355, 0.0926	0.1247, 0.3578	0.0800, 0.2076	0.0491, 0.1464	0.0461, 0.1365	0.0489, 0.1453
<i>R</i> 1, <i>wR</i> 2 (all data)	0.0497, 0.1157	0.1492, 0.3811	0.1232, 0.2503	0.0586, 0.1598	0.0732, 0.1809	0.0592, 0.1622
goodness of fit	1.116	1.478	1.012	1.040	1.131	1.055
CCDC number	1842679	1842680	1842681	1842682	1842683	1842684

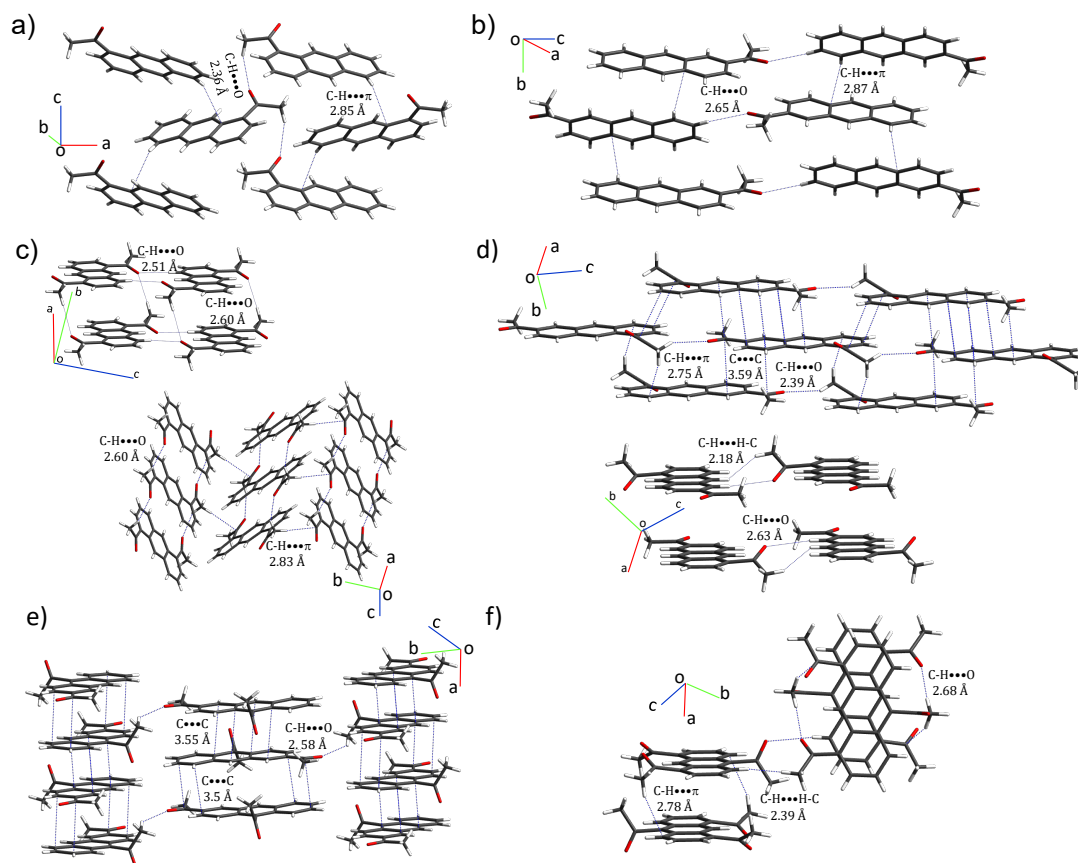


**Figure 2.2.** Close-packing arrangement in acetylanthracene derivatives guided by weak intermolecular interactions ( $C-H\cdots H-C$ ,  $C-H\cdots O$ ,  $C\cdots C$ , and  $C-H\cdots\pi$ ) in a) 1A; b) 1B; c) 2A; d) 2B; e) 2C; and f) 3.

2.2a) in 1A reinforce the  $C-H\cdots\pi$  interaction ( $d = 2.85 \text{ \AA}$ , c-axis), facilitating the formation of a compact two dimensional (2D) interpenetrated zigzag network of anthracene dimers (edge-to-face) inclined at  $56.2^\circ$  (Figure 2.3a). While in 1B, the  $C-H\cdots O$  interaction ( $d = 2.65 \text{ \AA}$ , c-axis) along with the  $C-H\cdots\pi$  interaction ( $d = 2.87 \text{ \AA}$ , b-axis) constitutes edge-to-face ( $\theta = 50^\circ$ ) anthracene dimers propagating in a conventional herringbone pattern (Figure 2.2b and 2.3b). Though, the inclined dimers possess certain  $\pi$ -overlap, the T-shaped (edge-to-face) arrangement hampers the precise assessment of  $\pi$ -

**Table 2.2.** Shows the various packing arrangements,  $\pi$ -stacking distances and % $\pi$ -overlap in crystalline 2A-C, and 3 derivatives.

	Arrangement	$d_{c-c}$ (Å)	% overlap
2A	Slip-stacked	3.53	24.4
2B	Brickwork	3.65	15.4
2C	2D columnar Stacks	3.52	49.6
3	2D Lamellar $\pi$ -stack	3.67	71.8

overlap among the nearest-neighbours in 1A and 1B (Scheme 2.2a,b).

The close-packing in 2A reveals a one dimensional (1D) lamellar/slip-stacked arrangement where the slip stacks of anthracene propagate in an end-

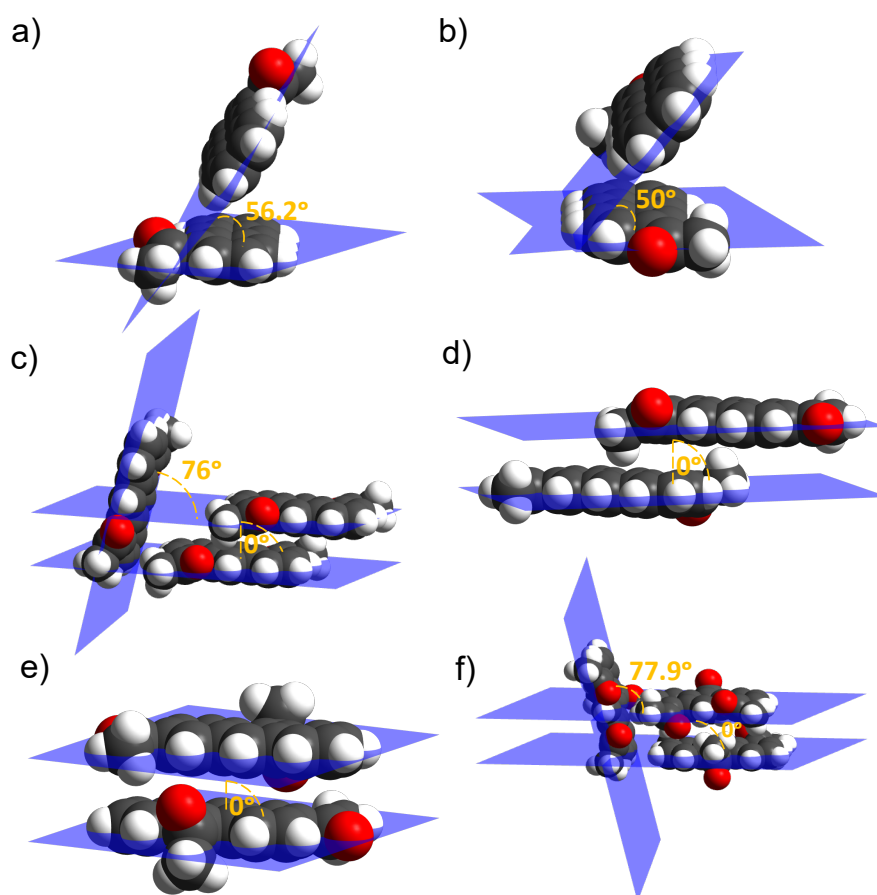


**Figure 2.3.** Angle between the mean planes of adjacent molecules in the crystal packing of a) 1A; b) 1B; c) 2A; d) 2B; e) 2C; and f).

to-face manner (Figure 2.1c). The C-H•••O interaction ( $d = 2.60 \text{ \AA}$ , a-axis and  $d = 2.51 \text{ \AA}$ , c-axis) guides the formation of slip stacks with an average interplanar distance of  $3.53 \text{ \AA}$  and a  $\pi$ -overlap of 24.4% between the nearest anthracenes units (Scheme 2.2c, Figure 2.2c, Table 2.2.). The C-H••• $\pi$  interaction ( $d = 2.83 \text{ \AA}$ , b-axis) between the methyl hydrogen and the carbonyl carbon accounts for the propagation of slip stacks in an end-to-face manner with an inclination of  $76^\circ$  between the adjacent anthracenes (Figure 2.3c). The packing motif in 2B resembles a pile of bricks directing a “2D lamellar/brickwork” arrangement with an average interplanar distance of  $3.65 \text{ \AA}$  and a  $\pi$ -overlap of 15.4% among the stacked anthracene units (Scheme 2.2d, Figure 2.2d, Table 2.2). The C-H•••O ( $d = 2.55 \text{ \AA}$ , a-axis and  $d = 2.63 \text{ \AA}$ , ac-plane) and the dihydrogen interaction (C-H•••H-C,  $d = 2.18 \text{ \AA}$ , ab-plane) between the aromatic and the methyl hydrogens guides a 2D-brickwork network of the anthracene units (Figure 2.2d). The derivative 2C exhibits a two dimensional (2D) columnar arrangement where the anthracene units are stacked in an antiparallel fashion with an interplanar distance and  $\pi$ -overlap of  $3.55 \text{ \AA}$  and 49.6%, respectively (Scheme 2.2e, Figure 2.2e). The C-H•••O ( $d = 2.58 \text{ \AA}$ , b-axis) interaction guide the antiparallel orientation, whereas the  $\pi$ - $\pi$  interaction ( $d = 3.55 \text{ \AA}$ , a-axis) lend a columnar stacking among the anthracene units, ensuing a  $\beta$ -motif assembly in 2C (Figure 2.1e and 2.2e). The acetylanthracene derivative 3 forms a 2D-lamellar arrangement where the

antiparallel sandwich dimers with a  $\pi$ -overlap of 71.8% propagate in a slip-stacked array (Scheme 2.2f, Figures 2.1f). The C-H $\cdots$ O interaction ( $d = 2.48$  Å, bc-plane and  $d = 2.33$  Å, ab-plane) is responsible for the development of the antiparallel sandwich dimer, while the C-H $\cdots$  $\pi$  ( $d = 2.78$  Å, a-axis) and dihydrogen (C-H $\cdots$ H-C,  $d = 2.37$  and  $2.39$  Å, ac-plane) contacts ensue an edge-to-face geometry with an inclination of  $77.9^\circ$  between the adjacent sandwich pairs (Figures 2.2f and 2.3f).

### 2.2.3. Quantum Theory of Atoms in Molecules (QTAIM) and Hirshfeld Analyses

Furthermore, the presence of C-H $\cdots$ H-C interaction perceived in the packing motifs of 2B and 3 were further substantiated by quantum theory of atoms in molecules (QTAIM) analyses (Figure 2.4) [103, 105, 124]. QTAIM illustrate a substantial accumulation of electron density at the (3, -1) bond critical point (BCP;  $\rho_b(r)$ ) and its Laplacian ( $\nabla^2\rho_b(r)$ ), depicting a bond and virial path in the potential energy density map, thereby emphasizing the dihydrogen (C-H $\cdots$ H-C) bonding in the crystalline 2B and 3 (Table 2.3).

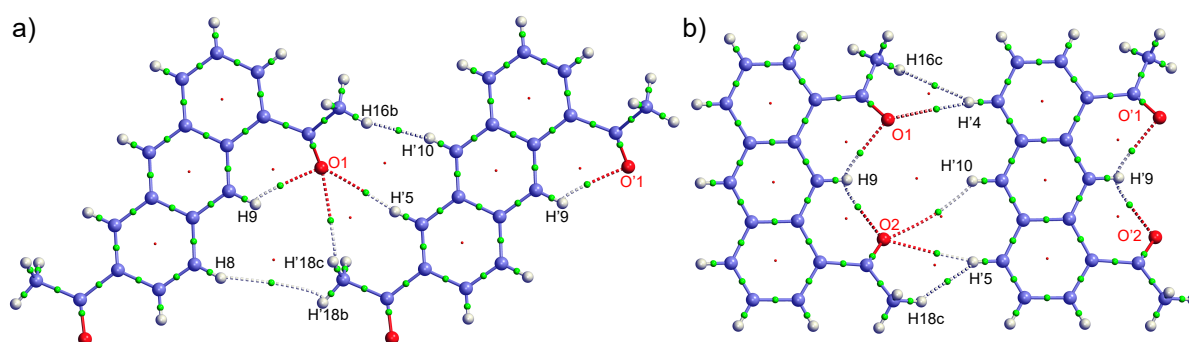


**Figure 2.4.** QTAIM electron density map of a) 2B; and b) 3.

**Table 2.3.** Calculated topological properties of the electron density for the intra- and intermolecular interaction in 2B and 3 crystal derivatives.

Description	Interaction	<sup>a</sup> <i>d</i> , (Å)	<sup>b</sup> $\rho_b(r)$ , (e Å <sup>-3</sup> )	<sup>c</sup> $\nabla^2\rho_b(r)$ , (e Å <sup>-5</sup> )
<b>2B</b>	H16b···H'10	2.180	0.047	0.549
	H8···H'18b	3.214	0.006	0.084
	O1···H9	2.316	0.098	1.434
	O1···H'18c	2.972	0.025	0.362
	O1···H'5	2.635	0.044	0.506
	O'1···H'9	2.316	0.098	1.434
<b>3</b>	H4···H'20b	2.376	0.028	0.327
	H20b···H'5	2.376	0.028	0.327
	O1···H9	2.351	0.092	1.345
	O2···H9	2.293	0.103	1.521
	O'1···H'9	2.293	0.103	1.521
	O'2···H'9	2.351	0.092	1.345
	O3···C'20	3.591	0.019	0.283
	O'3···C20	3.591	0.019	0.283

<sup>a</sup>*d*=distance, <sup>b</sup> $\rho_b(r)$ =electron density at the BCP and <sup>c</sup> $\nabla^2\rho_b(r)$ = Laplacian of the electron density at the BCP

Hirshfeld surface analyses[125] (Figures 2.5. and A2.1.) provided an additional insight into the intermolecular interactions present in crystalline 1-3 [103]. The evaluation of the packing motif of anthracene units in the crystalline state were carried out by quantifying the relative contribution of intermolecular interactions in the derivatives 1-3 (Table 2.4.) [103, 126]. The ratio of (%C···H)/(%C···C) interaction provided the  $\rho$  value, a  $\rho$  value of 4.5 or more indicates a herringbone structure where the molecules are arranged in an inclined fashion due to the prevalent C···H interaction.

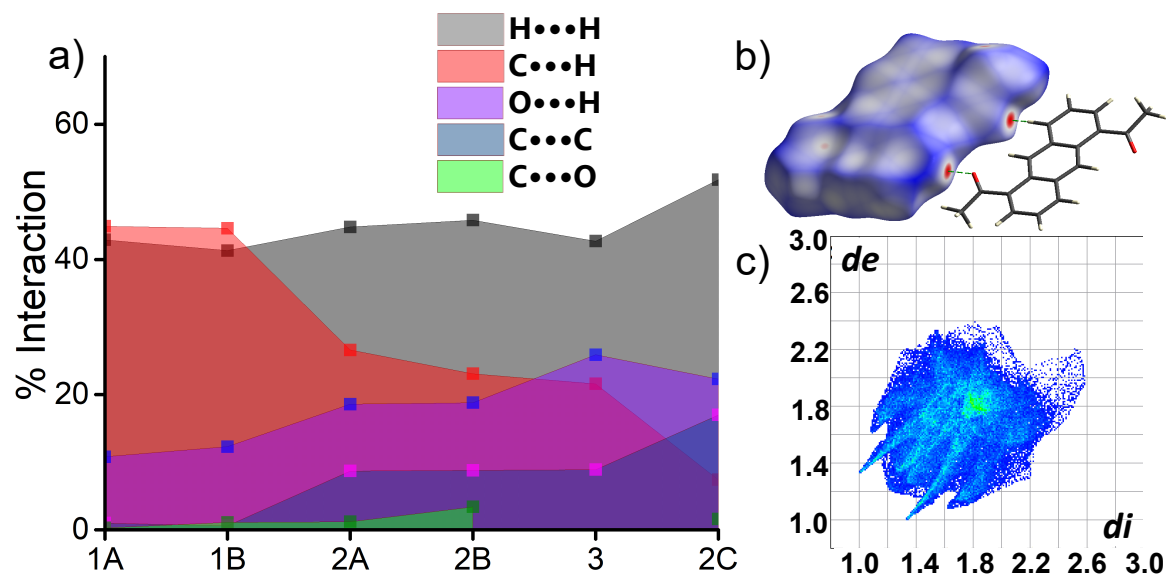


**Figure 2.5.** a) Percentage contribution of intermolecular interactions in crystalline acetylanthracenes (1-3); b) Hirshfeld surface mapped with  $d_{norm}$  depicting hydrogen (C-H...O) bonding and c) 2D fingerprint plot obtained from Hirshfeld surface analysis of 2A.

Sandwich herringbone ( $3.2 < \rho < 4.0$ ) structures are intermediate cases with moderate C...H and C...C interactions, whereas  $\gamma$  ( $1.2 < \rho < 2.7$ ) and  $\beta$  ( $0.46 < \rho < 1.0$ ) structures are parallel stacked molecules with strong C...C and a

**Table 2.4.** Percentage of intermolecular contacts of a single molecule in 1-3 crystal derivatives.

Interaction	1A	1B	2A	2B	2C	3
H...H %	42.9	41.3	44.8	45.8	51.8	42.7
C...H %	44.9	44.6	26.6	23.1	7.4	21.6
O...H %	10.8	12.3	18.6	18.8	22.3	25.9
C...C %	1.0	0.6	8.7	8.8	17.0	8.9
C...O %	0.3	1.1	1.2	3.4	1.6	-

<sup>a</sup>Total percentage of intermolecular contacts ca. 99.9% (1A), 99.9% (1B), 99.9% (2A), 99.4% (2B), 100.1% (2C), 99.1% (3)

weak C•••H interaction [103, 105].

## 2.2.4. Pitch and Roll Analyses

To correlate the molecular packing with the optical properties and estimate the accurate longitudinal and transverse slips, pitch and roll displacement analyses were carried out among the nearest anthracene units as per the procedure given by Curtis and co-workers (Figures 2.6., A2.2.-2.6., Table 2.5.) [127]. Compared to a perfect co-facial motif, pitch expresses the displacement of the molecule along the long molecular axis, whereas the roll outlines the

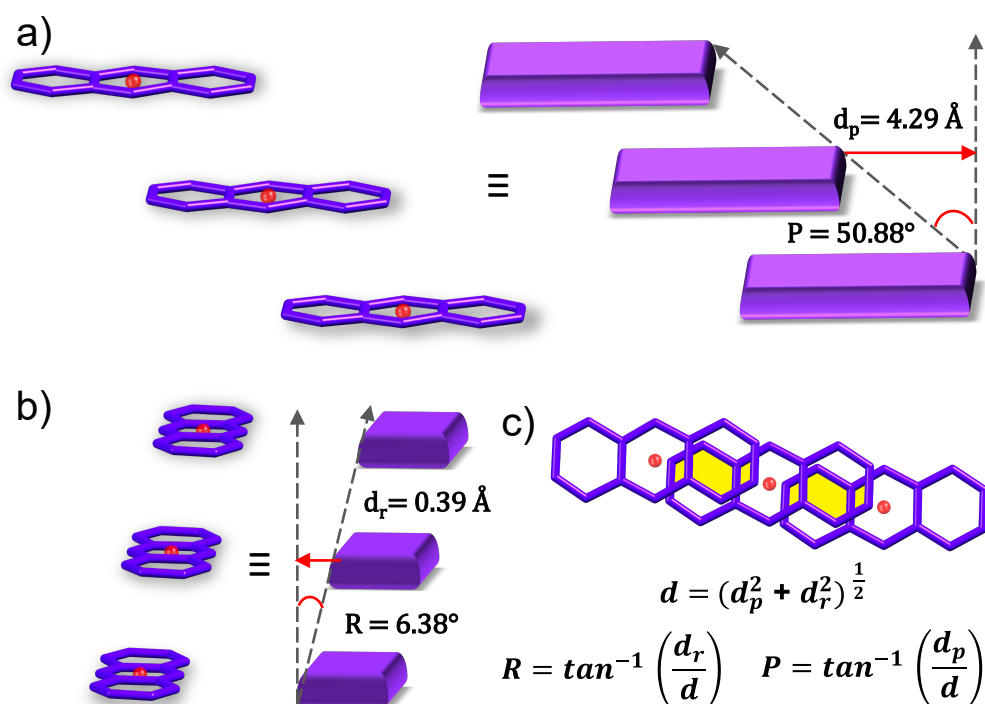


**Figure 2.6.** a) Pitch and b) roll displacement analysis and c) co-facial stacking motif and the definition of pitch ( $P$ ) and roll ( $R$ ) angles and associated distances among nearest co-facial anthracene units in 2A. The acetyl group and the hydrogen atoms are omitted for clarity. The sphere at the center of the ring denotes the centroid of the molecule.

**Table 2.5.** Pitch and roll displacement angles and distances for the crystalline 1-3.

	$d_p$ (Å)	$d_r$ (Å)	${}^a d_{\text{total}}$ (Å)	${}^b z$ (Å)	${}^c r$ (Å)	P (deg)	R (deg)
1A	3.53	4.87	6.01	6.63	6.64	51.7	60.20
1B	1.14	5.42	5.53	6.07	6.05	24.71	65.42
2A	4.29	0.39	4.30	5.54	5.55	50.88	6.38
2B (Dimer 1)	5.12	1.68	5.39	6.41	6.08	55.90	25.97
2B (Dimer 2)	5.34	2.18	5.76	6.84	7.23	55.46	30.62
2C	1.36	0.65	1.51	3.83	3.45	21.14	10.44
3 (Dimer 1)	0.99	0.96	1.38	3.88	3.82	15.28	14.78
3 (Dimer 2)	0.88	1.119	1.423	3.85	3.443	13.81	17.33

${}^a d_{\text{total}} = (d_p^2 + d_r^2)^{1/2}$ ;  ${}^b z = (d_p^2 + d_r^2 + d_{\text{total}}^2)^{1/2}$ ;  ${}^c r$  = centroid-to-centroid distance

displacement along the short molecular axis. A large roll translation can considerably impede the  $\pi$ -overlap, as seen in herringbone motifs 1A and 1B (Figures A2.2.-2.3.). Alternatively, larger pitch displacements can cause slip along the long molecular axis, creating a staircase and/or brickwork-type chromophoric assembly, while still maintaining the  $\pi$ -overlap, as observed in lamellar 2A and 2B motifs (Figures 2.6. and A2.4.). The AA derivative, 2C and 3, exhibit a small pitch and roll displacements/inclinations, facilitating a much larger electronic coupling and  $\pi$ -orbital overlap among the nearest anthracene units in the packing motif (Figures A2.5.-2.6., Table 2.5.).

### 2.2.5. Excited-State Properties in Isotropic Solution

To investigate the preliminary photophysical characteristics of AA derivatives (1-3), steady-state and time-resolved experiments were carried out in dilute

chloroform solutions (16-35  $\mu\text{M}$ , Figure 2.7, Table 2.6). The derivatives 1-3 exhibit pale yellow-yellow color in dilute chloroform solution with blue/blue-

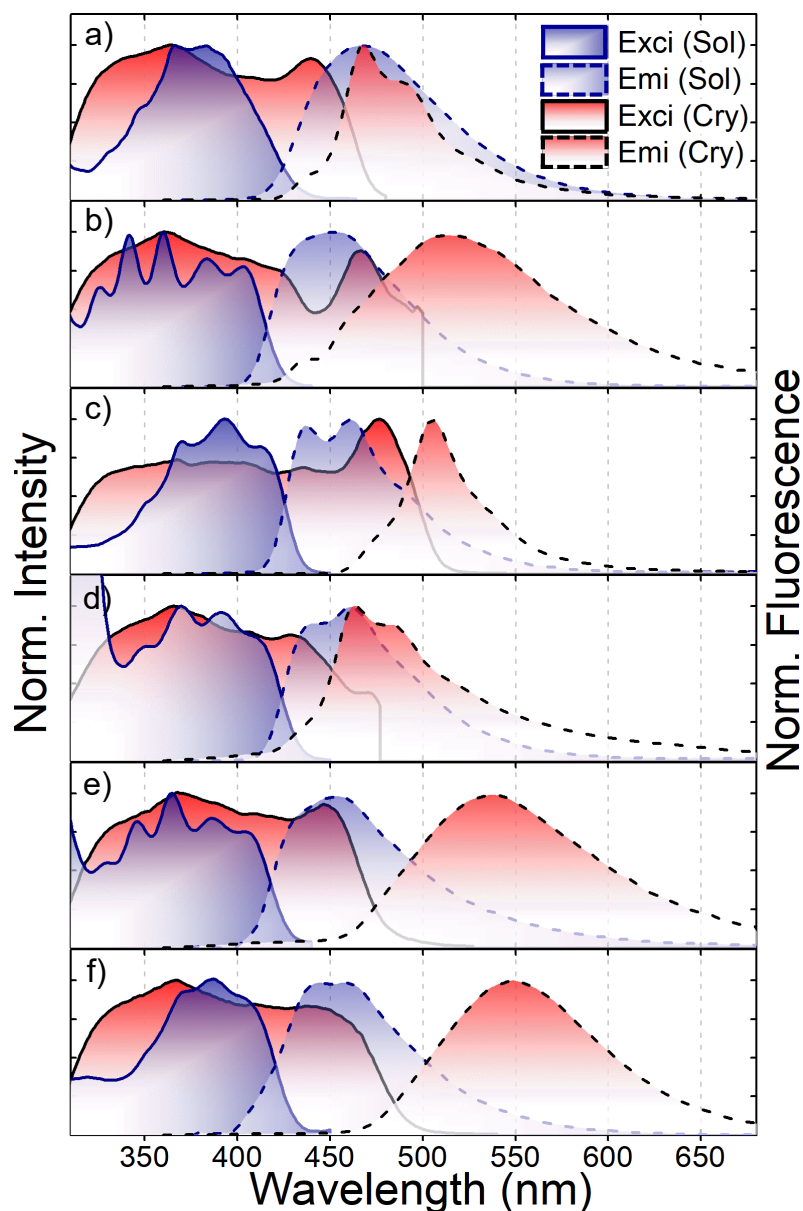


**Figure 2.7.** Normalized fluorescence excitation (solid) and emission (dashed) spectra of a) 1A; b) 1B; c) 2A; d) 2B; e) 2C and f) 3 in  $\text{CHCl}_3$  (shaded blue,  $\lambda_{\text{ex}} = 350 \text{ nm}$ ) and crystalline (shaded red,  $\lambda_{\text{ex}} = 360 \text{ nm}$ ) state. Excitation spectra were monitored at 474 and 490 nm (1A); 450 and 513 nm (1B); 450 and 555 nm (2A); 461 and 487 nm (2B); 451 and 538 nm (2C); and 460 and 550 nm (3) for solution and crystalline state, respectively.

**Table 2.6.** Photophysical properties of 1-3 derivatives in solution and crystalline state.

	<sup>a</sup> $\lambda_{\text{abs}}$ (nm)	<sup>a</sup> $\lambda_{\text{f}}$ (nm)	<sup>a</sup> $\tau_{\text{f}}$ (ns) [Amplitude] (%)	<sup>a</sup> $\Phi_{\text{f}}$	<sup>a</sup> $k_{\text{r}}$	<sup>a</sup> $k_{\text{nr}}$	<sup>b</sup> $\lambda_{\text{abs}}$ (nm)	<sup>b</sup> $\lambda_{\text{f}}$ (nm)	<sup>b</sup> $\tau_{\text{f}}$ (ns) [Amplitude] (%)	<sup>b</sup> $\Phi_{\text{f}}$	<sup>b</sup> $k_{\text{r}}$	<sup>b</sup> $k_{\text{nr}}$
<b>1A</b>	387	466	2.98 [100]	0.143	$4.8 \times 10^7$	$2.87 \times 10^8$	388	468	1.40 [51.0] 2.57 [49.0]	0.159	$7.39 \times 10^7$	$3.91 \times 10^8$
								525	1.47 [43] 2.71 [42.1] 11.63 [14.9]			
<b>1B</b>	342	451	11.9 [100]	0.509	$4.28 \times 10^7$	$4.12 \times 10^7$	389	450	0.65 [3.14] 4.87 [32.02] 14.24 [64.84]	0.048	$3.73 \times 10^6$	$7.40 \times 10^7$
								512	0.66 [3.7] 4.85 [27.7] 16.16 [68.6]			
<b>2A</b>	395	460	0.54 [80.1] 3.90 [19.9]	0.078	$2.89 \times 10^7$	$3.41 \times 10^8$	416	505	0.88 [17.84] 3.35 [42.3] 12.54 [39.9]	0.16	$1.55 \times 10^7$	$8.17 \times 10^7$
			560					0.87 [13.3] 3.71 [38.8] 14.3 [47.9]				

<b>2B</b>	392	462	0.45 [98.5] 5.6 [1.5]	0.071	$5.59 \times 10^7$	$7.31 \times 10^8$	415	464	0.37 [38.3] 2.02 [22.1] 9.80[39.6]	0.027	$3.09 \times 10^6$	$1.11 \times 10^8$
								570	0.53 [10.95] 3.69[30.67] 14.80[58.38]			
								470	0.65 [18.3] 4.02[38.2] 17.96 [43.5]			
<b>2C</b>	365	453	1.33 [51.0] 8.25 [49.0]	0.025	$3.44 \times 10^6$	$1.34 \times 10^8$	400	538	1.34 [29.9] 8.42[33.3] 32.8 [37.8]	0.125	$4.53 \times 10^6$	$3.17 \times 10^7$
								490	0.59 [1.94] 8.33 [7.72] 31.67 [90.34]			
								549	10.88 [7.6] 32.43 [92.4]			
<b>3</b>	388	459	---	0.026	---	---	392	490	0.59 [1.94] 8.33 [7.72] 31.67 [90.34]	0.125	$4.01 \times 10^6$	$2.81 \times 10^7$
								549	10.88 [7.6] 32.43 [92.4]		$3.92 \times 10^6$	$2.74 \times 10^7$

<sup>a</sup>chloroform solution; <sup>b</sup>crystalline state; abs – absorption; f – fluorescence.

green emission (Figures 2.7. and A2.7.). Depending on the position of acetyl substitution, the derivatives 1-3 display a red-shifted absorption with characteristic vibronic features as compared to model derivative anthracene (Figure A2.7a). Though an alteration of the vibronic character was seen, successive addition of the acetyl groups revealed insignificant bathochromic shift in the ground state absorption, plausibly due to the limited conjugation arising from rotational motion of the flanking acetyl group(s) in solution. Upon exciting at 350 nm, the fluorescence emission spectra of 1-3 display a similar trend (Figure A2.7b) and the excitation spectra monitored at individual emission wavelength reveals no perturbation in the ground-state properties (Figure 2.8.). Picosecond time-resolved fluorescence decay ( $\lambda_{\text{ex}} = 377 \text{ nm}$ ) measurements indicate a decrease in the lifetime of derivatives 1-3 with the progressive addition of the acetyl groups (Figure 2.9., Table 2.6.). The fluorescence quantum yield ( $\phi_f$ ) of the 1-3 derivatives exhibit a similar decrease, indicating the accessibility of an alternate decay pathway ( $k_{\text{nr}} \approx k_{\text{isc}} \gg k_r$ ) for the excited-state with successive addition of the acetyl groups (Table 2.6.) [103, 128].

### **2.2.6. Excited-State Properties in Crystalline Assembly**

The crystalline AA derivatives (1-3) exhibit pale yellow-yellow color under ambient conditions as shown in Scheme 2.1. The diffuse reflectance and the excitation spectra of the crystalline derivatives 1-3 exhibit a red-shifted, broad

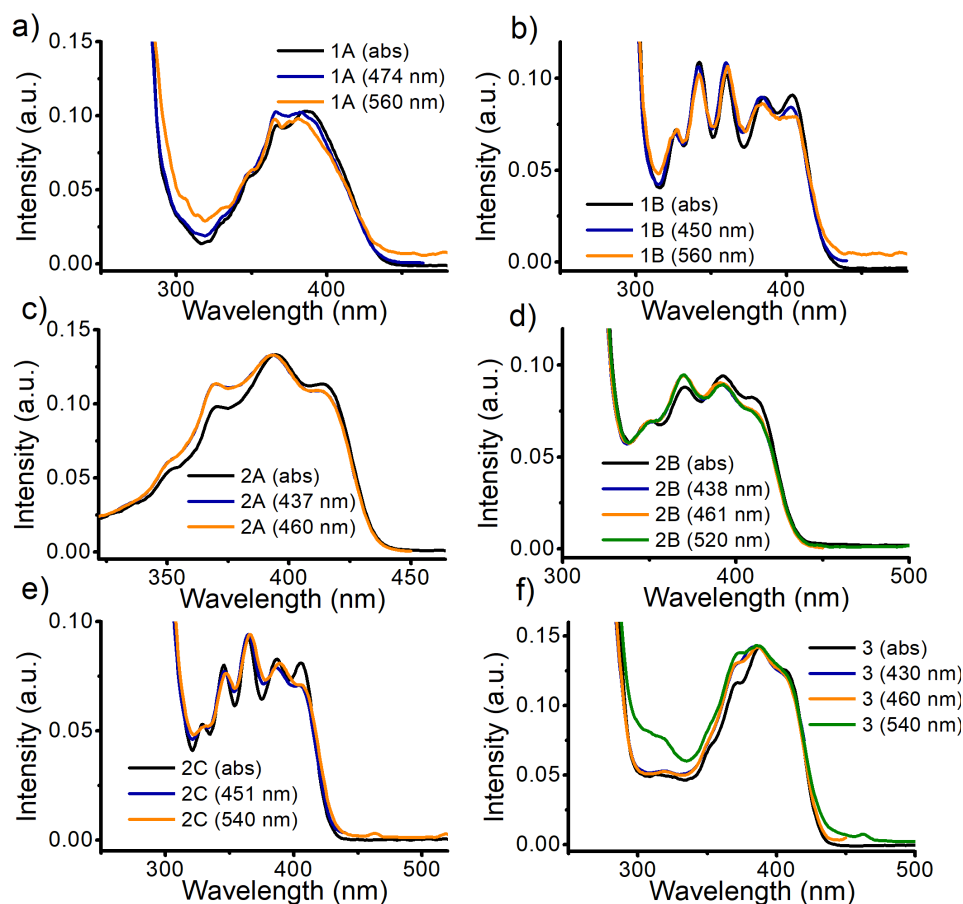


**Figure 2.8.** Fluorescence excitation spectra of a) 1A; b) 1B; c) 2A; d) 2B; e) 2C and f) 3 in  $\text{CHCl}_3$  as compared to absorption spectrum (black).

UV-vis absorption as compared to the isotropic solutions (Figures 2.7. and A2.8.). Red-shifted broad absorbance and excitation spectra in crystalline state can be a consequence of interplay among the nonresonant and excited-state resonant interactions [38, 90, 92, 129]. Upon excitation at 360 nm, crystalline 1-3, reveals distinct fluorescence emission (blue-green-yellow) signatures evolving from discrete packing motif of the anthracene units in the molecular ensemble (Figures 2.7. and A2.9.). Pre-associated co-facial dimers/oligomers can also catalyse the excimer formation at short stacking distances, thereby

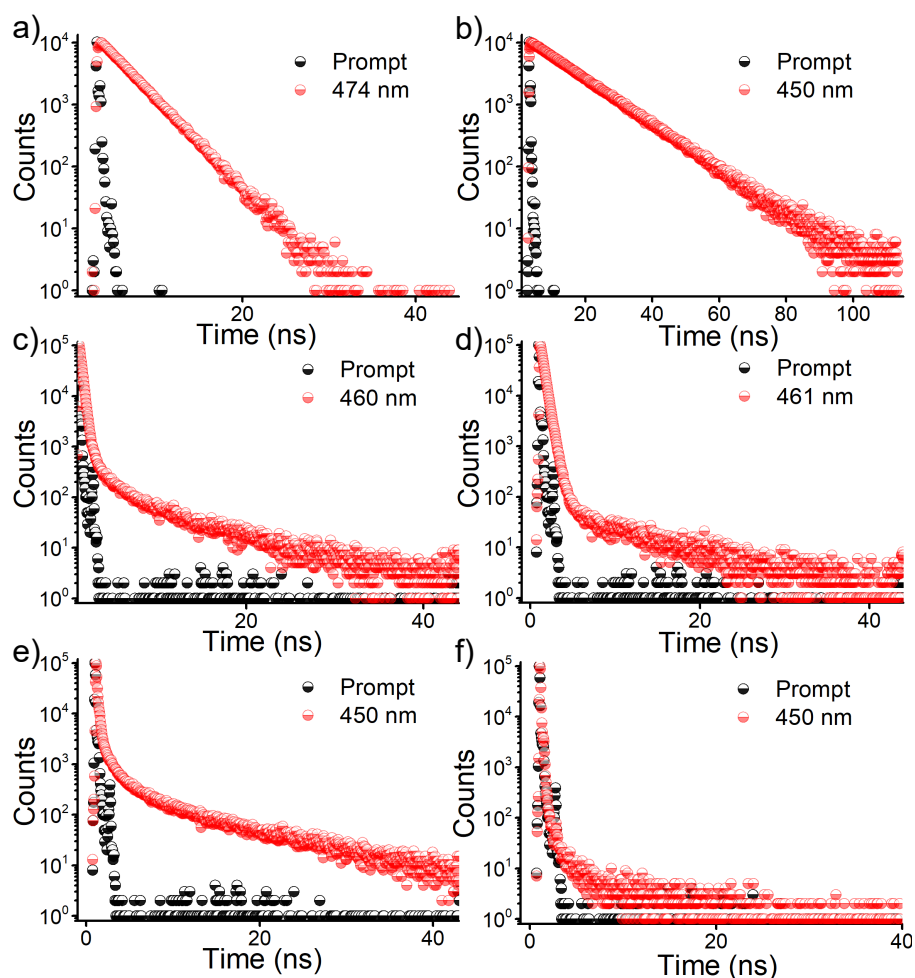


**Figure 2.9.** Picosecond time-resolved fluorescence decay profiles of a) 1A (474 nm); b) 1B (450 nm); c) 2A (460 nm); d) 2B (461 nm); e) 2C (450 nm) and f) 3 (450 nm) in  $\text{CHCl}_3$ . Excitation wavelength,  $\lambda_{\text{ex}} = 377 \text{ nm}$  (pulsewidth = 100 ps). The fluorescence decay of the derivative 3 could not be fitted as the decay was fast compared to the pulsewidth of the excitation source.

entailing an independent investigation of the cooperative ground/excited-state electronic interactions in crystalline 1-3.

Herringbone assembly in crystalline 1A, exhibit a vibronically resolved cyan emission centred at 466 nm and diffuse bands at 492, 536 and 568 nm (Figure 2.7a). Comparable quantum yields and fluorescence emission

signatures in the isotropic solution and crystalline state, suggest a monomer-like behaviour of 1A in the interpenetrated zigzag herringbone assembly (Table 2.6.). The fluorescence excitation spectra of crystalline 1A collected at different wavelengths display a negligible perturbation as compared to the ground-state absorption (Figure 2.10a). Picosecond time-resolved fluorescence decay measurements monitored at the emission maxima (468 nm), reveal a bi-exponential decay with an average lifetime comparable to that of monomeric

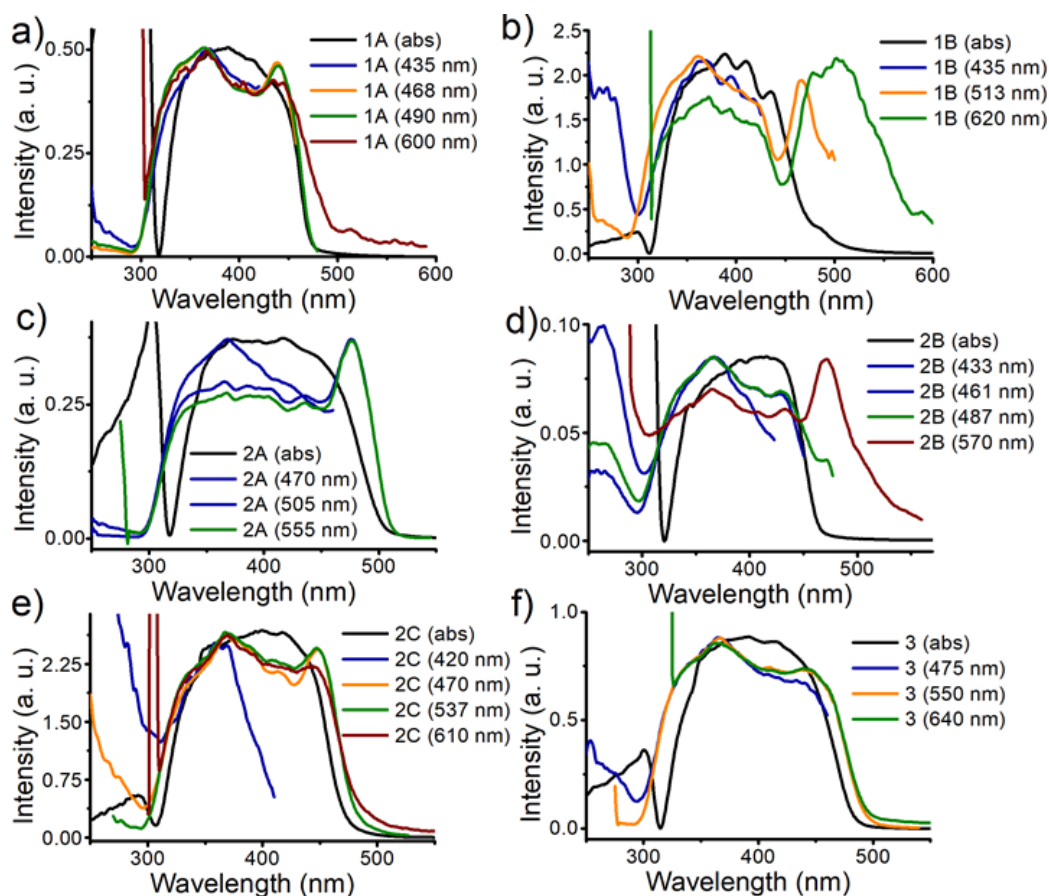


**Figure 2.10.** Fluorescence excitation spectra of crystalline a) 1A; b) 1B; c) 2A; d) 2B; e) 2C; and f) 3 as compared to the absorption spectra. Absorption spectra of crystalline 1-3 derivative are reproduced for comparison. Emission maxima, where the excitation spectra are monitored, are indicated in the bracket.

solution (Figures 2.11. and A2.10, Table 2.6). Examination of the fluorescence decay towards the red-edge (525 nm) of the emission spectra, reveal a minor long-lived component, suggesting an excimer-like excited-state aggregation in crystalline 1A (Figure 2.10a). Contrastingly, the herringbone packed 1B, exhibit a broad green fluorescence spanning 420-680 nm with emission maxima centred at 512 nm (Figure 2.7b). Broad featureless emission and mismatch with the emission in  $\text{CHCl}_3$ , signifies an apparent role of pre-

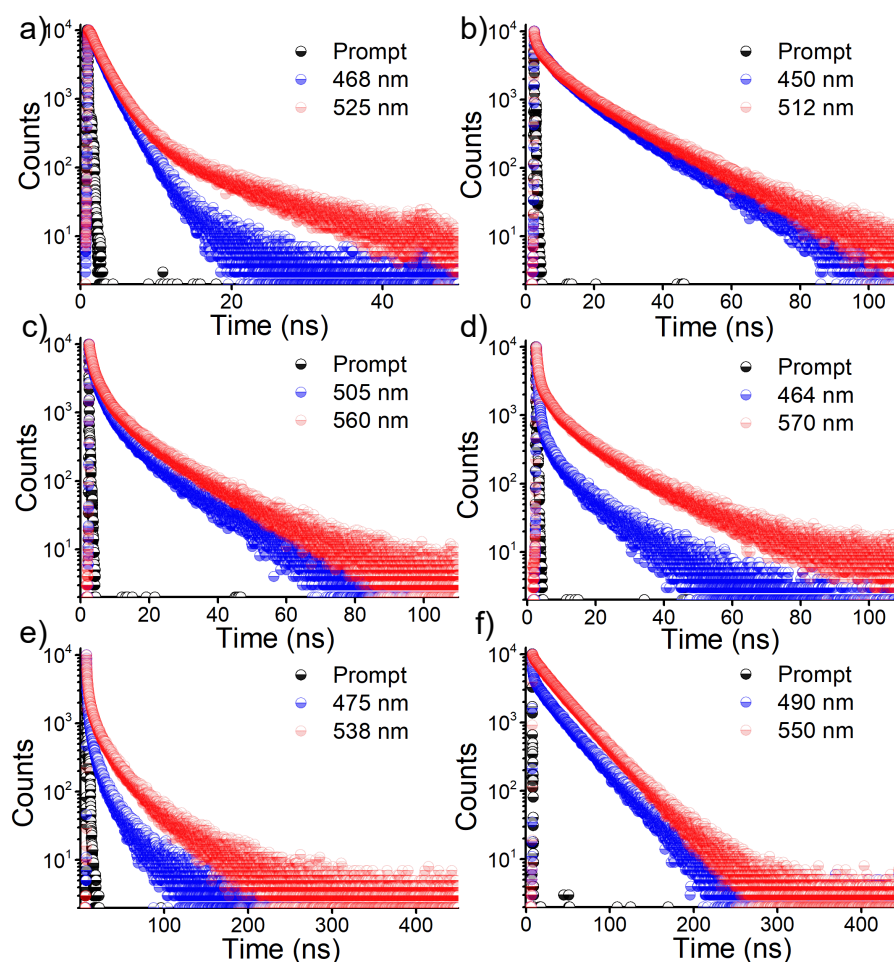


**Figure 2.11.** Picosecond time-resolved fluorescence decay profiles of crystalline a) 1A; b) 1B; c) 2A; d) 2B; e) 2C and f) 3 monitored at different wavelengths. Excitation wavelength,  $\lambda_{ex} = 377 \text{ nm}$  (pulsewidth = 100 ps).

associated dimer/oligomer in modulating the optical properties of 1B via ground/excited state interactions. The fluorescence excitation spectra of 1B monitored at longer wavelength reveal the emergence of a new red-shifted band, suggesting a ground-state association phenomenon (Figure 2.10b). The time-resolved fluorescence decay of crystalline 1B reveal a tri-exponential decay with lifetime components of 0.66, 4.8 and 16.2 ns (Figure 2.11b). Quenched fluorescence, tri-exponential fluorescence decay and a long-lived emitting species (16.2 ns) as compared to that in the solution, suggests an excimer-like association in crystalline 1B. Though, the photophysical characteristics in crystalline 1B suggest a major excimer-like character, the probability of the transition dipole coupling among the nearest-neighbors in the molecular ensemble cannot be overlooked.

Slip-stacked lamellar motif in 2A exhibit emission ranging from 450-600 nm with a sharp maximum centred at 505 nm (Figure 2.7c). The fluorescence excitation spectrum of 2A depicts a sharp red-shifted band while monitoring at longer wavelength (Figure 2.10c). Fluorescence lifetime analysis of the crystalline 2A depicts a tri-exponential decay with fast decaying components similar to that in monomeric solution ( $\tau_f = 0.88$  and 3.35 ns) and a slow decaying species ( $\tau_f = 12.54$  ns, Table 2.6.). Contrarily, the brickwork/2D lamellar motif in crystalline 2B corroborate a monomer-like cyan emission centred at 462 nm and diffuse bands at 485, 527 and 592 nm (Figure 2.7d). The

fluorescence excitation spectra recorded at different wavelength reveals the presence of a marginal ground-state association (Figure 2.10d). Picosecond time-resolved fluorescence decay monitored at the emission maxima display a similar lifetime to that of the monomeric solution with an additional long-lived species (Figure 2.11d, Table 2.6.). Slower fluorescence decay in crystalline 2A and 2B, when compared to the monomeric solution and while monitoring at the red-edge of the emission, evokes an excimer-like character (Figure 2.11c-d and A2.10c-d).

Interestingly, the  $\pi$ -stacked columnar motif in 2C exhibit a broad, featureless yellow emission centred at 538 nm with a large Stokes shift (Figure 2.7e). Large orbital overlap among the  $\pi$ -stacked columnar anthracenes and close-stacking distances can catalyse strong excitonic interaction, while simultaneously instigating a plausible excimer formation. Red-shifted fluorescence excitation spectra of crystalline 2C as compared to the monomeric solution, suggest the apparent ground-state interaction among the  $\pi$ -stacked anthracenes in 2C. Concurrently, the structureless broad emission and the large Stokes shift in the co-facial assembly of columnar anthracenes proposes an apparent excimer-like character. A longer fluorescence lifetime component of 32.8 ns further supports the excimer-like character in crystalline 2C (Table 2.6.). Analogously, the 2D lamellar stack in crystalline triacetylanthracene (3) display (i) broad structureless emission with large Stokes shift; (ii) a red-

shifted excitation spectrum as compared to the solution and (iii) a longer lifetime component of 32.43 ns, substantiating the influence of the excimer and dipole interactions in corroborating a yellow emission in 3 (Figure 2.7f, Table 2.6.). Observed progressive red-shift in the fluorescence emission of crystalline mono to triacetylanthracene can be a consequence of (i) increase in the number of the acetyl groups and/or (ii)  $\pi$ -overlap regulated cooperation of short-range excimer and long-range Coulomb (dipole) interactions. Discrete molecular structures and the packing motifs in crystalline 1-3 and the consequent intricate spectroscopic signatures, necessitate a partition of the co-operative and/or competitive excimer and dipole interactions in the molecular ensemble.

### **2.2.7. Estimating the Dipole Coupling (Mean Field Approximation)**

Spatially proximate chromophoric units in the molecular ensemble can electronically couple via Coulomb interaction among the transition dipoles which can lend a resonance splitting of the excited state into two non-degenerate states as discussed in section 1.3.2.3. (Scheme 2.1.) [37]. To unravel the impact of the diverse geometric stacking, dipole orientation and effect of more than one molecule/unit cell on the spectroscopic emission signatures of crystalline 1-3, dipole-dipole coupling among the nearest and non-nearest anthracene units were evaluated following the Kasha's exciton coupling formalism [37].

Kasha's exciton model approximates the interacting chromophores in a dimer as point-dipoles, wherein the Coulomb coupling among the two transition dipole moments render resonance splitting (exciton splitting,  $2\Delta\epsilon_{Dip}$ ) of the excited state [37]. The dipole-dipole interaction among the transition densities ( $M$ ) of the two molecules A and B can be given as [37, 130, 131],

$$V_{AB}^{d-d} = 2\Delta\epsilon_{Dip} = \frac{e^2}{4\pi\epsilon_0} \iint \frac{M_A M_B}{|r_1 - r_2|} d\mathbf{r}_1 d\mathbf{r}_2 \quad (2.1)$$

$$\approx \frac{1}{4\pi\epsilon_0 |R^3|} \{P_A P_B - 3(P_A \cdot \hat{R})(P_B \cdot \hat{R})\} \quad (2.2)$$

$$\approx -\frac{57.17 \cdot 10^{27} \cdot P_A P_B}{|R^3|} (\cos \alpha - 3 \cos \theta_A \cos \theta_B) eV \quad (2.3)$$

where  $M_A$  and  $M_B$  are the transition densities of the molecules A and B.  $P_A/P_B$  can be viewed as the dipole moment of the transition density  $M_A/M_B$ ;  $|R|$  denotes the distance between the centres of the molecules A and B and  $\hat{R}$  is the unit vector in that direction;  $\alpha$  denotes the angle between the polarisation axes for the component absorbing units and  $\theta_A/\theta_B$  are the angle made by the polarisation axes of molecules A/B respectively, with the line joining the molecular centres.

The above-mentioned formalism (equation 2.1-2.3) can quantitatively account the resonance splitting arising from exciton (Coulomb) interaction in an ideal chromophoric dimer pair [37]. Nearest-neighbour approach fails when a molecular ensemble possesses more than two molecules in vicinity, each with a difference in their relative orientations with respect to a central

molecule, akin a periodic crystal with more than one molecule/unit cell (Figure 2.12.) [38, 41]. Given the exact diagonalisation of Hamiltonian becomes hard with the increasing number of constituent molecules in unit cell, a simpler approximation is to add up all the nearest and non-nearest neighbour interactions in a mean-field approximation [132]. Herein, a central molecule is assumed to be electronically affected by a mean-field created by all the nearest and non-nearest neighbours (Figure 2.12b).

Using this approximation, the exciton coupling to the central molecules

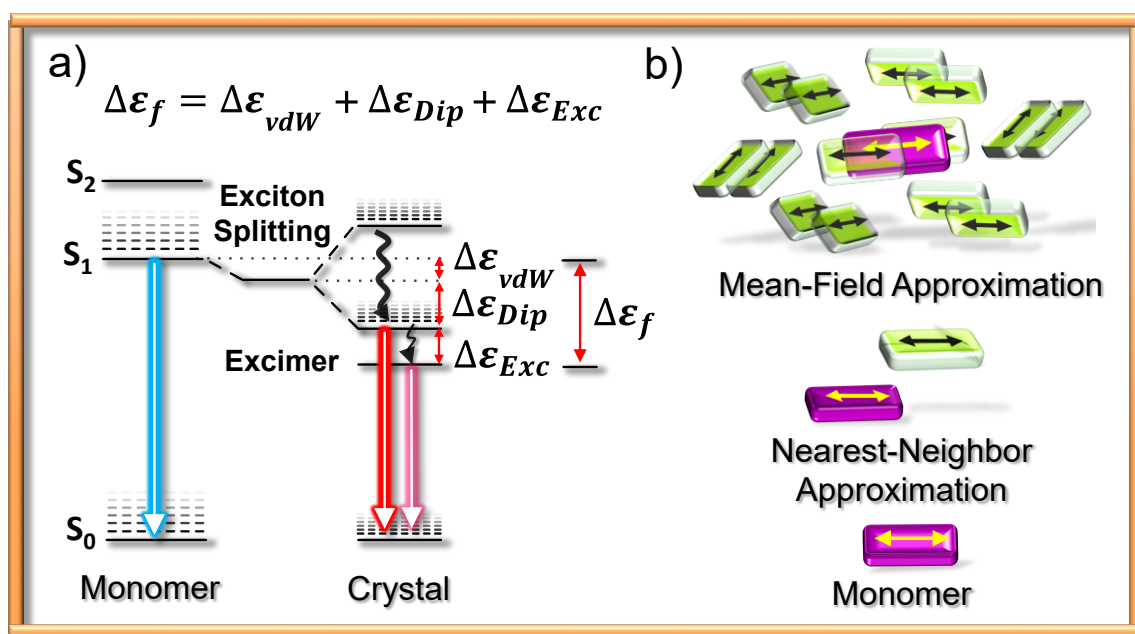


**Figure 2.12.** a) Characteristic excited-state transitions illustrating concerted excimer and dipole couplings in monomer vs. crystalline state and b) monomer, dimer (nearest-neighbour) and molecular ensemble (mean-field approximation) used for exciton coupling calculations in crystalline 1-3 [133]. For clarity the central molecule of the assembly in Figure 2.12b is depicted in purple.

due to the presence of the all the neighbours can be approximated as,

$$V_{total}^{d-d} = \sum_{i=1}^N V_{Ai}^{d-d} \quad (2.4)$$

where A is the central molecule and the exciton coupling of A with i (i = 1, 2, ..., N) of its neighbours are added up. This is a much superior approximation for a crystal assembly compared to the widely used nearest-neighbour approximation as it accounts the interaction between all the non-nearest neighbours with diverse dipole orientations.

To evaluate the dipole coupling among the nearest anthracene units in a crystalline ensemble, transition density cubes of the individual chromophores (1-3) were generated for a HOMO→LUMO transition (n=1) by performing TDDFT calculations at B3LYP/6-311G++(d,p) in *Gaussian 09* [134]. The numerically calculated transition density cubes (TDCs) of an individual molecular unit was used to replicate a dimer pair with spatial orientation and distances similar to that seen in the crystal structures (see Appendix) [130]. The interaction of the transition densities employing the formalism depicted in equation 2.1-2.3, furnished the dipole-dipole coupling interaction energies ( $2\Delta\varepsilon_{Dip}$ ) for a dimer pair. The same routine was used to calculate the dipole-dipole interactions for all the symmetrically non-equivalent dimer pairs present in a molecular ensemble and summed up to get the mean dipole-dipole interaction energies in crystalline 1-3 (Figure 2.12., Table 2.7.). The explicit effect of the exciton splitting energies on the emission character of

**Table 2.7.** Excimer and dipole coupling (mean field approximation) mediated spectral shifts and the optical properties of acetylanthracene derivatives (1-3) in solution/crystalline.

	1A	1B	2A	2B	2C	3
$\lambda_f^{\text{Cry}}$ (nm)	468	512	505	464	539	549
$\lambda_f^{\text{Sol}}$ (nm)	466	451	460	462	453	459
$\Delta\lambda_f$ (nm)	2	61	45	2	86	90
$\Delta\epsilon_{\text{Dip}}$ (meV)	-1.9	-39	-0.01	-18.9	241	110.7
$\lambda_f^{\text{Dip}}$ (nm)	465.5	456.6	459.1	464.4	495.8	477.7
Dipole Shift (nm)	-0.5	5.6	-0.9	2.4	42.8	18.7
Excimer Shift (nm)	2.5	55.4	45.9	-0.4	43.2	71.3

$\lambda_f^{\text{Cry}}$  and  $\lambda_f^{\text{Sol}}$  = fluorescence emission maxima in crystalline and solution state respectively;  $\Delta\lambda_f = \lambda_f^{\text{Cry}} - \lambda_f^{\text{Sol}}$ ;  $\Delta\epsilon_{\text{Dip}} = 1/2$  (mean field approximated dipole-dipole interaction energy);  $\lambda_f^{\text{Dip}} = 1240/(\Delta\epsilon_{\text{Sol}} - |\Delta\epsilon_{\text{Dip}}|)$ ; Dipole Shift =  $(\lambda_f^{\text{Dip}} - \lambda_f^{\text{Sol}})$ ; Excimeric Shift =  $\Delta\lambda_f - \text{Dipole shift}$ .

crystalline 1-3 was further assessed. The sign of the exciton splitting energies, i.e. positive (H-type) or negative (J-type), in Table 2.7., signifies a global effect of the exciton interactions (mean-field approximated) on the spectral properties of the molecular ensemble. Negative exciton splitting energies in molecular motifs of 1A (-1.9 meV), 1B (-39 meV), 2A (-0.013 meV) and 2B (-18.9 meV) suggest a low-to-moderate J-type coupling, whereas 2C (241 meV) and 3 (110.7 meV) with positive exciton interaction energy suggest a strong H-type

coupling. The computed exciton splitting energies (mean-field approximation) suggests a definite role of the dipole coupling in modulating the fluorescence emission characteristics of crystalline 1-3 derivatives.

### **2.2.8. Time-Resolved Emission Spectral (TRES) Analyses**

Having quantified the influence of the dipole interactions on the molecular ensemble, the role of the excited-state interactions in modulating the spectral characteristics of crystalline 1-3 were explored. Long lifetime components in the picosecond time-resolved fluorescence decay of crystalline 1-3 suggest an apparent presence of excited dimer (excimer, Table 2.6.). To probe the origin of the long fluorescence lifetimes, time-resolved emission spectral (TRES) measurements followed by global analysis (GA) of the kinetic traces (at all wavelengths) were performed (Figure 2.13., A2.11.). The GA of the time vs. wavelength plots furnished an evolution associated spectra (EAS) based deconvolution of the temporal components in the fluorescence emission. Depending on the discrete structure and stacking in the molecular ensemble, the EAS of crystalline 1-3 reveals an initial short-lived species evolving to an excimer-like emission. The evolution (lifetime) and the spectral character of the long-lived species irrefutably defines the role of the excited dimer/oligomer in moderating the optical properties of the crystalline 1-3. The computed exciton splitting interaction energies and the experimentally observed excimer emission validate a concerted role of excimer and dipole

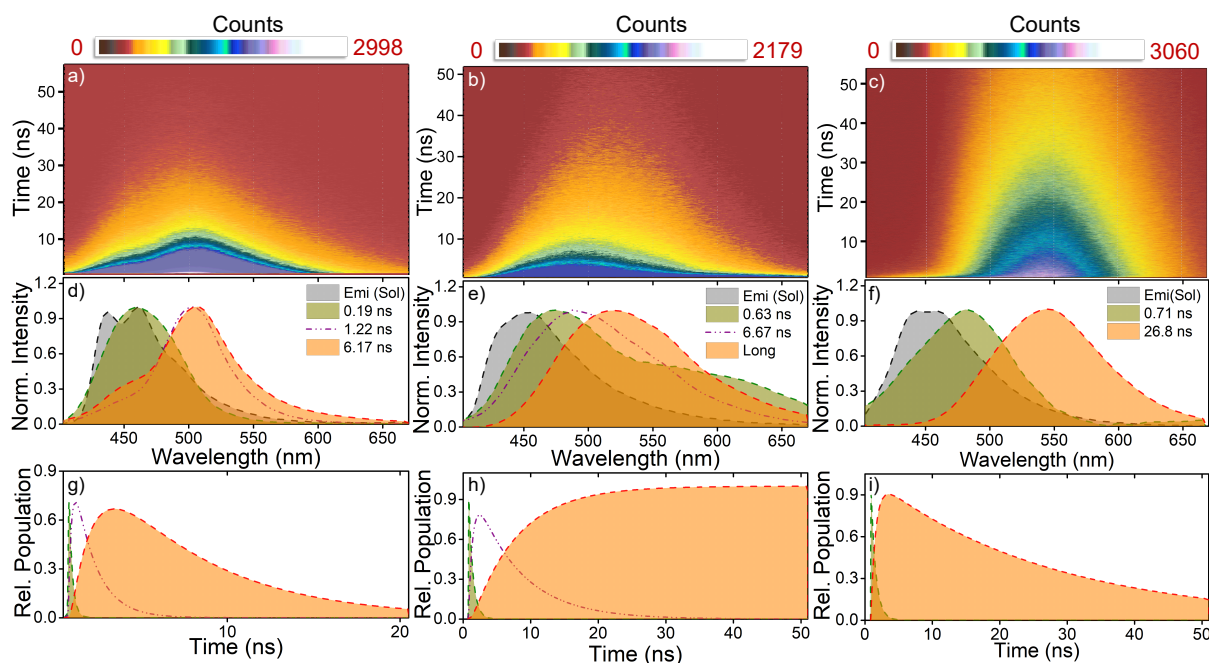


**Figure 2.13.** Time-resolved emission spectrum (TRES) (a, b, c); normalized evolution associated spectra (EAS; d, e, f) and the relative population profiles (g, h, i) of crystalline 2A, 2C and 3 respectively; excitation wavelength is 377 nm (pulse width  $\leq 100$  ps). The emission spectra of 2A, 2C and 3 in  $\text{CHCl}_3$  (shaded grey) solution are depicted for comparison in Figure 2.12d, e and f.

couplings in regulating the fluorescence emission of crystalline 1-3 (Figure 2.12a, Table 2.7.). Assuming that the fluorescence always evolve from the lowest exciton state (Kasha's rule)[29] and a cooperation of the excimer and dipole coupling exist [112], the energy difference between the excited state in crystalline and monomeric solution can be rationalized by equation 2.5 (Figure 2.12a) [101, 112],

$$\Delta\epsilon_f = \Delta\epsilon_{vdW} + \Delta\epsilon_{Dip} + \Delta\epsilon_{Exc} \quad (2.5)$$

where  $\Delta\epsilon_{vdW}$ ,  $\Delta\epsilon_{Exc}$  and  $\Delta\epsilon_{Dip}$  are the relative stabilisation of the excited state in crystalline assembly via van der Waals, dipole-dipole and excimer

interactions [133]. Estimated dipole interaction energy ( $\Delta\varepsilon_{Dip}$ ) and the apparent difference between the emission in crystalline and monomeric solution ( $\Delta\lambda_f/\Delta\varepsilon_f$ ) can further provide the excimer ( $\Delta\varepsilon_{Exc}$ ) contribution towards the spectral shifts observed in crystalline 1-3 derivatives [112, 133]. The above-mentioned relation offers a quantitative method to deconvolute the spectral shifts arising from excimer and dipole couplings and narrate the exciton relaxation dynamics in crystalline 1-3 (Table 2.7.).

The excited-state properties of crystalline 1-3 can be further substantiated by correlating the computed excimer and dipole shifts with the experimentally estimated temporal components of the TRES data. TRES measurements of crystalline 1A (herringbone) and 2B (brickwork) reveals the presence of an initial short-lived species transforming to a long-lived excimeric emission, substantiating the slow decaying components in the fluorescence lifetimes (Figure A2.11.). Though having a long lifetime, the excimer formation yield in the crystalline 1A and 2B seems low from the relative amplitude of the long lifetime component, a significant monomer-like vibronic and a diffuse excimer character. Concurrently, the computed excimer (2.55 [1A] and  $\approx 0$  [2B] nm) and the dipole ( $\approx 0$  [1A] and 2.4 [2B] nm) shifts also emphasize a monomer-like character in crystalline 1A and 2B (Table 2.7.). Contrastingly, crystalline 1B (herringbone) and 2A (lamellar) display a major excimer component as is seen from a red-shifted emission (centered at 510-530 [1B] and 505 [2A] nm) and

high relative amplitudes of the long-lived components (Figure 2.7b-c, Table 2.6.). Edge-to-face geometry of the nearest-neighbors and excimer band centered at 510-530 nm in 1B, suggests a T-shaped excimer as proposed earlier by Ma and co-workers for substituted anthracenes [116, 117]. The computed excimer (55.4 nm) and dipole (5.6 nm) shifts agree with the experimentally observed excimer character in 1B (Table 2.7.). Derivative 2A being a symmetric molecule (low transition dipole moment, dipole shift  $\approx 0$  nm), the slip-stack dimer/oligomer might play a crucial role in moderating a major excimer-like ( $\approx 45.9$  nm) emission (Table 2.7.).

Lamellar motifs 2C and 3 with considerable orbital overlap display a broad featureless (H-type/excimer-like) emission with a large Stokes' shift and a high fluorescence lifetimes (Figure 2.7e-f, Table 2.6.). Large  $\pi$ -orbital overlap and close stacking distances between the dimer/oligomer ensure a strong electronic communication in the molecular ensemble, enabling the occurrence of cooperative Coulomb and excimer-like interactions (Scheme 2.2.) [115, 117]. Deconvoluted spectral shift in 2C suggests equal contributions from dipole (42.8 nm) and excimer (43.2 nm) interaction in the crystalline state as compared to monomeric solution (Table 2.7.). On the other hand, the lamellar motif in triacetylanthracene (3) display a marginal dipole ( $\approx 18.7$  nm) and a major excimer (71.3 nm) character owing to a relatively higher orbital overlap in 3 as compared to 2C (Scheme 2.2., Table 2.7.). Interestingly, the

bathochromic-shift of the long-lived EAS temporal component in crystalline 1-3 can be correlated to the computed excimeric shifts (Figures 2.13. and A2.11.). Spectral shift of the experimentally deconvoluted long-lived EAS temporal component (63 nm) corresponding to the excimer emission in triacetylanthracene (3) nearly agrees with the theoretically computed excimeric shift (71.3 nm, Table 2.7., Figures 2.13. and A2.11.). An analogous trend is also observed among the experimental (EAS temporal component) and the computed excimer shifts in 1B, 2A and 2C.

Minor disparity among the experimentally observed EAS temporal components and the theoretically computed excimer shifts (Table 2.7.) can be a consequence of (i) incomplete decay of the long-lived EAS component in the given experimental window; (ii) stabilization of the monomeric acetylanthracene excited-states in chloroform (gas-to-solvent shift); and/or (iii) molecular self-absorption in the crystalline state [42]. Manifestly an interplay of dipole and excimer interactions ensue a monomer-like emission in 1A and 2B, a major excimer contribution in 1B and 2A, whereas 2C and 3 reveals a cooperation of both the excimer and dipole coupling in modulating the spectroscopic characteristics of the aggregate. Consistent experimental and theoretical narration of the observed spectroscopic/excited-state character in crystalline 1-3, denotes the significance of a global understanding of the various factors affecting the excited-state characteristics of a molecular

ensemble. The insights gained from a comprehensive experimental/theoretical investigation of excimer/dipole coupling controlled emission can further shed light on the fundamentals of manipulating the molecular aggregates for optoelectronic applications.

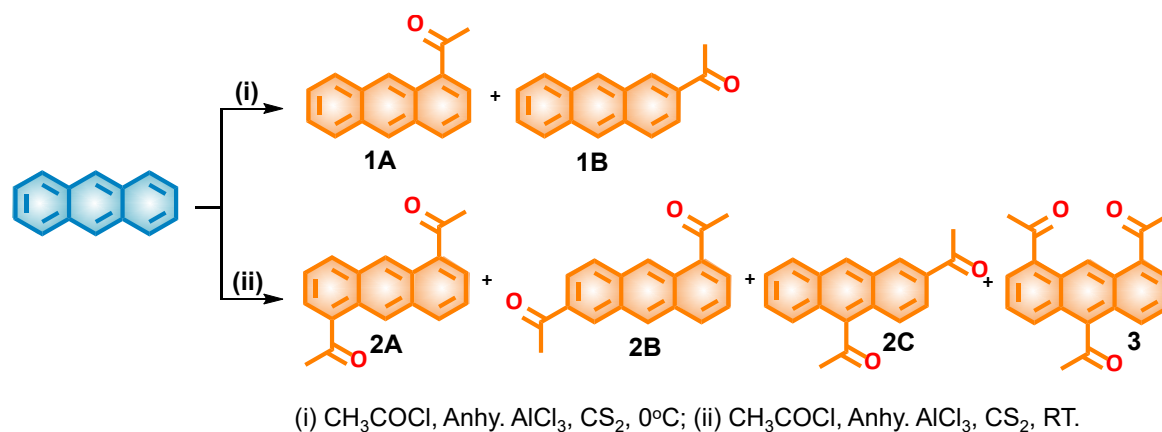
## **2.3. Conclusions**

In summary, we report an elegant approach to decipher the subtlety of the excimer and dipole interaction mediated exciton relaxation dynamics in the molecular ensemble of crystalline 1-3 derivatives. Classical Friedel-Crafts acylation of anthracene core rendered a series of AA derivatives (1-3) with (i) discrete molecular structure; (ii) varied orbital overlap/spatial orientation and (iii) diverse packing motif. Distinct molecular orientation and the packing arrangement in crystalline 1-3, ensued a perturbed electronic communication among the nearest anthracene units via an interplay of the excimer and dipole couplings. The manifestation of the cooperative dipole and excimer interactions was reflected in the excited-state characteristics of crystalline 1-3, rendering distinct blue-green-yellow emission. Independent assessment of the excimer and dipole coupling via TRES analyses and Kasha's exciton coupling formalism (mean field approximation) offered a quantitative estimation of the excimer and dipole coupling mediated spectral shifts in crystalline 1-3. Good agreement between the experimentally evaluated (long-lived EAS components) spectral shifts and the numerically computed excimer shifts narrate a comprehensive approach to unravel the excited-state properties in

crystalline molecular ensembles. We believe that a tacit understanding of cooperative fundamental phenomena (excimer/dipole interaction) controlling the excited-state characteristics of molecular ensemble can help rationalize the design of novel photofunctional materials.

## 2.4. Experimental section

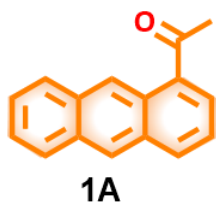
### 2.4.1. Syntheses and Characterization



**Scheme A2.1.** Shows the synthesis of acetylanthracene derivatives (1-3).

#### General procedure for the synthesis of acetylanthracenes:

Anthracene (A, 1.0 eq.) was dissolved in  $\text{CS}_2$  and subsequently anhydrous  $\text{AlCl}_3$  (1.2, 2.5 or 8 eq.) was added. Acetyl chloride (1.2, 2.5 or 8 eq.) was then slowly syringed to the suspension maintaining the appropriate temperature. The progress of the reaction was monitored through thin layer chromatography (TLC). After completion of the reaction, the reaction mixture was added slowly to a vigorously stirred mixture of ice and concentrated hydrochloric acid. The resulting suspension was filtered and vacuum dried and purified through column chromatography [silica gel, pet. ether:chloroform] to give acetylanthracene (1-3) derivatives.



**1A** [Pale yellow solid (45.1%)]: **Melting point:** 109.6 °C;

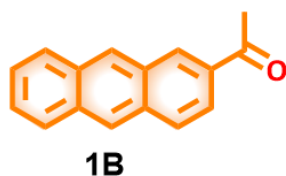
**<sup>1</sup>H NMR** [500 MHz, CDCl<sub>3</sub>, δ (ppm)]: 9.51 (s, 1H), 8.48 (s, 1H), 8.21 (d, J = 8.4 Hz, 1H), 8.11 (dd, J = 9.5 Hz, 1H), 8.04 (m, 2H), 7.54 (dd, J = 9.6 Hz, 2H), 7.51 (t, J = 7.8 Hz, 1H), 2.85 (s, 3H);

**<sup>13</sup>C NMR** [125 MHz, CDCl<sub>3</sub>, δ (ppm)]: 201.6, 135.0, 134.0, 133.1, 132.0, 131.6, 129.7, 129.2, 127.8, 127.7, 126.9, 126.67, 126.2, 126.0, 125.8, 123.5, 29.8;

**IR** (KBr, cm<sup>-1</sup>): 3047, 2983, 1664;

**HRMS** (ESI): m/z calculated for C<sub>16</sub>H<sub>12</sub>O [M]<sup>+</sup>: 220.0888, found: 220.0872.

---



**1B** [Pale yellow solid (19.4%)]: **Melting point:** 191.4 °C;

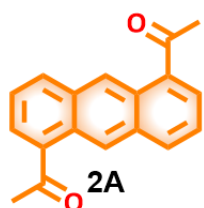
**<sup>1</sup>H NMR** [500 MHz, CDCl<sub>3</sub>, δ (ppm)]: 8.55 (s, 1H), 8.48 (s, 1H), 8.34 (s, 1H), 7.91 (m, 4H), 7.44 (m, 2H), 2.67 (s, 3H);

**<sup>13</sup>C NMR** [125 MHz, CDCl<sub>3</sub>, δ (ppm)]: 197.9, 134.1, 133.3, 132.7, 132.1, 131.6, 130.4, 129.0, 128.7, 128.4, 128.2, 126.7, 126.3, 126.0, 122.7, 26.5;

**IR** (KBr, cm<sup>-1</sup>): 3053, 2993, 1672;

**HRMS** (ESI): m/z calculated for C<sub>16</sub>H<sub>12</sub>O [M]<sup>+</sup>: 220.0888, found: 220.0991.

---



**2A** [Yellow-green solid (37.5%)]: **Melting point:** 217.5 °C;

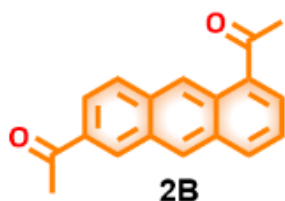
**<sup>1</sup>H NMR** [500 MHz, CDCl<sub>3</sub>, δ (ppm)]: 9.49 (s, 2H), 8.19 (d, J = 8.3 Hz, 2H), 8.01 (d, J = 6.5 Hz, 2H), 7.46 (t, J = 7.1 Hz, 2H), 2.74 (s, 6H);

**<sup>13</sup>C NMR** [125 MHz, CDCl<sub>3</sub>, δ (ppm)]: 201.3, 135.2, 134.2, 133.4, 130.7, 127.7, 126.7, 124.2, 29.6;

**IR** (KBr, cm<sup>-1</sup>): 3042, 2998, 1656;

**HRMS** (ESI): m/z calculated for C<sub>18</sub>H<sub>14</sub>O<sub>2</sub> [M]<sup>+</sup>: 262.0994, found: 262.0981.

---



**2B** [Yellow solid (18.9%)]: **Melting point:** 168.4 °C;

**<sup>1</sup>H NMR** [500 MHz, CDCl<sub>3</sub>, δ (ppm)]: 9.43 (s, 1H), 8.58 (s, 1H), 8.54 (s, 1H), 8.14 (d, J = 8.5 Hz, 1H), 8.05 (d, J = 9.0 Hz, 1H), 8.01

(d,  $J = 7.0$  Hz, 1H), 7.96 (d,  $J = 9.0$  Hz, 1H), 7.47 (t,  $J = 7.5$  Hz, 1H), 2.75 (s, 3H), 2.70 (s, 3H);

$^{13}\text{C}$  NMR [125 MHz,  $\text{CDCl}_3$ ,  $\delta$  (ppm)]: 201.2, 197.8, 134.9, 134.7, 134.0, 132.4, 131.0, 130.7, 130.3, 129.8, 129.5, 129.3, 125.8, 124.1, 123.4, 29.8, 26.6;

IR (KBr,  $\text{cm}^{-1}$ ): 3044, 1669;

HRMS (ESI):  $m/z$  calculated for  $\text{C}_{18}\text{H}_{14}\text{O}_2$   $[\text{M}]^+$ : 262.0994, found: 262.0891.

---



**2C** [Yellow solid (4.6%)]: **Melting point:** 153.5 °C;

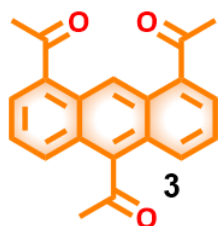
$^1\text{H}$  NMR [500 MHz,  $\text{CDCl}_3$ ,  $\delta$  (ppm)]: 8.56 (d,  $J = 12.6$  Hz, 2H), 7.97 (d,  $J = 8.5$  Hz, 2H), 7.79 (t,  $J = 7.7$  Hz, 2H), 7.5 (m, 2H), 2.74 (s, 3H), 2.68 (s, 3H);

$^{13}\text{C}$  NMR [125 MHz,  $\text{CDCl}_3$ ,  $\delta$  (ppm)]: 207.3, 197.5, 137.0, 134.0, 131.9, 131.6, 130.8, 130.0, 129.9, 129.1, 128.2, 128.1, 127.6, 126.2, 125.0, 124.5, 124.2, 33.8, 26.47;

IR (KBr,  $\text{cm}^{-1}$ ): 3061, 2997, 1683;

HRMS (ESI):  $m/z$  calculated for  $\text{C}_{18}\text{H}_{14}\text{O}_2$   $[\text{M}]^+$ : 262.0994, found: 262.0958.

---



**3** [Yellow solid (4.6%)]: **Melting point:** 195.2 °C;

$^1\text{H}$  NMR [500 MHz,  $\text{CDCl}_3$ ,  $\delta$  (ppm)]: 10.10 (s, 1H), 7.91 (d,  $J = 7.5$  Hz, 4H), 7.51 (t,  $J = 8.0$  Hz, 2H), 2.77 (s, 6H), 2.73 (s, 3H);

$^{13}\text{C}$  NMR [125 MHz,  $\text{CDCl}_3$ ,  $\delta$  (ppm)]: 207.5, 201.6, 137.6, 137.1, 128.8, 128.7, 128.1, 126.5, 126.1, 125.9, 34.2, 30.2;

IR (KBr,  $\text{cm}^{-1}$ ): 3001, 2918, 1674;

HRMS (ESI):  $m/z$  calculated for  $\text{C}_{20}\text{H}_{16}\text{O}_3$   $[\text{M}]^+$ : 304.1099, found: 304.1109.

## 2.5. Additional Figures and Tables

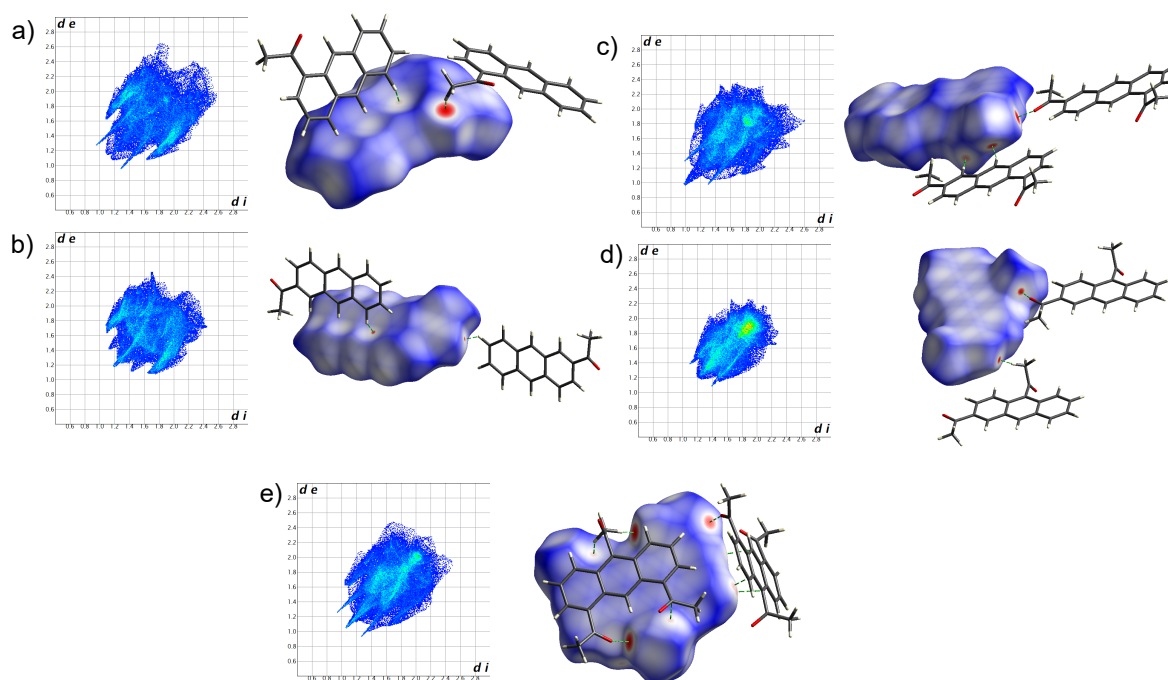


**Figure A2.1.** 2D fingerprint plot (left) and the Hirshfeld surface mapped with  $d_{norm}$  (right) for a) 1A; b) 1B; c) 2B; d) 2C; and e) 3.

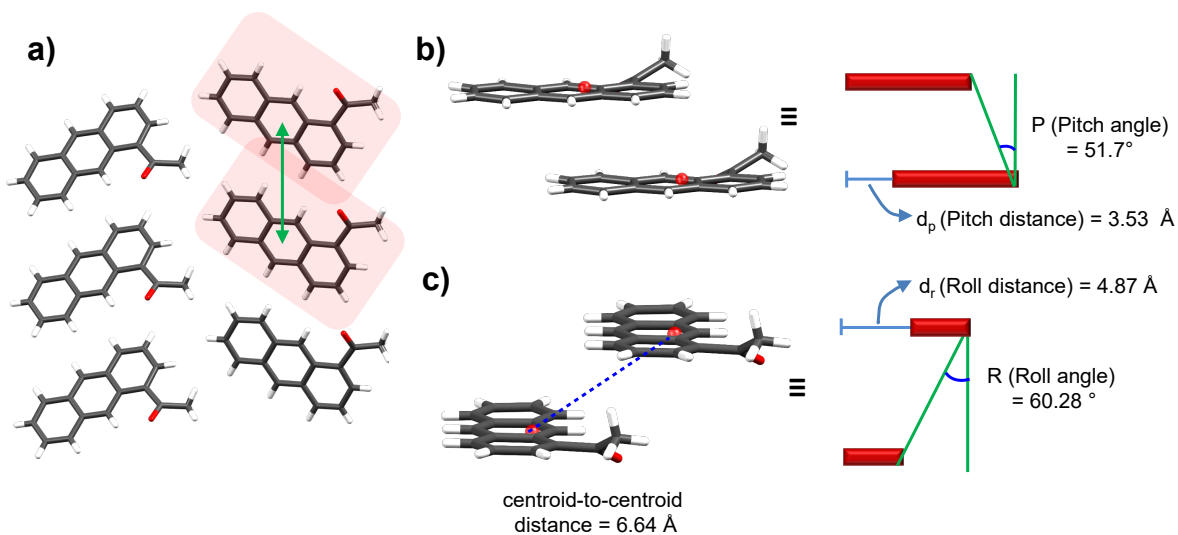


**Figure A2.2.** a) Herringbone motif in 1A; b) the pitch and c) roll translations among nearest co-facial anthracene units in 1A.

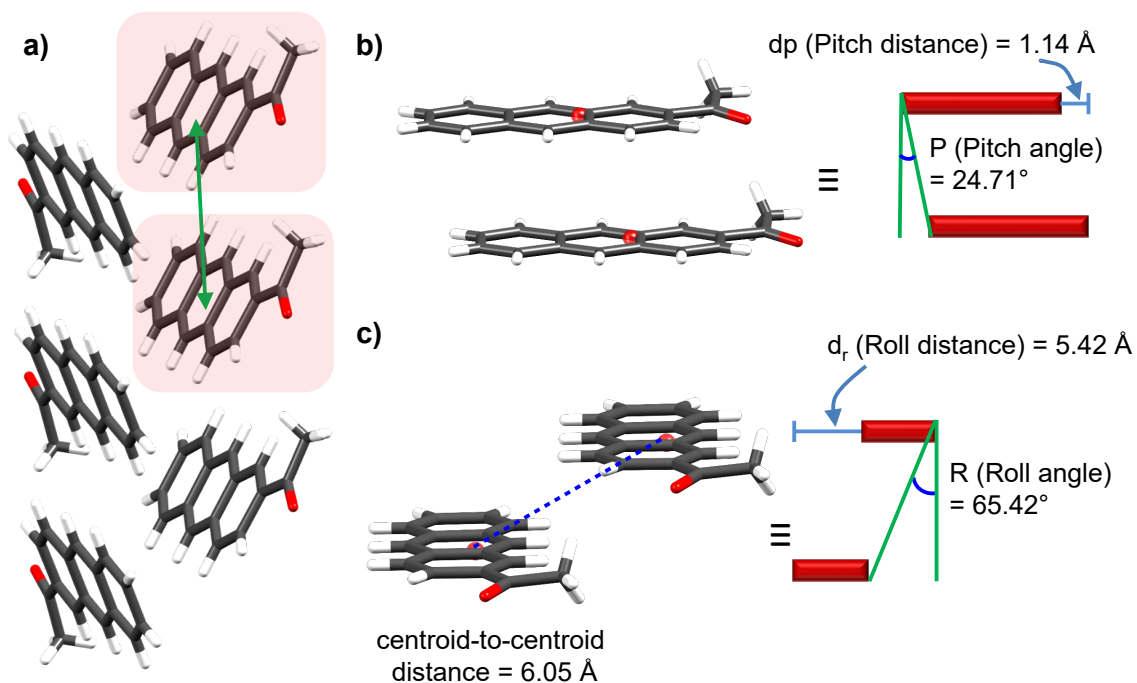


**Figure A2.3.** a) Herringbone motif in 1B; b) the pitch and c) roll translations among nearest co-facial anthracene units in 1B.

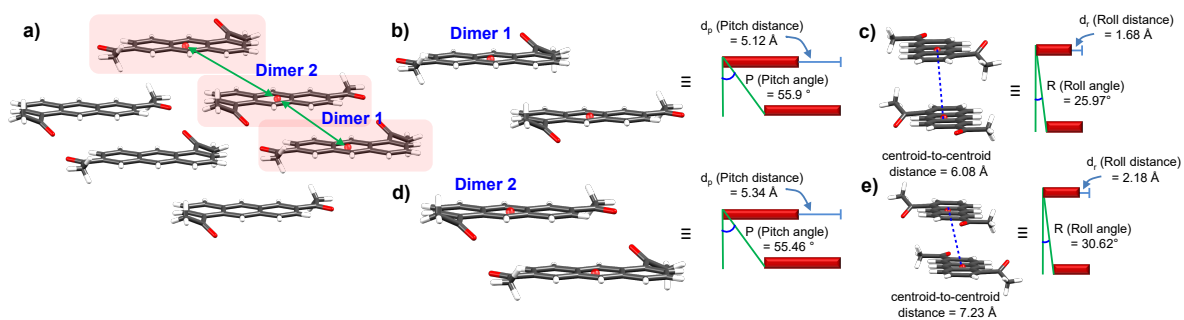


**Figure A2.4.** a)  $\gamma$ -motif in 2B; b) the pitch and c) roll translations among dimer 1; d) the pitch and e) roll translations among dimer 2.

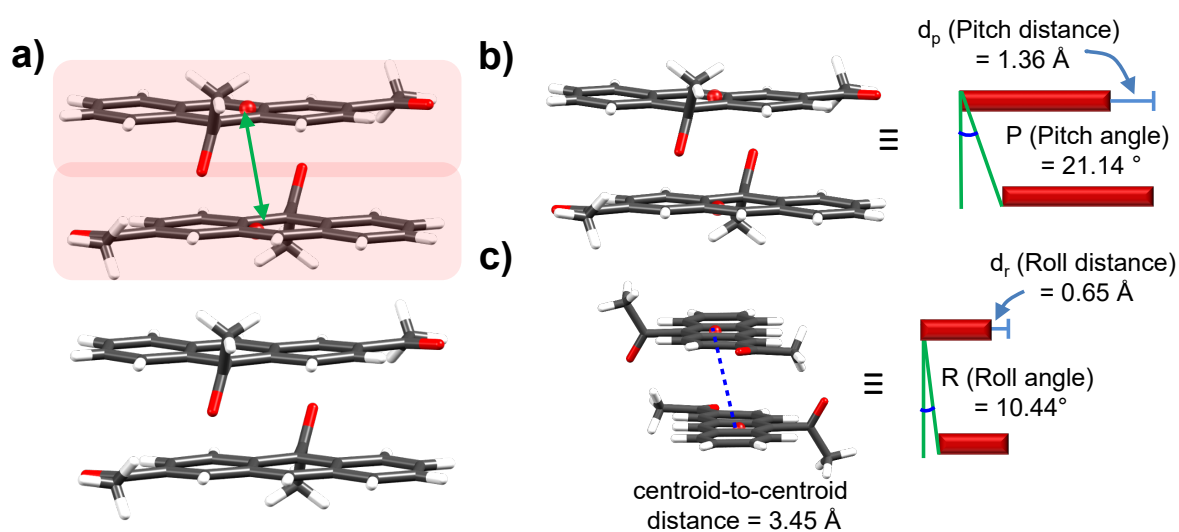


**Figure A2.5.** a) Columnar  $\beta$ -motif in 2C; b) the pitch and c) roll translations among the nearest anthracenes in 2C.

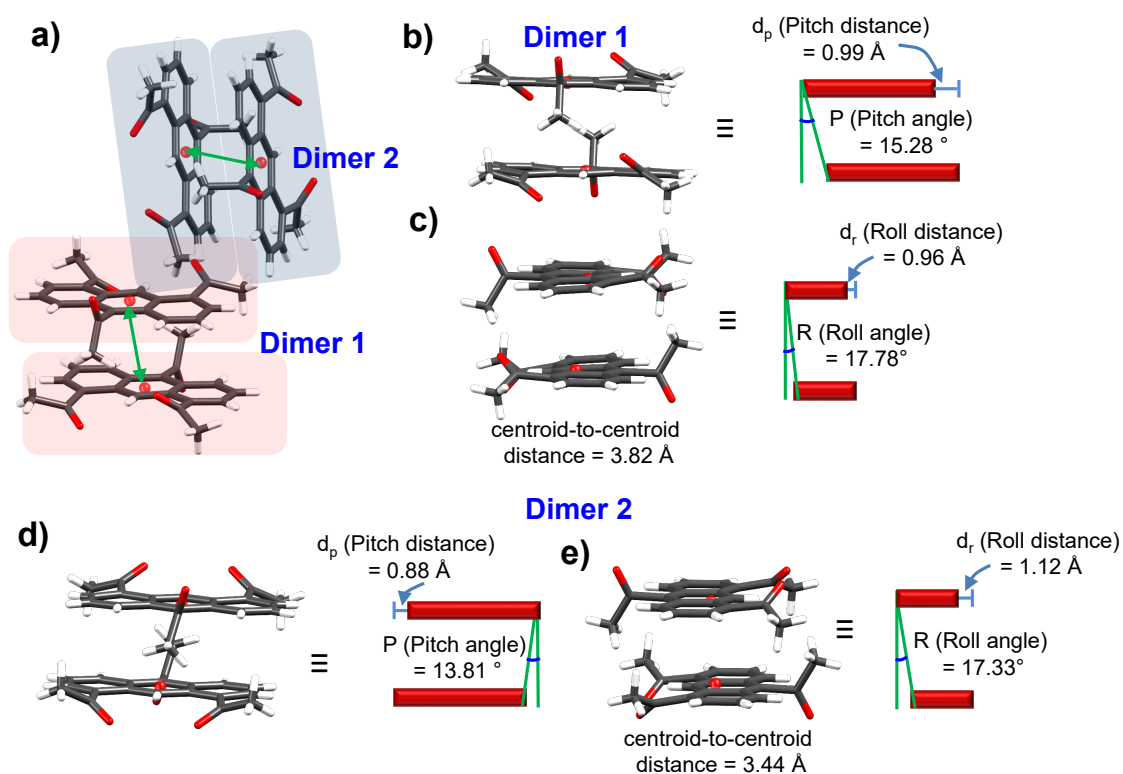


**Figure A2.6.** a)  $\beta$ -motif in triacetylanthracene derivative 3; b) the pitch and c) roll translations among dimer 1; d) the pitch and e) roll translations among dimer 2.

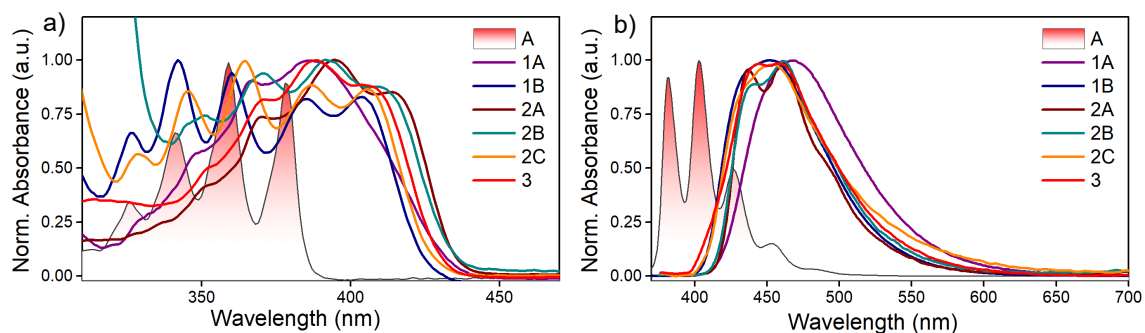


**Figure A2.7.** Normalized a) UV-vis absorption and b) fluorescence emission spectra of the model derivative anthracene (A) and the acetylanthracene (1-3) derivatives (16-35  $\mu\text{M}$ ) in  $\text{CHCl}_3$ . Excitation wavelength,  $\lambda_{\text{ex}} = 360 \text{ nm}$ .

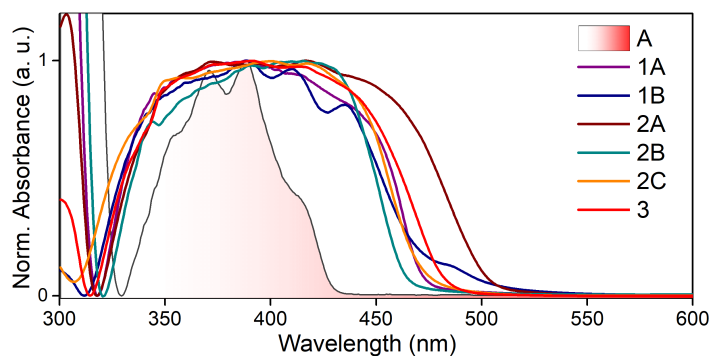


**Figure A2.8.** Diffuse reflectance spectra of crystalline 1-3 derivatives.

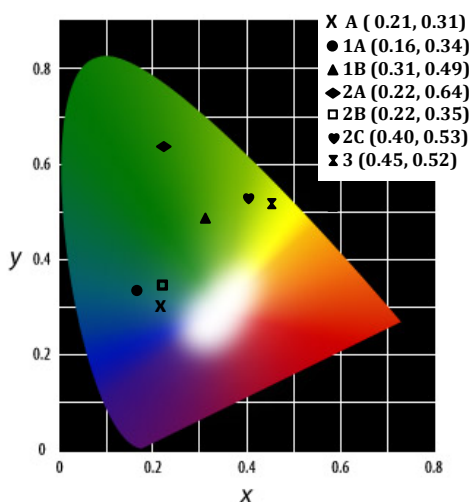


**Figure A2.9.** Commission Internationale de l'Eclairage (CIE) color diagram displaying the spectral emission properties of crystalline 1-3 derivatives.

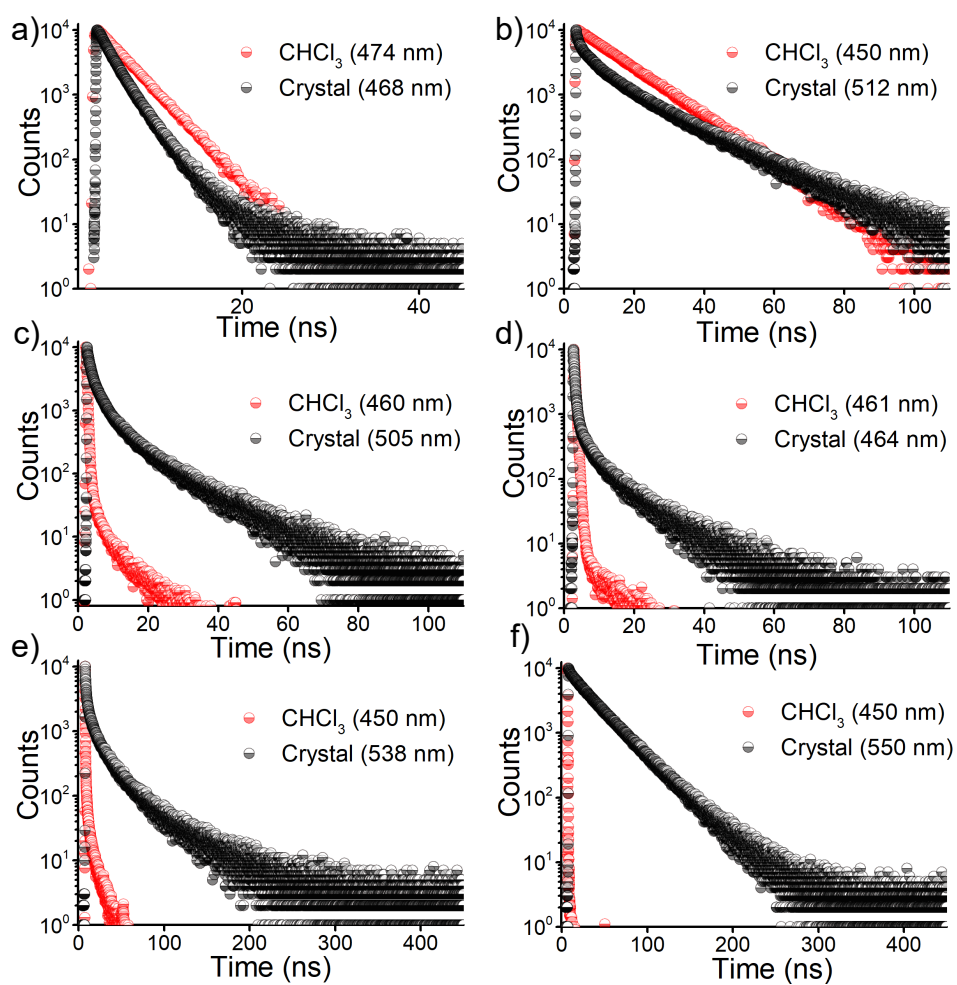


**Figure A2.10.** Picosecond time-resolved fluorescence decay profiles of normalized a) 1A; b) 1B; c) 2A; d) 2B; e) 2C and f) 3 in CHCl<sub>3</sub> (red) and crystalline state (black) monitored at the respective emission maxima. Excitation wavelength,  $\lambda_{ex} = 377$  nm (pulsewidth = 100 ps).

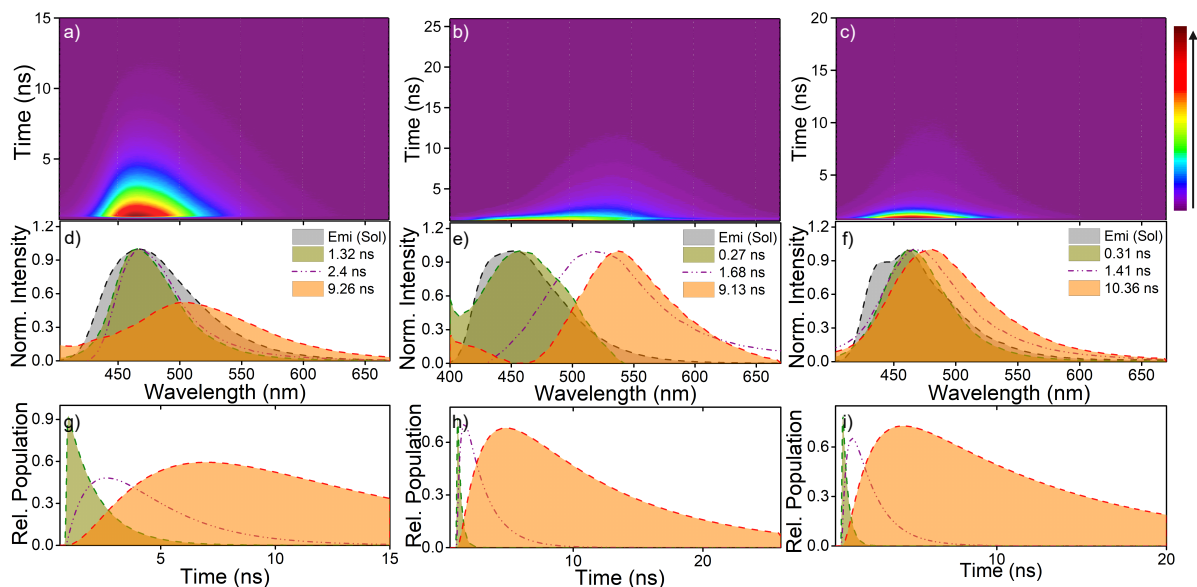


**Figure A2.11.** Time-resolved emission spectrum (TRES) (a, b, c); normalized evolution associated spectra (d, e, f) and the population profiles (g, h, i) of crystalline 1A, 1B and 2B respectively; excitation wavelength is 377 nm (pulse width = 100 ps). The emission spectra of 1A, 1B and 2B in  $\text{CHCl}_3$  solution (shaded grey) are depicted for comparison with the normalized EAS in Figure A2.11d, e and f.

**Table A2.1:** Shows melting temperature ( $T_{m,p}$ ) and change in enthalpy ( $\Delta H$ ) values for 1-3 crystal derivatives.

	<sup>a</sup> $T_{m,p}$ (°C)	<sup>b</sup> $\Delta H$ (kJ/mole)
<b>1A</b>	109.6	22.2
<b>1B</b>	191.4	35.9
<b>2A</b>	217.5	38.8
<b>2B</b>	168.4	37.3
<b>2C</b>	153.5	32.0
<b>3</b>	195.2	38.7

<sup>a</sup>Melting temperature and <sup>b</sup>change in enthalpy during melting

## 2.6. Appendix

### 2.6.1. Materials and methods

All chemicals were obtained from commercial suppliers and used as received without further purification. All reactions were carried out in oven-dried glassware prior to use and wherever necessary, were performed under dry nitrogen in dried, anhydrous solvents using standard gastight syringes, cannulae, and septa. Solvents were dried and distilled by standard laboratory purification techniques. TLC analysis were performed on precoated aluminum plates of silica gel 60 F254 plates (0.25 mm, Merck) and developed TLC plates were visualized under short and long wavelength UV lamps. Flash column chromatography was performed using silica gel of 200-400 mesh employing a solvent polarity correlated with the TLC mobility observed for the substance of interest. Yields refer to chromatographically and spectroscopically homogenous substances. Melting points were obtained using a capillary melting point apparatus and are uncorrected. IR spectra were recorded on a Shimadzu IRPrestige-21 FT-IR spectrometer as KBr pellets.  $^1\text{H}$  and  $^{13}\text{C}$  NMR spectra were measured on a 500 MHz Bruker Avance DPX spectrometer. Internal standard used for  $^1\text{H}$  and  $^{13}\text{C}$  NMR is 1,1,1,1-tetramethyl silane (TMS). High resolution mass spectra (HRMS) were recorded on Thermo Scientific Q Exactive mass spectrometer using electrospray ionization (ESI, positive mode) technique.

### 2.6.2. X-ray crystallography

Single crystal of acetylanthracene derivatives (1-3, chloroform) were obtained by slow evaporation of solvent from homogenous solution at room temperature. High-quality specimen of acetylanthracene crystals were selected for the X-ray diffraction experiments. Crystallographic and refinement data are presented in Table 2.1. Single crystal was mounted using oil (Infineum V8512) on a glass fibre. All measurements were made on a CCD area detector with graphite monochromated Mo  $K\alpha$  radiation. The data was collected using Bruker APEXII detector and processed using APEX2

from Bruker. The structure was solved by direct method and expanded using Fourier technique. The non-hydrogen atoms were refined anisotropically. Hydrogen atoms were included in idealized positions, but not refined. Their positions were constrained relative to their parent atom using the appropriate HFIX command in SHELX-97 [135]. All programs used during the crystal structure analysis are incorporated in the WINGX software [136]. The full validation of CIF and structure factor of crystalline 1-3 were performed using the checkCIF utility and found to be free of major alert levels. 3D structure visualization and the exploration of the crystal packing of 1-3 were carried out using Mercury 3.5.1 [137, 138]. The face-to-face overlap between the anthracene stacks were visualized and imaged from the crystal structure. The ratio of the overlapped area and the total area of the donor and acceptor rings gave the percentage (%) overlap between the face-to-face stacked anthracenes [121].

### 2.6.3. Steady-State Spectroscopy

Photophysical measurements of the acetylanthracenes derivatives were carried out in a cuvette of 3 mm path length unless otherwise mentioned. Absorption and emission spectra were recorded on Shimadzu UV-3600 UV-VIS-NIR and Horiba Jobin Yvon Fluorolog spectrometers respectively. To avoid the distortion arising from the inner filter effect, the concentration-dependent steady-state measurements were carried out in a cuvette of 1 mm path length [139]. Solution state relative quantum yield measurements of 1-3 were performed using quinine sulphate in 0.1 M H<sub>2</sub>SO<sub>4</sub> ( $\lambda_{ex} = 350$  nm, reported quantum yield,  $\phi_f = 0.577$ ) as the standard [44]. The solid-state quantum yield of crystalline 1-3 was measured using an integrating sphere for which the accuracy was verified using tris(8-hydroxyquinolate)aluminium (Alq<sub>3</sub>) as a standard and is determined to be  $0.32 \pm 0.04$  (reported quantum yield,  $\phi_f = 0.40$ ) [140]. Picosecond time-resolved fluorescence lifetime measurements were carried out in Horiba Jobin Yvon-IBH time-correlated

single photon counting system. Solutions were excited at 377 nm using a pulsed diode laser (NanoLED-375L; <100 ps pulse width) and the decay traces were recorded using a long-pass filter (395 nm) to minimize the scatter from the laser source. The detection system consisted of a microchannel plate photomultiplier tube (model Hamamatsu R3809U-50) having an instrument response time of 38.6 ps, coupled to a monochromator (5000M) and TCSPC electronics (Data station Hub including Hub-NL, NanoLED controller). The luminescence lifetime values were evaluated using DAS6.3 fluorescence decay analysis software. The fluorescence decay profiles were de-convoluted and fitted with exponential decay, minimizing the  $\chi^2$  values. The triacetylanthracene (3) derivative in chloroform was found to have lifetime significantly shorter than the excitation pulse width and hence were not able to not be fitted.

The radiative ( $k_r$ ) and non-radiative ( $k_{nr}$ ) rate constants for 1-3 derivatives were calculated using the equations 3 and 4 [103].

$$\phi_f = \frac{k_r}{k_r + k_{nr}} \quad (2.6)$$

$$\tau_f = \frac{1}{k_r + k_{nr}} \quad (2.7)$$

$$k_r = \frac{\phi_f}{\tau_f} \quad (2.8)$$

$$k_{nr} = \frac{1}{\tau_f} - k_r \quad (2.9)$$

where  $\phi_f$  is the fluorescence quantum yield and  $\tau_f$  is the fluorescence lifetime. In case of multi-exponential decay, the weighted average of the fluorescence lifetime values was used for estimation of rates of radiative and non-radiative processes using equation 2.10 [44],

$$\tau_f = \frac{\alpha_1 \tau_1^2 + \alpha_2 \tau_2^2 + \alpha_3 \tau_3^2 + \dots}{\alpha_1 \tau_1 + \alpha_2 \tau_2 + \alpha_3 \tau_3 + \dots} \quad (2.10)$$

where  $\alpha$  = amplitude corresponding to the fluorescence lifetime ( $\tau_i$ ) decay.

#### 2.6.4. Time-Resolved Emission Measurements

Time-resolved emission spectral (TRES) investigations of crystalline 1-3 derivatives

were carried out by exciting at 377 nm (NanoLED-375L; pulsewidth = 100 ps) and the fluorescence decay profiles were collected in the spectral range of 400-670 nm (3 nm interval) with a 395 nm long-pass filter (Newport) to minimize the scatter arising from the laser source. Decay at each wavelength was collected with an identical acquisition time and the emission observed immediately after the laser excitation pulse was assigned as zero time.

### 2.6.5. Global Analysis

The measured time-resolved emission spectral (TRES) data of crystalline 1-3 derivatives were subject to global analysis using the program Glotaran [141, 142]. Singular value decomposition followed by the global analysis of the time vs. wavelength plots furnished a temporal de-convolution of the short and the long-lived (excimer) components in the TRES data. The global analysis procedure takes into account instrument response function (IRF) and simultaneously fits kinetic traces measured at all wavelengths. During the global analysis, fitting of the kinetic traces at all the wavelengths were carried out using a sequential model to provide the evolution associated spectra (EAS). The EAS signifies the evolution of the spectra in time and do not necessarily represent a real physical/chemical species.

### 2.6.6. Computational methods:

#### 2.6.6.1. Exciton Coupling Calculations

The unrestricted open shell time-dependent density functional theory (TDDFT) calculations of crystalline 1-3 were carried out to compute the vertical excitation energies and the oscillator strengths in *Gaussian 09 Rev. A.02* and the output of the calculations were viewed and analysed using GaussView 5.0 [134]. The molecular structures of crystalline 1-3 derivatives were used without any optimisation for the TDDFT calculations at the Becke's three parameter functional in combination with the Lee-Yang-Parr correlation functional (B3LYP) and 6-311G++(d,p) basis set.

To evaluate the dipole coupling among the nearest anthracene units in a

crystalline ensemble, transition density cubes of the individual chromophores (1-3) were generated for a HOMO→LUMO transition ( $n=1$ ) by performing TDDFT calculations at B3LYP/6-311G++(d,p) and further using the cubegen utility in *Gaussian 09 Rev. A.02* [134]. Numerically computed transition density cubes (TDCs) are not functions over space but rather values defined on a grid [130]. The transition density values on the grid points are treated as integrals of the continuous transition density in equation 2.1 over cubes of volume  $V_\delta = \delta_x \delta_y \delta_z$ , where  $\delta_x$ ,  $\delta_y$ , and  $\delta_z$  are the lattice constants defining the computational grid. During computation of the TDC elements, the sum is assumed to extend over spin dependencies, if any, of the continuous transition density [130]. The numerically calculated transition density cubes (TDCs) of an individual molecular unit was used to replicate a dimer pair with spatial orientation and distances similar to that seen in the crystal structures.

The independently computed TDCs of crystalline 1-3 were read into a Matlab (R2009) program for implementing the coordinate transformation that fixes the relative orientation of the two constituent units in a dimer. This gives the freedom to change the distance and the relative orientation as well as the rotational angles between the individual units in a dimer at will. The calculated pitch and the roll distances (following the method reported by Curtis and co-workers[127]) were used to alter the relative distances between the individual TDC units in co-facial parallel dimers. For oblique dimers, relative orientation between the two individual TDC units were evaluated by measuring the rotational angles (in Mercury 3.10) and relative orthogonal coordinates of the individual molecular centroids in a dimer to fix the two TDCs in the exact spatial orientation and distances as that seen in the crystal packing. Modified TDCs with shifted/rotated distances and coordinates were used for evaluating the dipole-dipole interaction using the Kasha's exciton coupling formalism (equation 2.1-2.3) in a custom Matlab program.

The selection of the molecular ensemble in crystalline 1-3 were carried out by choosing a single molecule at centre and creating a molecular shell comprising all

the molecules in contact with the central one within a radius of 4.2 Å. A typical molecular ensemble comprised of 12-14 nearest and non-nearest neighbours to the central molecule giving rise to 12-14 different dimer pairs. To avoid the over estimation of the dipole-dipole coupling, the symmetrically equivalent dimer-pair (out of the 12-14 different dimers) were averaged out to derive the mean field approximated exciton splitting in crystalline 1-3.

### 2.6.6.2. Quantum theory of atoms in molecules (QTAIM)[103, 124]

The wave function for the acetylanthracene derivatives (1-3) were obtained employing the geometries taken from the crystal structure using Gaussian set of codes at B3LYP/6-311+G(d,p) level in *Gaussian 09 Rev. A.02*. Quantum theory of atoms in molecules (QTAIM) analysis aims at understanding the description of interatomic interaction in the single crystal X-ray structure. A bond is defined along the bond line between two nuclei, called a bond path, along which electron density is concentrated. In a three dimensional space there are four types of critical points, corresponding to non-degenerate points: termed (3, -3), (3, -1), (3, +1) and (3, +3). The (3, -3) and (3, +3) types represent a maximum (which corresponds to a nuclear position) and a minimum, respectively. While (3, -1) and (3, +1) types represent saddle points called bond critical points and the ring critical points, respectively. The bond critical point (BCP) is a point along the bond path at the interatomic surface, where the shared electron density reaches a minimum. The physical characteristics of the BCPs [the electron density at BCP,  $\rho(r_{\text{BCP}})$ , and its Laplacian,  $\nabla^2\rho(r_{\text{BCP}})$ ] reveal the approximate measure of the amount of electron density built up in the bonding region and as such could be taken as characteristic of the bond. When  $\nabla^2\rho(r_{\text{BCP}}) < 0$  and is large in magnitude,  $\rho(r_{\text{BCP}})$  is also large which means that there is a concentration of electronic charge in the internuclear region. This is also an indication of a sharing of electronic charge between both nuclei that defines the covalent (polar) bond. When  $\nabla^2\rho(r_{\text{BCP}}) > 0$  there is a depletion of electronic charge in the internuclear region. Using the AIM 2000 software package, the electron density

was integrated over atomic basins according to the quantum theory of atoms in molecules using PROAIM, and thus the BCP data and the molecular graphs were obtained.

### **2.6.6.3. Hirshfeld Analysis[125]**

Important intermolecular interactions within the crystal structure of 1-3 were identified through Hirshfeld surface analysis using Crystal Explorer 3.1 [143]. The Hirshfeld surface is defined as a set of points in 3D space where the ratio of promolecule and procrystal electron densities is equal to 0.5. The exploration of intermolecular contacts is provided by mapping normalized contact distances ( $d_{\text{norm}}$ ), which is a function of a closest distance from the point to the nuclei interior ( $d_i$ ) and exterior ( $d_e$ ) to the surface as well as on the van der Waals radii ( $r^{\text{vdw}}$ ). 2D fingerprint which were generated by deriving from the Hirshfeld surface by plotting the fraction of points on the surface as the function of  $d_i$  and  $d_e$  which provide a visual summary of intermolecular contacts within the crystal.

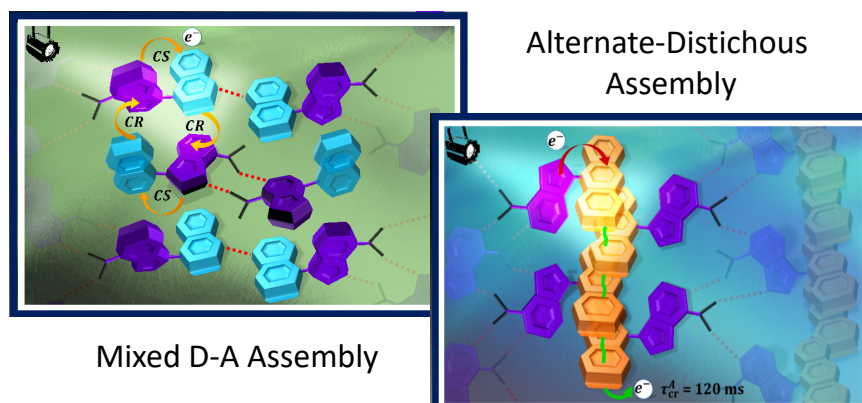


## Chapter 3

# Nucleobase-Arene Assembly for Long-Lived Charge Separation

### Abstract

Self-assembly is ubiquitous and plays a critical role in moderating the photoexcited state processes of multichromophoric systems. Herein, we explore the influence of assembly on the ultrafast photoexcited-state processes in nucleobase-arene (AdNp, and AdAn) motifs in organic solvent. By virtue of the strong base-pairing and  $\pi$ - $\pi$  interactions, AdNp form a mixed donor-acceptor (D-A) motif, whereas AdAn forms an alternate distichous assembly wherein the adenines are near-orthogonally flanked to the columnar anthracene stacks. Upon photoexcitation, the mixed D-A assembly in AdNp ( $\lambda_{ex} = 266$  nm) reveal the presence of only a triplet excited state ( $^3Np^*$ ), whereas alternate distichous AdAn assembly ( $\lambda_{ex} = 266$  and/or 355 nm) reveals the formation of radical ion-pair intermediates (RIP,  $\tau_{CR}^A = 120$  ms) as demonstrated via nanosecond and femtosecond transient absorption analyses. Lack of the RIP intermediates in the mixed D-A assembly suggest the ultrafast charge recombination in AdNp. Contrarily, segregated trajectories of the charge carriers in the alternate distichous assembly offers delocalization of the electron through the columnar  $\pi$ -channels of anthracenes and the diffusion of the holes across hydrogen bonded adenines, resulting in persistent radical ion-pair intermediates. "Emergence-upon-assembly" mediated long-lived charge-separated state in the alternate distichous D-A stack proposes an elegant self-assembly strategy for retarding the rates of the charge recombination in multichromophoric D-A architectures.



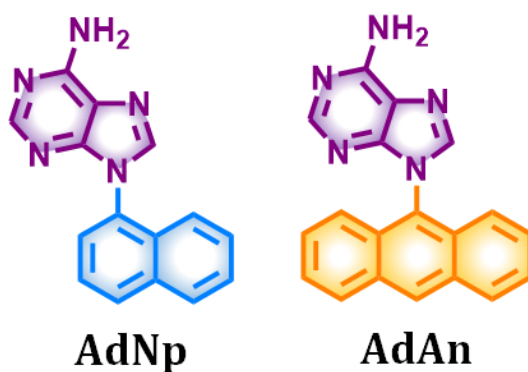
### 3.1. Introduction

Hierarchical assembly of small molecule donor-acceptor (D-A) chromophores into well-defined nanostructures is crucial for light-to-energy conversion in natural photosynthetic mimics [3, 144]. Weak intermolecular  $\pi$ - $\pi$  [66], C-H $\cdots$ O [74], C-H $\cdots$  $\pi$  [63], and dispersion[145] interaction-guided precise three-dimensional (3-D) array of the D-A chromophores can create organized segregated bicontinuous domains for the photoinduced energy and electron transport [73, 80, 146]. Nucleobases, i.e., adenine (Ad), guanine (G), cytosine (C), thymine (T), etc., by virtue of the strong base-pairing interactions, regulate the  $\pi$ -stacked helical array in DNA [147]. Modular nucleobases, with the propensity to self-assemble in solution, can construct nanoscale molecular architectures for light-harvesting applications [33, 83].

Purine nucleobase analogues (Ad and G) are well-known hole carriers for the transport of charges over nanometer lengths in chromophore-appended DNAs [148-150]. Aforementioned attributes stimulate the utility of the chromophore-appended nucleobases for the design and syntheses of D-A architectures for photofunctional applications [83]. In addition, the photoexcited processes in the nucleobases can provide fundamental insights to the UV-induced lesions in DNA and relevant biomolecules [151-153]. Herein, we report a comprehensive investigation of photoexcited-state processes in self-assembled nucleobase-arene conjugates, 9-(adenin-9-yl)naphthalene

(AdNp) and 9-(adenin-9-yl)anthracene (AdAn) in organic solvents by deep-UV (exciting both Np/An and Ad) and indirect (exciting An) photoexcitation of the nucleobase.

Our prolonged interest in emergent near-orthogonal[120, 154, 155]/nonplanar[63, 121] D-A assemblies motivated us to exploit the base pairing proficiency of adenines for defining a self-assembled architecture in AdNp and AdAn (Scheme 3.1). The self-sorted intermolecular hydrogen ( $N\cdots H$ ) bonding among the adenines and  $\pi$ - $\pi$  stacking renders a mixed D-A stack (AdNp) and an alternate distichous (AdAn) arrangement in the nucleobase-arene conjugates. Photoexcitation ( $\lambda_{\text{ex}} = 266$  nm) of the AdNp assembly reveal the presence of only a triplet excited state ( $^3\text{Np}^*$ ), whereas the AdAn ( $\lambda_{\text{ex}} = 266$  and 355 nm) assembly in  $\text{CHCl}_3$  reveals the evolution of long-lived radical ion-pair (RIP) intermediates ( $\tau_{\text{cr}}^A = 120$  ms) and a gradual formation of AdAn photoproducts as evinced via nanosecond (nTA) and femtosecond (fTA) transient absorption and high-resolution mass spectrometric (HRMS) analysis. Inability to perceive the RIP intermediates in

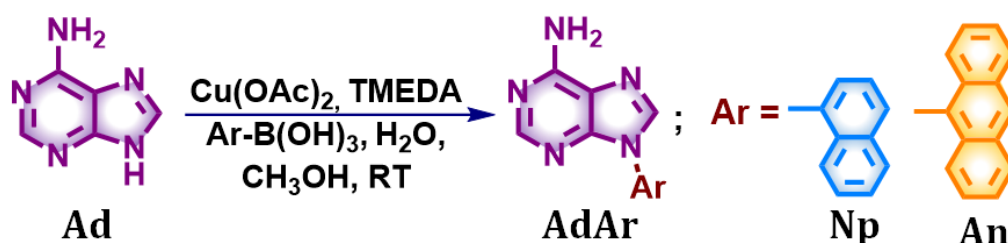


**Scheme 3.1.** Molecular structures of the N-arylated adenine (AdNp, and AdAn) conjugates under discussion.

AdNp assembly suggest the ultrafast recombination of the RIP intermediates in the mixed D-A stack assembly. Contrarily the alternate distichous assembly provides a “ $\pi$ -way” for the electron to delocalize along the columnar anthracenes in self-assembled AdAn. “Emergence upon assembly”[64] based persistent charge-separated states in the alternate distichous assembly endorse an ideal strategy for light harvesting and ingenious device applications.

### 3.2. Synthesis and Structure of N-Arylated Adenines

Copper-catalyzed Chan-Lam-Evans[156, 157] cross-coupling of adenine with 9-arylboronic acid afforded the N-arylated nucleobase conjugates, AdNp and AdAn (Scheme 3.1.-3.2.). The slow evaporation of a solution of AdNp (in chloroform) and AdAn (in *n*-hexane:chloroform [1:1] mixture) offered good quality crystals for single crystal X-ray diffraction (Table 3.1.). The dyad AdNp (colorless block) and AdAn (yellow plates) crystallized in monoclinic *P21/c* and *C2/c* centrosymmetric space group with eight molecules in the unit cell, respectively (Table 3.1.). Steric congestion among the hydrogen of the covalently connected adenyl (H8) and the arene counterpart results in a



**Scheme 3.2.** General synthesis scheme for the nucleobase-arene (AdNp, and AdAn) conjugates.

**Table 3.1.** Crystallographic data and refinement parameters for AdNp and AdAn crystal derivatives.

Parameters	AdNp	AdAn
Formula	C <sub>15</sub> H <sub>11</sub> N <sub>5</sub>	C <sub>19</sub> H <sub>13</sub> N <sub>5</sub>
Formula wt.	261.29	311.34
Colour, shape	Colourless, block	Yellow, plate
Dimens, mm	0.20 x 0.15 x 0.15	0.25 x 0.20 x 0.05
Crystal system	Monoclinic	Monoclinic
Space group, Z	<i>P</i> 21/ <i>c</i> , 8	<i>C</i> 2/ <i>c</i> , 8
<i>a</i> , Å	21.8291 (13)	17.907 (8)
<i>b</i> , Å	7.7845 (4)	7.805 (3)
<i>c</i> , Å	15.1600 (9)	25.346 (11)
$\alpha$ , deg.	90°	90°
$\beta$ , deg.	109.490° (3)	92.386° (9)
$\gamma$ , deg.	90°	90°
<i>V</i> , Å <sup>3</sup>	2428.5 (2)	3539 (3)
Temp, K	296 (2)	296 (2)
<i>d</i> <sub>calcd</sub> , mg/m <sup>3</sup>	1.429	1.169
No. of reflections collected	18015	13383
No. of unique reflections	4778	3469
2 $\theta$ <sub>max</sub> , deg.	52°	48.1°
No. of parameters	377	225
R1, wR2 ( <i>I</i> > 2s( <i>I</i> ))	0.0730, 0.1817	0.0549, 0.1442
R1, wR2 (all data)	0.1286, 0.2199	0.1304, 0.1865
Goodness of fit	1.029	0.9873
CCDC number	not published	1558361

nonplanar ( $\theta = 48.8^\circ$ ) and a near-orthogonal ( $\theta = 80^\circ$ ) geometry in AdNp and AdAn dyad, respectively (Figures 3.1.-3.2.) [122].

A thorough inspection of the crystal packing in the nucleobase-arene

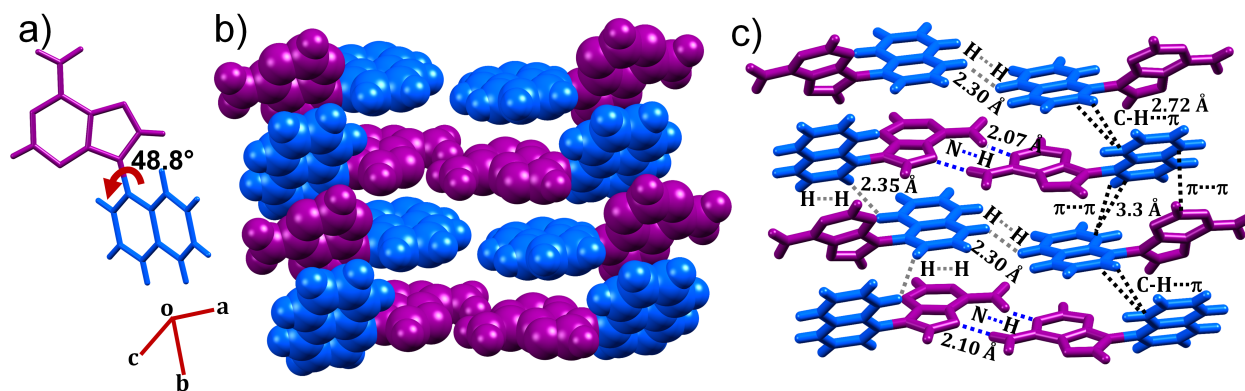


**Figure 3.1.** (a) Molecular structure, (b) mixed D-A stack and (c) close-packing analysis depicting the intermolecular interactions in crystalline AdNp.

derivatives AdNp and AdAn reveals a mixed/alternating D-A stacking and a novel ‘alternate distichous’ packing arrangement, respectively (Figure 3.1.-3.2.). The term ‘alternate distichous’ is taken from phyllotaxis nomenclature wherein the leaves are arranged alternately in two longitudinal rows on the opposite sides of a central columnar axis (see inset of Figures 3.2b) [158]. The close-packing analysis of AdNp reveals the dual influence of the self-sorted hydrogen ( $N\cdots H$ ) bonding and  $\pi$ - $\pi$  interactions in guiding the two dimensional (2D) mixed/alternating D-A stack formation (Figure 3.1c). Additionally, dihydrogen ( $C-H\cdots H-C$ ) and  $C-H\cdots\pi$  interactions also play a critical role in guiding the formation of mixed/alternating D-A assembly in AdNp (Figure 3.1c). Similarly, the close-packing analysis of the ‘alternate distichous’ AdAn assembly also features the influence of self-sorted hydrogen ( $N\cdots H$ ) bonding and  $\pi$ - $\pi$  interaction as the major forces driving the assembly of the AdAn (Figure 3.2b, d). The self-assembly alternate distichous stacks features a central columnar stack of anthracenes which possess considerable overlap (13.6 and 15.3 %) and the adenines near-orthogonally flanked alternately on the

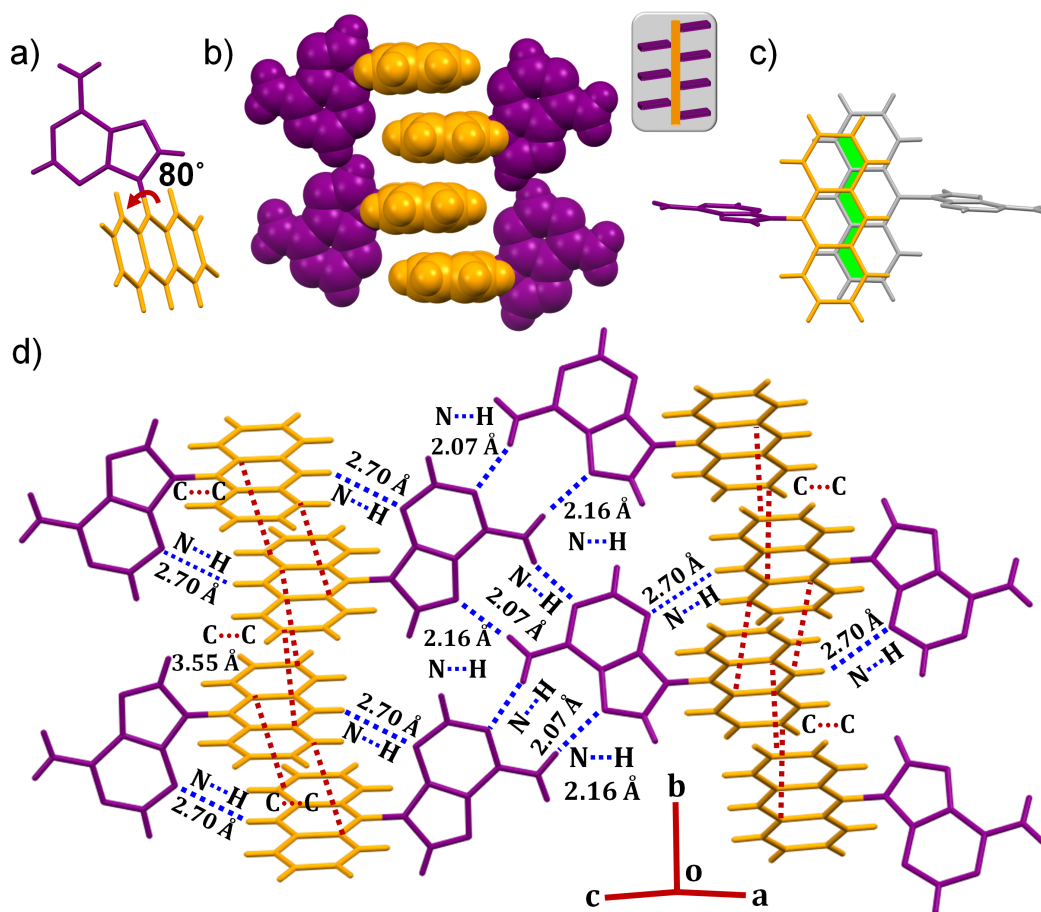


**Figure 3.2.** (a) Molecular structure; (b) alternate distichous stacks; (c) the percentage of An-An overlap in  $\pi$ -stacked anthracenes; and (d) close-packing analysis depicting the intermolecular interactions in crystalline AdAn.

either sides of the column without any significant overlap (Figure 3.2b-d).

Furthermore, to probe the weak intermolecular interactions guiding the assembly in nucleobase-arene conjugates, quantum theory of atoms in molecules (QTAIM)[103, 124] and Hirshfeld surface analyses[125, 143] of AdNp and AdAn were performed (Figure 3.3.-3.4., Table 3.2.-3.3.). Apart from the typical short contact intermolecular interactions below the van der Waal's radii, the QTAIM analyses can additionally perceive the presence of weak intermolecular interactions among the atoms organized beyond the van der

**Table 3.2.** Calculated topological properties of the electron density for the intermolecular interaction in crystalline AdNp and AdAn.

Description	Interaction	<sup>a</sup> <i>d</i> , (Å)	<sup>b</sup> $\rho_b(\mathbf{r})$ , (eA <sup>-3</sup> )	<sup>c</sup> $\nabla^2\rho_b(\mathbf{r})$ , (eA <sup>-5</sup> )	<sup>d</sup> DE, (kJ/mol)
AdNp (Stacked Dimer)	H4...C18	2.523	0.070817	1.041766	8.48
	H17...N27	2.656	0.061605	0.868640	7.34
	C22...C40	3.358	0.039059	0.422114	3.52
	C3...H48	2.719	0.052414	0.655969	5.16
	C20...C43	3.624	0.028924	0.261713	2.37
	H35...C49	2.523	0.070547	1.038898	8.45
	C9...C51	3.779	0.021034	0.196887	1.75
	C5...C52	3.929	0.015757	0.173174	1.42
	H48...N58	2.656	0.061349	0.863074	7.29
AdNp (Self- Sorted Dimer)	H48...N58	2.755	0.061457	0.862640	7.29
	H35...C49	2.606	0.070965	1.043188	8.49
	H31...N57	2.104	0.115714	1.330542	12.40
	N28...H61	2.073	0.140541	1.594761	16.42
AdAn (Stacked Dimer)	N33...H49	2.707	0.047292	0.489880	4.48
	H12...N70	2.707	0.047298	0.489880	4.48
	C6...C51	3.636	0.028693	0.265303	2.38
	C8...C50	3.581	0.029625	0.298583	2.59
	C10...C48	3.564	0.030644	0.304439	2.68
	C11...C47	3.564	0.030644	0.304439	2.68
	C13...C45	3.581	0.029625	0.298583	2.59
	C14...C43	3.636	0.028693	0.265303	2.38
AdAn (Self- Sorted Dimer)	H37...N69	2.159	0.125161	1.585603	14.60
	N34...H73	2.070	0.154483	1.951712	20.02

<sup>a</sup>*d*=distance, <sup>b</sup> $\rho_b(\mathbf{r})$ =electron density at the BCP and <sup>c</sup> $\nabla^2\rho_b(\mathbf{r})$ = Laplacian of the electron density at the BCP, <sup>d</sup>DE = dissociation energy.

Waal's radii (Table 3.2.). QTAIM analyses of AdNp and AdAn illustrate the presence of synergistic intermolecular  $\pi$ - $\pi$ , C-H... $\pi$ , intramolecular N...H and intermolecular self-sorted base-pairing (N...H) interactions guiding the mixed/

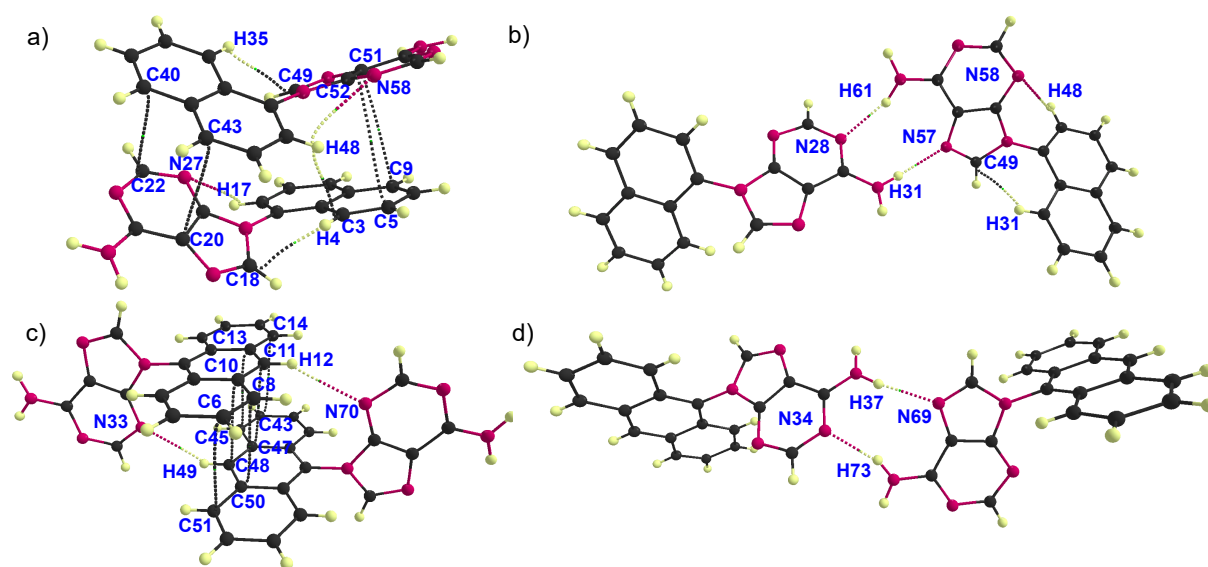


**Figure 3.3.** QTAIM electron density map depicting intermolecular interactions among the stacked dimers (a,c) and self-sorted adenines (b,d) in AdNp (a,b) and AdAn (c, d).

alternating and columnar stacking, respectively (Figure 3.3.).

Likewise, Hirshfeld surface analysis of AdNp and AdAn allows the quantification of the relative percentage of intermolecular interactions in the crystalline assembly (Figure 3.4., Table 3.3.). Evaluation of the packing motif in the nucleobase-arene motifs suggest a two dimensional (2D)  $\gamma$ -motif arrangement in crystalline AdNp ( $\rho = 1.39$ ) and AdAn ( $\rho = 1.95$ ) assemblies

**Table 3.3.** The percentage intermolecular interactions obtained from Hirshfeld surface analysis in crystalline AdNp and AdAn.

Interaction	% C...H	% C...C	% H...H	% C...N	% N...H	% N...N	$\rho$
AdNp	14.8	10.6	47.3	8.3	19.1	0	1.39
AdAn	18.0	9.2	39.3	0.2	18.9	0	1.95

<sup>a</sup>total percentage of intermolecular contacts ca. 100% (AdNp) and 95.6% (AdAn).

$\rho = [(\%C\cdots H)/(\%C\cdots C)]$ . Herringbone ( $\rho > 4.5$ ), sandwich herringbone ( $3.2 < \rho < 4.0$ ),  $\gamma$  ( $1.2 < \rho < 2.7$ ) and  $\beta$  ( $0.46 < \rho < 1.0$ ).

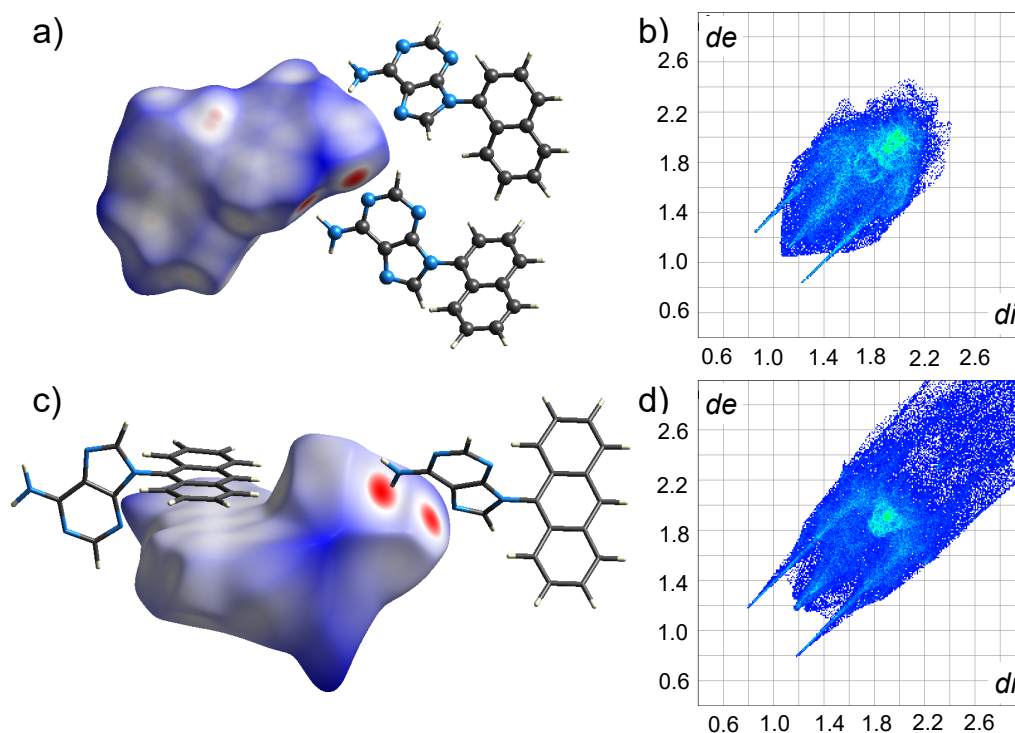


**Figure 3.4.** Hirshfeld surface mapped with  $d_{norm}$  (left) and 2D fingerprint plots (right) for crystalline AdNp (a,b) and AdAn (c, d).

(Figures 3.1.-3.4., Table 3.3.).

Though the mixed/alternating D-A type of stacking does not affect the charge separation dynamics, it can affect the charge recombination dynamics. Mixed/alternating D-A stacked has been known to be an unfavorable geometry in terms of maximizing the utility of the charge separated state and is usually avoided due to generation of large dipoles that trap the radical ion-pair intermediates and hamper efficient charge transport [65]. The face-to-face D-A stacking in AdNp might enhance the charge separation character, however the charge recombination would also be fast. On the contrary, the alternate distichous motif in AdAn is a favorable arrangement, wherein the acceptor (anthracenes) is stacked in a columnar fashion creating efficient

electron transport channels and the donor (adenines) are near-orthogonally flanked with no virtual  $\pi$ -overlap, alternately on the both sides of central columnar acceptor (anthracenes) [122]. Ideally, once the charge is injected by donor (Ad) into the acceptor (An) stack, the separated charge can delocalize across the columnar stacks which can preferably limit the rate of the charge recombination in AdAn as compared to the mixed/alternating D-A arrangement in AdNp. While the face-to-face (13.6 and 15.3 % An-An overlap) stacking of anthracenes (An) can facilitate delocalization of the electron across the stack [159], it could also trigger a facile monomer-to-dimer transformation (detrimental) under UV-irradiation (Figure 3.2b-d).

### 3.3. Results and Discussion

#### 3.3.1. Steady-State Photophysical and Aggregation Studies

To evaluate the preliminary photophysical features of AdNp and AdAn, steady-state UV-vis absorption, emission and picosecond time-resolved lifetime measurements were carried out in dilute chloroform solutions (Figure 3.5., Table 3.4.). The electronic absorption of AdNp and AdAn in chloroform can be described as a summation of the nucleobase (Ad) and arene (Np/An) spectral features with minimum perturbation in the ground state. The UV-vis absorption of AdNp exhibit a broad absorption with a maxima centered at 265 nm having contribution from the  $\pi$ - $\pi^*$  transition of both Ad ( $S_0 \rightarrow S_n$ ) and Np ( $S_0 \rightarrow S_n$ ) chromophores (Figure 3.5a, Table 3.4. and A3.1). On the other hand,

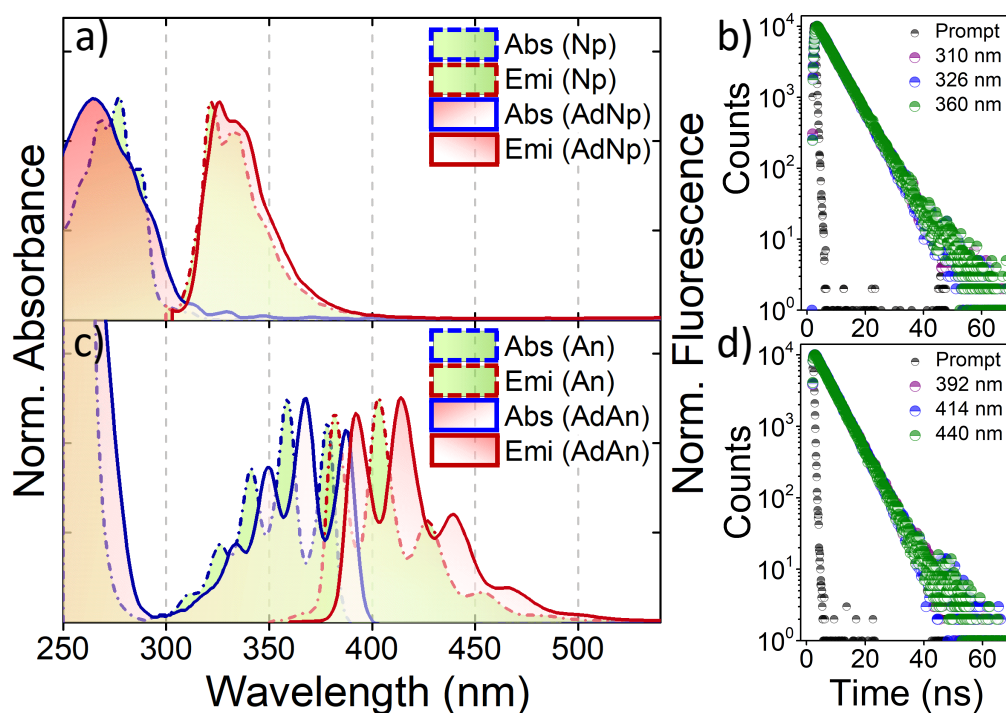


**Figure 3.5.** UV-vis absorption (blue), emission (maroon,  $\lambda_{ex} = 290$  [AdNp] and 350 [AdAn] nm) and time-resolved fluorescence decay spectra of the nucleobase-arene conjugates AdNp (a, b) and AdAn (c, d) in dilute chloroform solution. For comparison the UV-vis absorption and emission spectra of the model arene derivatives Np and An are shown in Figure 3.5 a, c (dashed lines).

AdAn possesses two distinct absorptions centered at 256 nm and 300-400 nm (vibronically structured, Figure 3.5c, Table 3.4.). The band at 256 nm has the contributions from the  $\pi$ - $\pi^*$  transitions of Ad ( $S_0 \rightarrow S_1$ ) and An ( $S_0 \rightarrow S_n$ ), while

**Table 3.4.** Photophysical properties of AdNp and AdAn in  $CHCl_3$ .

Derivative	$\lambda_{abs}(nm)$	$^a\lambda_f (nm)$	$\Phi_f$	$^b\tau_f (ns) [\chi^2]$
AdNp	265	326	0.25	5.86 [1.01]
AdAn	387, 368	414	0.51	5.46 [0.98]

abs – absorption; f – fluorescence;  $^a\lambda_{ex} = 290$  (AdNp) and 340 (AdAn) nm;  $^b\lambda_{ex} = 260$  nm (AdNp, pulsewidth  $\leq 1.2$  ns) and 340 nm (AdAn, pulsewidth  $\leq 1$  ns)

the vibronically structured bands at 300-400 nm correspond to the  $S_0 \rightarrow S_1$  transitions in An (Table A3.1.).

The emission spectra of AdNp ( $\lambda_{ex} = 290$  nm,  $\phi_f = 0.25$ ) and AdAn ( $\lambda_{ex} = 350$  nm,  $\phi_f = 0.51$ ) in  $\text{CHCl}_3$  reveal a mirror image symmetry to the absorption spectrum and decays monoexponentially with a fluorescence lifetime ( $\tau_f$ ) of 5.86 and 5.46 ns, respectively (Figures 3.5a-d). The absorption maxima of AdNp reveal a marginal blue-shift (10 nm) whereas the fluorescence emission maxima reveal a negligible red-shift (4 nm) as compared to the model arene derivative Np. Similarly, the absorption and fluorescence emission maxima of AdAn reveals a ca. 10 nm red-shift as compared to the constituent model derivative An. The negligible perturbation in the photoexcited state properties of the arene (Np and An) upon conjugation to nucleobase (Ad) is indicative of a marginal conjugation effect, possibly due to the nonplanar geometry of the constituent chromophores (Ad and Np/An). The excitation spectrum of AdNp and AdAn monitored at respective emission wavelengths shows a precise match with the ground-state absorption, further supporting a negligible perturbation in the ground state properties of the nucleobase-arene conjugates (Figure A3.1.).

To probe the effect of the aggregation of the photoexcited state properties of the nucleobase-arene conjugates, concentration dependent (CD) UV-vis absorption measurements were carried in chloroform (Figure 3.6.). The CD

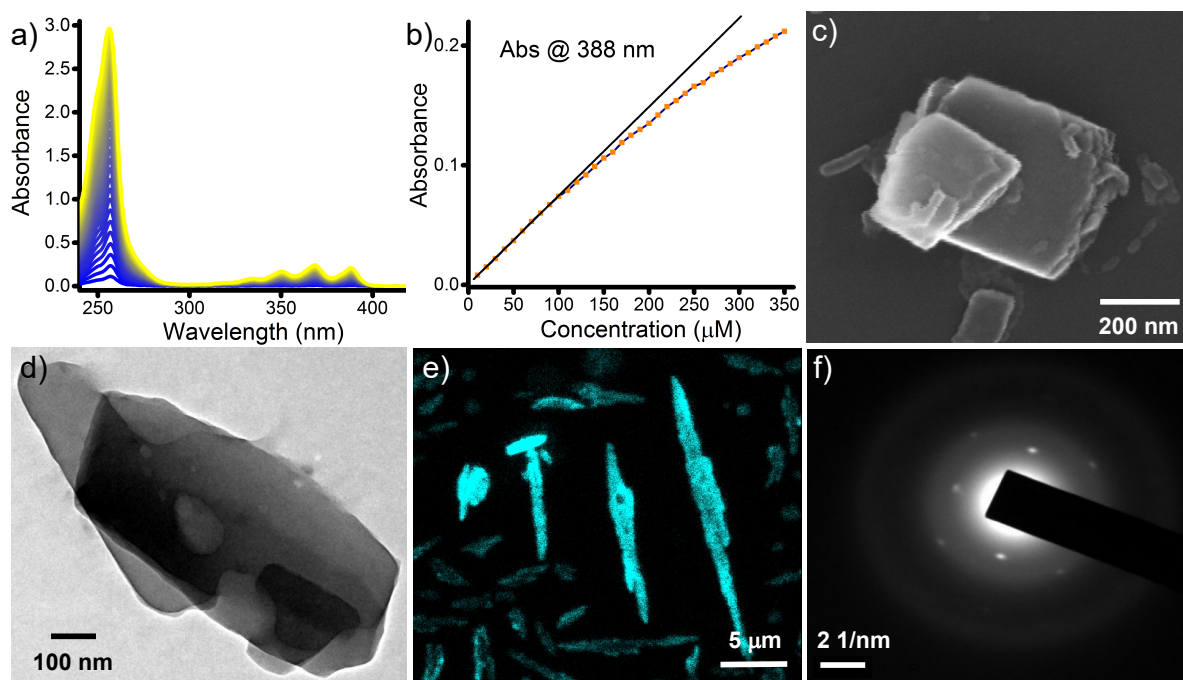


**Figure 3.6.** Concentration dependent a) absorption; b) Beer-Lambert's plot depicting the deviation from linearity while monitoring at 388 nm; c) SEM (silicon wafer); d) TEM (carbon coated Cu grid); e) confocal image and f) SAED pattern for AdAn (1 mM) in CHCl<sub>3</sub>.

absorption of AdAn monitored at 256 and 388 nm, indicates a deviation from linearity at concentration  $\geq 100 \mu\text{M}$  in CHCl<sub>3</sub> (Figure 3.6a and b). The CD deviation from the Beer-Lambert's law indicates the tendency of AdAn to self-sort/stack at low concentration (Figure 3.6b). Furthermore, to analyze the structure and the nature of AdAn aggregates (1 mM), morphological analysis using scanning electron (SEM), transmission electron (TEM) and confocal microscopy were carried out in CHCl<sub>3</sub> (Figure 3.6c-f). The microscopic analysis reveals the formation of 2D crystalline sheets (400-600 nm), arising from the extended self-sorted hydrogen bonding and  $\pi$ - $\pi$  interaction between the molecules in the  $\gamma$ -motif assembly of AdAn. The confocal microscopy further confirms the fluorescent sheet-like structure of the AdAn

aggregates (Figure 3.6e). The selected area electron diffraction (SAED) of the 2D nanosheets indicate bright diffraction spots, which further corroborates the crystalline nature of the AdAn aggregates in  $\text{CHCl}_3$  (Figure 3.6f). Similar morphological features were observed for the aggregated AdNp derivative also (Figure A3.2.).

### 3.3.2. Frontier Molecular Orbital and Weller Analysis

To evaluate the perturbation in the electronic interactions among the donor and acceptor and the feasibility of the electron transfer, frontier molecular orbital (FMO) and Rehm-Weller analyses of AdNp and AdAn were performed. The frontier molecular orbital (FMO) analyses of AdNp reveals that the electron density of LUMO is localized solely on the Np core, whereas the electron density of HOMO is delocalized across the entire AdNp core (Figure 3.7.). Likewise in AdAn, the electron density of LUMO is localized on An, whereas HOMO is distributed across An and partly across Ad unit (Figure 3.7.). The apparent perturbation in the electronic structure of the HOMO and LUMO orbitals is indicative of a plausible charge transfer characteristic in AdNp and AdAn dyad [160], which is further reinforced by the Weller analyses (Table 3.5., equation 3.1).

$$\Delta G_{et} = E_{ox} - E_{red} - E_S - \frac{e^2}{r_{DA} \epsilon_s} + \frac{e^2}{2} \left( \frac{1}{r_D} + \frac{1}{r_A} \right) \times \left( \frac{1}{\epsilon_s} + \frac{1}{\epsilon_{sp}} \right) \quad (3.1)$$

The negative value for the free energy of electron transfer from  $^1\text{Ad}^*$  to Np/An ( $\Delta G_{et}$  = -0.55 [AdNp] and -1.25 [AdAn] eV) and Ad to  $^1\text{Np}^*/^1\text{An}^*$  ( $\Delta G_{et}$  = -0.17 [AdNp] and -0.12 [AdAn] eV) calculated employing the Rehm-Weller relation [31, 63] encouraged

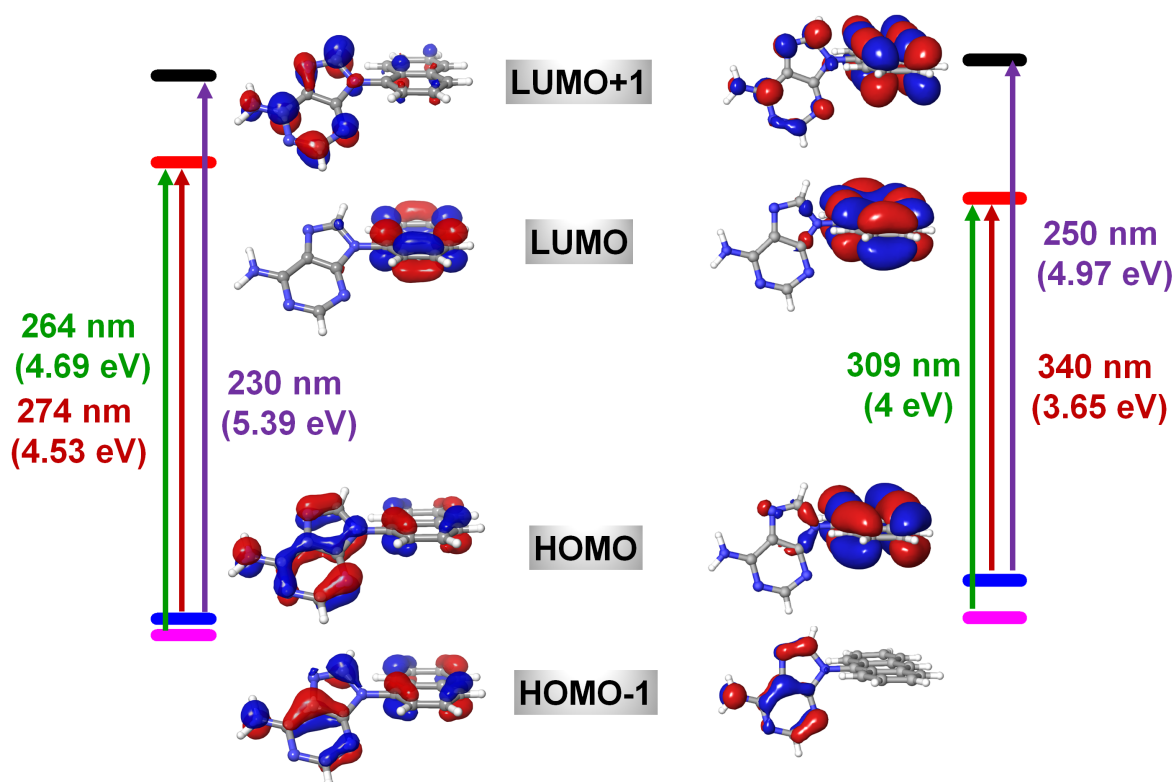


**Figure 3.7.** Frontier molecular orbital (FMO) analysis of AdNp (left) and AdAn (right) calculated from B3LYP-D3/6-31G+(d,p) level of theory in Schrödinger Materials Science Suite using Jaguar DFT engine.

us to explore the photoinduced electron transfer in the nucleobase-arene assemblies using fTA and nTA spectroscopy.

**Table 3.5.** Electrochemical redox potential and free energy of electron transfer ( $\Delta G_{CS}$ ) calculated for nucleobase-arene conjugates (AdNp and AdAn) in  $\text{CHCl}_3$ .

	$E_{D/D^+}^{ox}$ (V)	$E_{A/A^-}^{red}$ (V)	$E_{0,0}^D$ (eV)	$\Delta G_{CS}^D$ (eV)	$E_{0,0}^A$ (eV)	$\Delta G_{CS}^A$ (eV)
AdNp	1.39	-2.50	4.48	-0.55	4.06	-0.17
AdAn	1.39	-1.92	4.48	-1.25	3.26	-0.12

$E_{D/D^+}^{ox}$  - oxidation potential of donor;  $E_{A/A^-}^{red}$  - reduction potential of acceptor;  $E_{0,0}^{D/A}$  - singlet excited state of D/A;  $\Delta G_{CS}^{D/A}$  - free energy for charge separation when either D/A is excited.

### 3.3.3 Characterization of the Transient Radical Ion-Pair Intermediates

#### 3.3.3.1. Femtosecond Transient Absorption (fTA) Measurements

To gain insights into the ultrafast photoexcited state processes, fTA analyses of AdNp and AdAn conjugate were carried out in chloroform solution. Upon photoexcitation ( $\lambda_{ex} = 360$  nm) of An, the fTA spectra of AdAn (1 mM) in  $\text{CHCl}_3$  revealed positive transient absorption at 590 nm, which does not decay completely within the given experimental time window (3.2 ns, Figure 3.8.). The singular value decomposition followed by global analysis of the fTA spectra were carried using a sequential kinetic model to understand the principal components contributing to the

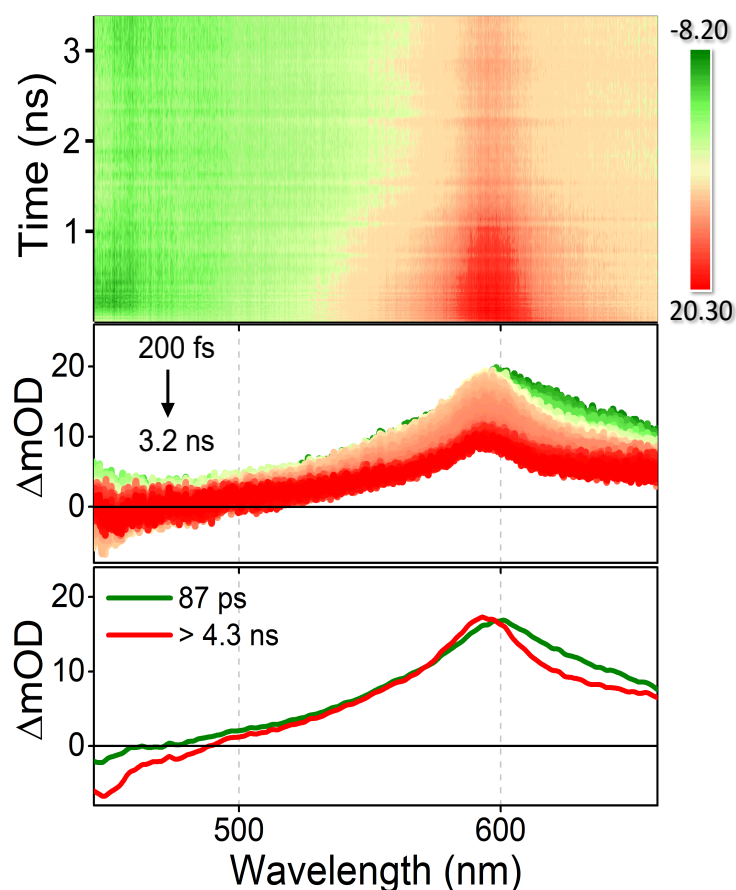


**Figure 3.8.** fTA spectra of AdAn ( $\lambda_{ex} = 360$  nm, pulsewidth = 110 fs, 1 mM in  $\text{CHCl}_3$ ) conjugates depicting the fTA 2D contour plot (top), spectra (middle) and evolution associated spectra (EAS, bottom).

transient absorption spectra shown in Figure 3.8. The evolution associated spectra (EAS) obtained from the global analysis of the fTA spectra display two principal components with broad transient absorption centered at 580-600 nm. The initial component at component at 595 nm can be attributed to a hot singlet-excited ( $S_1 \rightarrow S_n$ ) state of the AdAn ( $Ad^1An^*$ ) populated by the excitation at 360 nm, which further evolves to a marginally sharp transient species within  $\leq 87$  ps [161, 162]. The hot singlet excited state of AdAn ( $Ad^1An^*$ ) relaxes via vibrational cooling to the surrounding solvent within 87 ps. Subsequently, the singlet excited state of AdAn ( $Ad^1An^*$ ) relaxes via fluorescence emission to the ground state at time scales  $>100$  ps. The increased ground state depletion in 410-480 nm region of the second EAS component provides an indication of the stimulated emission arising from the relaxation of the singlet excited state of AdAn ( $Ad^1An^*$ ). The incomplete decay of the singlet excited state in the fTA spectra is complemented by the picosecond time-resolved fluorescence lifetime of AdAn ( $\tau_f = 5.46$  ns) in chloroform. Negligible charge-separation and lack of the features corresponding to the RIP intermediates and/or the triplet excited state in the fTA spectra ( $\lambda_{ex} = 360$  nm) of AdAn can be attributed to the (i) low free energy for electron transfer while exciting the arene ( $^1An^*$ ) chromophore as compared to the deep-UV (266 nm) excitation of nucleobase-arene conjugate; (ii) the slow intersystem crossing (ISC) phenomena (Table 3.5). Lack of the deep-UV (260-290 nm) excitation facility in the current femtosecond transient absorption spectrometer has hampered the monitoring of the photoexcited

state processes in self-assembled AdNp and AdAn dyads.

### 3.3.3.2. Nanosecond Transient Absorption (nTA) Measurements

Furthermore, to monitor the excited-state dynamics in nano-to-milliseconds timescale, the nTA measurements of AdNp and AdAn were carried out in nitrogen purged chloroform solutions (Figure 3.9.-3.10.). The nTA spectra ( $\lambda_{ex} = 266$  nm, 42 ns  $\rightarrow$  17.78  $\mu$ s) of self-assembled AdNp (1 mM) in nitrogen purged chloroform, reveal the presence of positive transient absorption at 440 nm which decays within  $\leq 1$   $\mu$ s, with a subsequent evolution of a new species at 330 nm (Figure 3.9a). The EAS of the nTA spectra in nitrogen purged solution exhibit two principal components with positive absorptions at (i) 440 nm (0.62  $\mu$ s) and (ii) 330 nm (4.44  $\mu$ s). The species at

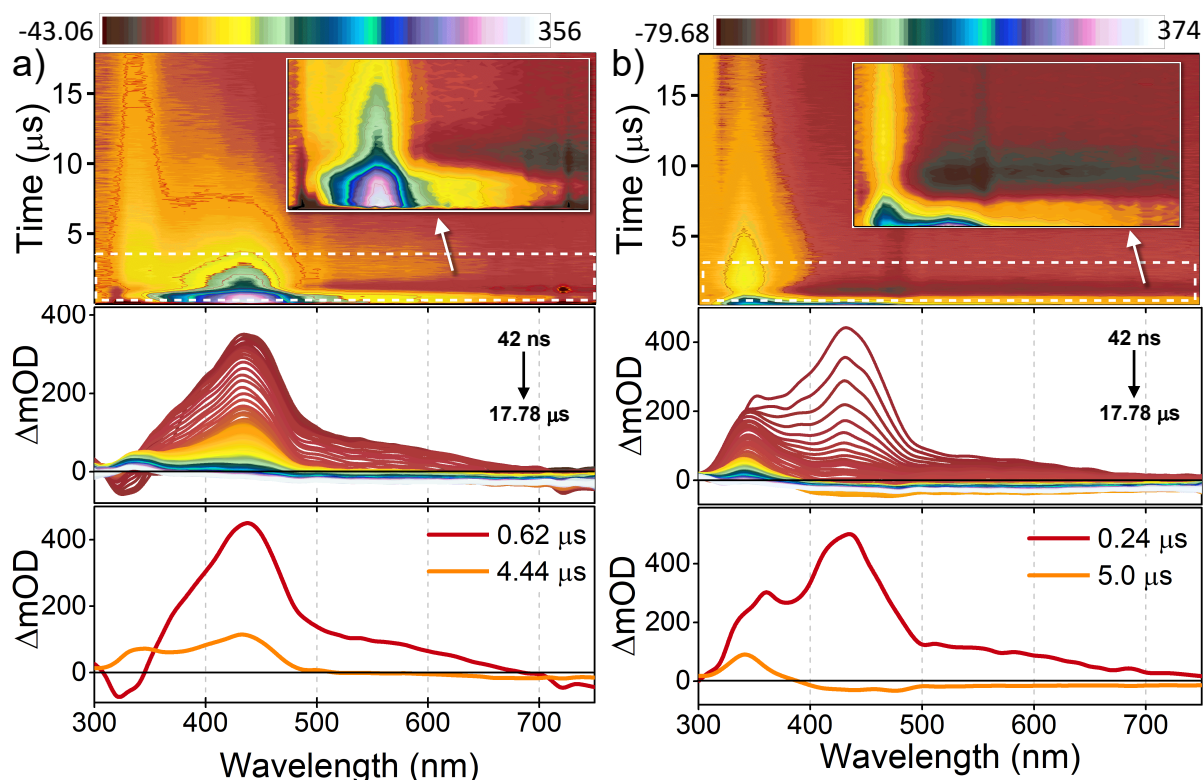


**Figure 3.9.** nTA spectra of AdNp ( $\lambda_{ex} = 266$  nm, pulsewidth = 7 ns, 1 mM in  $\text{CHCl}_3$ ) assembly depicting the nTA 2D contour plot (top), spectra (middle) and evolution associated spectra (EAS, bottom) in a) nitrogen and b) oxygen purged solutions.

440 nm can be attributed to the triplet excited state species of naphthalene ( $^3\text{Np}^*$ ) populated via intersystem crossing from the singlet excited state [162]. To confirm the species to be a triplet excited state, nTA measurements of AdNp were performed in oxygen purged chloroform (Figure 3.9b). As expected, the nTA measurements of AdNp in oxygen purged solution reveal a faster decay ( $0.24 \mu\text{s}$ ) for the EAS species centered at 440 nm via triplet-triplet energy transfer, thereby confirming the species to have a triplet origin. On the other hand, the EAS species centered at 330 nm exhibit negligible change in the decay rate upon oxygen purging, suggesting the species to be a deprotonated adenine moiety formed under deep-UV excitation.

The nTA analysis ( $\lambda_{ex} = 355 \text{ nm}$ ,  $100 \text{ ns} \rightarrow 20 \mu\text{s}$ ) of  $0.12 \text{ mM}$  AdAn were further

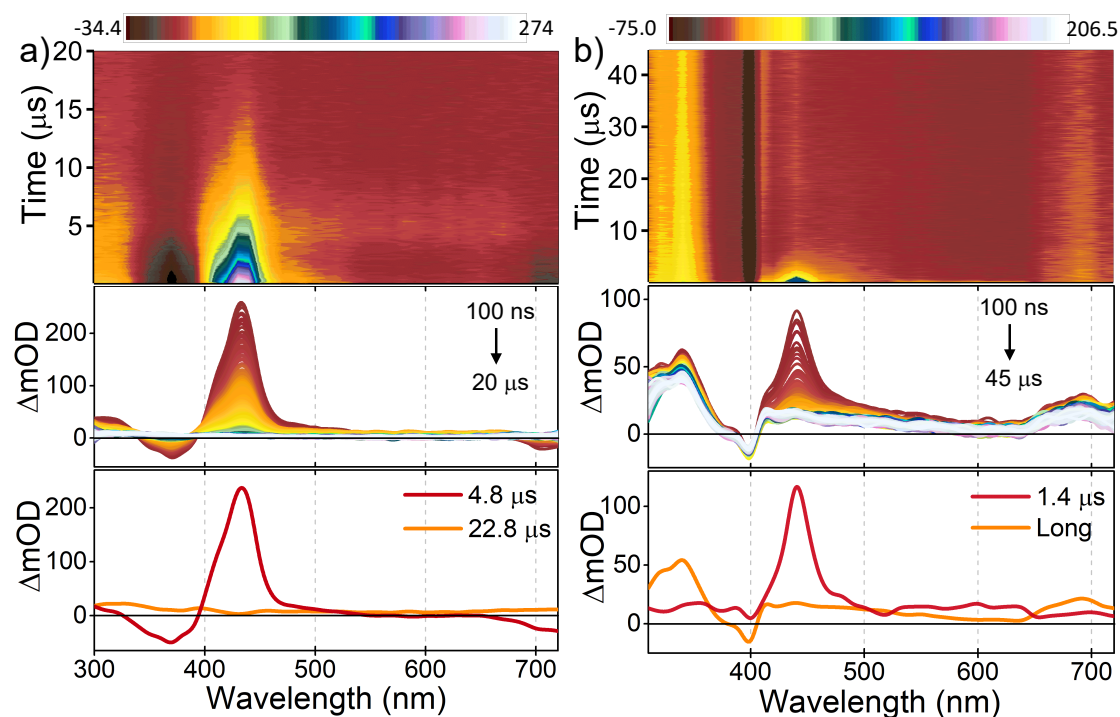


**Figure 3.10.** nTA spectra of AdAn ( $\lambda_{ex} = 355 \text{ nm}$ , pulsewidth =  $7 \text{ ns}$ ,  $0.12 \text{ mM}$ ) assembly depicting the 2D contour plot (top), spectra (middle) and evolution associated spectra (EAS, bottom) in a) diethylether ( $100 \text{ ns} \rightarrow 20 \mu\text{s}$ ) and b) chloroform ( $100 \text{ ns} \rightarrow 45 \mu\text{s}$ ) solution.

carried out to understand the dynamics of the photoexcited state processes at longer timescale (Figure 3.10). Upon exciting An ( $\lambda_{ex} = 355$  nm) unit, the nTA spectra (100 ns–45  $\mu$ s) of AdAn in chloroform displays positive absorption centered at 330, 440, 500-600 (diffuse) and 690 nm and a shallow bleach (370-400 nm) arising from the ground-state depletion (Figure 3.10b). The EAS obtained from the global analysis of the nTA spectra in  $\text{CHCl}_3$ , reveals the presence of a faster (440 nm) and a slow (330, 500-600 and 690 nm) decaying component which virtually does not decay within the given timescale (Figures 3.10b and A3.3.). The fast decaying component with a broad absorption centered at 440 nm can be attributed to the triplet excited-state population of anthracene ( $^3\text{An}^*$ ,  $\tau_T = 1.4$   $\mu$ s) via ISC (Figure 3.10b) [162, 163]. Further confirmation for the triplet-excited state was envisaged by quenching of 440 nm band via triplet-triplet energy transfer to molecular oxygen (Figure A3.4.).

Alternatively, the singlet excited-state can undertake a charge transfer pathway to form the RIP intermediates i.e. radical anion of anthracene ( $\text{An}^{\bullet-}$ ) and radical cation of adenine ( $\text{Ad}^{\bullet+}$ ) via photoinduced electron transfer from the Ad to  $^1\text{An}^*$ . The twin absorption at 330 and 500-600 nm is attributed to  $\text{Ad}^{\bullet+}/(\text{Ad-H})^{\bullet}$  and their decay lifetime are virtually unaffected by purging with  $\text{O}_2$  as reported earlier for Ad radicals [164]. Congruently, the absorption at 690 nm is allied to the radical anion of anthracene ( $\text{An}^{\bullet-}$ ) as reported earlier [165, 166]. The nTA spectra ( $\lambda_{ex} = 355$  nm, 100 ns–45  $\mu$ s) of 0.12 mM AdAn in methanol bear a resemblance to that observed in chloroform (Figure 3.11a). On the contrary, nTA spectra ( $\lambda_{ex} = 355$  nm, 100 ns–20  $\mu$ s)

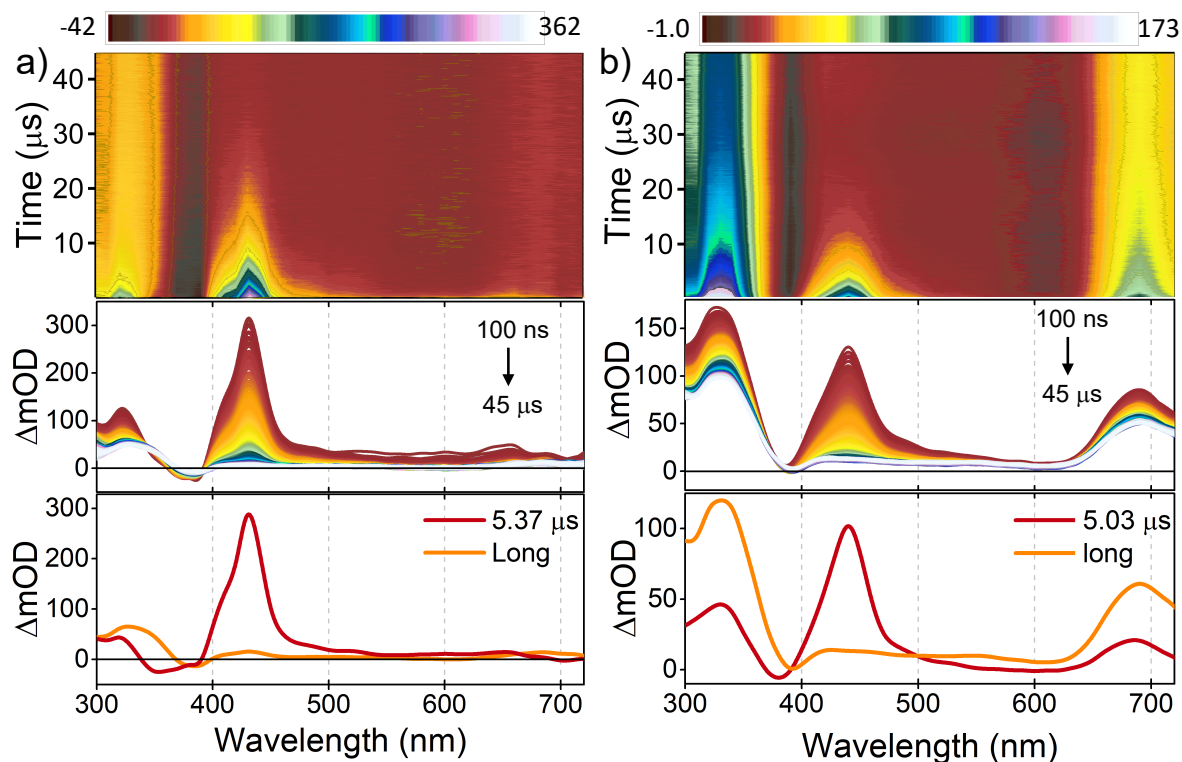


**Figure 3.11.** *nTA spectra (100 ns → 45 μs) of AdAn assembly depicting the 2D contour plot (top), spectra (middle) and evolution associated spectra (EAS, bottom) in a) methanol ( $\lambda_{ex} = 355$  nm, 0.12 mM) and b) chloroform ( $\lambda_{ex} = 266$  nm, 0.12 mM) solutions.*

of 0.12 mM AdAn in diethyl ether (DEE) exhibits positive absorption only at 440 nm and ground-state depletion at 350-400 nm (Figure 3.10a). The EAS corresponding to the nTA spectrum in DEE, reveals a major component centered at 440 nm and a diffuse component with dual absorption at 300-340 nm and 690-720 nm (Figure 3.10a). The species at 440 nm is attributed to  $^3\text{An}^*$  ( $\tau_T = 4.8$  μs) whereas the second component with diffuse absorption can be attributed to the presence of a negligible/minor CS state similar to that observed in  $\text{CHCl}_3$  and methanol. The presence of diffuse signature corresponding to the RIP intermediate in DEE suggests a shallow charge separation in nonpolar solvent as compared to that in  $\text{CHCl}_3$  and methanol [167, 168]. Interestingly, the transient spectroscopic features corresponding

to the radical ion-pair intermediates are strongly evident from the nTA spectrum ( $\lambda_{ex} = 266$  nm, 100 ns  $\rightarrow$  45  $\mu$ s) obtained by deep-UV excitation of both the chromophores in AdAn (0.12 mM in  $\text{CHCl}_3$ , Figure 3.11b). The EAS of nTA spectra acquired by deep-UV excitation ( $\lambda_{ex} = 266$  nm) is similar to that shown in Figure 3.11b with a faster decaying (440 nm) and an intense slow decaying absorption at 330, 500-600 (diffuse) and 690 nm (Figure A3.5.). The fast decaying component at 440 nm ( $\tau_T = 5.03$   $\mu$ s) is oxygen sensitive and is attributed to  $^3\text{An}^*$ , whereas the slow decaying component is attributed to the long-lived radical ion-pair intermediates. The relatively intense features corresponding to the radical ion-pair intermediates by deep-UV ( $\lambda_{ex} = 266$  nm) excitation is a consequence of the higher feasibility ( $\Delta G_{CS} = -1.25$  eV) of electron transfer from  $^1\text{Ad}^*$  to An as corroborated by the Rehm-Weller analyses (Table 3.5.).

### 3.3.3.3. Spectroelectrochemistry and Simulation of RIP Intermediates

To validate the presence of the radical ion-pair intermediates, spectroelectrochemical (SEC) measurements of AdAn were carried out in  $\text{CHCl}_3$  (Figure A3.6.). The SEC analysis of AdAn in  $\text{CHCl}_3$  shows the evolution of a new broad absorption around 300-330 nm and a diffuse absorption in 500-600 nm upon oxidation (0 to +1.8 V). The differential absorption spectrum obtained before and after oxidation shows a good match with the nTA spectrum in 300-330 and 500-600 nm regions, thereby depicting an oxidized Ad species (Figure A3.6b). Moreover, the computed absorption spectrum of adenine radical cation (Figure 3.12a) using TD-M06-2X/6-311G+(d,p)

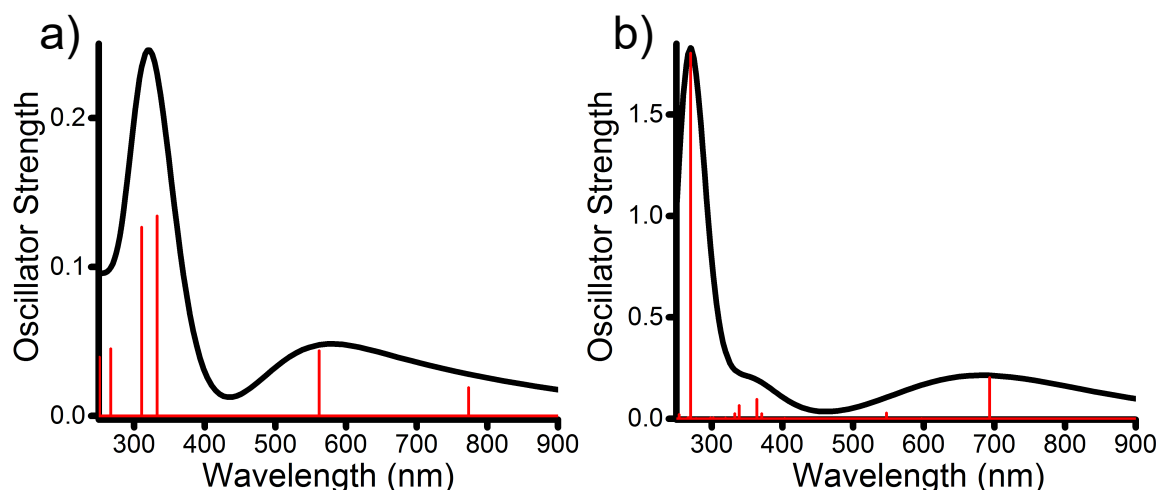


**Figure 3.12.** Absorption spectra of a)  $Ad^{\bullet+}$  (shift = -0.55 eV) and b)  $An^{\bullet-}$  (shift = -0.21 eV) computed at PCM/TD-M06-2X/6-311G+(d,p) level of theory.

level of theory show a fair match with the experimental nTA spectra in the 330 and 500-600 nm region (Figure 3.12a) [164]. Likewise, the SEC absorption spectrum obtained by reduction (0 to -2.5 V) shows a gradual decrease in the intensity of the vibronically resolved bands corresponding to An and depicts the emergence of a new band around 300 nm region for reduction of AdAn in  $CHCl_3$  (Figure A3.6c-d). Correspondingly, the absorption spectrum for  $An^{\bullet-}$  computed using TD-M06-2X/6-311G+(d,p) level of theory corroborates a fair match with the experimental nTA spectra at 300, 370 and 690 nm (Figure 3.12b) [169, 170].

### 3.3.3.4. Concentration Dependent Cyclic Voltammetry and FMO analyses

The cyclic voltammetric (CV) analysis of 1 mM AdAn (in 0.1 M  $nBu_4NPF_6$  in  $CH_2Cl_2$ ) displayed the appearance of first reduction at -1.88 V (Figure 3.13a). The observed first reduction at -1.88 V can be attributed to the reduction of anthracene core as reported earlier [171]. The concentration dependent cyclic voltammetric (CDCV) analysis of AdAn in  $CH_2Cl_2$  corroborated a decrease (ca. 220 mV) in the reduction

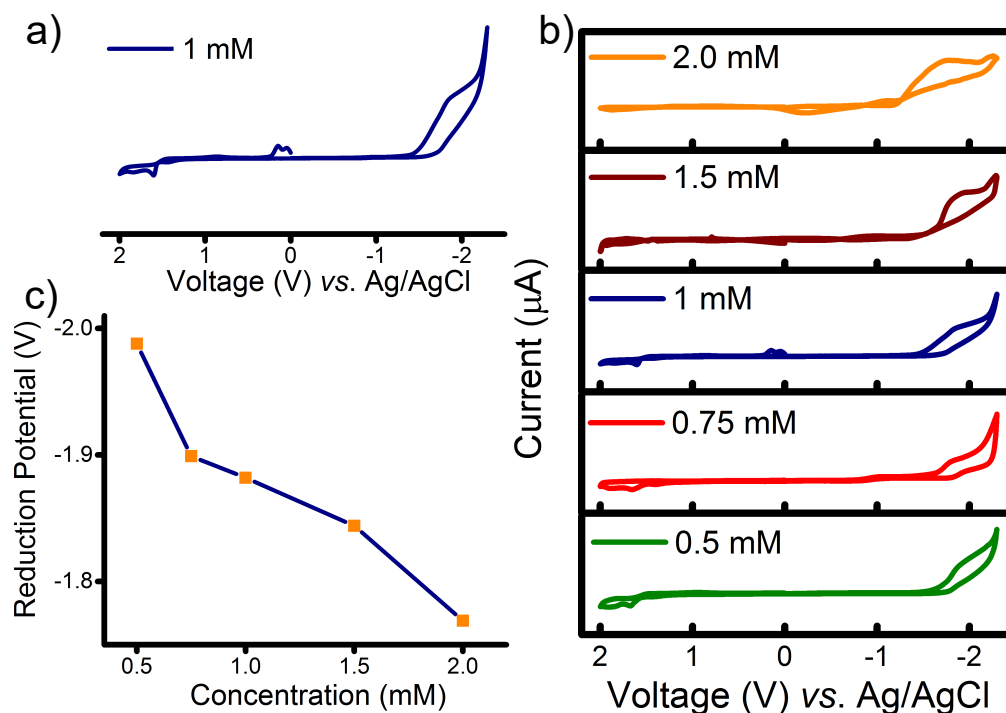


**Figure 3.13.** a) Cyclic voltammetric (CV) analysis of AdAn (1 mM in  $\text{CH}_2\text{Cl}_2$ ); b) concentration dependent (0.5 - 2 mM) CV measurements and c) decrease in reduction potential of AdAn with increasing concentration. Scan rate =  $50\text{-}100\text{ mV s}^{-1}$  with  $0.1\text{ M}$   $n\text{Bu}_4\text{NPF}_6$  as supporting electrolyte in  $\text{CH}_2\text{Cl}_2$ .

potential with the increasing concentration (from 0.5 to 2 mM, Figure 3.13b-c). The facile electrochemical reduction of aggregated AdAn relative to the monomer is a direct consequence of decrease in the free energy of reduction due to the stabilization/delocalization of the electron by nearby chromophores in AdAn assembly [33, 63, 121]. Interestingly, a decrease in bandgap ( $\Delta E_g = E_{\text{HOMO}} - E_{\text{LUMO}}$ ) for the di/tetra/octameric *vs.* monomeric AdAn indicates the possibility of a more facile and stabilized CS state in aggregated condition, corroborating with the CDCV analysis (Figure 3.14) [63, 121].

Furthermore, nTA experiments at longer timescales (500  $\mu\text{s}$ -4.5 s) were carried

out to monitor the kinetics of the species at 330 and 690 nm (Figure A3.7.). The nTA spectra ( $\lambda_{ex}$  =266 nm, 500  $\mu$ s-4.5 s) of 0.12 mM AdAn in  $\text{CHCl}_3$  displays the

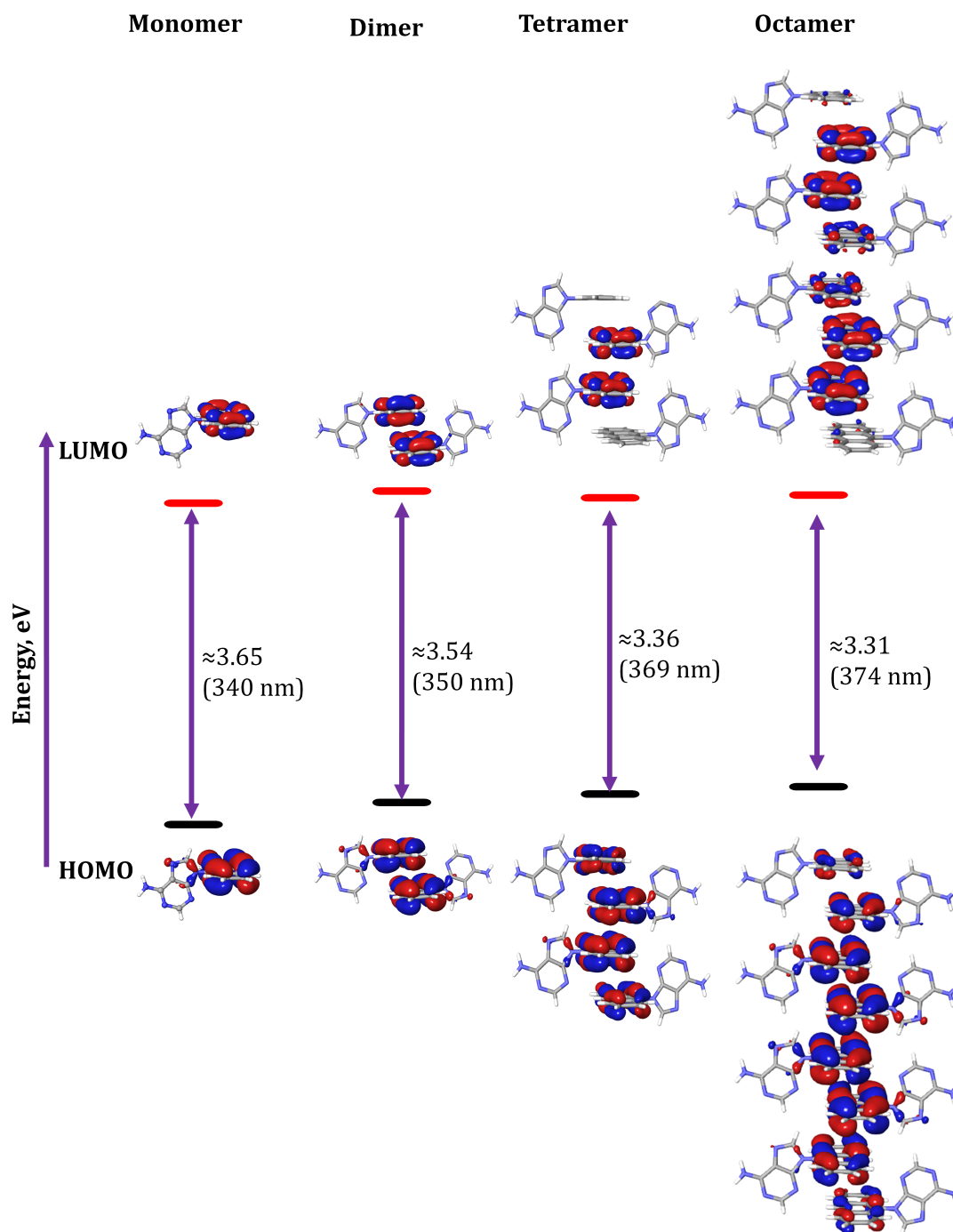


**Figure 3.14.** Frontier molecular orbital (FMO) analysis of AdAn (mono, dimer, tetramer and octamer) calculated from B3LYP-D3/6-31G+(d,p) level of theory in Schrödinger Materials Science Suite using Jaguar DFT engine.

component at 330 and 690 nm to decay with a lifetime of milliseconds (Figure A3.7.). The transient species at 330 nm decays bi-exponentially and can be attributed to have contributions from the adenine radical cation ( $\text{Ad}^{\bullet+}$ ,  $\tau_{\text{cr}}^{\text{A}} = 120 \text{ ms}$ ) and its deprotonated ( $\text{Ad-H}^{\bullet}$ ) form ( $\tau = 0.57 \text{ s}$ , Figure A3.7.) or can arise from some unsolicited photoexcited state processes [164]. The UV-vis absorption spectra of the samples after nTA measurements showed trends indicating the photo dimerization/decomposition of the AdAn conjugate arising from the unsolicited photoexcited state processes (Figure 3.15., A3.8.) [172]. A thin layer chromatographic (TLC) analysis of AdAn sample after nTA experiment evidently exhibits the presence of multiple photoproducts (Figure 3.15a). Intriguingly, the AdAn sample (in  $\text{CHCl}_3$ ) after nTA analysis forms pale yellow precipitate when left undisturbed for 12 hours (Figure 3.15b). The high resolution mass spectrum of the pale yellow

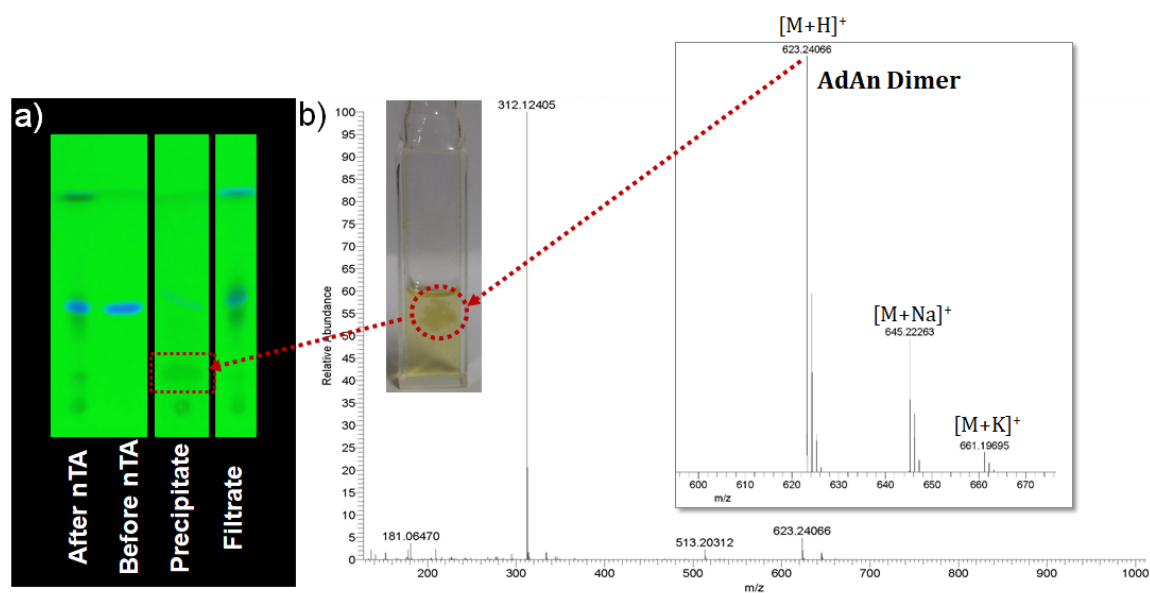


**Figure 3.15.** a) TLC analysis of the AdAn (in  $\text{CHCl}_3$ ) before and after nTA analysis; B) high resolution mass spectrum of precipitate (AdAn dimer) obtained after nTA analysis in  $\text{CHCl}_3$  ( $\lambda_{\text{ex}} = 355 \text{ nm}$ ).

precipitate reveals a mass ( $m/z = 623.2406$ ) corresponding to AdAn photodimer (Figure 3.15b). By exciting An at 355 nm, the photodimerized product should majorly be corresponding to the 9,10-photoadduct of the anthracene core in AdAn. However, the possibility of adenine photodimerization cannot be neglected while undergoing a deep-UV excitation at 266 nm. The integration of the area under the absorption curve (325-400 nm) for AdAn, recorded before and after nTA analysis indicates a >56 % yield of the photoproduct under the light irradiation. However, the actual yield of the photoproduct can only be more than the calculated value (>56 %) as the photodimerized product also has tail end absorption in the same region.

Implications of the self-assembly on the photoexcited state processes adopted by the AdNp/AdAn assembly and its effect on the rate of the charge recombination can be summarized via Figure 3.16. The mixed/alternating D-A stack in AdNp ( $\lambda_{ex} = 266 \text{ nm}$ ) upon photoexcitation can populate either the singlet excited state of Ad or Np (i.e.  $^1\text{Ad}^*\text{Np}$  or  $\text{Ad}^1\text{Np}^*$ ). The singlet excited state can subsequently form the charge separated RIP intermediates, however due to unfavorable arrangement of D-A assembly the charged RIP intermediates can recombine in an ultrafast manner to

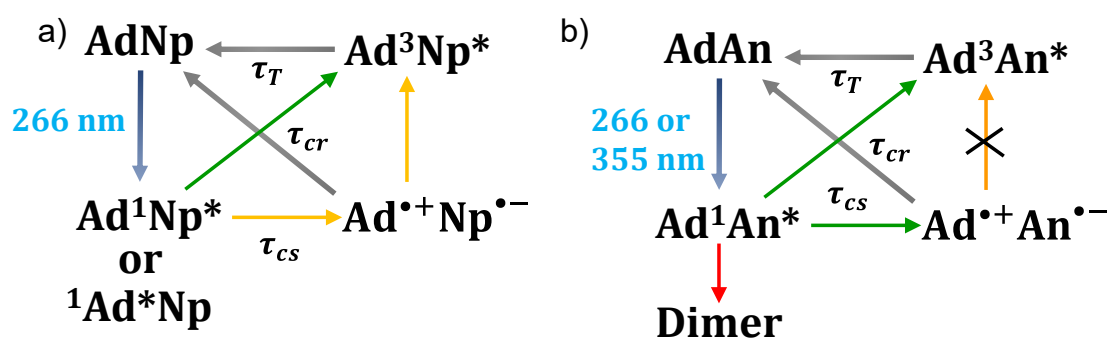


**Figure 3.16.** Photoexcited state processes and kinetic pathways adopted by a) AdNp ( $\lambda_{ex} = 266 \text{ nm}$ ) and b) AdAn ( $\lambda_{ex} = 266 \text{ or } 355 \text{ nm}$ ) assembly upon photoexcitation.

populate the triplet excited state of the arene chromophore ( $\text{Ad}^3\text{Np}^*$ ) which is perceived in the nTA spectrum of the self-assembled AdNp in chloroform (Figure 3.16a). On the other hand, the favorable arrangement of D-A components in the alternate-distichous AdAn assembly can initially populate the single excited state of An ( $\text{Ad}^1\text{An}^*$ , upon  $\lambda_{ex} = 355$  nm), which can independently form the charge separated RIP intermediates or the triplet excited state of An ( $\text{Ad}^3\text{An}^*$ ) as has been seen in the nTA spectra of aggregated AdAn in chloroform (Figure 3.16b). Apart from the formation of the long-lived RIP intermediates, the face-to-face An-An stacks exhibits an unsolicited photochemistry which lends the photo dimerized/decomposed AdAn.

Perseverance of the RIP intermediates in AdAn alternate distichous assembly as compared to the mixed/alternating D-A stack in AdNp, can be attributed to the favorable organization achieved while the nucleobase-arene conjugate self-sorts into a near-orthogonal D-A columnar architecture. Delocalization of the electron through the An-An stacks and the diffusion of hole across near-orthogonally flanked hydrogen bonded adenines lead to a resultant long-lived charge separated state. The facile electrochemical reduction and the considerable decrease of the redox potential in aggregated AdAn could be an outcome of the stabilization and/or delocalization of electrons across the two dimensional sheet-like assembly crafted via synergistic weak intermolecular interactions. The alternate distichous assembly illustrates a rational and efficient design of stacked acceptor and the near-orthogonally flanked

donor chromophore, which facilitates the trajectories of the complementary charge carriers in segregated and sovereign channels. Despite of the decomposition/dimerization of the AdAn in  $\text{CHCl}_3$  under high energy UV irradiation, the long-lived charge separation in the alternate distichous assembly projects an innovative self-assembly rationale for delaying the rate of charge recombination for photofunctional applications.

### 3.4. Conclusions

In summary, we report the design and syntheses of two novel nucleobase-arene assembly i.e. mixed/alternating (AdNp) and alternate-distichous (AdAn) D-A assembly aimed to perceive the effect of self-assembly on the charge separated RIP intermediates. The AdNp dyad forms nonplanar ( $\theta = 48.8^\circ$ ) mixed/alternating D-A assembly whereas AdAn ( $\theta = 80^\circ$ ) dyad tends to form near-orthogonal adenine-anthracene stacks from the co-operative weak intermolecular hydrogen bonding and  $\pi$ - $\pi$  interactions. Owing to the nonplanar nature of the donor and acceptor chromophores, AdNp and AdAn dyads exhibit a minimal perturbation in the ground state properties as corroborated by preliminary photophysical and redox analysis in organic solvents. The negative value of the  $\Delta G_{CS}$  (ca. -0.55 [AdNp] and -1.25 [AdAn] eV) obtained from the Weller analysis and the frontier molecular orbital analysis suggests favorable charge-transfer characteristics in the dyads. Upon photoexcitation, AdNp ( $\lambda_{ex} = 266$ ) assembly reveal the presence of only the triplet excited state of Np ( $\text{Ad}^3\text{Np}^*$ ) probably arising from the unfavorable arrangement of

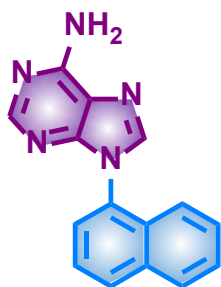
the D and A components in the mixed/alternating stacks. On the other hand, the photoexcitation ( $\lambda_{ex} = 266$  and  $355$  nm) of the favorable D-A stack in the AdAn alternate-distichous assembly in  $\text{CHCl}_3$  displays the evolution of a long-lived radical ion-pair intermediates ( $\tau_{cr}^A = 120$  ms) which displays a solvent polarity dependence as substantiated via nTA spectroscopic measurements. The self-assembled AdAn represents a novel design for a hierarchical D-A nanoarchitecture which can circumvent the geminate charge recombination via segregating the transport pathways of the charge carriers. Alternately, the AdAn assembly undergoes photo-damage to yield the undesirable/unsolicited photoproducts. Although, self-assembled AdAn displays undesirable photodecomposition upon UV-irradiation, the persistent charge separated state in an unprecedented alternate distichous assembly demonstrate a novel rational D-A design for extending the lifetimes of the charge separated states in emergent photofunctional applications.

## 3.5. Experimental Section

### 3.5.1. Syntheses and Characterization

**General procedure for the synthesis N-arylated adenines [122]:**

A solution of adenine (1 eq.), arylboronic acid (2 eq.), copper(II) acetate monohydrate (1 eq.) in methanol : water (4 : 1, 800 ml) mixture and TMEDA (2 eq.) was stirred at room temperature in presence of air for 48 hours. Progress of the reaction was monitored through TLC. After completion of reaction, solvent was evaporated under reduced pressure and the crude mixture was extracted with chloroform. The chloroform layer was then concentrated and the crude product was purified via column chromatography [silica gel, EtOAc:Pet ether (4:1)].



**AdNp**

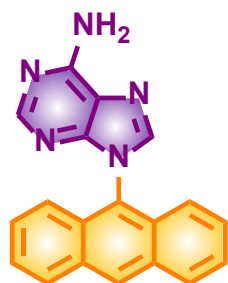
**AdNp** [Brown solid (89 mg, 6%)]: **Melting point:** 238-240 °C;

$^1\text{H NMR}$  [500 MHz, DMSO,  $\delta$  (ppm)]: 8.34, (s, 1H), 8.10 (d,  $J = 5.0$  Hz, 1H), 8.05 (d,  $J = 8.25$  Hz, 1H), 7.99 (s, 1H), 7.64-7.62(m, 2H), 7.56 (t,  $J = 7.35$  Hz, 1H), 7.46 (t,  $J = 8.05$  Hz, 1H), 7.35 (broad, 2H), 7.21 (d,  $J = 8.5$  Hz, 1H);

$^{13}\text{C NMR}$  [125 MHz, DMSO,  $\delta$  (ppm)]: 131.4, 130.0, 129.8, 128.7, 127.9, 127.3, 126.2, 126, 122.8, 118.9;

**IR** (KBr,  $\text{cm}^{-1}$ ): 3313, 1666;

**HRMS** (ESI):  $m/z$  calculated for  $\text{C}_{15}\text{H}_{12}\text{N}_5$   $[\text{M}+\text{H}]^+$  : 262.1093, found : 262.1078.



**AdAn**

**AdAn** [Light yellow solid (30 mg, 4.3% )]: **Melting point:** >300 °C;

$^1\text{H NMR}$  [500 MHz, DMSO,  $\delta$  (ppm)]: 8.94 (s, 1H), 8.50 (s, 1H), 8.28 (d,  $J = 8.5$  Hz, 2H), 7.99 (s, 1H), 7.62 (t,  $J = 10$  Hz, 2H), 7.56-7.50 (m, 4H), 7.23 (d,  $J = 10$  Hz, 2H);

$^{13}\text{C NMR}$  [125 MHz, DMSO,  $\delta$  (ppm)]: 156.8, 153.8, 152.3, 142.8, 131.4, 129.4, 129.1, 128.4, 126.5, 126.1, 122.5, 118.7;

**IR** (KBr,  $\text{cm}^{-1}$ ): 3297, 1674;

**HRMS** (ESI):  $m/z$  calculated for  $\text{C}_{19}\text{H}_{14}\text{N}_5$   $[\text{M}+\text{H}]^+$  : 312.1249, found : 312.1237.

### 3.6. Additional Figures and Tables

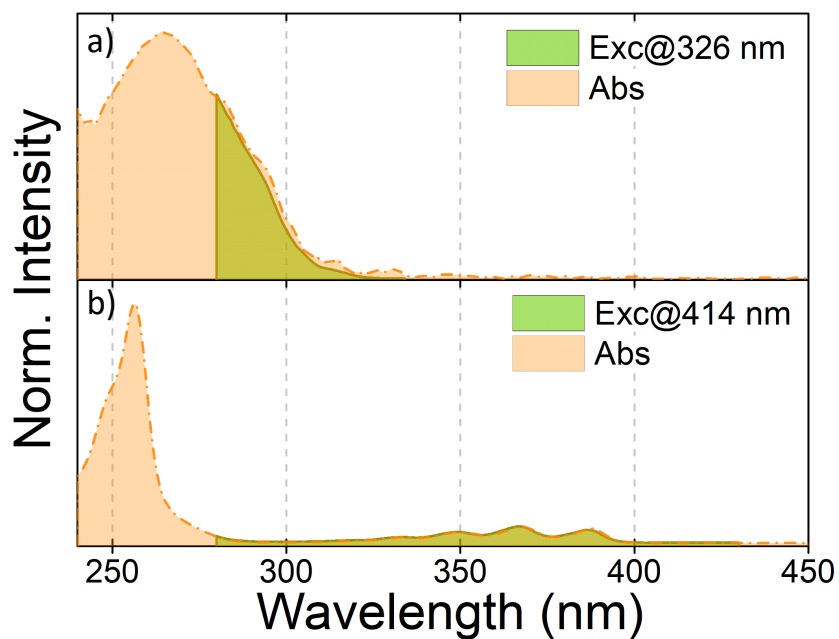


**Figure A3.1.** Excitation spectra monitored at individual wavelengths for a) AdNp and b) AdAn.

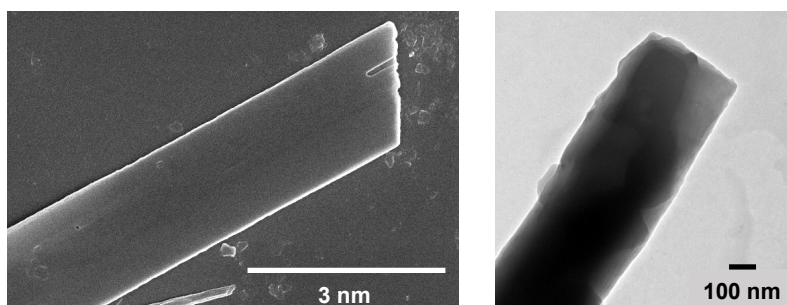


**Figure A3.2.** Morphological character of the AdNp aggregate ( $\text{CHCl}_3$ ) in SEM (left) and TEM (right).

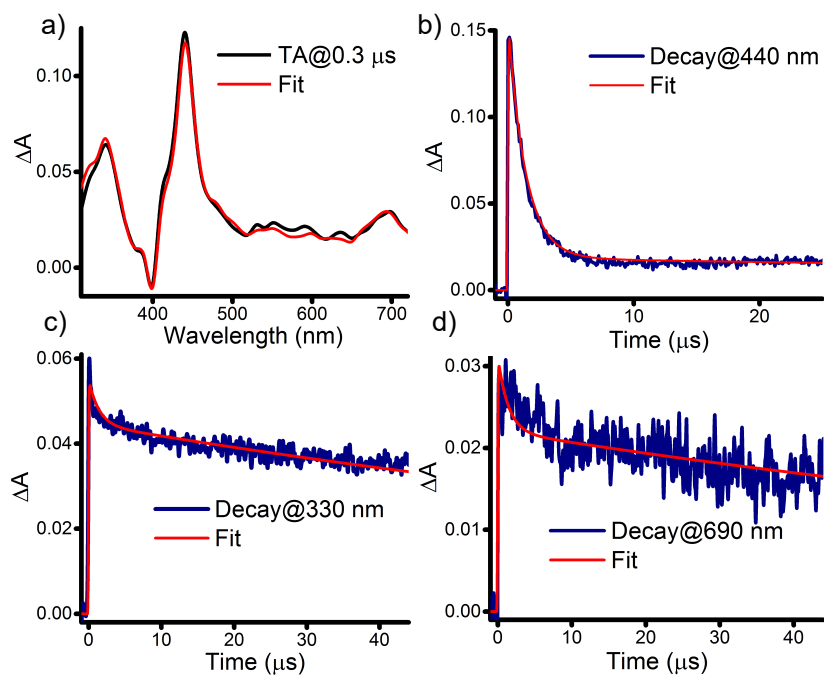


**Figure A3.3.** a) *nTA* spectrum ( $\lambda_{ex} = 355$  nm) after 0.3  $\mu$ s delay; decay traces at b) 440; c) 330 and d) 690 nm for 0.12 mM AdAn in  $\text{CHCl}_3$  obtained from the global analysis. Black and blue trace: raw data; Red: fit for the corresponding data.

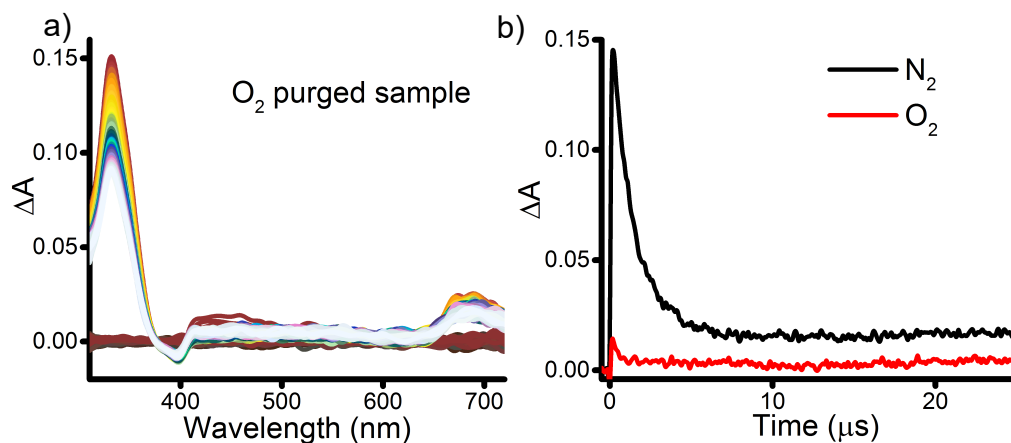


**Figure A3.4.** a) *nTA* spectrum (78 nm – 44  $\mu$ s,  $\lambda_{ex} = 355$  nm) of oxygen purged solution and b) decay monitored at 440 nm (in nitrogen and oxygen purged solutions) for 0.12 mM AdAn in  $\text{CHCl}_3$ .

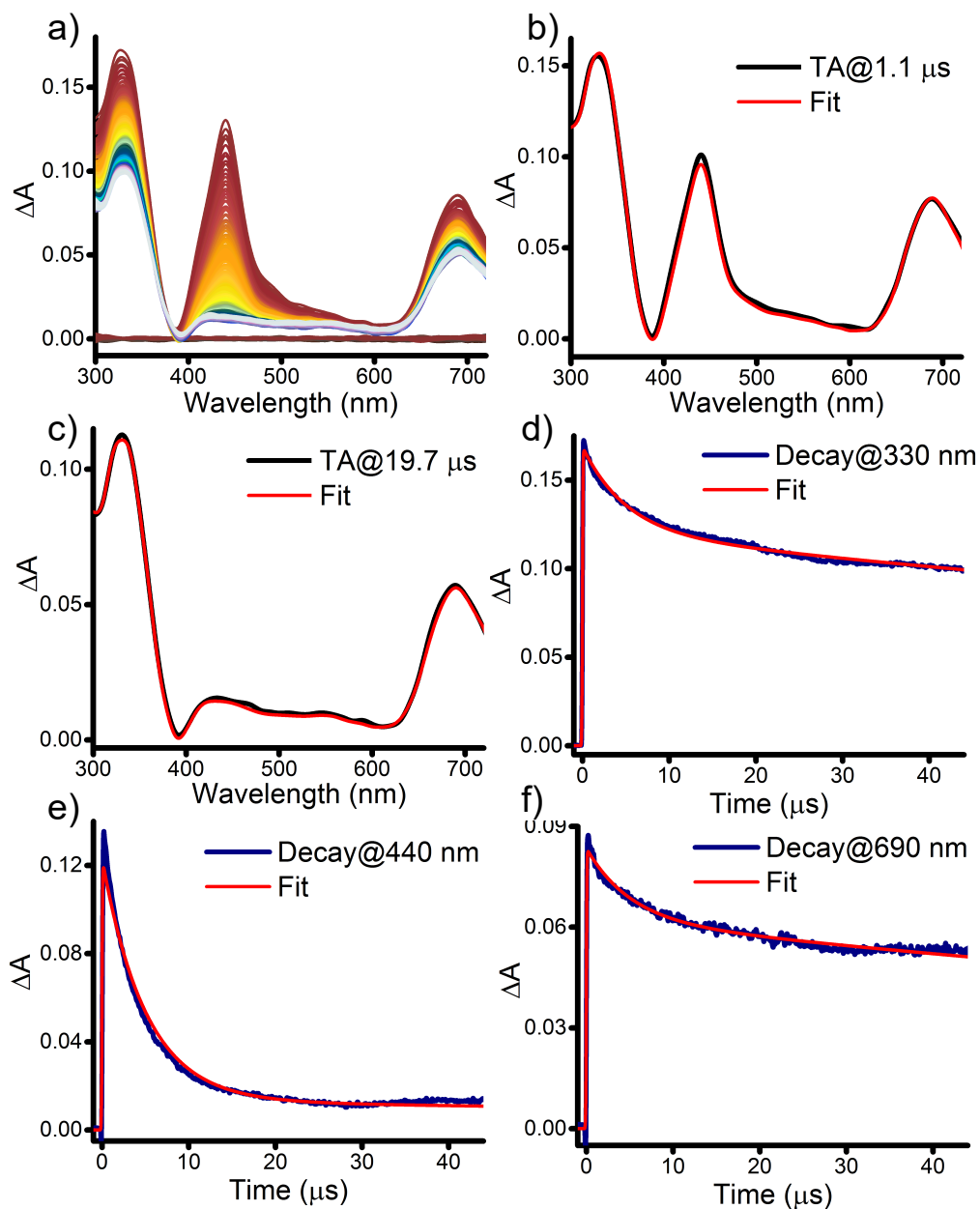


**Figure A3.5.** a) nTA spectrum (100 ns-45  $\mu$ s,  $\lambda_{ex}$  = 266 nm); nTA spectrum after b) 1.1  $\mu$ s and c) 19.7  $\mu$ s; decay traces at d) 330; e) 440 and f) 690 nm for 0.12 mM AdAn in  $\text{CHCl}_3$ . Black and blue trace: raw data; Red: fit for the corresponding data.

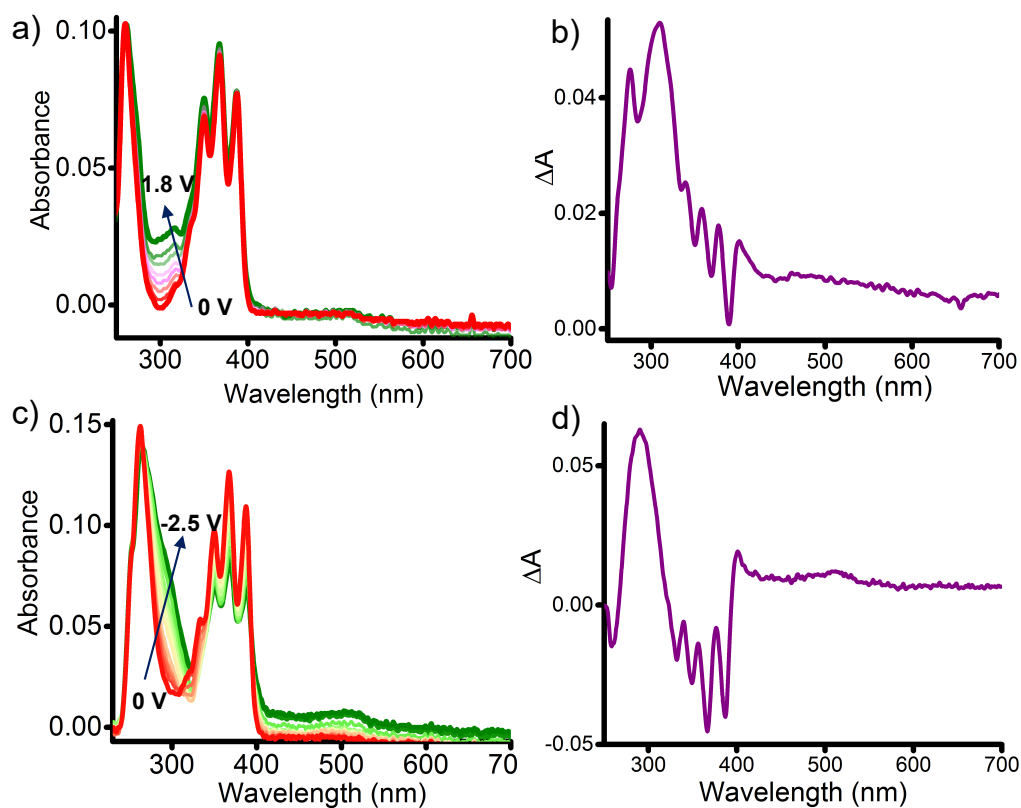


**Figure A3.6.** UV-vis spectroelectrochemical (SEC) analysis for a) oxidation (0 to 1.8 V) and c) reduction (0 to -2.5 V) of AdAn in  $\text{CHCl}_3$ . Differential absorption spectrum attained by subtracting the UV-vis SEC absorption plots obtained before and after applying potentials for b) oxidation and d) reduction of AdAn. Solvent used is  $\text{CHCl}_3$  with 0.1 M  $n\text{Bu}_4\text{NPF}_6$  as supporting electrolyte.

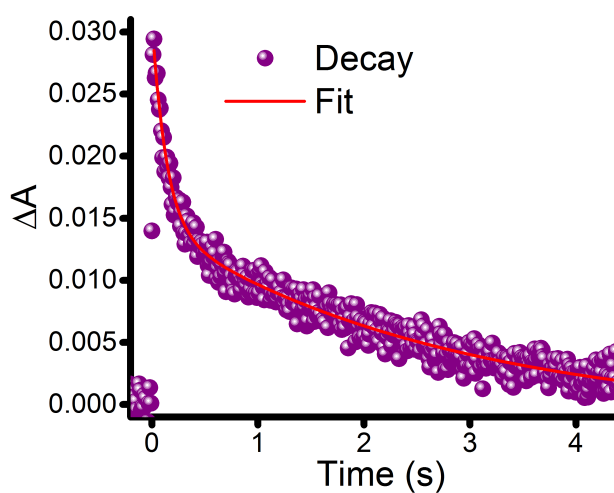


**Figure A3.7.** Complete decay profile of the RIP intermediate.

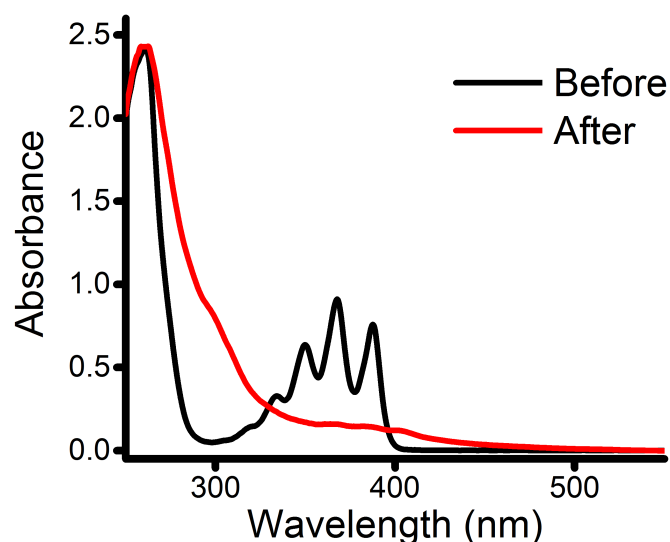


**Figure A3.8.** UV-vis absorption of AdAn before and after nTA analysis in  $\text{CHCl}_3$ .

**Table A3.1.** Excitation energy, oscillator strength, main transition orbital, and their contribution calculated for adenine (Ad), naphthalene (Np), anthracene (An), AdNp and AdAn derivatives using TD-M06-2X/6-311G+(d,p).[164].

State	Excitation Energy		$f$	Main transition orbital	Contribution	
	$\Delta E$ , (eV) [nm]	$\Delta E$ , (eV) [nm]				
Ad (shift = -0.55 eV)	S6	6.4442 [192.40]	5.8942 [210.35]	0.0016	HOMO→LUMO+2	0.61857
					HOMO→LUMO+4	0.21027
					HOMO→LUMO+1	0.10300
	S5	6.0576 [204.68]	5.5076 [225.11]	0.0025	HOMO-2→LUMO+3	0.65470
					HOMO-2→LUMO	0.10258
	S4	5.8227 [212.93]	5.2727 [235.14]	0.0057	HOMO→LUMO+1	0.66726
S3	5.5576 [223.09]	5.0076 [247.59]	0.0307	HOMO-1→LUMO	0.32536	
				HOMO→LUMO+3	0.60801	
S2	5.5110 [224.97]	4.9610 [249.92]	0.0008	HOMO-2→LUMO	0.66606	
S1	5.3530 [231.62]	4.8030 [258.14]	0.3702	HOMO→LUMO	0.69323	
Np (shift = -0.23 eV)	S6	6.0751 [204.09]	5.8451 [212.12]	0.0000	HOMO→LUMO+4	0.68583
					HOMO-2→LUMO+2	0.12121

	S5	6.0220 [205.89]	5.7920 [214.06]	0.0000	HOMO→LUMO+3	0.69285
	S4	6.0070 [206.40]	5.7770 [214.62]	0.0000	HOMO→LUMO+5	0.69943
	S3	5.7956 [213.93]	5.5656 [222.77]	0.0000	HOMO→LUMO+2	0.68461
	S2	4.7222 [262.56]	4.4922 [275.99]	0.0793	HOMO→LUMO	0.68788
	S1	4.6499 [266.64]	4.4199 [280.55]	0.0001	HOMO→LUMO+1 HOMO-1→LUMO	0.50074 0.49202
	S6	5.3652 [231.09]	5.3102 [233.48]	0.0000	HOMO→LUMO+2	0.64750
	S5	5.3188 [233.10]	5.2638 [235.54]	0.0000	HOMO-2→LUMO HOMO→LUMO+3	0.53212 0.44677
An (shift = -0.05 eV)	S4	5.1538 [240.57]	5.0988 [243.16]	0.0000	HOMO→LUMO+3	0.53673
	S3	5.1314 [241.62]	5.0764 [244.24]	2.3016	HOMO-1→LUMO HOMO→LUMO+1	0.50379 0.48994
	S2	4.0685 [304.75]	4.0135 [308.92]	0.0006	HOMO→LUMO+1	0.50248
	S1	3.5332 [350.91]	3.4782 [356.46]	0.1057	HOMO→LUMO	0.70279
	S6	5.4879 [225.92]	5.4879 [225.92]	0.0104	HOMO-1→LUMO+2	0.24643
	S5	5.3134 [233.34]	5.3134 [233.34]	0.3292	HOMO→LUMO+2 HOMO-3→LUMO+2	0.59709 0.19021
	S4	5.2984 [234.00]	5.2984 [234.00]	0.0420	HOMO→LUMO+2 HOMO-3→LUMO+1	0.19611 0.16669
AdNp (shift = -0 eV)	S3	5.0122 [247.37]	5.0122 [247.37]	0.0047	HOMO→LUMO HOMO-1→LUMO	0.66494 0.13624
	S2	4.6104 [268.92]	4.6104 [268.92]	0.0188	HOMO-2→LUMO HOMO-1→LUMO	0.45885 0.20904
	S1	4.5872 [270.28]	4.5872 [270.28]	0.1669	HOMO-1→LUMO HOMO-1→LUMO+1 HOMO-2→LUMO+2	0.64352 0.13615 0.12405

					HOMO→LUMO+2	0.56977
	S6	5.3414 [232.12]	5.1314 [241.62]	0.1951	HOMO-5→LUMO+2	0.11999
					HOMO→LUMO+6	0.11740
	S5	5.2716 [235.19]	5.0616 [244.95]	1.1372	HOMO-3→LUMO	0.45689
					HOMO→LUMO+2	0.10379
AdAn					HOMO-3→LUMO	0.44949
(shift = -	S4	5.1843 [239.15]	4.9743 [249.25]	0.8169	HOMO→LUMO+1	0.36108
0.21 eV)					HOMO-2→LUMO	0.32603
					HOMO→LUMO+6	0.14481
	S3	4.7129 [263.08]	4.6129 [268.78]	0.0007	HOMO-1→LUMO	0.69799
	S2	4.1380 [299.62]	3.928 [315.64]	0.0056	HOMO-2→LUMO	0.51530
					HOMO→LUMO+2	0.15671
	S1	3.5924 [345.13]	3.3824 [366.56]	0.1694	HOMO→LUMO	0.70176

*f* – oscillator strength

## 3.7. Appendix

### 3.7.1. Materials and methods

Similar to that discussed in section 2.6.1. (Chapter 2).

### 3.7.2. X-ray crystallography

Single crystal of AdNp (Chloroform) and AdAn (1:1, *n*-hexane:Chloroform) were obtained by slow evaporation of solvent from homogenous solution at room temperature. High-quality specimen of approximate 0.20 × 0.15 × 0.15 (AdNp) and 0.25 × 0.20 × 0.05 (AdAn) mm<sup>3</sup> dimension were selected for the X-ray diffraction experiments. Crystallographic and refinement data are presented in Table 3.1. All the instrumental parameters and the single crystal refining/solving methods were similar to that mentioned in Section 2.6.2. (Chapter 2). Additionally, in case of AdAn, as the electron densities corresponding to the disordered solvent molecules was difficult to model the structure was flattened using ‘Squeeze’[173] option of

PLATON [174]. The full validation of CIF and structure factor of AdNp and AdAn were performed using the checkCIF utility and found to be free of major alert levels. 3D structure visualization and the exploration of the crystal packing of AdAn was carried out using Mercury 3.5.1 [137, 138]. The face-to-face overlap between the anthracene-on-anthracene stacks was visualized and imaged from the crystal structure. The ratio of the overlapped area and the total area of the donor and acceptor rings gave the percentage (%) overlap between the face-to-face stacked anthracenes [121].

### 3.7.3. Steady-State Spectroscopy

Instrumental parameters were same as that mentioned in section 2.6.3. (Chapter 2). To avoid the distortion arising from the inner filter effect, the concentration-dependent steady-state measurements were carried out in a cuvette of 1 mm path length [139]. Solution state relative quantum yield measurements of AdNp and AdAn were performed using naphthalene ( $\lambda_{ex} = 270$  nm, reported quantum yield,  $\phi_f = 0.23$ )[175] in cyclohexane and quinine sulphate in 0.1 M H<sub>2</sub>SO<sub>4</sub> ( $\lambda_{ex} = 350$  nm, reported quantum yield,  $\phi_f = 0.577$ ) as the standard [44]. Lifetime measurements were carried out in an IBH picosecond time correlated single photon counting (TCSPC) system. Pulse width of the excitation ( $\lambda_{ex} = 260$  nm) and ( $\lambda_{ex} = 340$  nm) sources are determined to be <1.2 and <1 ns, respectively. The fluorescence decay profiles were de-convoluted using DAS6.3 fluorescence decay analysis software, and fitted with exponential decay, minimizing the  $\chi^2$  values.

### 3.7.4. Femtosecond transient absorption measurement (fTA)

Spectra-Physics Tsunami Oscillator (80 MHz, 800 nm) was used as seed for a Spectra-Physics Spitfire Regenerative Amplifier (1 kHz, 4 mJ). A fraction of the amplified output was used to generate 400 nm pump pulse. Residual 800 nm pulse was sent through a delay line inside an Excipro pump-probe spectrometer from CDP systems. A rotating CaF<sub>2</sub> plate (2 mm thickness) was used to generate continuum of white light from the delayed 800 nm pulses. The continuum of white light was split

into two and the streams were used as probe and reference pulses. Transient absorption spectra were recorded using a dual diode array detector having a 200 nm detection window with an optical delay of 1.6 fs. Sample solutions were prepared in a rotating sample cell with 4 mm path length. IRF was determined by solvent (10% benzene in methanol) two photon absorption and was found to be approximately 110 fs at about 530 nm. Energy per pulse incident on the sample is attenuated employing 80 % neutral density filter when required.

fTA measurements of self-assembled solution of AdAn in  $\text{CHCl}_3$  (0.12 mM) were excited with 360 nm, 200 nJ,  $\approx 110$  fs pulses, to moderate singlet-singlet annihilation that occurs often in multichromophoric assemblies [33]. AdAn in the aggregated state possesses positive absorptions at 590 nm in  $\text{CHCl}_3$ . Kinetic components observed at 590 nm are laser intensity independent, ruling out the assignment of kinetic components to singlet-singlet annihilation [33].

### 3.7.5. Nanosecond transient absorption measurement (nTA)

Nanosecond laser flash photolysis experiments of the argon purged solutions of AdNp and AdAn were carried out in an Applied Photophysics Model LKS-60 laser kinetic spectrometer using the third and fourth harmonic (355 and 266 nm respectively, pulse duration  $\approx 7$  ns) of a Quanta Ray INDI-40-10 series pulsed Nd:YAG laser as the excitation source. The lamp pulser was switched off and a variable load resistor (100  $\Omega$  – 500  $\Omega$ ) was attached to the oscilloscope of the nTA setup during the measurements at longer time scales ( $> 50 \mu\text{s}$ ).

### 3.7.6. Global Analysis

Global analysis of the fTA and nTA spectra were performed using the program Glotaran [141, 142, 176]. Singular value decomposition followed by the global analysis of the time vs. wavelength plots furnished a temporal de-convolution of the short and the long-lived components in the fTA and nTA data. The global analysis procedure takes into account instrument response function (IRF) and simultaneously fits kinetic traces measured at all wavelengths. During the global analysis, fitting of

the kinetic traces at all the wavelengths were carried out using a sequential model to provide the evolution associated spectra (EAS). The EAS signifies the evolution of the spectra in time and do not necessarily represent a real physical/chemical species. EAS of AdNp and AdAn obtained by global analysis of  $\Delta A$  vs. time and wavelength based two-dimensional map of the fTA and the nTA data is demonstrated in Figures 3.8.-3.11.

### **3.7.7. Morphological Analysis**

#### **3.7.7.1. Scanning Electron Microscopy (SEM)**

FE-SEM measurements of AdAn was carried out on FEI Nova NanoSEM 450 (FEG type) by drop casting AdNp (1 mM) and AdAn (0.12 mM) in  $\text{CHCl}_3$  on the flat surface of silicon wafer (Ted Pella, Inc.) and allowing to evaporate the excess solvent under air in dust free conditions. The samples were further dried under vacuum and subjected to thin chromium sputtering using Quorum Q150T ES fine coater to increase the signal/noise ratio. The probing side was inserted into the scanning electron microscope for obtaining the images.

#### **3.7.7.2. Transmission Electron Microscopy (TEM)**

TEM measurements were carried out on JEOL 2010 with an accelerating voltage of 200 kV. The samples were prepared by drop casting  $\text{CHCl}_3$  solutions of AdNp (1 mM) and AdAn (0.12 mM) on a 400 mesh carbon-coated copper grid (Ted Pella, Inc.) at ambient conditions and allowing the excess solvent to evaporate under air in dust free conditions. The samples were further dried under vacuum and the TEM images were obtained without staining.

#### **3.7.7.3. Laser Scanning Confocal Microscopy**

Laser scanning confocal microscopic images of AdAn derivative was obtained from inverted optical microscope (LeicaSP5-DMRX Optical Microscope) equipped with a wide range of objective lenses, the samples were excited under the illumination of UV light ( $\lambda_{ex}$  = 405 nm, continuous laser,  $\geq 10$  mW, pulse width < 100 ps) and the emission was monitored at 425 nm. The AdAn sample (1 mM solutions in  $\text{CHCl}_3$ )

was drop-casted on a freshly cleaned glass slide, and allowed to dry under air. The slide was sealed with a coverslip avoiding air bubbles and kept undisturbed. Further, slides were imaged at 63X magnification in the presence of immersion oil. Owing to the lack of UV excitation in the confocal microscope, the laser scanning confocal microscopic images of the AdNp aggregate in  $\text{CHCl}_3$  could not be acquired.

### 3.7.8. Cyclic Voltammetry (CV)

Electrochemical measurements were performed on a BASi (Bioanalytical Systems, Inc.) C-3 cell stand controlled by Epsilon electrochemical workstation. A three electrode system is then constructed constituting a glassy carbon as the working electrode, a platinum-wire as the counter electrode, and an Ag/AgCl (3 M NaCl) as the reference electrode. The electrochemical measurements of AdNp (1 mM) and AdAn (1 mM) were conducted under nitrogen atmosphere (5 psi, 10 minutes) in a deoxygenated anhydrous dichloromethane solution of tetra-n-butylammonium hexafluorophosphate (supporting electrolyte, 0.1 M) with a scan rate of  $100 \text{ mV s}^{-1}$ . Calibration of the instrument was performed using the ferrocene/ferrocenium ( $\text{Fc}/\text{Fc}^+$ ) redox couple as an external standard and measured under same condition before and after the measurement of samples. The energy level of  $\text{Fc}/\text{Fc}^+$  was assumed to be  $-4.8 \text{ eV}$  with respect to vacuum [177]. The half-wave potential of  $\text{Fc}/\text{Fc}^+$  was estimated to be  $0.5 \text{ V}$  with reference to the Ag/AgCl electrode.

The HOMO and LUMO energy levels were calculated from the following equations 3.2.-3.3.

$$E_{\text{HOMO}} = -(E_{\text{ox}}^{\text{onset}} + 4.8) \text{ eV} \quad (3.2)$$

$$E_{\text{LUMO}} = -(E_{\text{red}}^{\text{onset}} + 4.8) \text{ eV} \quad (3.3)$$

respectively, where  $E_{\text{ox}}^{\text{onset}}$  and  $E_{\text{red}}^{\text{onset}}$  are the onset oxidation and reduction potentials relative to the Ag/AgCl reference electrode.

The electrochemical energy gap ( $E_g$ ) is estimated as follows,

$$E_g = (E_{\text{LUMO}} - E_{\text{HOMO}}) \text{ eV} \quad (3.4)$$

where  $E_{\text{LUMO}}$  and  $E_{\text{HOMO}}$  are the corresponding to HOMO and LUMO energy levels calculated after converting the values in Ag/AgCl convention to SCE convention.

The concentration dependent (0.5 - 2 mM) cyclic voltammetric studies of AdAn in  $\text{CH}_2\text{Cl}_2$  were carried out at a scan rate of 100 mV/s. The broader spread of potentials in Figure 3.13 could result from the temporal modification of the electrode and/or due to slower diffusion of the aggregates compared to monomers [178, 179]. The spectroelectrochemical experiments were performed on a hybrid BASi Epsilon-Ocean Optics UV-Vis-NIR spectroelectrochemical setup using a UV-vis quartz cuvette (10 mm path-length) with a Pt gauze working electrode, a Pt wire counter electrode and an Ag/AgCl reference electrode.

### 3.7.9. Rehm-Weller Analysis

The change in free energy for the electron transfer ( $\Delta G_{et}$ ) was estimated employing the Rehm-Weller relation[31] based on the Born dielectric continuum model. The oxidation potentials of Adenine (donor) and the reduction potential of naphthalene/anthracene (acceptor) are found to be 1.39 and -2.54/-1.92 V respectively against saturated calomel electrode (SCE) [171, 180]. The singlet excited state energies ( $E_{0,0}$ ) of donor (Ad,  $E_{0,0} = 4.6$  eV) and acceptor (Np:  $E_{0,0} = 4.06$  eV; An:  $E_{0,0} = 3.26$  eV) is taken from the literature [181-183].

$$\Delta G_{et} = E_{\text{ox}} - E_{\text{red}} - E_S - \frac{e^2}{r_{DA} \epsilon_s} + \frac{e^2}{2} \left( \frac{1}{r_D} + \frac{1}{r_A} \right) \times \left( \frac{1}{\epsilon_s} + \frac{1}{\epsilon_{sp}} \right) \quad (3.5)$$

where  $E_{\text{ox}}$  and  $E_{\text{red}}$  = oxidation and reduction potential of the donor and acceptor respectively;  $e$  = the charge of an electron;  $r_{DA}$  = distance between the donor and the acceptor;  $r_D$  and  $r_A$  = ionic radii of the cation and anion respectively;  $\epsilon_s$  = static dielectric constant of the non-polar solvent;  $\epsilon_{sp}$  = static dielectric constant of the polar solvent.

At finite distances, the Coulombic attraction energy between the radical ion-pair to a first approximation is given by a point-charge model as  $\left( \frac{e^2}{r_{DA} \epsilon_s} \right)$ . The term  $r_{DA} = 5.19 \text{ \AA}$  is determined for adenine and anthracene by estimating the center-to-

center distance using Mercury 3.5.1. The dielectric constant also influences the solvation free energy of the ions and should be corrected for if we wish to apply these potentials to calculate  $\Delta G_{CS}$  in different solvents. According to the Rehm-Weller relation[31] based on the Born model the solvation free energy of an ion pair is given by equation 3.5, where  $r_D$  and  $r_A$  are effective radii of the cation and the anion radical which were approximated as  $r_{DA}/2$ . The Rehm-Weller relation (eq. 3.5) gives the free energy of charge separation as -0.55 eV ( ${}^1Ad^* \rightarrow Np$ ); -0.17 eV ( $Ad \rightarrow {}^1Np^*$ ); -1.25 eV ( ${}^1Ad^* \rightarrow An$ ) and -0.12 eV ( $Ad \rightarrow {}^1An^*$ ) for the electron transfer from donor to acceptor via direct excitation of donor (Ad) and acceptor (Np/An), respectively. The enhanced free energy of charge separation obtained upon the direct excitation of donor (Ad) is reflected in the nTA spectra ( $\lambda_{ex} = 266$  nm) as improved signatures corresponding to the RIP intermediates.

### 3.7.10. Computational methods

#### 3.7.10.1. Gaussian calculations

Ground-state optimized structure and harmonic oscillator frequencies of Ad, An and AdAn were computed using density functional theory (DFT) at the Becke's three parameter functional in combination with the Lee-Yang-Parr correlation functional (B3LYP) and 6-311G+(d,p) basis set. The vertical excitation energies and oscillator strengths were calculated employing time dependent DFT (TDDFT) calculations at PCM/M06-2X/6-311G+(d,p) level of theory following the procedure reported by Markovitsi, Improta and co-workers [164]. The optimization of the geometries of radical ions of adenine ( $Ad^+$ ) and anthracene ( $An^-$ ) were carried out using M06-2X/6-311+G(d,p) level of theory. The optimized geometries of the radical ions were further used for the time dependent DFT (TD-DFT) calculations at PCM/M06-2X/6-311G+(d,p) level of theory. The computed vertical excitation energies of the most intense transition are blue-shifted by -0.55 (Ad), -0.055 (An), -0.21 (AdAn), -0.55 ( $Ad^+$ ) and -0.21 ( $An^-$ ) eV with respect to the experimental absorption maxima. This discrepancy can be further minimized by increasing the basis set and/or including

the vibrational effects [184]. Each spectrum was plotted by convoluting each transition using a Gaussian with a width of 0.4 eV (half width at half maxima). All the computations were performed using the *Gaussian 09* suite [134].

#### **3.7.10.2. Quantum theory of atoms in molecules (QTAIM)[103, 124]**

Similar to that discussed in section 2.6.6.2. (Chapter 2).

#### **3.7.10.3. Hirshfeld Analysis[125]**

Similar to that discussed in section 2.6.6.3. (Chapter 2).

#### **3.7.10.4. Material Science Suite:**

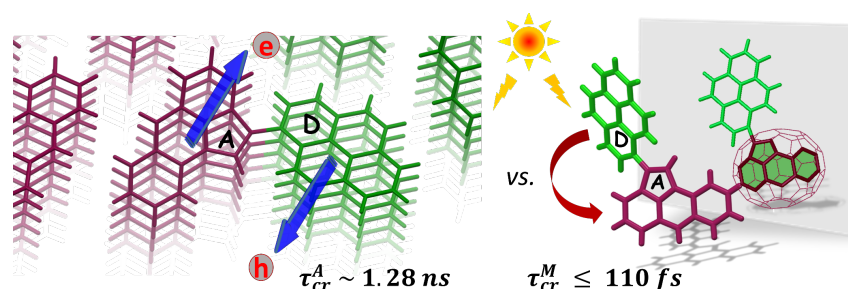
Materials Science Suite 2015-1 provides diverse set of tools for predicting and computing reactivity and properties of chemical systems. The core simulation engine, Jaguar[185] is a high performance abinitio quantum mechanical package commercially produced and maintained by Schrodinger Inc. Employing pseudospectral approach, Jaguar estimates the Coulomb and exchange terms, providing significant advantages of exact exchange terms. Geometry optimization and single point energy calculations for monomer, dimer, tetramer and octamer were performed at B3LYP-D3/6-31G+(d,p) level of theory using the crystal structure as the input for the frontier molecular orbital (FMO) analyses. Energy gap is determined as the difference between energies of LUMO and HOMO as described in equation 3. Energy level diagram is plotted using the energies obtained from FMO analyses.

## Chapter 4

# Prolonged Charge Separated States in Twisted Stacks of All-Carbon Donor and Acceptor Chromophores

### Abstract

Long-range photoinduced electron transfer is ubiquitous in nature and plays a crucial role in light harvesting in green plants and respiration in animals. Simulating natural photosynthesis in laboratory necessitates a precise control over the dynamics of the photogenerated excitons in artificial donor-acceptor motifs. Herein, we report the exploration of photoinduced electron transfer in a series of donor-bridge-acceptor ( $D-B_n-A$ ,  $n = 0, 1, 2$ ) motifs, wherein pyrene (electron donor) and aceanthrylene (electron acceptor) are separated via 0, 1 and 2 phenyl bridges. Aceanthrylene, a functional analog of  $C_{70}$ , acts as a versatile electron acceptor owing to its high electron affinity and visible light absorption. Preliminary spectroscopic investigation suggests a shallow distance dependent ( $\beta = 0.11 \text{ \AA}^{-1}$ ) fluorescence quenching in  $P_nA$  ( $n = 0, 1, 2$ ) dyads. Interestingly, the all-carbon pyren-1-ylaceanthrylene ( $P_0A$ ) dyad forms a self-assembled donor-on-donor and acceptor-on-acceptor bicontinuous assembly which results in extended survival time of the photoinduced radical ion-pair intermediates. Antithetical trajectories of the excitons in the nonparallel  $\pi$ -ways renders persistent radical ion-pair intermediates in aggregated ( $\tau_{cr}^A \sim 1.28 \text{ ns}$ ) vs. monomeric ( $\tau_{cr}^M \leq 110 \text{ fs}$ )  $P_0A$  as observed using femtosecond transient absorption spectroscopy. Marcus theory of charge transfer rates predicts an ambipolar charge transport characteristic in crystalline  $P_0A$ , thereby endorsing  $P_0A$  as an all-carbon D-A hybrid for nonfullerene photovoltaic applications.



## 4.1. Introduction

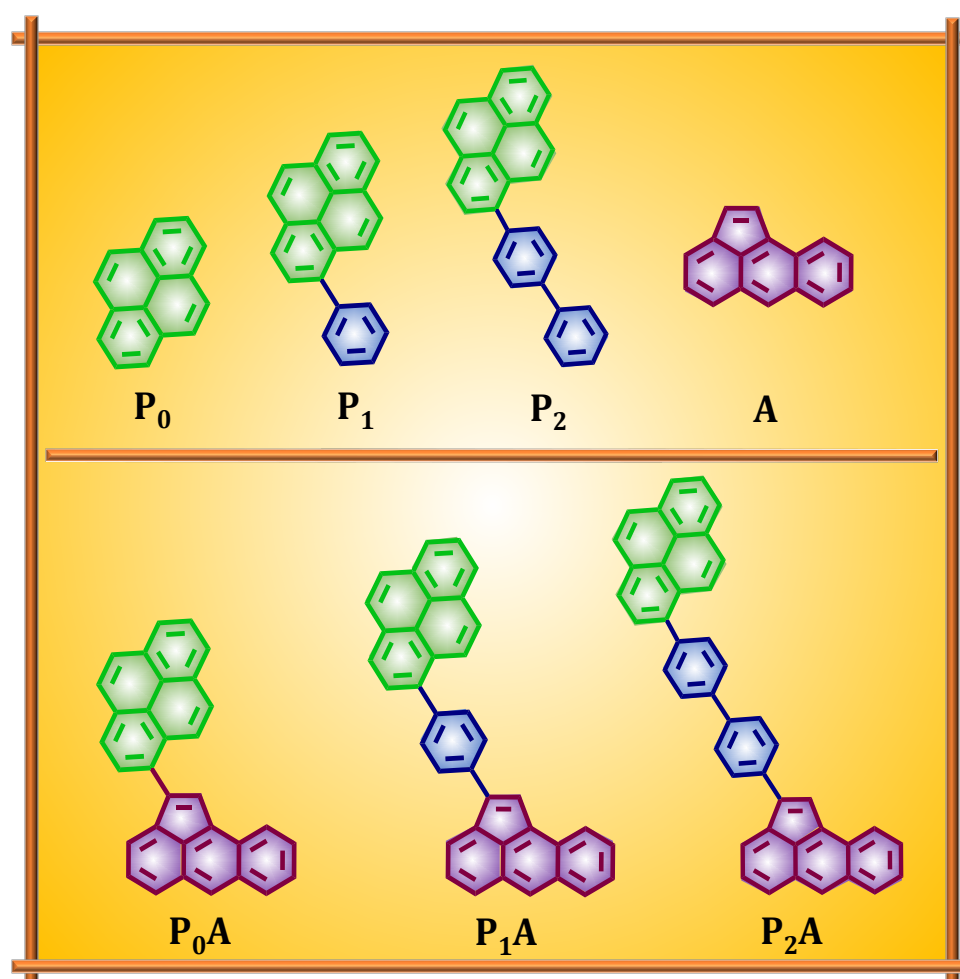
Nanoallotropic forms of carbon such as fullerenes ( $C_{60}$ ,  $C_{70}$ , etc.), carbon nanotubes (CNT), graphenes (G) and carbon nanodots (CND) hold promising optical and photovoltaic properties [186-190]. By virtue of degenerate low-lying excited states, fullerenes act as an ideal electron sink to mimic the charge separation in natural photosynthesis [139, 190, 191]. Fullerene-based all-carbon donor-acceptor (D-A) hybrids, for e.g. CNT- $C_{60}$  [192], G- $C_{60}$  [85], carbon nanohorn- $C_{60}$  [193], G-CNT- $C_{60}$  [194], etc. exhibit emergent behavior to convert light into electrical energy [188, 189]. Hierarchical interpenetrating  $C_{60}$  domains with controlled molecular-scale morphology can endorse superior performance in organic photovoltaics (OPVs) [195]. Nevertheless, photodimerization of fullerenes in stacked assemblies can lead to performance losses in OPVs [196]. Further enhancement in efficiency of fullerene-based materials can be achieved by improving (i) solubility [197], (ii) range/extinction coefficient of visible light absorption [197, 198], (iii) chemical stability [196], and (iv) the economy of synthesis [196]. Alternatively, planar analogs of fullerenes possessing similar electronic and structural features could emerge as novel photofunctional materials [199-201]. Garcia-Garibay and co-workers reported a simple and elegant synthesis of planar aceanthrylene (A) and cyclopenta[hi]aceanthrylene (CPA) that possess fullerene-like redox characteristics [199, 200]. Inclusion of planar fullerene

analog in D-A constructs could offer precise control over the hierarchical structure and exciton trajectories in molecular wire/junction [202]. Understanding the photoexcited processes of D-A hybrids comprising cyclopenta-fused polycyclic aromatic hydrocarbons (CP-PAHs) and electronically complementary polyarenes could offer new insights to develop non-fullerene D-A systems for device application [203, 204].

Moderating the charge transfer (CT) and separation (CS) efficiencies of D-A ensemble demands subtle balance between the forward and back (geminate) electron transfer dynamics [205-208]. The forward electron transfer characteristics ( $k_{cs}$ ) of a D-A hybrid can be partially regulated via modulating (i) electronic coupling ( $V_{D-A}$ ); (ii) the distance between the D and A components and/or (iii) electron donor/acceptor units [205, 207, 209-218]. Photogenerated excitons at D-A interface can instantaneously annihilate due to the Coulomb interactions. Further improvement in CS efficiency demand attention towards delaying the geminate recombination [213, 219]. Bio-inspired self-assembly approach of constructing organized covalently linked D-A systems has resulted in improving the CS efficiency [2, 63, 65]. Seminal supramolecular strategies demonstrated by several groups have proved fruitful in decelerating the instantaneous recombination of radical ion-pair intermediates [32, 64, 66, 72, 73, 77, 85, 207, 220]. Thus, the concept of 'emergence upon assembly'[64] promote the design of innovative D-A

architectures for solar light harvesting.

Our concomitant efforts in developing emergent nonplanar[63, 139, 221] and orbitally decoupled near-orthogonal[120, 122, 130, 154] bichromophoric assembly prompted us to explore the twisted all-carbon D-A dyads ( $P_{0-2}A$ ) based on aceanthrylene as a nonfullerene electron acceptor (Scheme 4.1). The chromophore A with significant electron affinity[222] ( $\sim 2.70$  eV, see Appendix for details), visible light absorption (upto 610 nm) and structural resemblance to fullerene fragment, formulate an excellent all-carbon electron acceptor. The



**Scheme 4.1.** Molecular structures of the all-carbon D-A dyads (bottom) and the model D and A components (top) under discussion.

steric block, amidst the donor and acceptor units coupled via 0, 1 and 2 phenyl bridges offer a twisted geometry among the planes of the D and A chromophores in P<sub>0</sub>A ( $\theta = 49.0^\circ$ ); P<sub>1</sub>A ( $\theta = 19.3^\circ$ ) and P<sub>2</sub>A ( $\theta = 62.4^\circ$ ) dyads. Preliminary spectroscopic studies on the D-B-A dyads (P<sub>0-2</sub>A) reveal a shallow distance dependent fluorescence quenching with a  $\beta$  value of  $0.11 \text{ \AA}^{-1}$ . Interestingly, the twisted D-B-A dyad with no phenyl spacer (P<sub>0</sub>A) self assembles to form segregated donor-on-donor (D-D) and acceptor-on- acceptor (A-A) bicontinuous stacks which can craft 'π-channels' for the transport of photodissociated charge carriers [146]. The photoexcitation of aggregated P<sub>0</sub>A in tetrahydrofuran (THF) reveals the presence of persistent ( $\tau_{cr}^A \sim 1.28 \text{ ns}$ ) radical ion-pair intermediates via femtosecond transient absorption (fTA) spectroscopy. Additionally, the state-of-the-art computational method based on Marcus theory of charge transfer rates estimate P<sub>0</sub>A as an ambipolar dyad with  $\mu_h = 0.20\text{-}0.24$  and  $\mu_e = 0.16\text{-}0.17 \text{ cm}^2 \text{ V}^{-1} \text{ s}^{-1}$  respectively.

## 4.2. Results and Discussion

### 4.2.1. Synthesis and Structure of All-Carbon Donor-bridge-Acceptor Dyads

The schematic depiction and the complete syntheses details of the donor-bridge-acceptor (D-B-A) motifs and the model compounds based on pyrene (electron donor) and aceanthrylene (electron acceptor) are provided in the experimental section (Scheme 4.1., section 4.4.). Copper free palladium catalyzed Sonogashira type cross-coupling between 9-bromoanthracene and trimethylsilylacetylene (TMS-acetylene) followed by tandem cyclization

provided the aceanthrylen-2-yltrimethylsilane intermediate (A-TMS) in a single-step reaction (see section 4.4.) [199, 200]. Subsequent, nucleophilic substitution of the trimethylsilane by bromine was carried out via reacting with N-bromosuccinimide (NBS) in THF to provide 2-bromoaceanthrylene (A-Br) [201, 223]. Palladium-catalyzed Suzuki-Miyaura cross-coupling of A-Br with pyrene-1-boronic acid afforded the all-carbon D-A dyad P<sub>0</sub>A. The model derivatives (P<sub>1</sub> and P<sub>2</sub>), the cross-coupling partners (P<sub>1</sub>-Br and P<sub>2</sub>-Br) and the D-B-A (P<sub>1</sub>A and P<sub>2</sub>A) motifs were synthesized via Suzuki-Miyaura cross-coupling reactions under inert atmosphere (see section 4.4.).

Slow evaporation (Table 4.1.) of a solution of A-Br (in ethanol), P<sub>0</sub>A (in ethyl acetate/*n*-hexane [1:1] mixture) and P<sub>1</sub>A (in chloroform/toluene [1:1] mixture) offered good quality crystals for X-ray diffraction measurements (Figure A4.1.). The derivative A-Br provided dark brown needles in orthorhombic, *P*2<sub>1</sub>2<sub>1</sub>2<sub>1</sub> (enantiomorphic) space group with 4 molecules per unit cell. The D-B-A dyads, P<sub>0</sub>A and P<sub>1</sub>A afforded brownish black crystals in monoclinic, *P*2<sub>1</sub>/*c* (centrosymmetric) and *Cc* (polar) space groups with 4 and 8 molecules per unit cell, respectively (Table 4.1.). Though, the D-B-A derivative P<sub>2</sub>A provided plate type crystals, the X-ray structure was not obtained owing to the bad quality of the crystal.

The molecular structure of dyad P<sub>0</sub>A displays a twisted ( $\theta = 49^\circ$ ) geometry with a C-C bond length of 1.48 Å, depicting a single bond with 4.6 kJmol<sup>-1</sup>

**Table 4.1.** Crystallographic data and refinement parameters for crystalline A-Br, P<sub>0</sub>A and P<sub>1</sub>A.

Parameters	A-Br	P <sub>0</sub> A	P <sub>1</sub> A
Formula	C <sub>16</sub> H <sub>9</sub> Br	C <sub>32</sub> H <sub>18</sub>	C <sub>38</sub> H <sub>22</sub>
Formula wt.	281.14	402.46	478.55
Colour, shape	Brown, block	Brown, block	Brown, plate
Dimens, mm <sup>3</sup>	0.25 x 0.20 x 0.15	0.20 x 0.15 x 0.10	0.20 x 0.20 x 0.05
Crystal system	Orthorhombic	Monoclinic	Monoclinic
Space group, Z	<i>P</i> 2 <sub>1</sub> 2 <sub>1</sub> 2 <sub>1</sub> ; 4	<i>P</i> 2 <sub>1</sub> / <i>c</i> ; 4	<i>Cc</i> ; 8
<i>a</i> , Å	4.266(5)	30.4984(11)	10.9021(7)
<i>b</i> , Å	13.533(5)	3.9613(2)	10.8631(8)
<i>c</i> , Å	19.669(5)	16.2415(6)	40.445(3)
$\alpha$ , deg	90.00(5)	90	90°
$\beta$ , deg	90.00(5)	92.412(3)	95.141(4)
$\gamma$ , deg	90.00(5)	90	90°
<i>V</i> , Å <sup>3</sup>	1135.5(14)	1960.45(14)	4770.6(6)
Temp, K	296 (2)	296 (2)	296(2)
<i>d</i> <sub>calcd</sub> , gcm <sup>-3</sup>	1.644	1.365	1.333
No. of reflections collected	5132	26291	35137
No. of unique reflections	1952	3826	9294
2 $\theta$ <sub>max</sub> , degree	50	52	46.7
No. of parameters	154	289	686
<i>R</i> <sub>1</sub> ; <i>wR</i> <sub>2</sub> ( <i>I</i> > 2 $\sigma$ ( <i>I</i> ))	0.0379; 0.0744	0.0489; 0.1106	0.0929, 0.2357
<i>R</i> <sub>1</sub> ; <i>wR</i> <sub>2</sub> (all data)	0.0591; 0.0851	0.1065; 0.1373	0.1489; 0.2612
Goodness of fit	1.116	1.011	1.076
CCDC number	1503155	1503156	not published

rotational barrier (Figures 4.1. and A4.2.). The molecular structures of crystalline P<sub>1</sub>A and geometry optimized (B3LYP/6-311g+(d,p)) P<sub>2</sub>A, wherein the D and A components are separated via one and two phenyl spacers, also

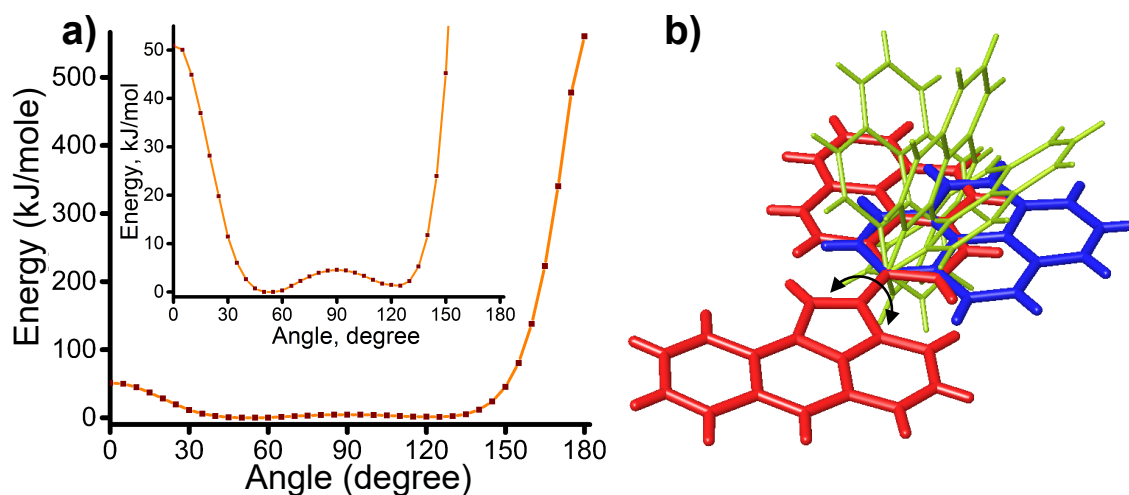


**Figure 4.1.** a) Potential energy surfaces for the change in the torsional angle along C1-C2-C17-C18 (inset shows the expanded view for the potential energy surface) and b) pictorial representation of the torsion angle variation (0 to 180°) along C1-C2-C17-C18 in the dyad P<sub>0</sub>A.

reveal a twisted geometry ( $\theta = 19.3^\circ$ [P<sub>1</sub>A] and  $62.4^\circ$ [P<sub>2</sub>A]) among the pyrene and aceanthrylene planes (Figure A4.2.). Furthermore to get in-depth insights into the weak intermolecular interactions present in the crystalline assembly, close-packing analyses of crystalline A-Br, P<sub>0</sub>A and P<sub>1</sub>A were carried out. A comprehensive inspection of crystal packing in A-Br, reveal that the slip-stack motif progressing mutually in a skewed fashion to emerge as a two-dimensional (2D) network (Figure 4.2.). The intermolecular  $\pi$ - $\pi$  interactions at a distance of 3.47-3.50 Å leads to a slipped columnar arrangement along a-axis (Figure 4.2.).

Quantum theory of atoms in molecules (QTAIM, Figure 4.3.)[124] reveals a C...Br interaction ( $d_{C\dots Br} = 3.53$  Å) between stacks which direct the skew columns along the c-axis (Figures 4.3., Table 4.2.). Hirshfeld surface analyses

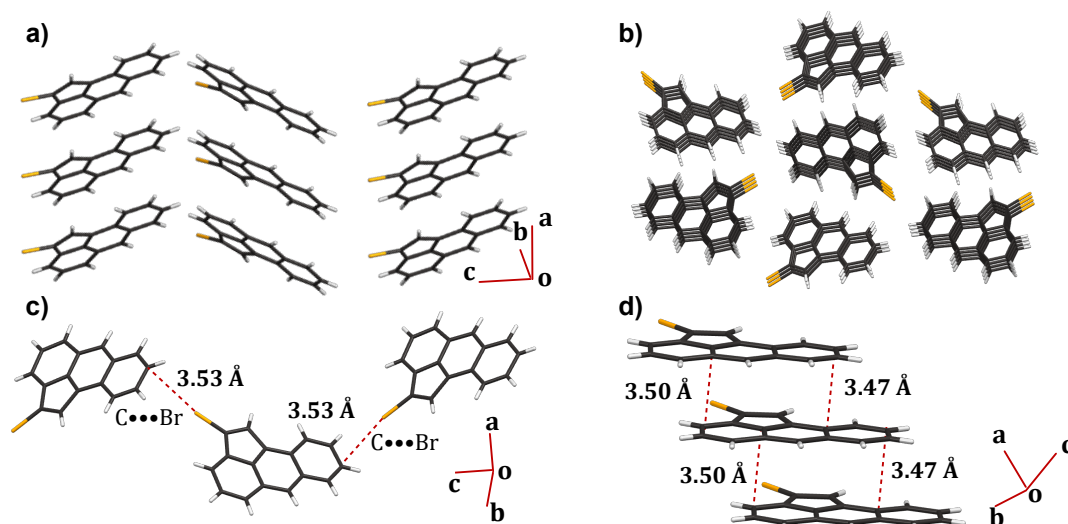


**Figure 4.2.** a) Packing motif; b) packing view along *a*-axis; c) the C•••Br interaction propagating along *c*-axis and d) the  $\pi$ - $\pi$  interaction propagating along *a*-axis in the derivative A-Br.

[125, 143] of A-Br demonstrates a marginally dominant C-H••• $\pi$  vs.  $\pi$ - $\pi$  interaction which establishes a  $\gamma$ -motif ( $\rho[126] = 1.47$ ) arrangement with four molecules in the

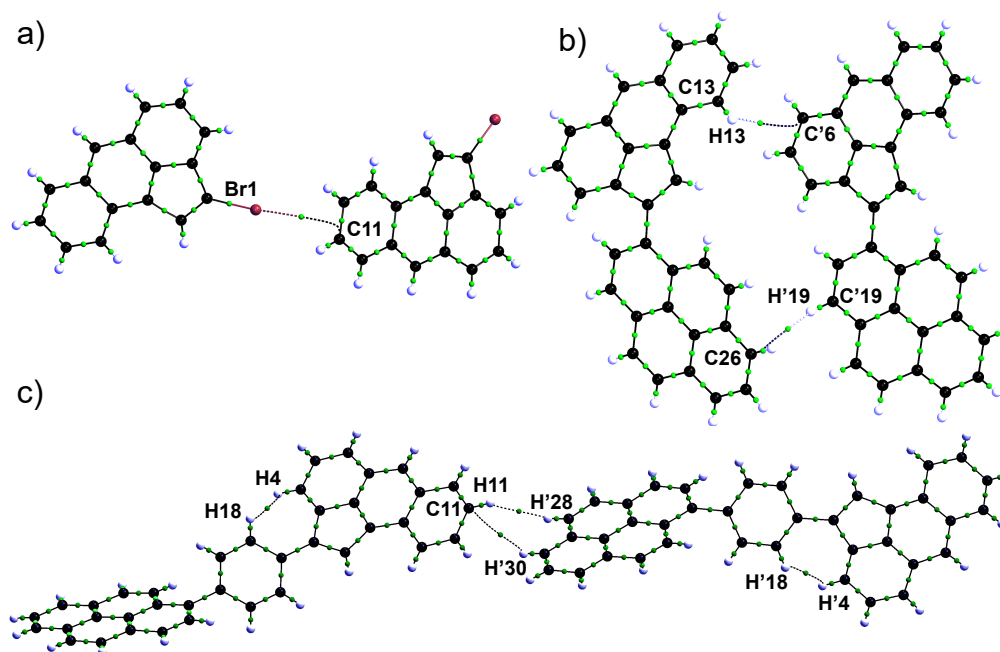


**Figure 4.3.** QTAIM electron density map depicting intermolecular a) C•••Br interaction in crystalline A-Br; b) C-H••• $\pi$  interaction in crystalline P<sub>0</sub>A and c) C-H•••H-C and C-H•••C interactions in P<sub>1</sub>A.

**Table 4.2.** Calculated topological properties of the electron density for the intermolecular interaction in crystalline A-Br and P<sub>0</sub>A.

Description	Interaction	<sup>a</sup> <i>d</i> (Å)	<sup>b</sup> $\rho_b(r)$ (eÅ <sup>-3</sup> )	<sup>c</sup> $\nabla^2\rho_b(r)$ (eÅ <sup>-5</sup> )	<sup>d</sup> DE (kJmol <sup>-1</sup> )
A-Br	C11•••Br1	3.535	0.03553	0.43609	3.18
P <sub>0</sub> A	C'6•••H13	2.991*	0.03055	0.30198	2.64
	C26•••H'19	2.890	0.03190	0.34613	2.95
P <sub>1</sub> A	H11•••H'28	2.380	0.01608	0.16765	1.37
	C11•••H'30	3.270	0.02996	0.31637	2.98
	H4•••H18	2.180	0.05349	0.73369	5.82
	H'4•••H'18	2.180	0.05350	0.73371	5.82

<sup>a</sup>*d* = distance, <sup>b</sup> $\rho_b(r)$  = electron density at the BCP and <sup>c</sup> $\nabla^2\rho_b(r)$  = Laplacian of the electron density at the BCP, <sup>d</sup>DE = dissociation energy. \*Though C•••H distance is > 2.9 Å, QTAIM exhibited electron density at (3, -1) BCP.

unit cell (Figure 4.4., Table 4.3.). Molecular packing of P<sub>0</sub>A exhibits a one-dimensional (1D) columnar stacks of the dyad, progressing in a segregated D-D (50% overlap) and A-A (45% overlap) bicontinuous manner with an average  $\pi$ - $\pi$  distance of 3.54-3.59 Å along b-axis (Figures 4.5.). A C-H••• $\pi$  ( $d_{C-H\cdots\pi}$  = 2.87-2.89 Å) interaction between stacks drive the propagation of assembly

**Table 4.3.** Percentage intermolecular interactions in crystalline A-Br, P<sub>0</sub>A and P<sub>1</sub>A.

Interaction	%C•••H	%C•••C	%H•••H	%C•••Br	%H•••Br	%Br•••Br	q
A-Br	22.9	15.6	40	1.5	19.2	0.7	1.47
P <sub>0</sub> A	18.8	23.2	58.0	-	-	-	0.81
P <sub>1</sub> A	51.0	6.0	43.0	-	-	-	8.5

Total percentage of intermolecular contacts ca. 99.9% (A-Br); 100% (P<sub>0</sub>A) and 100% (P<sub>1</sub>A).  $q = [(\%C\cdots H)/(\%C\cdots C)]$ . Herringbone ( $q > 4.5$ ), sandwich herringbone ( $3.2 < q < 4.0$ ),  $\gamma$  ( $1.2 < q < 2.7$ ) and  $\beta$  ( $0.46 < q < 1.0$ )

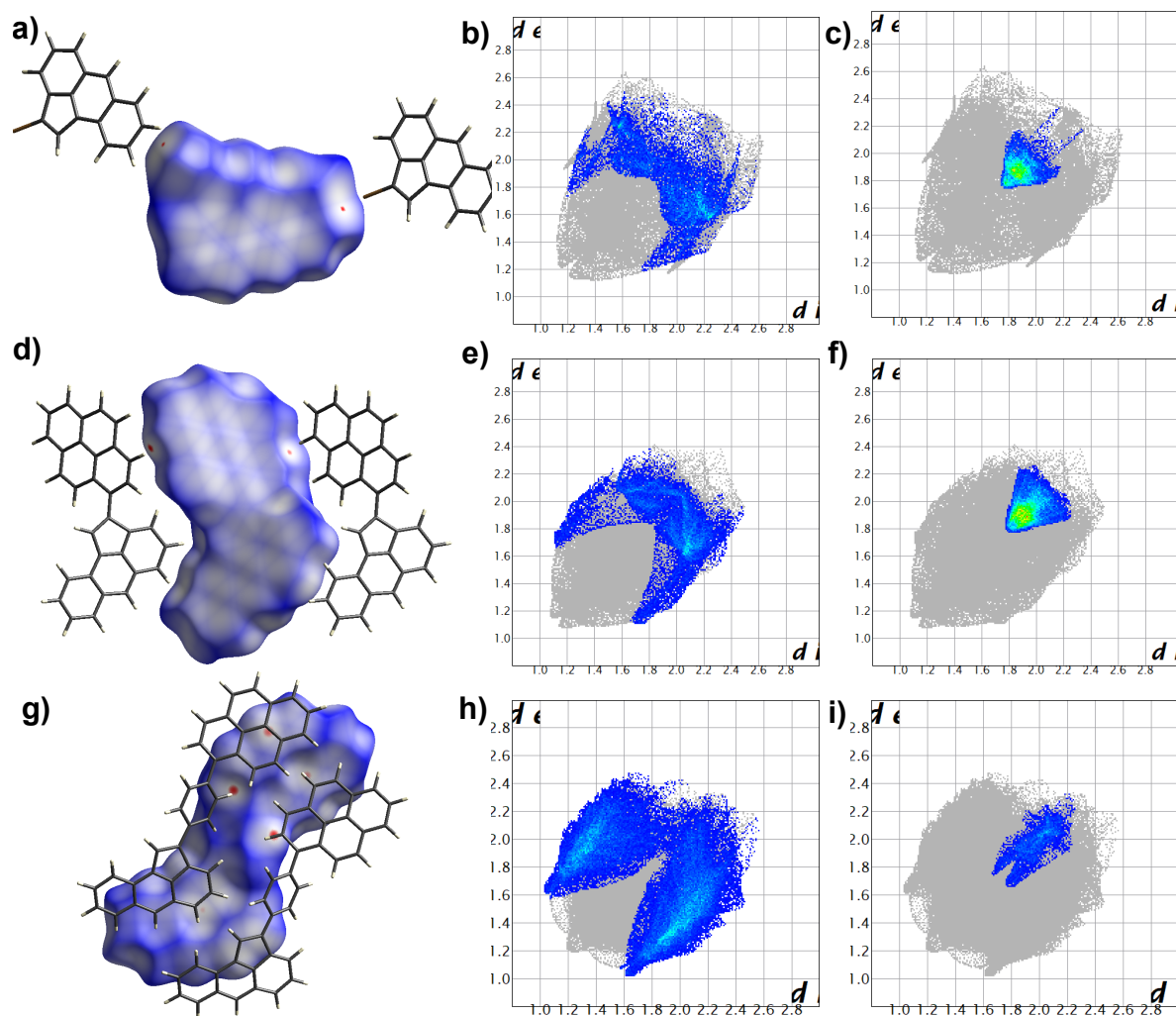


**Figure 4.4.** Hirshfeld surface mapped with  $d_{norm}$  (a, d,g); 2D fingerprint plots with the region corresponding to C-H... $\pi$  (b, e, h) and  $\pi$ - $\pi$  (c, f, i) interaction in A-Br, P<sub>0</sub>A and P<sub>1</sub>A, respectively.

along c-axis, leading to a 2D  $\beta$ -motif ( $\rho = 0.81$ ) arrangement (Figures 4.3b, 4.4 d-f, 4.5e)

Concurrently, the close-packing in P<sub>1</sub>A reveal a herringbone packing ( $\rho = 8.5$ ), wherein the P<sub>1</sub>A moieties are still arranged in a D-D and A-A fashion, albeit at a particular edge-to-face tilt angle (Figures 4.4g-i and 4.6., Table 4.3.). The C-H... $\pi$  and  $\pi$ - $\pi$  ( $d_{C-H... \pi} = 2.81$ - $2.89$  Å and  $d_{C...C} = 3.33$  Å) interactions

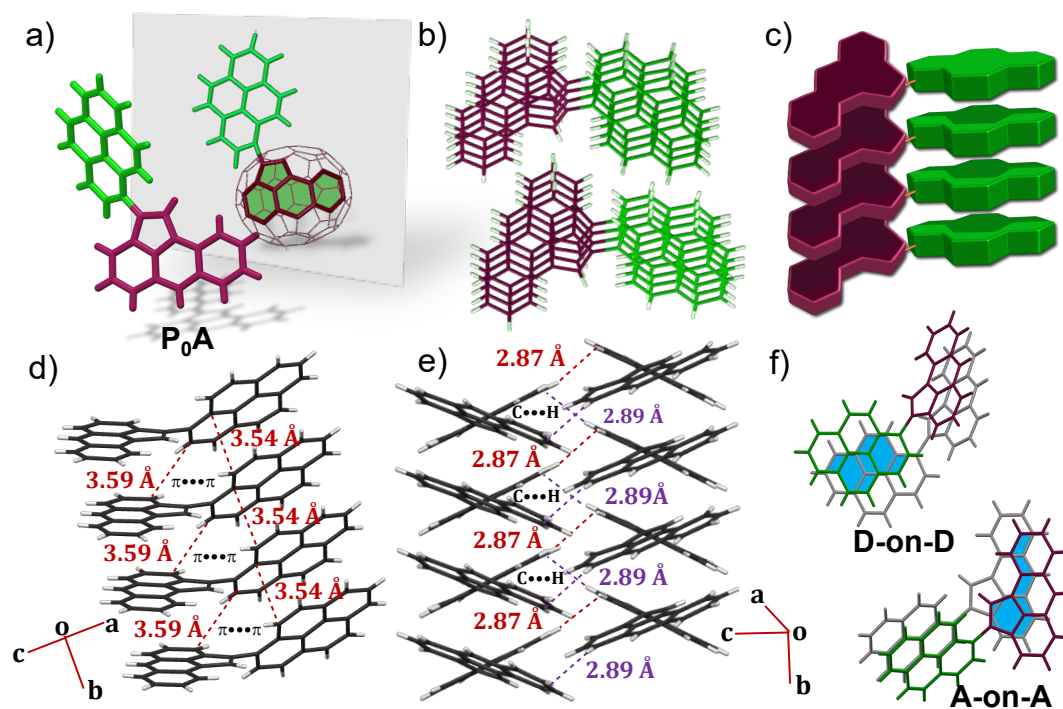


**Figure 4.5.** a) Schematic depiction of resemblance among crystalline P<sub>0</sub>A and P<sub>0</sub>C<sub>60</sub> (proposed structure) dyads; b, c) bicontinuous D-D and A-A packing motif in P<sub>0</sub>A; d) packing motif depicting the  $\pi$ - $\pi$  stacking; e) the intermolecular C-H... $\pi$  interaction propagating along c-axis and f) the stacking mediated D-D (50%) and A-A (45%) overlap in P<sub>0</sub>A.

play a crucial role in defining the criss-cross tilted columnar stacks, whereas inter-stack C-H...H-C interactions render the propagation of the stacks in a 2D array (Figure 4.3c).

#### 4.2.2. Steady-State Photophysical Studies

To evaluate the preliminary photophysical properties, steady-state UV-vis absorption, emission and time-resolved fluorescence lifetime spectra of the model derivatives (P<sub>0-2</sub>, A-Br) and D-B-A (P<sub>0-2</sub>A) motifs were recorded in toluene at ambient temperatures (Figure 4.7.). The UV-vis spectrum of A-Br characterizes vibrational bands at 367, 389, 410, and 432 nm, followed by a

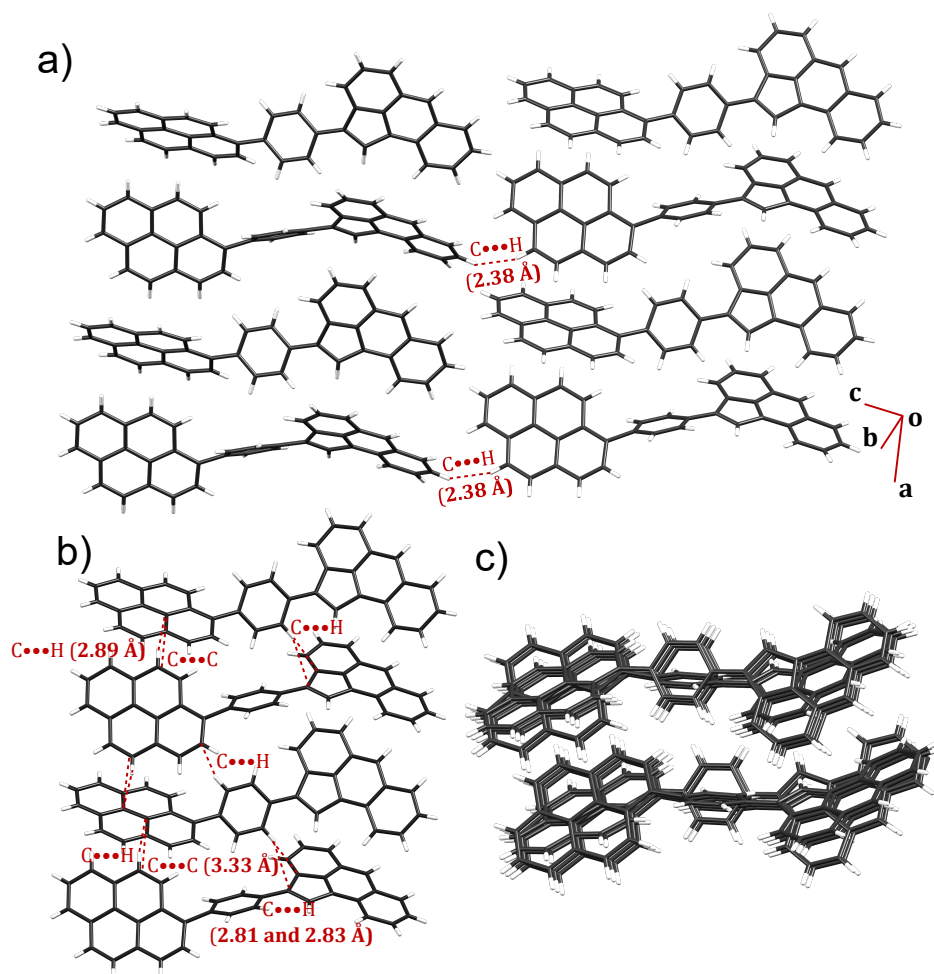


**Figure 4.6.** a) Packing motif; b) tilted D-D and A-A stacks and c) packing view (top view) along bc-plane in  $P_1A$  crystalline motif.

diffuse broad band that extends between 450-650 nm (Figure 4.7a, Table 4.4.). The low energy band (450-650 nm,  $f = 0.0532$ ) is attributed to the  $\pi-\pi^*$  (HOMO $\rightarrow$ LUMO) transition and is responsible for the prominent reddish-orange color of solution (Table A4.1.) [224]. The HOMO-1 $\rightarrow$ LUMO (410 nm,  $f = 0.0569$ ) and HOMO-2 $\rightarrow$ LUMO (367 nm,  $f = 0.0956$ ) transitions further lead to a vibronically resolved absorption in A-Br. The D-B-A dyad with no phenyl spacer,  $P_0A$ , exhibits an absorption resembling a linear combination of  $P_0$  and A-Br spectra in 300-400 nm region and has a marginally red-shifted broad

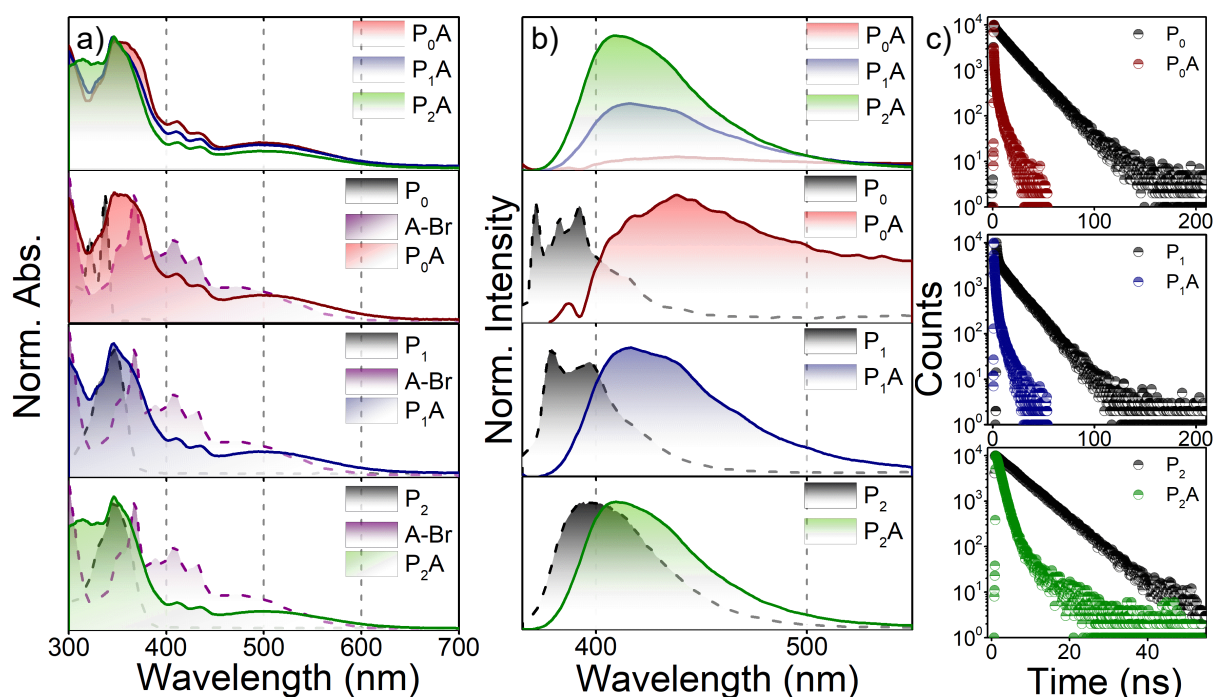


**Figure 4.7.** a) UV-vis absorbance; fluorescence b) emission and c) lifetime of model derivatives ( $A-Br$ ,  $P_{0-2}$ ) and  $D-B-A$  ( $P_{0-2}A$ ) motifs in toluene.

absorption in 450-700 nm region when compared to  $A-Br$  (Figure 4.7a). Analogous to  $P_0A$ , the UV-vis absorbance of the  $D-B-A$  derivatives  $P_{1-2}A$  also exhibit a linear combination of the model derivatives ( $P_{1-2}$  and  $A-Br$ ), albeit with a concomitant population of the higher excited state with the increasing number of phenyl substituents (Figure 4.7a, Table A4.1.).

Interestingly, the fluorescence emission of the  $D-B-A$  derivatives  $P_{0-2}$  reveal a systematic quenching of the fluorescence emission intensity with a concomitant decrease in the distance among the  $D$  and  $A$  components (Figure 4.7b, Table 4.4.). The quenching of the fluorescence with the decreasing distance among the  $D$  and  $A$  components suggests a distance dependent electron transfer phenomenon typically observed in  $D-B-A$  motifs.

**Table 4.4.** Photophysical properties of all-carbon  $P_{0-2}A$  dyads and the model derivatives (A-Br,  $P_{0-2}$ ) in toluene.

	$\lambda_{abs}(nm)$	$^a\lambda_f (nm)$	$\phi_f$ (%)	$^b\tau_f$ (ns) [Rel. Amp.]	$\tau_f^{avg}$ (ns)	$^ck_{CS}$ ( $s^{-1}$ ) $\times 10^9$	$^d\phi_{CS}$ (%)	$^eR_{D-A}$ (Å)
A-Br	367, 389, 410, 432 and 488 (br)	<i>nf</i>	<i>nf</i>	<i>nf</i>	-	-	-	-
$P_0$	308, 322 and 337 (i)	371, and 391	32.0 <sup>f</sup>	1.86 [2.7] 17.51 [97.3]	17.46	-	-	-
$P_1$	347 (i), 331, and 315	379 (i), and 398	11.5	1.20 [20] 15.77 [80]	15.50	-	-	-
$P_2$	346 (i), 329, and 315	398	51.5	5.98 [100]	5.98	-	-	-
$P_{0A}$	349 (i), 411, 436, and 506 (br)	387 (d), and 439 (i)	0.20	0.87 [35.65] 4.36 [64.35]	4.00	17.1	98.3	4.11
$P_{1A}$	346 (i), 413, 437, and 510 (br)	415 (i), 439 and 471	0.37	1.05 [62.8] 4.84 [37.2]	3.82	9.23	98.2	9.81
$P_{2A}$	347 (i), 413, 437, and 512 (br)	409 (i), 432 and 465	0.73	1.13 [88.2] 3.65 [11.8]	1.89	4.65	96.2	15.47

*abs* = absorption; *f* = fluorescence;  $^a\lambda_{ex}$  = 337 ( $P_0$ ) and 350 ( $P_{1-2}$  and  $P_{0-2}A$ ) nm;  $^b\lambda_{ex}$  = 340 (pulsewidth  $\leq 1$  ns,  $P_0$ ) and 377 (pulsewidth  $\leq 100$  ps,  $P_{1-2}$  and  $P_{0-2}A$ ) nm;  $^ck_{CS} = [(\phi_{ref}/\phi_f) - 1]1/\tau_{ref}$ ;  $^d\phi_{CS} = k_{CS}/[(1/\tau_{ref}) + k_{CS}]$ ;  $^e$ shortest centre-to-centre through-bond distance between D and A units;  $^f$  Taken from Ref. [175]; *nf* = nonfluorescent; *i* = intense; *br* = broad; *d* = diffuse

Concurrently, the picosecond time-resolved fluorescence lifetime of D-B-A motifs ( $P_{0-2}A$ ) reveal a faster depopulation of the singlet excited state as compared to the model derivatives  $P_{0-2}$  (Figure 4.7c). Estimation of the rates and quantum yields of the charge separation ( $k_{CS}$ ) employing the quantum yields ( $\phi_f$ ) and lifetimes ( $\tau_f$ ) of the model derivative ( $P_0$ ) and D-B-A ( $P_{0-2}A$ ) motifs further emphasize the distance dependent charge separation in  $P_{0-2}A$ .

$$k_{CS} = [(\phi_{ref}/\phi_f) - 1]1/\tau_{ref} \quad (4.1)$$

$$\phi_{CS} = k_{CS}/[(1/\tau_{ref}) + k_{CS}] \quad (4.2)$$

$$k_{CS} \propto e^{-\beta R_{D-A}} \quad (4.3)$$

A logarithmic plot of  $k_{CS}$  versus distance ( $R_{D-A}$ ) between the D and A components yields a straight line with a  $\beta$  value of  $0.11 \text{ \AA}^{-1}$  (Figure 4.8). A  $\beta$  value of  $0.11 \text{ \AA}^{-1}$  suggest a shallow distance dependence of the electron transfer between pyrene and acanthrylene moieties separated via 0, 1 and 2 phenyl bridges. Moreover, it also pronounces the effective electron accepting tendency of the acanthrylene core.

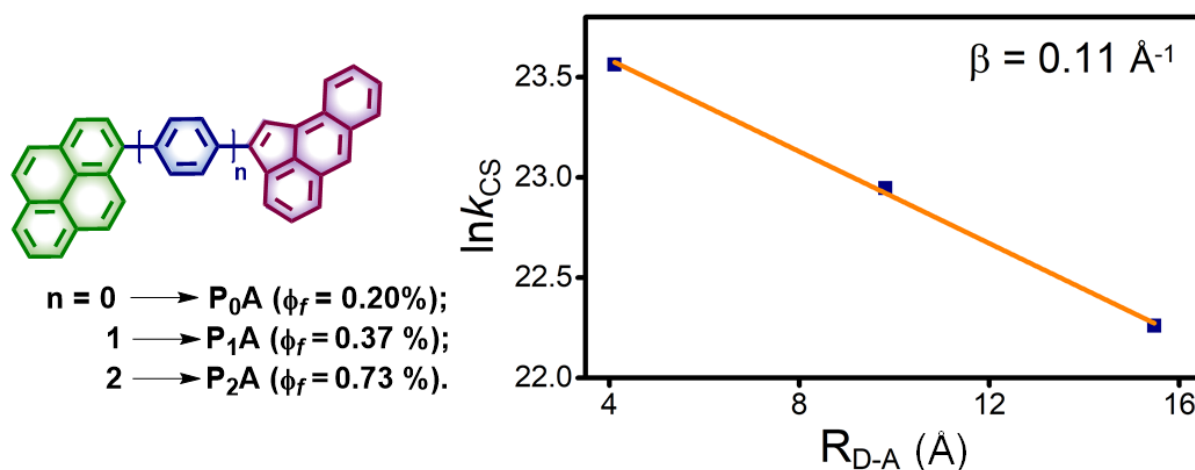


**Figure 4.8.** Exponential distance dependence of  $\ln(k_{CS})$  versus  $R_{D-A}$  for D-B-A ( $P_0$ - $2A$ ) motifs in toluene.

### 4.2.3. Concentration Dependence and Aggregation Studies

Intrigued by the unique D-on-D and A-on-A assembly in crystalline P<sub>0</sub>A, we decided to explore the effect of assembly on the survival time of the charge radical ion-pair intermediates. To probe the aggregation in P<sub>0</sub>A, concentration dependent UV-vis absorption were recorded in tetrahydrofuran (THF). The

steady-state concentration dependent UV-vis absorption studies of P<sub>0</sub>A demonstrate a deviation from linearity above 60  $\mu\text{M}$  dyad concentration in tetrahydrofuran and nonpolar organic solvents (Figure 4.9a and A4.3). Nonlinear increase in UV-vis absorbance as a function of dyad concentration signifies the ability of dyad P<sub>0</sub>A to aggregate in solvents of wide-ranging polarity beyond a critical concentration. Existence and the nature of P<sub>0</sub>A aggregate were further probed using scanning electron (SEM), tunnelling electron (TEM) and atomic force (AFM) microscopic analyses (Figures 4.9c-e). Morphological analyses of P<sub>0</sub>A (0.6 mM) in THF indicates a globular nanoassembly with a size ranging from 150 to 750 nm (Figure 4.10.). The

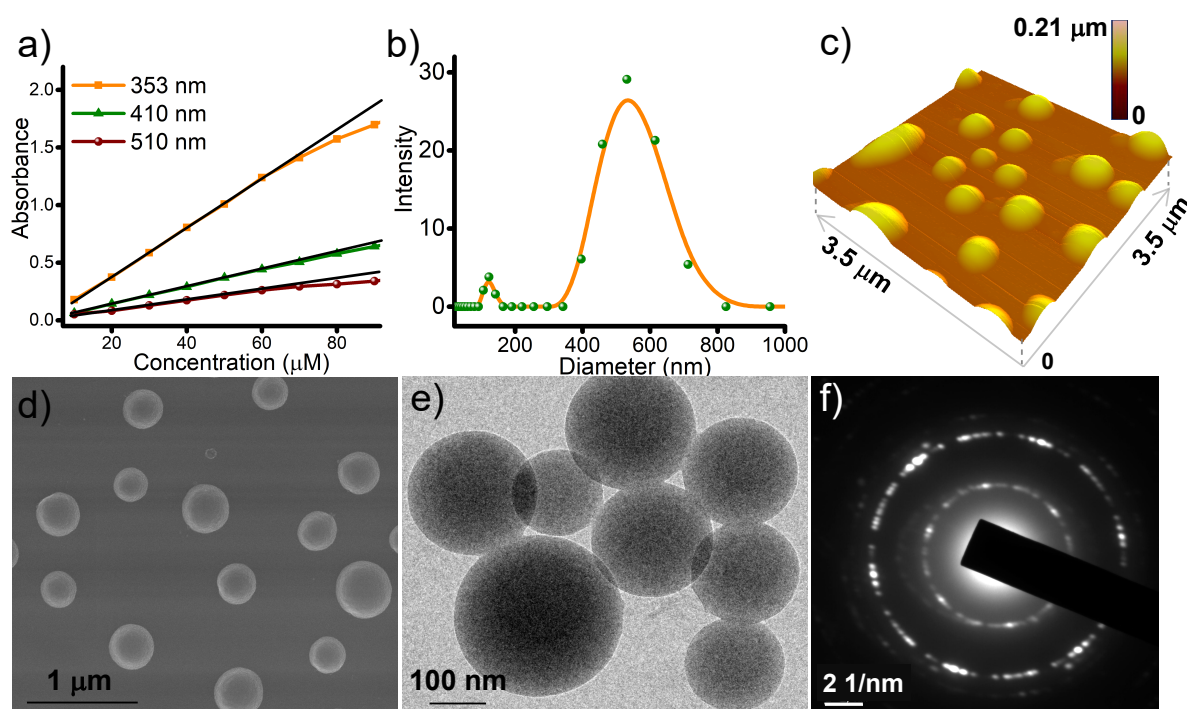


**Figure 4.9.** a) Concentration dependent absorption; b) DLS particle size distribution; c) 3D AFM (silicon wafer); d) SEM (silicon wafer); e) TEM (carbon coated Cu grid) images and f) SAED pattern of P<sub>0</sub>A (0.6 mM) in THF.

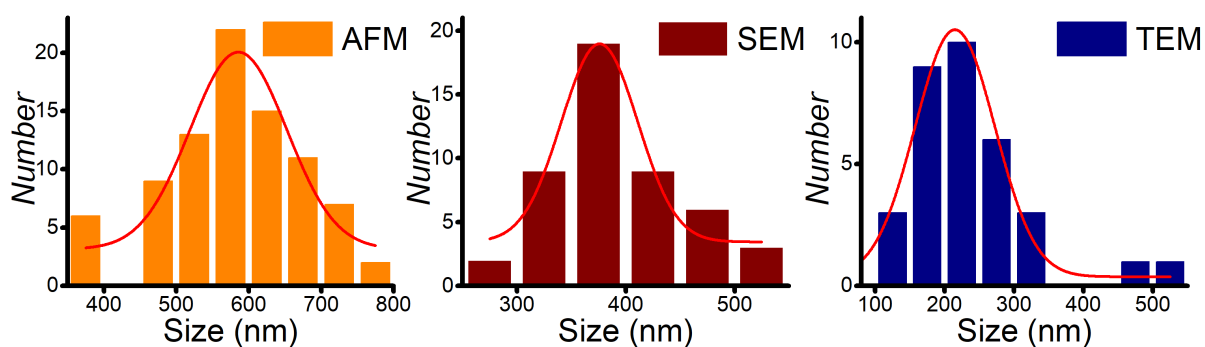


**Figure 4.10.** Particle size distribution of  $P_0A$  obtained from a) AFM; b) SEM; and c) TEM analyses in THF.

formation of globular nanoaggregate could be described as an oil-in-water type of assembly, wherein an apolar D-A dyad in a solvent of higher polarity, tend to stay away from the incompatible phase and forms spherical nanoagglomerates. The selected area electron diffraction (SAED) of globular nanoaggregate exhibit diffraction spots in concentric rings, suggesting a crystalline nature of the aggregated  $P_0A$  (Figure 4.9f). Dynamic light scattering (DLS) measurements of 0.6 mM  $P_0A$  in THF confirms the existence of a bimodal distribution of globular nanoaggregates with a hydrodynamic ( $D_H$ ) diameter of 150 and 580 nm, agreeing with the microscopic analyses (Figures 4.9b and 4.10.).

#### 4.2.4. Cyclic Voltammetry, FMO and Rehm-Weller Analysis

Interestingly, the  $P_0A$  dyad exhibit negligible emission in THF upon photoexcitation at 350 nm which can be attributed to plausible photoinduced electron transfer from singlet excited state of pyrene ( $^1P^*$ ) to the efficient electron acceptor aceanthrylene (A). Electrochemical studies of A-Br and  $P_0A$

in  $\text{CHCl}_3$  were carried out at ambient temperatures to evaluate the redox properties and the free energy for electron transfer (Figure 4.11a). Cyclic voltammogram (CV) and differential pulse voltammogram (DPV) of A-Br reveals two well-resolved reduction waves with  $E_{1/2}^1 = -1.16$  V and  $E_{1/2}^2 = -1.80$  V vs. Ag/AgCl consistent with earlier reports for substituted aceanthrylene derivative (Figure 4.11a) [200]. The first reduction wave of A-Br is only slightly higher than that of  $\text{C}_{70}$  which further endorses its similarity to fullerenes [225]. The dyad  $\text{P}_0\text{A}$  shows a reduction potential with  $E_{1/2}^1 = -1.25$  V;  $E_{1/2}^2 = -1.81$  V and  $E_{1/2}^3 = -2.26$  V vs. Ag/AgCl. The first two reduction waves are similar to redox potentials of A-Br whereas the third resembles with the reduction potential of pyrene ( $\text{P}_0$ ) [226]. HOMO, LUMO and bandgap energies obtained

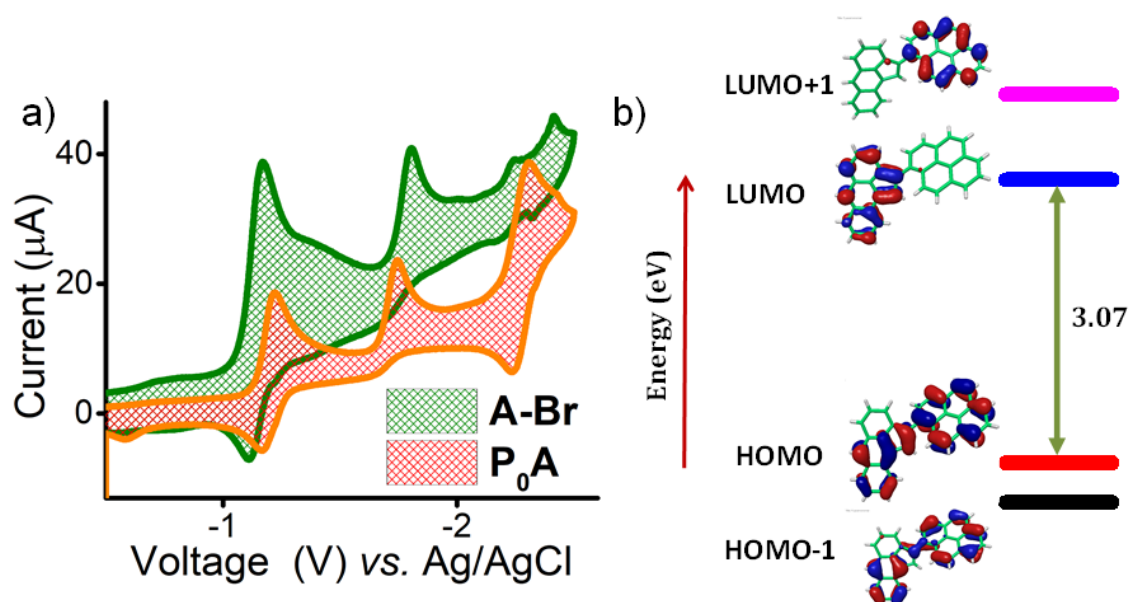


**Figure 4.11.** a) Cyclic voltammetric analyses of A-Br and  $\text{P}_0\text{A}$  in  $\text{CHCl}_3$  vs. Ag/AgCl and b) FMO analysis of  $\text{P}_0\text{A}$  monomer calculated using Jaguar DFT engine (B3LYP-D3/6-31G+(d,p)) in Schrödinger Materials Science Suite.

from electrochemical and DFT calculations on P<sub>0</sub>A dyad show a similar trend, thereby signifying a reasonable correlation between the experimental and DFT calculation (Table 4.5). FMO analysis of P<sub>0</sub>A displayed the electron density on HOMO delocalized across P and A units, whereas LUMO is exclusively located on acceptor unit suggesting the presence of CT interaction in D-A pair (Figure 4.11b) [63].

Rehm-Weller relation [31, 32] was further used to evaluate the thermodynamic feasibility ( $\Delta G_{et}$ ) of electron transfer from the photoexcited donor (<sup>1</sup>P\*) to acceptor (A) in P<sub>0</sub>A dyad (see equation 3.1, Chapter 3). The negative value of  $\Delta G_{et}$  (ca. -1.04 eV) from Rehm-Weller analysis encouraged us to explore the photoinduced electron transfer process in P<sub>0</sub>A using fTA spectroscopy (Figure 4.12.).

**Table 4.5.** Electrochemical redox properties vs. Ag/AgCl and geometry optimized optoelectronic calculations of P<sub>0</sub>A [B3LYP/6-31G+(d,p)] and A-Br using Jaguar DFT engine [B3LYP/LACVP+(d,p)] in Schrödinger Materials Science Suite.

	Optoelectronic (DFT) calculation					Experimental redox properties				
	Energy (eV)		<sup>a</sup> E <sub>g</sub> (eV)	Redox Potential (eV)		Energy (eV)		<sup>a</sup> E <sub>g</sub> (eV)	Redox Potential (V)	
	HOMO	LUMO		E <sub>ox</sub>	E <sub>red</sub>	HOMO	LUMO		E <sub>ox</sub>	E <sub>red</sub>
P <sub>0</sub> A	-5.75	-3.54	2.20	1.22	-0.99	-5.82	-3.55	2.21	<sup>1</sup> E <sub>1/2</sub> = 1.02 <sup>2</sup> E <sub>1/2</sub> = 1.36 <sup>3</sup> E <sub>1/2</sub> = 1.76	<sup>1</sup> E <sub>1/2</sub> = -1.25 <sup>2</sup> E <sub>1/2</sub> = -1.81 <sup>3</sup> E <sub>1/2</sub> = -2.26
A-Br	-6.04	-3.63	2.41	1.51	-0.90	-6.16	-3.64	2.50	E <sub>1/2</sub> = 1.36	<sup>1</sup> E <sub>1/2</sub> = -1.16 <sup>2</sup> E <sub>1/2</sub> = -1.80

<sup>a</sup>E<sub>g</sub> = (E<sub>LUMO</sub> - E<sub>HOMO</sub>)

### 4.2.5. Characterization of the Transient Radical Ion-Pair Intermediates

Having established the D-D and A-A assembly in aggregated  $P_0A$ , the ability of the assembly to extend the survival time of radical ion-pair (RIP) intermediates was further corroborated by fTA, CW-EPR and concentration

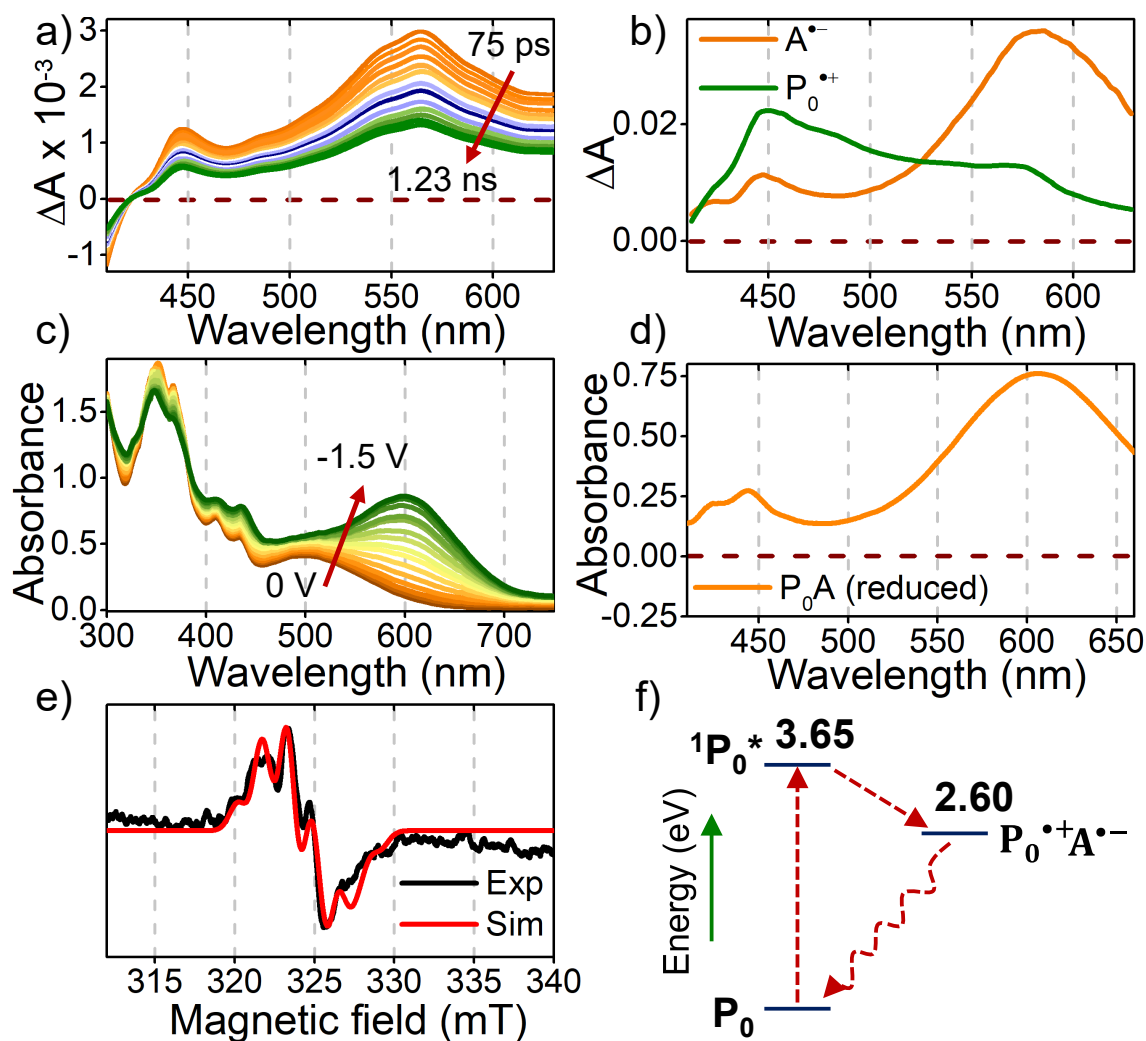


**Figure 4.12.** a) fTA spectra; b) DAS of 0.6 mM  $P_0A$  in THF. c) UV-vis SEC (0 to -1.5 V) analysis of  $P_0A$  in THF using 0.1 M  $n\text{-Bu}_4\text{NPF}_6$ ; d) differential absorption spectrum of reduced A ( $A^{\bullet-}$ ) attained by subtracting the absorption plots obtained before and after applying reduction potentials for the UV-vis spectroelectrochemistry data shown in Figures 4.12c; e) CW-EPR spectrum of  $P_0A$  (2 mM in THF) at 77 K; Smooth curve (red) is computer simulation for experimental spectra (black).

dependent redox investigations. Upon photoexcitation ( $\lambda_{ex} = 400$  nm), fTA spectrum of P<sub>0</sub>A (0.6 mM in THF) exhibited an initial short-lived component with positive absorption centered at 440-460 nm, which could not be resolved due to its presence within IRF of the instrument ( $\leq 110$  fs, Figure A4.4.). The short-lived component then transforms to a well-resolved spectrum with positive absorptions at 450 and 580 nm and ground state depletion below 420 nm (Figure 4.12a).

The global analysis of the fTA spectra yielded the decay associated spectra (DAS) as shown in Figure 4.12b. Two positive transient components with time constants of a) 6 ps; b) 1.28 ns and a ground state bleach component were sufficient to get a reasonable fit to fTA data (Figure 4.12b). The initial short-lived component in the fTA spectra can be attributed to singlet excited state of pyrene (<sup>1</sup>P\*), which undergoes charge separation to give the RIP intermediates. The first DAS (6 ps, orange) centered at 580 nm is attributed to A<sup>•-</sup> with the evidence from spectroelectrochemical (SEC) studies of P<sub>0</sub>A and A-Br in THF (Figures 4.12c-d and A4.5.). The UV-vis SEC analysis indicates the growth of a new band (570-600 nm) with increasing reduction potential (0 to -1.5 V) which depicts the formation of radical anion of aceanthrylene (A<sup>•-</sup>). The differential absorption spectrum of the UV-vis SEC data, before and after analysis, reveals a positive absorption at 580 nm and a diffuse band at 450 nm which agrees with the first component of DAS (Figures 4.12d and A4.5b). A

similar characteristic absorption spectrum was obtained by chemically reducing A-Br and P<sub>0</sub>A using fluoride reduction method (Figure A4.6.) [227]. Second DAS (1.28 ns, green) component at 450 nm can be ascribed to the radical cation of pyrene (P<sub>0</sub><sup>•+</sup>)[163] generated as a result of electron transfer occurring from the photoexcited donor (<sup>1</sup>P<sub>0</sub><sup>\*</sup>) to the acceptor (A) in dyad P<sub>0</sub>A. To confirm the radical cation of pyrene (P<sub>0</sub><sup>•+</sup>), UV-vis SEC analysis of P<sub>0</sub>A was carried out in THF. The difference spectrum obtained from the UV-vis SEC analysis indicates the formation of a broad absorption in 400-500 nm region, which clearly denotes the presence of pyrene radical cation (Figure A4.7.). Additionally, the transient signature corresponding to the ground state depletion at 400-450 nm can also be perceived in the fTA spectra (Figure 4.12a).

The absence of radical ion-pair intermediates in the fTA analysis of monomeric P<sub>0</sub>A (<60 μM in THF) suggests the instantaneous recombination ( $\tau_{cr}^M \leq 110$  fs) of the complimentary radical ion-pairs after photoexcitation. Nanosecond transient absorption spectrum of P<sub>0</sub>A ( $\lambda_{ex} = 355$  nm, 0.6 mM) in THF exhibits a ground-state bleach which is indicative of the absence of triplet excited state and recombination of radical ion-pair intermediates within the pulse width of the instrument (~10 ns, Figure A4.8.). Evaluation of the persistent radical ion-pair intermediates in aggregated P<sub>0</sub>A was further assessed by employing light-induced CW-EPR measurements. The first

derivative EPR spectrum of P<sub>0</sub>A (2 mM in THF) upon photoexcitation displays symmetric lines at 298 K ( $g \sim 2.0095$ , Figure A4.9.). Hyperfine splitting in photoexcited P<sub>0</sub>A at 77 K can be attributed to the interaction of the radical ion-pair spin with the nearby hydrogen nuclei spins (Figure 4.12e).

The concentration dependent electrochemical studies of P<sub>0</sub>A in THF indicate a concomitant decrease in the first reduction potential as a function of the increasing concentration (Figure A4.10.). The manifested facile reduction could be an outcome of favorable thermodynamic state attained as a result of charge delocalization across neighboring molecules in aggregated vs. monomeric P<sub>0</sub>A. The FMO calculations on dyad P<sub>0</sub>A (monomer to octamer) employing B3LYP-D3/6-31G+(d,p) level of theory corroborates a similar trend of decrease in bandgap ( $E_{\text{LUMO}}-E_{\text{HOMO}}$ ) energy with the increasing molecules in D-D and A-A stacks (Figure A4.11.). Persistence in the survival time of radical ion-pair intermediates in aggregated P<sub>0</sub>A suggests the importance of antiparallel route adopted by radical ion-pairs in nonparallel segregated D-D and A-A assembly. Semi-classical Marcus theory of charge transfer suggests an ambipolar semiconducting property in P<sub>0</sub>A as corroborated from the estimated hole and electron reorganization energies, the calculated mobilities of  $\mu_h \approx 0.20-0.24$  and  $\mu_e = 0.16-0.17 \text{ cm}^2\text{V}^{-1}\text{s}^{-1}$  respectively (Figure A4.12., Table 4.6.). Based on the lifetime of the charge carriers ( $\tau_h = 1.28 \text{ ns}$  and  $\tau_e = 6 \text{ ps}$ ) the estimated diffusion length ( $L$ ) of hole and electrons ( $L_h = 25.8 \text{ nm}$  and  $L_e = 1.59$

**Table 4.6.** Calculated hole/electron mobilities and reorganization energies for P<sub>0</sub>A using Jaguar DFT engine in Schrödinger Materials Science Suite.

	Method	Basis set	$\mu_h$ (cm <sup>2</sup> V <sup>-1</sup> s <sup>-1</sup> )	$\mu_e$ (cm <sup>2</sup> V <sup>-1</sup> s <sup>-1</sup> )	$\lambda_h$ (eV)	$\lambda_e$ (eV)
01.	B3LYP	6-31G+(d,p)	0.2032	0.1640	0.27	0.28
02.	B3LYP	6-311 G+(d,p)	0.2408	0.1764	0.28	0.29
03.	B3LYP-D3	6-31G+(d,p)	0.2250	0.1784	0.27	0.28
04.	B3LYP-D3	6-311 G+(d,p)	0.2405	0.1764	0.28	0.29

$\mu_h$  and  $\lambda_h$  - hole mobility and reorganization energies;  $\mu_e$  and  $\lambda_e$  - electron mobility and reorganization energies.

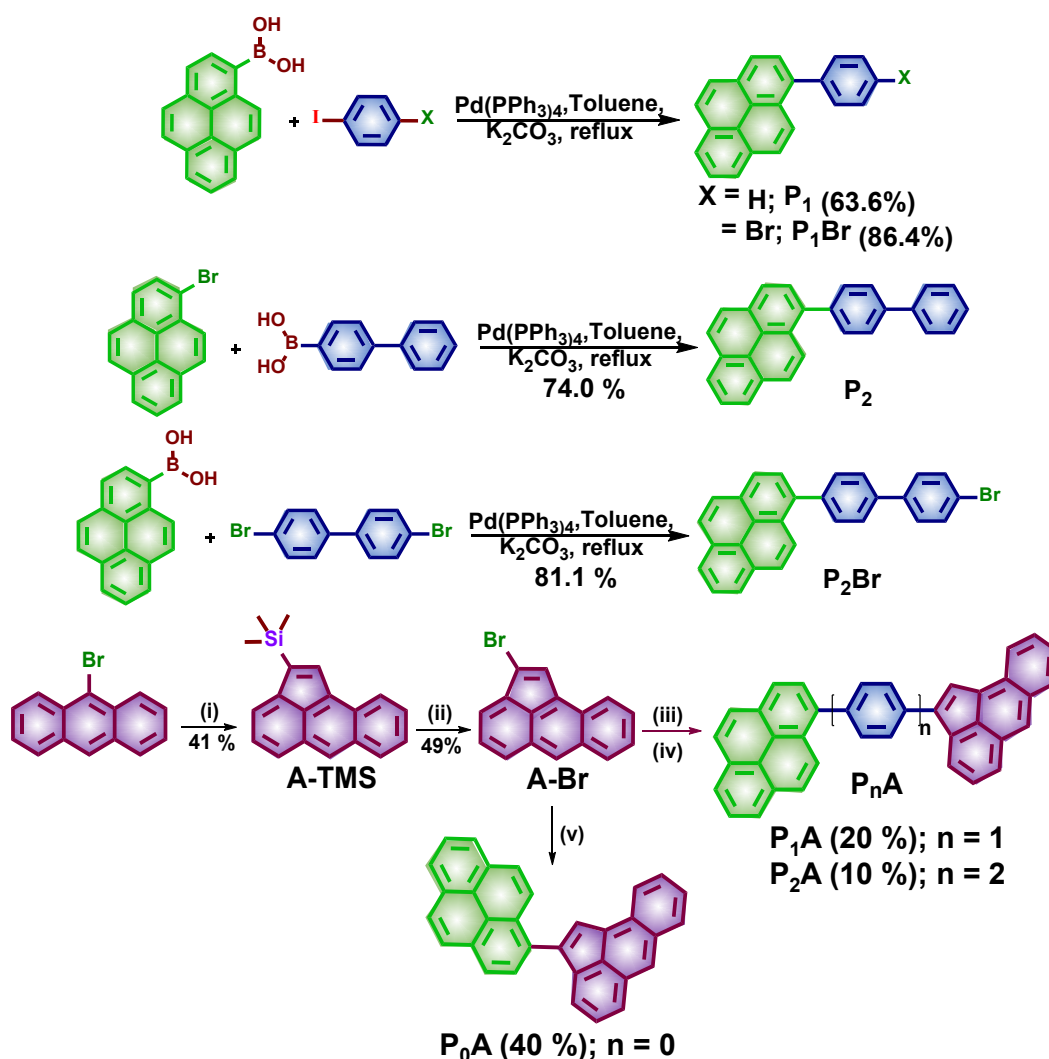
nm respectively) further support the utility of the all-carbon D-A dyad for optoelectronic applications.

### 4.3. Conclusions

In conclusion, we report the syntheses and photophysical properties of novel all-carbon donor-bridge-acceptor chromophores (P<sub>0-2</sub>A) for extending the survival times of photodriven charge-separated states. Miniaturized CP-PAHs such as aceanthrylene with fullerene-like electron affinity and degenerate low-lying excited states, depicts an excellent electron acceptor. Preliminary spectroscopic studies suggest a shallow distance dependence of the electron transfer in D-B-A (P<sub>0-2</sub>A) motifs. Interestingly, the P<sub>0</sub>A dyad with no phenyl spacer exhibits interesting self-assembly into globular nanoaggregates in THF. The quantitative fluorescence quenching along with the favorable negative value of the  $\Delta G_{et}$  (-1.04 eV) from Weller analysis suggest a strong CT characteristics in dyad P<sub>0</sub>A. The prolonged charge separated state in

aggregated ( $\tau_{cr}^A \sim 1.28$  ns) vs. monomeric ( $\tau_{cr}^M \leq 110$  fs) P<sub>0</sub>A, suggest the importance of antiparallel route in different spatial planes and delocalization of charge carriers while circuiting through the 1D  $\pi$ -columns. Electron-nuclear hyperfine resolved EPR spectrum further corroborates the presence of the radical ion-pair species in aggregated P<sub>0</sub>A, upon photoexcitation. Several complex synthetic strategies with all-carbon D-A hybrids have led to the rate of charge recombination in sub-picosecond to nanosecond regime (Table A4.3.). The introduction of a novel small molecule fullerene mimic, simple structural design, and ease of processing in our strategy have led to the rate of charge recombination that is similar to reported fullerene-based D-A dyads. Ambipolar transport characteristics predicted using Marcus theory of charge transfer rates suggests P<sub>0</sub>A as a potential bottom-up material for non-fullerene photovoltaic and semiconducting device applications.

## 4.4. Experimental Section



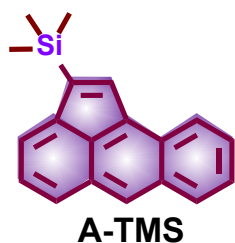
(i) trimethylsilylacetylene,  $\text{Pd(PPh}_3)_2\text{Cl}_2$ ,  $\text{PPh}_3$ , benzene, 120 °C, sealed tube, 24 hrs; (ii) *N*-bromosuccinimide, tetrahydrofuran, RT, 2 h; (iii) pinacolborane,  $\text{Pd(PPh}_3)_2\text{Cl}_2$ , anhydrous toluene,  $\text{Et}_3\text{N}$ , 110 °C and (iv)  $\text{P-P}_x\text{-Br}$ ,  $\text{Pd(PPh}_3)_4$ , Toluene,  $\text{Na}_2\text{CO}_3$ , reflux; (v) pyrene-1-boronic acid, THF,  $\text{Pd(PPh}_3)_4$ ,  $\text{K}_2\text{CO}_3$ , 65 °C.

**Scheme 1.** Schematic representation of the syntheses route adopted for  $\text{P}_n\text{A}$  derivatives.

#### Synthesis of aceanthrylen-2-yltrimethylsilane (A-TMS):

9-bromoanthracene (5.0 g, 1 eq.), TMS-acetylene (5.4 mL, 4 eq.),  $\text{Pd(PPh}_3)_2\text{Cl}_2$  (0.6 g, 0.04 eq.), benzene (7 mL) and triphenylphosphine (1.27g, 0.25 eq.), triethylamine (20 mL, 7.2 eq.) were added to a sealed tube under nitrogen. The reaction mixture was heated to 110 °C and was continued for 16 hours. The mixture was cooled to room temperature, filtered and the concentrated under reduced pressure. The residue was

purified by silica gel chromatography (Pet. ether) followed by recrystallization in ethanol to give scarlet red crystalline product (2.71 g, 37%).



**A-TMS** [Scarlet red crystals (2.71 g, 37%)]: **Melting point:** 102 – 103 °C;

$^1\text{H NMR}$  [500 MHz,  $\text{CDCl}_3$ ,  $\delta$  (ppm)]: 8.35 (s, 1H), 8.23 (d,  $J = 8.5$  Hz, 1H), 8.00 (d,  $J = 8.5$  Hz, 1H), 7.89 (d,  $J = 7.5$  Hz, 1H), 7.78 (d,  $J = 6.4$  Hz, 1H), 7.71 (s, 1H), 7.50 (t,  $J = 7.5$  Hz, 2H), 7.37 (t,  $J = 7.4$  Hz, 1H), 0.37 (s, 9H);

$^{13}\text{C NMR}$  [125 MHz,  $\text{CDCl}_3$ ,  $\delta$  (ppm)]: 143.89, 140.28, 135.98, 135.78, 134.27, 130.09, 128.75, 128.12, 128.04, 127.52, 127.43, 127.33, 126.66, 126.13, 124.66, 124.11, 0.00;

**IR** (KBr,  $\text{cm}^{-1}$ ): 3056, 2957, 1434, 1250;

**HRMS** (ESI):  $m/z$  calculated for  $\text{C}_{19}\text{H}_{19}\text{Si}[\text{M}+\text{H}]^+$ : 275.1256, found: 275.1257.

### Synthesis of 2-bromoaceanthrylene (A-Br):

A 100 ml double neck round bottom flask is arranged with a magnetic stirrer and nitrogen balloon. A-TMS (400 mg, 1 eq.) is charged into flask along with THF (40 mL). The mixture is cooled to 0 °C and stirred for 10 minutes keeping the temperature constant. N-bromosuccinimide (260 mg, 1 eq.) is charged into the reaction mixture. The stirring was continued for 10 more minutes at 0 °C and then the cooling bath is removed and the reaction is allowed to proceed at room temperature for 3 hours. The completion of the reaction was confirmed by TLC. The residue is filtered by passing through celite bed using hexane. The filtrate was distilled to get a dark brown oily liquid. The compound was purified by crystallization from ethanol to get the desired product. (143 mg, 45%).



**A-Br** [Brown red solid (143 mg, 45%)]: **Melting point:** 132-133 °C;

$^1\text{H NMR}$  [500 MHz,  $\text{CDCl}_3$ ,  $\delta$  (ppm)]: 8.36 (s, 1H), 8.07 (d,  $J = 8.5$  Hz, 1H), 7.99-7.97 (m, 2H), 7.73 (d,  $J = 7$  Hz, 1H), 7.58-7.55 (m, 2H), 7.53 (t,  $J = 3.2$  Hz, 1H), 7.37 (t,  $J = 4$  Hz, 1H);

$^{13}\text{C}$  NMR [125 MHz,  $\text{CDCl}_3$ ,  $\delta$  (ppm)]: 138.53, 134.38, 133.77, 130.40, 129.34, 128.66, 128.11, 128.02, 127.56, 127.12, 126.00, 125.28, 125.08, 124.88, 123.96;

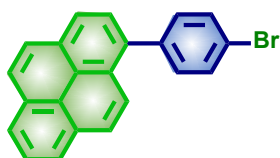
IR (KBr,  $\text{cm}^{-1}$ ): 3034, 1433, 607;

HRMS (ESI):  $m/z$  calculated for  $\text{C}_{16}\text{H}_9\text{Br}$   $[\text{M}]^+$ : 279.9888, found: 279.9890.

---

### Synthesis of 1-(4-bromophenyl)pyrene (**P<sub>1</sub>-Br**):

Pyrene-1-boronic acid (1.0 g, 1 eq.) and 4-iodo-1-bromobenzene (1.38 g, 1.2 eq.) were dissolved in toluene (40 ml) and subsequently an aqueous solution of  $\text{Na}_2\text{CO}_3$  (10 ml, 1 M) was added. The mixture was degassed and purged with nitrogen and consequently  $\text{Pd}(\text{PPh}_3)_4$  was added under nitrogen. The reaction mixture was refluxed for 55 hours and the completion of the reaction was monitored using TLC. After the completion of the reaction, the phases were separated and aqueous layer was extracted with toluene. The combined organic layers were dried with sodium sulphate and was distilled under vacuum to get brown residue. The pure product was obtained by purification using column chromatography (Pet. ether) to get pure product (pale green, 1.25 g, 86.4 %).



**P<sub>1</sub>-Br** [Pale green fluffy solid (1.25 g, 86.4%)]: **Melting point:** 147-149 °C;

$^1\text{H}$  NMR [500 MHz,  $\text{CDCl}_3$ ,  $\delta$  (ppm)]: 8.36 (d,  $J = 7.85$  Hz, 1H), 8.33 (d,  $J = 7.5$  Hz, 1H), 8.29 (d,  $J = 7.5$  Hz, 1H), 8.22 (s, 2H), 8.17 (d,  $J = 9.25$  Hz, 1H), 8.09 (t,  $J = 7.6$  Hz, 1H), 8.05 (d,  $J = 9.25$  Hz, 1H), 7.99 (d,  $J = 7.8$  Hz, 1H), 7.79 (d,  $J = 8.25$  Hz, 2H), 7.57 (d,  $J = 8$  Hz, 2H);

$^{13}\text{C}$  NMR [125 MHz,  $\text{CDCl}_3$ ,  $\delta$  (ppm)]: 140.01, 136.18, 132.88, 132.02, 131.43, 130.86, 130.84, 128.45, 128.11, 128.04, 128.00, 127.82, 126.97, 125.99, 125.61, 125.44, 124.76, 124.60, 124.45, 121.50;

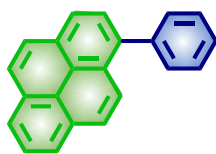
IR (KBr,  $\text{cm}^{-1}$ ): 3039, 1479;

HRMS (ESI):  $m/z$  calculated for  $\text{C}_{22}\text{H}_{13}\text{Br}$   $[\text{M}]^+$ : 356.0201, found: 356.0222.

---

**Synthesis of 1-phenylpyrene (P<sub>1</sub>):**

Pyrene-1-boronic acid (0.5 g, 1 eq.) and 1-iodobenzene (0.57 g, 1.2 eq.) were dissolved in toluene (40 ml) and subsequently an aqueous solution of Na<sub>2</sub>CO<sub>3</sub> (2 ml, 2 M) was added. The mixture was degassed and purged with nitrogen and consequently Pd(PPh<sub>3</sub>)<sub>4</sub> was added under nitrogen. The reaction mixture was refluxed for 16 hours and the completion of the reaction was monitored using TLC. After the completion of the reaction, the phases were separated and aqueous layer was extracted with dichloromethane. The combined organic layers were dried with sodium sulphate and was distilled under vacuum to get brown residue. The pure product was obtained by purification using column chromatography (Pet. ether) to get pure product (pale green fluffy solid, 0.35 g, 63.6 %).



**P<sub>1</sub>-Br** [Pale green fluffy solid (0.35 g, 63.6%)]: **Melting point:** 82-84 °C;

**<sup>1</sup>H NMR** [500 MHz, CDCl<sub>3</sub>, δ (ppm)]: 8.23-8.15 (m, 4H), 8.09 (s, 2H), 8.02-7.97 (m, 3H), 7.63 (d, *J* = 7.5 Hz, 2H), 7.56 (t, *J* = 7.5 Hz, 2H), 7.48 (t, *J* = 7.5 Hz, 1H);

**<sup>13</sup>C NMR** [125 MHz, CDCl<sub>3</sub>, δ (ppm)]: 141.20, 137.74, 131.48, 130.97, 130.59, 128.48, 128.36, 127.60, 127.45, 127.41, 127.24, 126.00, 125.28, 125.09, 124.94, 124.90, 124.81, 124.6350;

**IR** (KBr, cm<sup>-1</sup>): 3039, 1552;

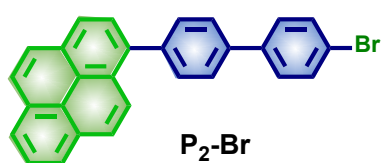
**HRMS** (ESI): *m/z* calculated for C<sub>22</sub>H<sub>14</sub>[M]<sup>+</sup>: 278.1096, found: 278.1105.

---

**Synthesis of 1-(4'-bromobiphenyl-4-yl)pyrene (P<sub>2</sub>-Br):**

Pyrene-1-boronic acid (1 g, 1.0 eq.) and 4,4'-dibromobiphenyl (1.04 g, 0.83 eq.) were dissolved in toluene (100 ml) and subsequently K<sub>2</sub>CO<sub>3</sub> (5 mL, 2M) was added and the entire reaction mixture was nitrogen purged for 30 minutes. Subsequently Pd(PPh<sub>3</sub>)<sub>4</sub> was added into the reaction mixture under nitrogen purging and the

reaction vessel was sealed and refluxed for 18 hours. The progress of the reaction was monitored using TLC and the starting material seemed to be consumed after 18 hours. The reaction mixture was concentrated under vacuum and organic compound was extracted using chloroform. The organic layer was dried on sodium sulphate and then distilled to get a crude product. The crude material was then purified using column chromatography (Pet. ether) to get the pure product as off white solid (1.42 g, 81.1%)



**P<sub>2</sub>-Br** [Off white solid (1.42 g, 81.1%)]: **Melting point:** 217-218°C;

<sup>1</sup>H NMR [500 MHz, CDCl<sub>3</sub>, δ (ppm)]: 8.14 (m, 4H), 8.04 (s, 2H), 7.96 (m, 3H), 7.66 (m, 4H), 7.54 (m, 4H);

<sup>13</sup>C NMR [125 MHz, CDCl<sub>3</sub>, δ (ppm)]: 139.61, 138.69, 137.82, 136.03, 130.97, 130.47, 130.12, 129.94, 129.69, 130.97, 130.47, 130.12, 129.94, 129.69, 127.70, 127.47, 126.57, 126.50, 126.38, 125.87, 125.04, 124.17, 124.12, 123.98, 123.87, 123.67, 120.68;

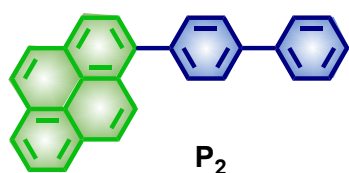
IR (KBr, cm<sup>-1</sup>): 3039.81, 1479.40;

HRMS (ESI): m/z calculated for C<sub>28</sub>H<sub>17</sub>Br[M]<sup>+</sup>: 432.0514, found: 432.0549.

### Synthesis of 1-([1,1'-biphenyl]-4-yl)pyrene (P<sub>2</sub>):

1-Bromopyrene (0.75 g, 1.0 eq.) and 4-biphenylboronic acid (0.53 g, 1.0 eq.) were dissolved in toluene (40 ml) and subsequently aqueous solution of Na<sub>2</sub>CO<sub>3</sub> (10 mL, 2 M) was added and the entire reaction mixture was nitrogen purged for 30 minutes. Subsequently Pd(PPh<sub>3</sub>)<sub>4</sub> was added into the reaction mixture under nitrogen purging and the reaction vessel was sealed and refluxed for 18 hours. The progress of the reaction was monitored using TLC and the starting material seemed to be consumed after 48 hours. The reaction mixture was concentrated under vacuum and organic compound was extracted using dichloromethane. The organic layer was dried on sodium sulphate and then distilled to get a crude product. The crude

material was then purified using column chromatography (Pet. ether) to get the pure product as off white solid (0.7 g, 74.0%)



**P<sub>2</sub>** [Off white solid (0.7 g, 74.0%)]: **Melting point:** 218-221 °C;

<sup>1</sup>H NMR [500 MHz, CDCl<sub>3</sub>, δ (ppm)]: 8.26 (d, *J* = 9 Hz, 2H), 8.21-8.17 (m, 2H), 8.11 (s, 2H), 8.06-8.0 (m, 3H), 7.80 (d, *J* = 8 Hz, 4H), 7.73 (t, *J* = 7.5 Hz, 4H), 7.51 (t, *J* = 7.5 Hz, 2H), 7.40 (t, *J* = 10 Hz, 1H);

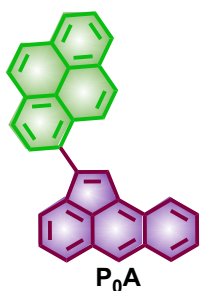
<sup>13</sup>C NMR [125 MHz, CDCl<sub>3</sub>, δ (ppm)]: 140.82, 140.19, 140.10, 137.30, 131.50, 131.03, 130.99, 130.64, 128.89, 128.52, 127.59, 127.53, 127.46, 127.43, 127.18, 127.12, 126.03, 125.28, 125.14, 125.00, 124.92, 124.86, 124.70;

IR (KBr, cm<sup>-1</sup>): 3032.10, 1598.99;

HRMS (ESI): *m/z* calculated for C<sub>28</sub>H<sub>18</sub>[M]<sup>+</sup>: 354.1409, found: 354.1412.

### Synthesis of 2-(pyren-1-yl)aceanthrylene (P<sub>0</sub>A):

Pyrene-1-boronic acid (133 mg, 0.4 eq.), A-Br (170 mg, 1 eq.), aqueous solution of K<sub>2</sub>CO<sub>3</sub> (1.4 mL, 2M), and THF (12 mL) was charged into a round bottom flask under nitrogen. The reaction mixture was degassed and Pd(PPh<sub>3</sub>)<sub>4</sub> (41 mg, 0.06 eq.) is charged into the mixture under nitrogen atmosphere. The reaction was heated at 65 °C for 24 hours and then cooled to room temperature. The solvent was removed under reduced pressure and the reaction mixture was extracted with ethyl acetate to obtain the blackish-brown solid. The product was purified by column chromatography [silica gel, Pet ether: CHCl<sub>3</sub> (9:1)] to obtain P<sub>0</sub>A as a black solid (40%, 78 mg).



**P<sub>0</sub>A** [Black solid (78 mg, 40%)]: **Melting point:** 190-191 °C;

<sup>1</sup>H NMR [500 MHz, CDCl<sub>3</sub>, δ (ppm)]: 8.57 (d, *J* = 9.25 Hz, 1H), 8.46 (s, 1H), 8.31 (d, *J* = 0.6 Hz, 1H), 8.23-8.21 (m, 2H), 8.15 (d, *J* = 7.6 Hz, 1H), 8.10 (t, *J* = 4.98 Hz, 2H), 8.09-8.06 (m, 2H), 8.04 (d, *J* = 5.7 Hz, 1H), 8.01-7.94 (m, 2H), 7.78 (s, 1H), 7.72 (d, *J* = 6.6 Hz, 1H), 7.58-7.53 (m, 2H), 7.43 (t, *J* = 8 Hz, 1H);

$^{13}\text{C}$  NMR [125 MHz,  $\text{CDCl}_3$ ,  $\delta$  (ppm)]: 140.00, 139.36, 134.09, 133.51, 130.77, 130.50, 130.09, 129.67, 129.40, 128.48, 128.28, 127.44, 127.10, 126.98, 126.69, 126.45, 126.4, 126.30, 126.16, 125.65, 125.40, 125.21, 125.07, 125.00, 124.27, 124.08, 123.95, 123.92, 123.87, 123.67, 123.28;

IR (KBr,  $\text{cm}^{-1}$ ): 3048, 2960, 1436;

HRMS (ESI):  $m/z$  calculated for  $\text{C}_{32}\text{H}_{19}$   $[\text{M}+\text{H}]^+$ : 403.1487, found: 403.1484.

---

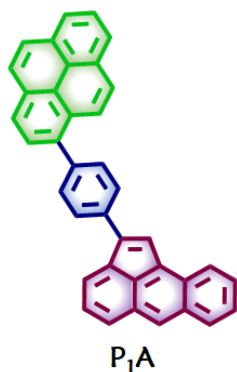
### Synthesis of 1-(4-(pyren-1-yl)phenyl)aceanthrylene ( $\text{P}_1\text{A}$ ):

2-bromoaceanthrylene (A-Br) (0.5 g, 1.0 eq.) and  $\text{Pd}(\text{PPh}_3)_2\text{Cl}_2$  (0.124 g, 0.06 eq.) is added into a clean and dry round bottom flask. The round bottom flask was evacuated and then 50 ml anhydrous toluene and 3 ml dry triethylamine is added to the reaction mixture. The reaction mixture is heated to 95 °C and subsequently pinacolborane (1.0 ml, 3.87 eq.) is carefully added to it. The heating is continued for 2-3 hours and the completion of the reaction was monitored by examining the complete consumption of the starting materials on thin layer chromatography. The product 2-(aceanthrylen-2-yl)-4,4,5,5-tetramethyl-1,3,2-dioxaborolane is unstable and was found to degrade under column chromatography. It was used as such for the succeeding reaction.

A mixture of  $\text{P}_1\text{-Br}$  (0.165 g, 1.0 eq.), 2-(aceanthrylen-2-yl)-4,4,5,5-tetramethyl-1,3,2-dioxaborolane (in situ reaction mixture from previous reaction), aqueous solution of  $\text{Na}_2\text{CO}_3$  (1.6 mL, 2M), and toluene (50 ml) were charged into a round bottom flask. The reaction mixture was then purged with nitrogen for 30 minutes and subsequently  $\text{Pd}(\text{PPh}_3)_4$  was added to it under nitrogen purging. The reaction mixture was then sealed under nitrogen and heated to 110 °C for 43 hour. The completion of the reaction was monitored by examining the complete consumption of the starting materials on thin layer chromatography. After the completion of the reaction, the solvent was removed under reduced pressure and the product was

extracted using dichloromethane. The organic layer was then distilled and crude product was purified using column chromatography (Petroleum ether: chloroform, 85:15) to get the pure product as brownish red powder (44 mg, 20%)

**P<sub>1</sub>A** [Brownish red solid (44 mg, 20%)]: **Melting point:** 248-252 °C;



<sup>1</sup>H NMR [500 MHz, CDCl<sub>3</sub>, δ (ppm)]: 8.43 (s, 1H), 8.28 (m, 2H), 8.20 (d, *J* = 8Hz, 1H), 8.14 (m, 3H), 8.03 (m, 8H), 7.96 (m, 1H), 7.78 (s, 1H), 7.74 (d, *J* = 8Hz, 2H), 7.65 (m, 1H), 7.57 (m, 1H), 7.43 (m, 1H);

<sup>13</sup>C NMR [125 MHz, CDCl<sub>3</sub>, δ (ppm)]: 134.91, 131.55, 131.13, 130.40, 128.59, 127.97, 127.68, 127.58, 127.50, 126.77, 126.38, 127.58, 127.50, 127.29, 126.77, 126.38, 126.06, 125.36, 125.16, 125.03, 124.89, 124.76, 124.31, 124.18;

IR (KBr, cm<sup>-1</sup>): 2921.67, 1434.56;

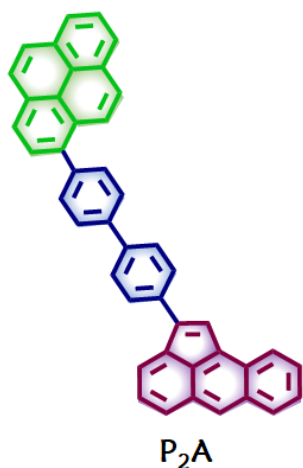
HRMS (ESI): *m/z* calculated for C<sub>38</sub>H<sub>22</sub> [M]<sup>+</sup>: 478.1722, found: 478.1744.

### Synthesis of 2-(4'-(pyren-1-yl)-[1,1'-biphenyl]-4-yl)aceanthrylene (P<sub>2</sub>A):

2-bromoaceanthrylene (A-Br) (0.5 g, 1.0 eq.) and Pd(PPh<sub>3</sub>)<sub>2</sub>Cl<sub>2</sub> (0.124 g, 0.06 eq.) is added into a clean and dry round bottom flask. The round bottom flask was evacuated and then 50 ml anhydrous toluene and 3 ml dry triethylamine is added to the reaction mixture. The reaction mixture is heated to 95 °C and subsequently pinacolborane (1.0 ml, 3.87 eq.) is carefully added to it. The heating is continued for 2-3 hours and the completion of the reaction was monitored by examining the complete consumption of the starting materials on thin layer chromatography. The product 2-(aceanthrylen-2-yl)-4,4,5,5-tetramethyl-1,3,2-dioxaborolane is unstable and was found to degrade under column chromatography. It was used as such for the succeeding reaction.

A mixture of P<sub>2</sub>-Br (0.25 g, 1.0 eq.), 2-(aceanthrylen-2-yl)-4,4,5,5-tetramethyl-1,3,2-dioxaborolane (in situ reaction mixture from previous reaction), Na<sub>2</sub>CO<sub>3</sub> (2 mL,

2M), and toluene (50 ml) were charged into a round bottom flask. The reaction mixture was then purged with nitrogen for the next 30 minutes and subsequently  $\text{Pd}(\text{PPh}_3)_4$  was added to it under nitrogen purging. The reaction mixture was then sealed under nitrogen and heated to 110 °C for 43 hours. The completion of the reaction was monitored by examining the complete consumption of the starting materials on thin layer chromatography. After the completion of the reaction, the solvent was removed under reduced pressure and the product was extracted using dichloromethane. The organic layer was then distilled and crude product was purified using column chromatography (Petroleum ether: chloroform, 85:15) to get pure product as brownish red powder (32.1 mg, 10%)



**P<sub>2</sub>A** [Brownish red solid (32.1 mg, 10%)]: **Melting point:** 270-273 °C;

**<sup>1</sup>H NMR** [500 MHz, CDCl<sub>3</sub>, δ (ppm)]: 8.42 (s, 1H), 8.28 (d, J=10 Hz, 1H), 8.22 (m, 2H), 8.13 (m, 3H), 8.02 (m, 9H), 7.84 (m, 4H), 7.74 (s, 1H), 7.70 (d, J=10 Hz, 2H), 7.64 (m, 1H), 7.56 (m, 1H), 7.42 (m, 1H);

**<sup>13</sup>C NMR** [125 MHz, CDCl<sub>3</sub>, δ (ppm)]: 139.68, 134.48, 131.15, 130.39, 129.13, 128.58, 127.94, 127.66, 127.63, 127.56, 127.50, 127.45, 127.27, 126.99, 126.74, 126.34, 126.06, 125.32, 125.17, 125.03, 124.89, 124.74, 124.30, 124.06;

**IR** (KBr, cm<sup>-1</sup>): 3039, 1435;

**HRMS** (ESI): m/z calculated for C<sub>44</sub>H<sub>26</sub>[M]<sup>+</sup>: 554.2035, found: 554.2029.

## 4.5. Additional Figures and Tables

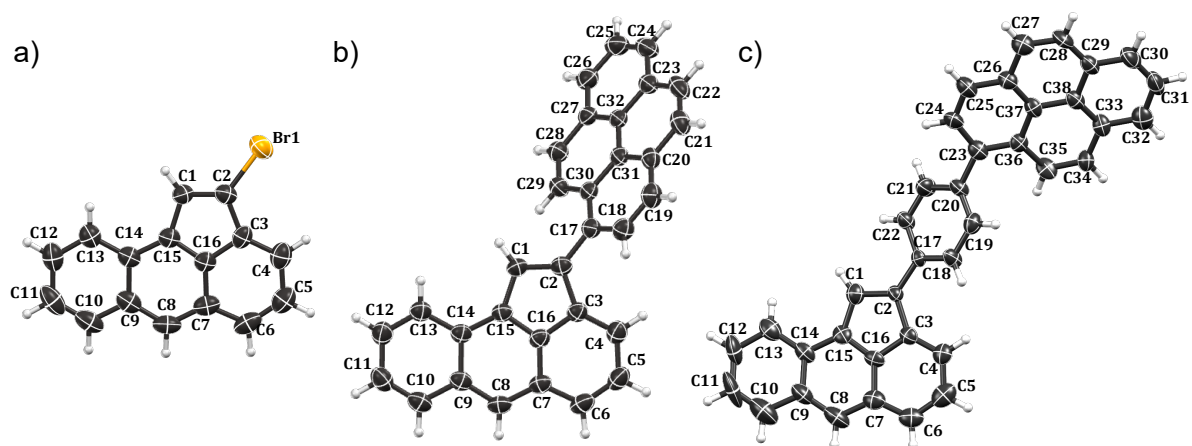


**Figure A4.1.** ORTEP diagram representing the molecular structure of crystalline a) A-Br; b) P<sub>0</sub>A and c) P<sub>1</sub>A with thermal ellipsoids drawn at the 50% probability level.

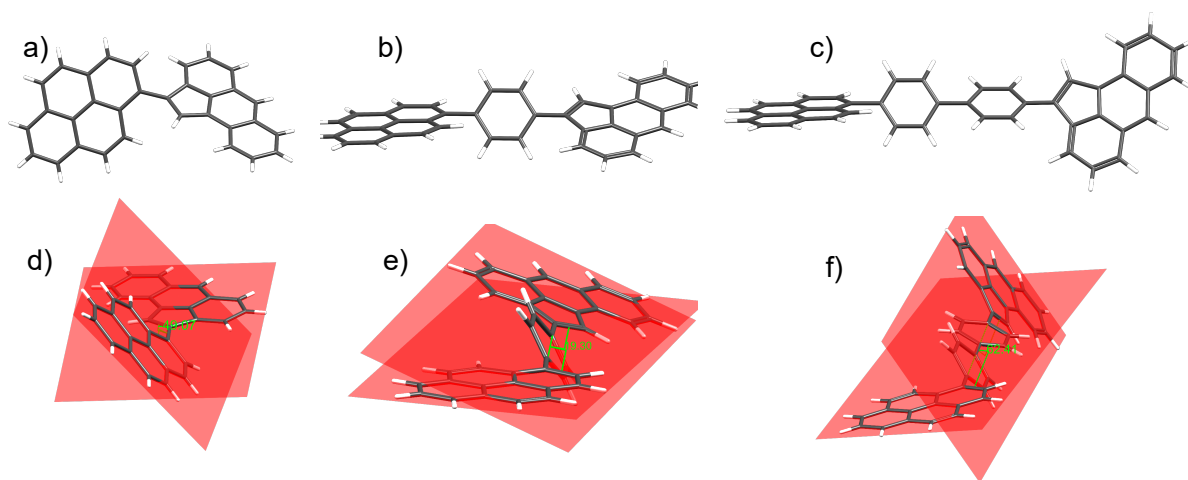


**Figure A4.2.** Molecular structure and angle between planes of the donor (pyrene) and acceptor (aceanthrylene) in crystalline P<sub>0</sub>A (a, d); P<sub>1</sub>A (b, e); and geometry optimized P<sub>2</sub>A (c, f).

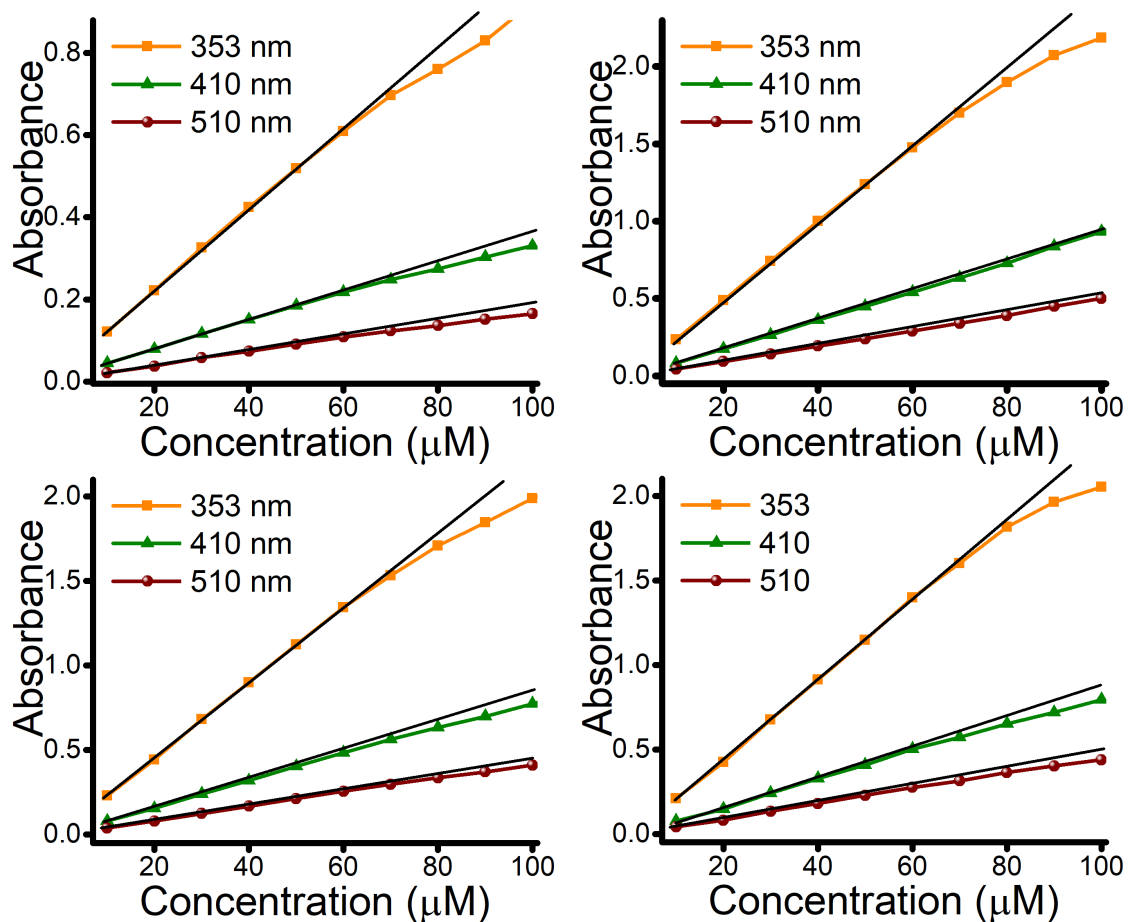


**Figure A4.3.** Concentration dependent linearity plot of P<sub>0</sub>A in a) *n*-hexane; b) toluene; c) benzene; and d) chloroform monitored at 353, 410 and 510 nm.

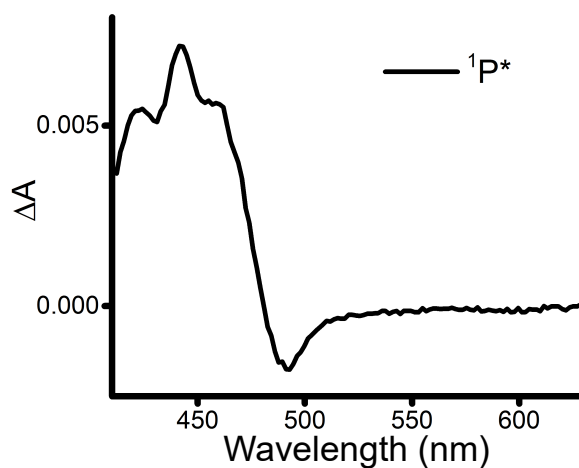


**Figure A4.4.** fTA spectrum of 0.6 mM P<sub>0</sub>A in THF after a delay of 100 fs, possibly indicating the presence of singlet excited state of pyrene ( $^1P^*$ ).

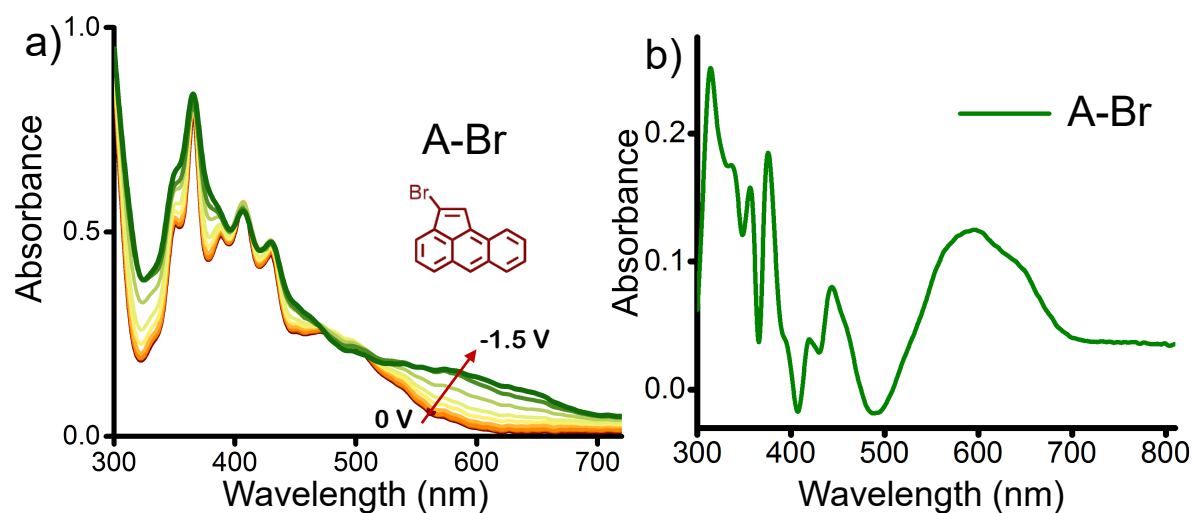


**Figure A4.5.** a) UV-vis SEC (0 to -1.5 V) analysis of A-Br in THF using 0.1 M  $n\text{-Bu}_4\text{NPF}_6$ ; and b) differential absorption spectrum of reduced A ( $A^-$ ) attained by subtracting the absorption plots obtained before and after applying reduction potentials to A-Br.

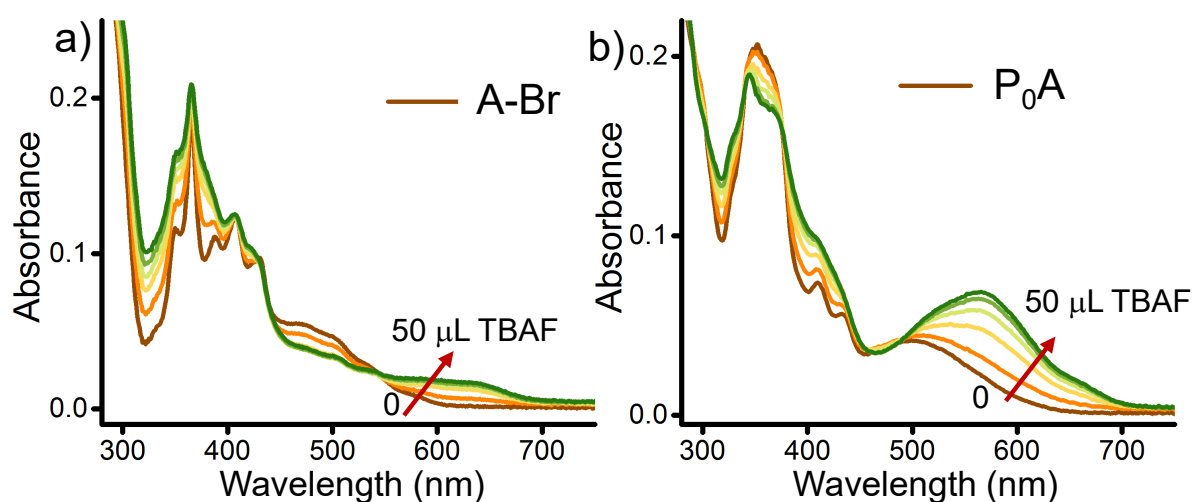


**Figure A4.6.** Absorption spectrum of reduced a) A-Br and b)  $P_0A$  achieved by fluoride chemical reduction method using tetrabutylammonium fluoride (TBAF, 0.33 M).

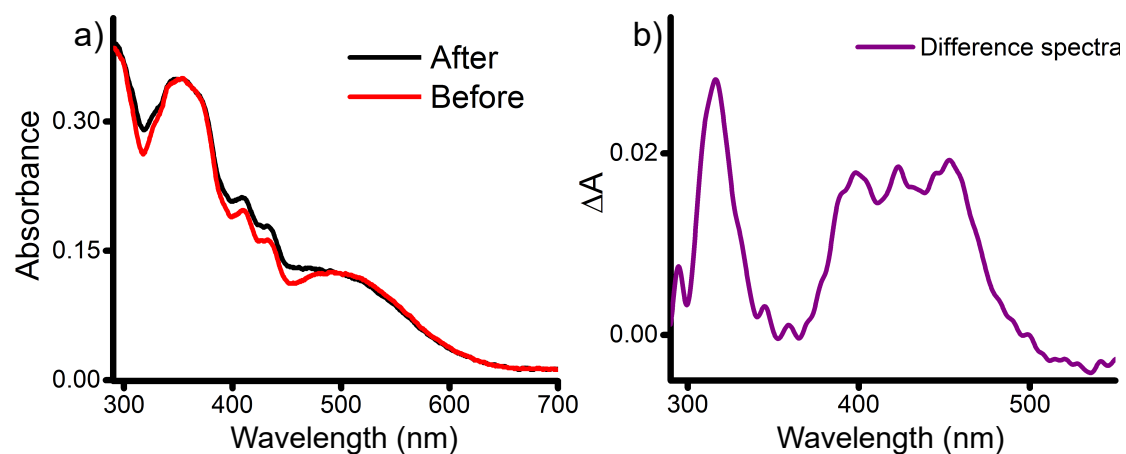


**Figure A4.7.** a) UV-vis SEC (0 to 2.5 V) analysis depicting the oxidation of  $P_{0A}$ . Solvent used is THF with 0.1 M  $n\text{-Bu}_4\text{NPF}_6$  as supporting electrolyte at 303 K; b) differential absorption spectrum of oxidized P ( $P^+$ ) attained by subtracting the absorption plots obtained before and after applying oxidation potentials to  $P_{0A}$ .

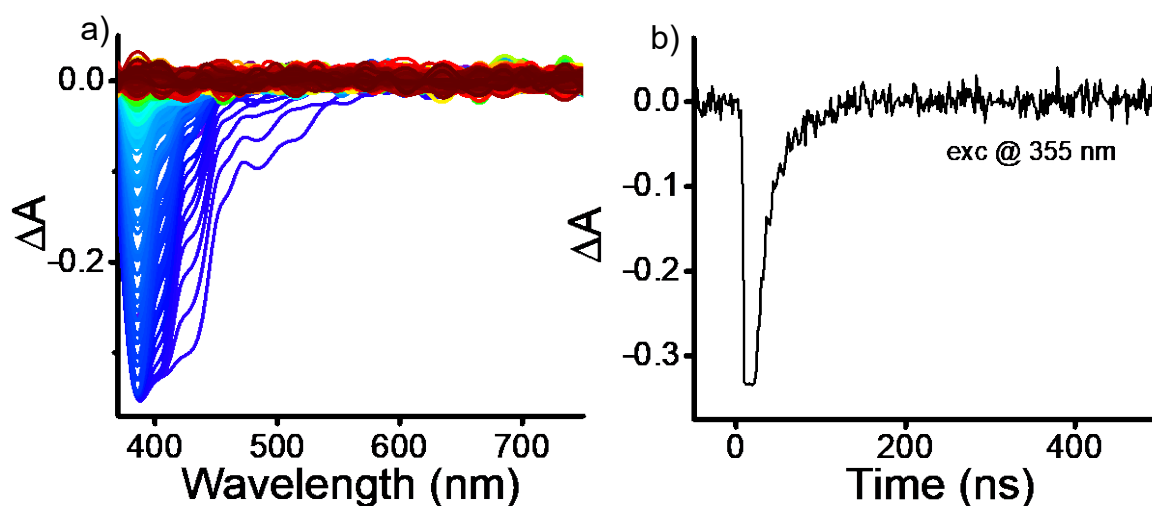


**Figure A4.8.** a) Nanosecond transient absorption spectra of  $P_{0A}$  (0.6 mM,  $\lambda_{exc} = 355$  nm) in THF and b) corresponding rate of bleach recovery at 390 nm.

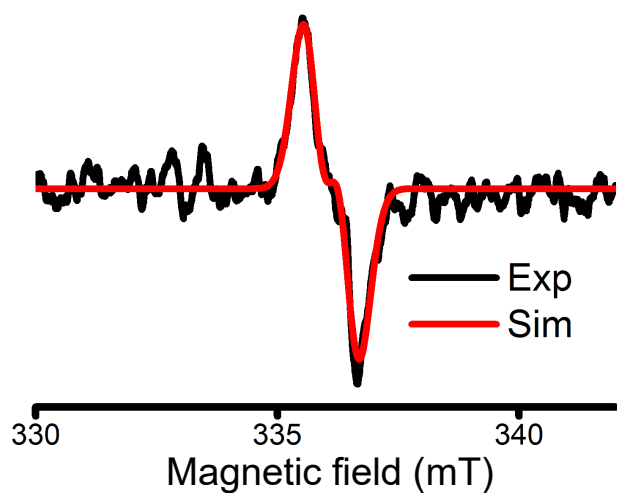


**Figure A4.9.** Light induced CW-EPR spectrum of 2 mM P<sub>0</sub>A in THF at 298 K. Smooth curve (red) is computer simulation for the experimental spectrum (black).

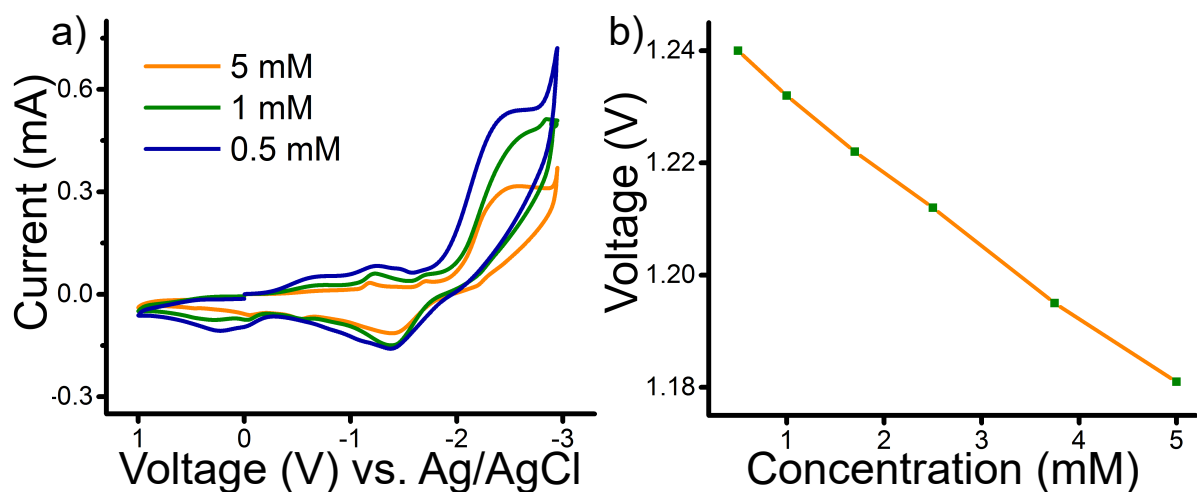


**Figure A4.10.** a) Concentration dependent (0.5–5 mM) cyclic voltammetric measurements of P<sub>0</sub>A in THF; and b) the linear decrease in the first reduction potential with the increasing concentration.

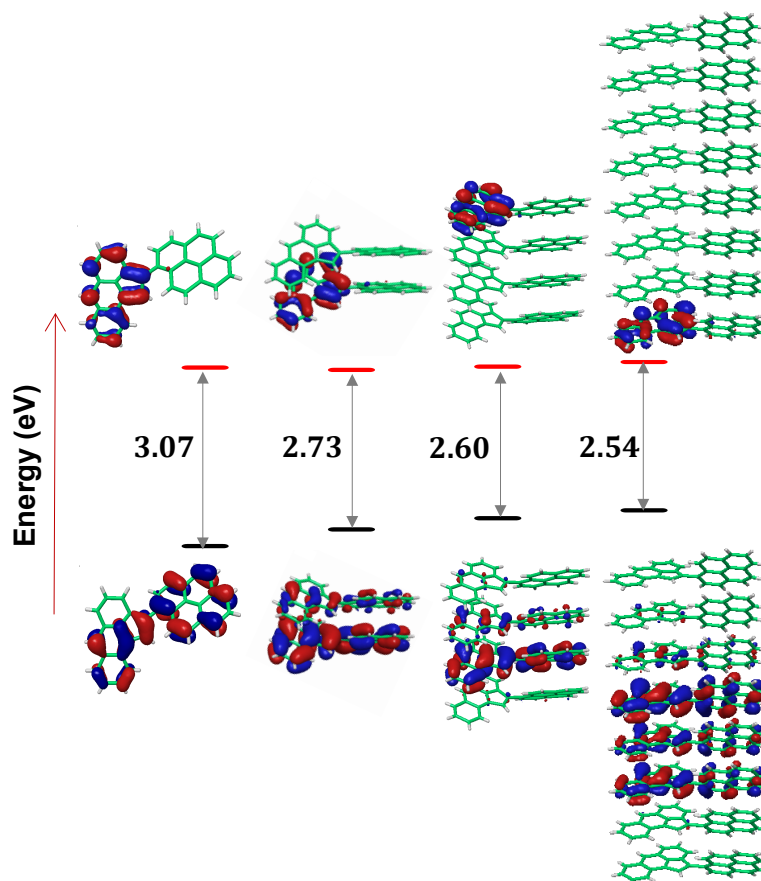


**Figure A4.11.** Frontier molecular orbital (FMO) analysis of PoA (monomer, dimer, tetramer and octamer) calculated using Jaguar DFT engine (B3LYP-D3/6-31G+(d,p)) in Schrödinger Materials Science Suite.

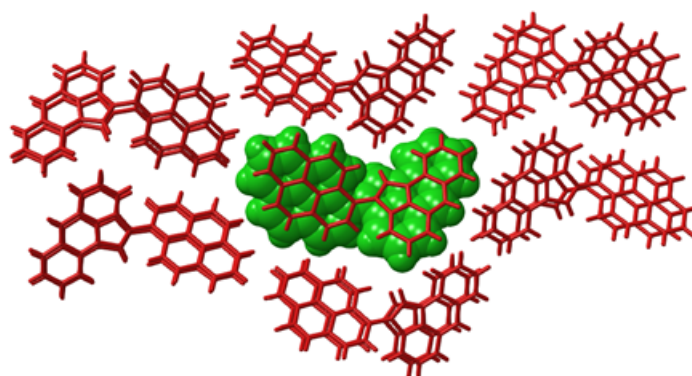


**Figure A4.12.** The ensemble of molecules selected from the crystal packing for the mobility (electronic coupling) calculations using Jaguar DFT engine in Schrödinger Materials Science Suite. The molecules within the 4.2 Å distance from the central molecule (highlighted in green spacefill model) were selected for the mobility calculations.

**Table A4.1.** Excitation energy, oscillator strength, main transition orbital and their contribution calculated for the model derivatives ( $P_0$  and A-Br) and D-B-A ( $P_{0-2A}$ ) motifs using TD-DFT [B3LYP/6-311G+(d,p)].

State	Excitation Energy (eV)	Oscillator strength ( $f$ )	Main transition orbital	Contribution	
$P_0$	S6	4.9186	0.0000	HOMO→LUMO+3	0.59260
	S5	4.5859	0.0000	HOMO-2→LUMO	0.68834
	S4	4.5637	0.2760	HOMO→LUMO+1	0.46141
				HOMO-1→LUMO	0.50413
	S3	4.2875	0.0000	HOMO→LUMO+2	0.69027
	S2	3.7284	0.0002	HOMO→LUMO+1	0.52043
	S1	3.6517	0.2768	HOMO→LUMO	0.67269
A-Br	S6	4.4304	0.0000	HOMO-4→LUMO	0.70258
	S5	4.2450	0.0276	HOMO→LUMO+1	0.55214
	S4	4.1414	0.0332	HOMO-3→LUMO	0.59966
	S3	3.6441	0.0956	HOMO-2→LUMO	0.59816
	S2	3.0638	0.0569	HOMO-1→LUMO	0.66377
	S1	2.3713	0.0532	HOMO→LUMO	0.67386
$P_{0A}$	S6	3.6264	0.0297	HOMO→LUMO+2	0.50327
	S5	3.3385	0.0094	HOMO-3→LUMO	0.65402
	S4	3.2115	0.2446	HOMO→LUMO+1	0.64039
	S3	3.0156	0.1824	HOMO-2→LUMO	0.62234
	S2	2.7196	0.0134	HOMO-1→LUMO	0.66091
	S1	2.1235	0.1533	HOMO→LUMO	0.69439
$P_{1A}$	S6	3.5618	0.2852	HOMO-1→LUMO+1	0.62082
				HOMO-3→LUMO+2	0.13179
	S5	3.4706	0.0363	HOMO→LUMO+1	0.12908
				HOMO-3→LUMO	0.64149
				HOMO-4→LUMO	0.17175
				HOMO→LUMO+1	0.31173
	S4	3.2388	0.0000	HOMO-8→LUMO	0.17557
				HOMO-5→LUMO	0.15358
	S3	3.0211	0.1340	HOMO→LUMO+6	0.15019
				HOMO-2→LUMO	0.65506

				HOMO-1→LUMO	0.12028
	S2	2.6236	0.0024	HOMO-1→LUMO	0.65819
				HOMO→LUMO	0.23400
	S1	2.2429	0.1965	HOMO-2→LUMO	0.13547
				HOMO→LUMO	0.65584
	S6	3.4923	0.2707	HOMO-1→LUMO+1	0.66348
				HOMO→LUMO+2	0.13485
				HOMO-3→LUMO+3	0.10824
	S5	3.3624	0.1335	HOMO-3→LUMO	0.46947
				HOMO-5→LUMO	0.12959
P <sub>2</sub> A	S4	3.2752	0.4173	HOMO-1→LUMO+1	0.11540
				HOMO→LUMO+1	0.68655
	S3	3.0172	0.1175	HOMO-2→LUMO	0.65499
				HOMO-3→LUMO	0.11928
	S2	2.6606	0.0054	HOMO-1→LUMO	0.65573
				HOMO→LUMO	0.64447
	S1	2.2568	0.2114	HOMO-1→LUMO	0.23911

**Table A4.2.** A comparative account of the charge recombination lifetimes of photo-generated radical ion pair intermediates in the various reported literatures.

Sl. No.	Authors (Reference)	Assembly	Intermediates	Ion-pair survival time
01.	Guldi and co-workers ( <i>Chem. Sci.</i> <b>2015</b> , 6, 6878)	CND/SWCNT	Ox. CND and Red. SWCNT	105 and 20 ps
02.	Nakanishi, Shen and co-workers ( <i>Chem. Sci.</i> <b>2011</b> , 2, 2243)	SWCNT/C <sub>60</sub>	C <sub>60</sub> <sup>-</sup>	$\tau_{CS} = 0.44$ ns (CHCl <sub>3</sub> )
03.	Langa, Fukuzumi and co-workers ( <i>Chem. Sci.</i> <b>2014</b> , 5, 2072)	CNH/C <sub>60</sub>	CNH <sup>+</sup> and C <sub>60</sub> <sup>-</sup>	1 ns
04.	D'Souza, Ito and co-workers ( <i>Chem. Commun.</i> <b>2010</b> , 46, 8749)	SWCNT(7,6)/PyrC <sub>60</sub>	SWCNT(7,6) <sup>+</sup> and C <sub>60</sub> <sup>-</sup>	55.5 ns
		SWCNT(6,5)/PyrC <sub>60</sub>	SWCNT(6,5) <sup>+</sup> and C <sub>60</sub> <sup>-</sup>	82.6 ns
05.	Ito, D'Souza and co-workers ( <i>J. Am. Chem. Soc.</i> <b>2007</b> , 129, 15865)	SWCNT/Pyr-NH <sub>3</sub> <sup>+</sup> /C <sub>60</sub>	SWCNT <sup>+</sup> and C <sub>60</sub> <sup>-</sup>	100 ns

SWCNT = Single wall carbon nanotube, CND = Carbon nanodots, CNH = Carbon nanohorn, C<sub>60</sub> = fullerene

## 4.6. Appendix

### 4.6.1. Materials and methods

Similar to that discussed in section 2.6.1. (Chapter 2).

### 4.6.2. X-ray crystallography

Single crystal of A-Br (ethanol), P<sub>0</sub>A (*n*-hexane/ethyl acetate (1:1) mixture) and P<sub>1</sub>A (ethyl acetate/chloroform (1:1) mixture) were obtained by slow evaporation of solvent from homogenous solution at room temperature. High-quality specimen of approximate 0.25 × 0.20 × 0.15 (A-Br); 0.20 × 0.15 × 0.10 (P<sub>0</sub>A) and 0.20 × 0.20 × 0.05 (P<sub>1</sub>A) mm<sup>3</sup> dimension were selected for the X-ray diffraction experiments. Crystallographic and refinement data are presented in Table 4.1. All the instrumental parameters and the single crystal refining/solving methods were similar to that mentioned in Section 2.6.2. and 3.6.2. (Chapter 2 and 3).

### 4.6.3. Steady-State Spectroscopy

Instrumental parameters were same as that mentioned in section 2.6.3. (Chapter 2). To avoid the distortion arising from the inner filter effect, the concentration-dependent steady-state measurements were carried out in a cuvette of 1 mm path length [139]. Solution state relative quantum yield measurements of P<sub>0-2</sub> and P<sub>0-2</sub>A were performed using quinine sulphate in 0.1 M H<sub>2</sub>SO<sub>4</sub> ( $\lambda_{ex} = 350$  nm, reported  $\phi_f = 0.577$ ) as the standard [44]. Lifetime measurements were carried out in an IBH picosecond time correlated single photon counting (TCSPC) system. Pulse width of the excitation ( $\lambda_{ex} = 377$  nm) sources is determined to be  $\leq 100$  ps. The fluorescence decay profiles were de-convoluted using DAS6.3 fluorescence decay analysis software, and fitted with exponential decay, minimizing the  $\chi^2$  values.

### 4.6.4. Femtosecond transient absorption measurement (fTA)

Similar to that discussed in section 3.7.4. (Chapter 3).

### 4.6.5. Nanosecond transient absorption measurement (nTA)

Experimental technique was similar to that discussed in section 3.7.5. (Chapter 3).

The nanosecond transient spectrum of P<sub>0</sub>A (0.6 mM) in THF exhibit only ground-state bleach with no substantial positive transient absorption, indicative of the absence of triplet excited state and recombination of the radical-ion pair intermediates (if any) within the pulse width of the instrument.

#### 4.6.6. Global Analysis

Global analysis of the fTA spectra were performed using the program Glotaran [141, 142, 176]. The procedure takes into account instrument time response function and group velocity dispersion of the white continuum, and allows one to calculate decay time constants and dispersion-compensated time-resolved transient absorption spectra. In global analysis all the wavelengths were analyzed simultaneously using a parallel model to give decay associated spectra (DAS). The parallel sum-of-exponentials decay scheme produces the decay-associated spectra (DAS). DAS indicate the spectral changes that occur with their associated time constants. DAS of P<sub>0</sub>A (0.6 mM in THF) obtained by global analysis of  $\Delta A$  vs. time and wavelength based two-dimensional map of the fTA data is demonstrated in Figure 4.12b.

#### 4.6.7. Continuous-wave electron paramagnetic resonance (CW-EPR) spectroscopy

Continuous-wave EPR (CW-EPR) measurements with X band (8.75-9.65 GHz) were carried using JEOL JES-FA200 ESR spectrometer at room temperature and liquid nitrogen (77 K) temperatures. Samples were prepared by loading the THF solutions of P<sub>0</sub>A in 5 mm o.d. (4 mm i.d.) quartz tubes, subjecting them to nitrogen purging cycles and was sealed later using a rubber septum. Samples were photoexcited inside the EPR cavity with a USHIO Optical Modulex-XENON lamp-ES-UXL 500 (input current = 20 amperes). The acquisition of the EPR samples were carried out with a modulation frequency (100 kHz, width = 0.1 mT), phase (0 degree), sweep time (30.0 s) and time constants of 0.1 and 0.03 s. The EPR spectra was calibrated against an internal manganese (Mn) standard for accurate determination of  $g$  values. Simulations of CW-EPR spectra for P<sub>0</sub>A radical pairs were carried out using

EasySpin 5.0.21 [228]. Simulation of the hyperfine resolved spectrum demonstrates an uncoupled characteristics of the two complimentary radicals with  $S = \frac{1}{2}$  spins, which could be attributed to the twisted geometry of the donor and acceptor in the P<sub>0</sub>A dyad. Attempts to simulate the coupled spin of the radical centers lead to inaccurate simulation as compared to experimental EPR spectrum.

#### **4.6.8. Morphological Analysis**

##### **4.6.8.1. Dynamic light scattering (DLS) measurement**

Dynamic light scattering (DLS) measurement of P<sub>0</sub>A in THF (0.6 mM) was carried out on a Malvern Zeta Sizer Nano Zs equipped with 655 nm laser. The solutions of P<sub>0</sub>A for DLS analysis were prepared in THF and the experiment was carried out in a 3 ml square quartz cuvette (10 mm pathlength) at 25 °C at a back scattering angle of 173°.

##### **4.6.8.2. Atomic force microscopy (AFM)**

AFM analyses were carried out on multimode scanning probe microscope (Veeco Nanoscope V, digital instruments). Samples for analyses were prepared by drop casting 0.6 mM solutions of the samples (P<sub>0</sub>A) in THF on a silicon wafer surface and dried under vacuum. To exclude any artefacts, blank experiments were performed with solvent alone evaporated on silicon wafer. Imaging was done under ambient conditions in tapping mode regime. Micro-fabricated antimony doped silicon cantilever (MPP-11100-10, resonance frequency- 279–379 KHz, spring constant- 20–80 Nm<sup>-1</sup>) tip was used to probe the sample surface. The scan rates were varied from 0.5 Hz to 1.5 Hz and AFM section analyses were carried out offline. The average diameter of the spherical particles of P<sub>0</sub>A were estimated from the Lorentzian fit of the histogram of the particle size distribution curves obtained after correcting for the tip-broadening effect.

##### **4.6.8.3. Scanning Electron Microscopy (SEM)**

FE-SEM measurements of P<sub>0</sub>A was carried out on FEI Nova NanoSEM 450 (FEG type) by drop casting P<sub>0</sub>A (0.6 mM) in THF on the flat surface of silicon wafer (Ted Pella, Inc.) and allowing to evaporate the excess solvent under air in dust free

conditions. The samples were further dried under vacuum and subjected to thin chromium sputtering using Quorum Q150T ES fine coater to increase the signal/noise ratio. The probing side was inserted into the scanning electron microscope for obtaining the images. The average diameter of the particles was determined from the Lorentzian fit of the size distribution curve.

#### **4.6.8.4. Transmission Electron Microscopy (TEM)**

TEM measurements were carried out on JEOL 2010 with an accelerating voltage of 200 kV. The samples were prepared by drop casting THF solutions of P<sub>0</sub>A (0.6 mM) on a 400 mesh carbon-coated copper grid (Ted Pella, Inc.) at ambient conditions and allowing the excess solvent to evaporate under air in dust free conditions. The samples were further dried under vacuum and the TEM images were obtained without staining. The average diameter of the particles was determined from the Lorentzian fit of the histogram of the particle size distribution curves. To investigate and verify whether the packing arrangement of the aggregates is in agreement with that observed in the crystal structure, we carried out the selected area electron diffraction (SAED) for P<sub>0</sub>A in THF and estimated the interplanar distance (*d*-spacing). Analyzing the first and the second concentric rings in the SAED pattern of P<sub>0</sub>A in THF (Figure 4.9f) led to the *d*-spacing values of 5.14 and 3.02 Å respectively.

#### **4.6.9. Cyclic Voltammetry (CV)**

Similar to that discussed in section 3.7.8. (Chapter 3).

#### **4.6.10. UV-vis spectroelectrochemical (SEC) analysis**

The UV-vis spectroelectrochemical experiments were performed on a hybrid BASi Epsilon-Ocean Optics UV-Vis-NIR spectroelectrochemical setup using a UV-vis quartz cuvette (10 mm path-length) with a Pt gauze working electrode, a Pt wire counter electrode and an Ag/AgCl reference electrode. The UV-vis SEC analysis of P<sub>0</sub>A and A-Br in THF indicates the growth of a new band (570-600 nm) with increasing reduction potential (0 to -1.5V) which depicts the formation of radical anion of aceanthrylene (A<sup>-</sup>). To the best of our knowledge we report radical anion of

A ( $A^-$ ) for the first time, which have been unknown to-date owing to low photostability of the parent compound (A) [200]. Similarly, to characterize the radical cation of pyrene, SEC analysis of  $P_0A$  and pyrene ( $P_0$ ) were carried out in THF by applying a potential of 2500 mV. The difference spectra obtained before and after the oxidation shows the presence of the pyrene radical cation with a broad absorption in the region of 400-500 nm.

#### 4.6.11. Rehm-Weller Analysis

Similar to that discussed in section 3.7.9. (Chapter 3). The term  $r_{DA} = 7.73 \text{ \AA}$  is determined for  $P_0A$  by estimating the center-to-center distance between  $P_0$  and A using Mercury 3.5.1. The dielectric constant also influences the solvation free energy of the ions and should be corrected for if we wish to apply these potentials to calculate  $\Delta G_{et}$  in different solvents. According to the Rehm-Weller relation[31] based on the Born model the solvation free energy of an ion pair is given by equation 4, where  $r_D$  and  $r_A$  are effective radii of the cation and the anion radical which were approximated as  $r_{DA}/2$ . The Rehm-Weller relation (equation 3.1., Chapter 3) gives the free energy of charge separation as -1.04 eV ( $^1P_0^* \rightarrow A$ ) for the electron transfer from photoexcited donor to the acceptor.

#### 4.6.12. Electron affinity

The gas-phase electron affinity (EA) is the ability of a molecule to accept an electron and form an anion. However, in solution the stabilization of the anion by the surrounding solvent molecules is another criteria which has to be taken into account while discussing EA's. The gas-phase EA can be related to solution phase electrode potentials ( $E_{1/2}$ ) of the neutral/radical anion pair obtained from the electrochemical techniques and can be written as[229]

$$E_{1/2} = EA - \Delta E_{sol} + E_{ref} \quad (4.4)$$

where  $\Delta E_{sol}$  is the free energy of solvation of the radical anion and  $E_{ref}$  is the reference potential ( $Ag/AgCl \approx -5.24 \text{ V}$ )[230] of the electrode used for the electrochemical

experiments.  $E_{1/2}$  for the aceanthrylene (A) was found to be -1.07 V from the optoelectronic (DFT) calculation of A at B3LYP/6-31G+(d,p) level of theory in Schrödinger Materials Science Suite using Jaguar DFT engine.

The free energy of the solvation of the radical anion can be determined from the Born relation[231] as

$$\Delta E_{sol} = -\frac{z^2 e^2}{2r} \left(1 - \frac{1}{\epsilon}\right) \left(\frac{1}{4\pi\epsilon_0}\right) \frac{1}{1.6 \times 10^{-19}} \text{ eV} \quad (4.5)$$

where  $\epsilon$  is the dielectric constant of the solvent and  $r$  is the radius of the anion, approximated herein as  $r_{DA}/2$ . The significant value of the calculated electron affinity ( $\approx 2.70$  eV) and a smaller value of  $\Delta E_{sol}$  (-1.47 eV) emphasize the capability of A to accept and delocalize the additional incoming charge. Weak paratropic ring current in five-membered ring, envisaged by nucleus independent chemical shift (NICS) calculations further validate the exceptional electron affinity of A [222, 232].

### 4.6.13. Computational methods

#### 4.6.13.1. Gaussian calculations

Ground-state optimized structure and harmonic oscillator frequencies were computed using density functional theory (DFT) at the Becke's three parameter functional in combination with the Lee-Yang-Parr correlation functional (B3LYP) and 6-31G+(d,p) basis set. The vertical excitation energies and oscillator strengths were calculated employing time dependent DFT (TDDFT) calculations at B3LYP/6-311G+(d,p) level of theory. All the computations were performed using the Gaussian 09 Rev. A.02 [134].

#### 4.6.13.2. Quantum theory of atoms in molecules (QTAIM)[103, 124]

Similar to that discussed in section 2.6.6.2. (Chapter 2).

#### 4.6.13.3. Hirshfeld Analysis[125]:

Similar to that discussed in section 2.6.6.3. (Chapter 2).

#### 4.6.13.4. Schrodinger Material Science Suite:

Schrodinger Materials Science Suite 2015-1 provides diverse set of tools for predicting and computing reactivity and properties of chemical systems. The core simulation engine, Jaguar[185] is a high performance abinitio quantum mechanical package commercially produced and maintained by Schrodinger Inc. Employing pseudospectral approach, Jaguar estimates the Coulomb and exchange terms, providing significant advantages of exact exchange terms. Geometry optimization and single point energy calculations for monomer, dimer, tetramer and octamer were performed at B3LYP-D3/6-31G+(d,p) level of theory using the crystal structure as the input for the frontier molecular orbital (FMO) analyses. Energy gap is determined as the difference between energies of LUMO and HOMO as described in equation 3. Energy level diagram is plotted using the energies obtained from FMO analyses.

DFT calculations of the Marcus theory reorganization energies ( $\lambda$ ) and electronic coupling constants ( $V$ ) were performed using optoelectronics panel of the Jaguar package. The nonadiabatic charge transfer and hopping between adjacent molecules in the  $P_0A$  ensemble can be considered as an incoherent hopping model. The rate of charge motion ( $W$ ) between neighboring molecules, in terms of the reorganization energy  $\lambda$  and the coupling matrix element  $V$  could be described by the following equations[233]

$$W = \frac{V^2}{\hbar} \left( \frac{\pi}{\lambda k_B T} \right)^{\frac{1}{2}} e^{\left( -\frac{\lambda}{4k_B T} \right)} \quad (4.6)$$

where  $k_B$  is Boltzmann constant and  $T$  is temperature. The diffusion rate arising from the hopping between neighboring molecules in the organic crystals can be assumed having no correlation between hopping events and that charge motion is a homogeneous random walk.

$$D = \frac{1}{2n} \sum_i r_i^2 W_i P_i \quad (4.7)$$

Here  $n$  is the spatial dimensionality,  $W_i$  is the hopping rate due to charge transfer to  $i$ th neighbor,  $r_i$  is the distance to the  $i$ th neighbor,  $P_i$  is the hopping probability for the charge carrier to a particular  $i$ th neighbor, which can be calculated as

$$P_i = \frac{W_i}{\sum_i W_i} \quad (4.8)$$

Furthermore, the drift mobility arising from the hopping could be evaluated by Einstein relation as,

$$\mu = \frac{e}{k_B T} D \quad (4.9)$$

The charge carrier diffusion length can be obtained from the diffusion coefficient and lifetime of the charge separated state by the following relation,

$$L = \sqrt{D\tau} \quad (4.10)$$

where  $\tau$  is lifetime of the charge separated state. Based on the lifetime of the charge carriers ( $\tau_h = 1.28$  ns and  $\tau_e = 6$  ps) the diffusion length of hole and electrons are obtained as  $L_h = 25.8$  nm and  $L_e = 1.59$  nm respectively.



## 5. Bibliography

- [1] Gray, H. B.; Winkler, J. R., Electron flow through proteins, *Chem. Phys. Lett.* **2009**, *483*, 1-9.
- [2] Gust, D.; Moore, T. A.; Moore, A. L., Mimicking Photosynthetic Solar Energy Transduction, *Acc. Chem. Res.* **2001**, *34*, 40-48.
- [3] Wasielewski, M. R., Self-Assembly Strategies for Integrating Light Harvesting and Charge Separation in Artificial Photosynthetic Systems, *Acc. Chem. Res.* **2009**, *42*, 1910-1921.
- [4] Wasielewski, M. R., Photoinduced electron transfer in supramolecular systems for artificial photosynthesis, *Chem. Rev.* **1992**, *92*, 435-461.
- [5] Mirkovic, T.; Ostroumov, E. E.; Anna, J. M.; van Grondelle, R.; Govindjee; Scholes, G. D., Light Absorption and Energy Transfer in the Antenna Complexes of Photosynthetic Organisms, *Chem. Rev.* **2017**, *117*, 249-293.
- [6] Kodis, G.; Terazono, Y.; Liddell, P. A.; Andréasson, J.; Garg, V.; Hambourger, M.; Moore, T. A.; Moore, A. L.; Gust, D., Energy and Photoinduced Electron Transfer in a Wheel-Shaped Artificial Photosynthetic Antenna-Reaction Center Complex, *J. Am. Chem. Soc.* **2006**, *128*, 1818-1827.
- [7] Fukuzumi, S.; Ohkubo, K.; Suenobu, T., Long-Lived Charge Separation and Applications in Artificial Photosynthesis, *Acc. Chem. Res.* **2014**, *47*, 1455-1464.
- [8] Graham, L. E.; Graham, J. M.; Graham, J. M.; Wilcox, L. W., *Plant Biology: Pearson New International Edition*. Pearson Higher Education & Professional Group: 2013.
- [9] Listorti, A.; Durrant, J.; Barber, J., Solar to fuel, *Nat. Mater.* **2009**, *8*, 929.
- [10] Zhou, H.; Yan, R.; Zhang, D.; Fan, T., Challenges and Perspectives in Designing Artificial Photosynthetic Systems, *Chem. Eur. J.* **2016**, *22*, 9870-9885.
- [11] Strümpfer, J.; Şener, M.; Schulten, K., How Quantum Coherence Assists Photosynthetic Light-Harvesting, *J. Phys. Chem. Lett.* **2012**, *3*, 536-542.
- [12] Mirkovic, T.; Scholes, G. D., Photosynthetic Light Harvesting. in *Photobiology: The Science of Light and Life*, Björn, L. O., Ed. Springer New York: New York, NY, 2015; 231-241.
- [13] Vatter, A. E.; Wolfe, R. S., The Structure of Photosynthetic Bacteria, *J. Bacteriol.* **1958**, *75*, 480-488.
- [14] Şener, M.; Strümpfer, J.; Timney, J. A.; Freiberg, A.; Hunter, C. N.; Schulten, K., Photosynthetic Vesicle Architecture and Constraints on Efficient Energy Harvesting, *Biophys. J.* **2010**, *99*, 67-75.

- [15] Şener, M. K.; Olsen, J. D.; Hunter, C. N.; Schulten, K., Atomic-level structural and functional model of a bacterial photosynthetic membrane vesicle, *Proc. Natl. Acad. Sci. U. S. A.* **2007**, *104*, 15723-15728.
- [16] Cardona, T.; Sedoud, A.; Cox, N.; Rutherford, A. W., Charge separation in Photosystem II: A comparative and evolutionary overview, *Biochim. Biophys. Acta - Bioenerg.* **2012**, *1817*, 26-43.
- [17] McDermott, G.; Prince, S. M.; Freer, A. A.; Hawthornthwaite-Lawless, A. M.; Papiz, M. Z.; Cogdell, R. J.; Isaacs, N. W., Crystal structure of an integral membrane light-harvesting complex from photosynthetic bacteria, *Nature* **1995**, *374*, 517.
- [18] Koepke, J.; Hu, X.; Muenke, C.; Schulten, K.; Michel, H., The crystal structure of the light-harvesting complex II (B800–850) from *Rhodospirillum rubrum*, *Structure* **1996**, *4*, 581-597.
- [19] Herek, J. L.; Fraser, N. J.; Pullerits, T.; Martinsson, P.; Polívka, T.; Scheer, H.; Cogdell, R. J.; Sundström, V., B800→B850 Energy Transfer Mechanism in Bacterial LH2 Complexes Investigated by B800 Pigment Exchange, *Biophys. J.* **2000**, *78*, 2590-2596.
- [20] van Oijen, A. M.; Ketelaars, M.; Köhler, J.; Aartsma, T. J.; Schmidt, J., Unraveling the Electronic Structure of Individual Photosynthetic Pigment-Protein Complexes, *Science* **1999**, *285*, 400-402.
- [21] Linnanto, J. M.; Korppi-Tommola, J. E. I., Modelling excitonic energy transfer in the photosynthetic unit of purple bacteria, *Chem. Phys.* **2009**, *357*, 171-180.
- [22] Damjanović, A.; Ritz, T.; Schulten, K., Energy transfer between carotenoids and bacteriochlorophylls in light-harvesting complex II of purple bacteria, *Phys. Rev. E* **1999**, *59*, 3293-3311.
- [23] Lee, H.; Cheng, Y.-C.; Fleming, G. R., Coherence Dynamics in Photosynthesis: Protein Protection of Excitonic Coherence, *Science* **2007**, *316*, 1462-1465.
- [24] Heldt, H. W.; Heldt, F.; Piechulla, B., *Plant Biochemistry*. Elsevier Science: 2005.
- [25] Chapter 19 - Mitochondria, Chloroplasts, Peroxisomes. in *Cell Biology*, Third ed.; Pollard, T. D.; Earnshaw, W. C.; Lippincott-Schwartz, J.; Johnson, G. T., Eds. Elsevier: 2017; 317-329.
- [26] Müller, P.; Li, X.-P.; Niyogi, K. K., Non-Photochemical Quenching. A Response to Excess Light Energy, *Plant Physiol.* **2001**, *125*, 1558-1566.
- [27] Valeur, B.; Berberan-Santos, M. N., *Molecular Fluorescence: Principles and Applications*. Wiley: 2012.
- [28] Turro, N. J.; Ramamurthy, V.; Scaiano, J. C., *Modern Molecular Photochemistry of Organic Molecules*. University Science Books: 2010.

- [29] Kasha, M., Characterization of electronic transitions in complex molecules, *Discuss. Faraday Soc.* **1950**, *9*, 14-19.
- [30] Wardle, B., *Principles and Applications of Photochemistry*. Wiley: 2009.
- [31] Weller, A., Photoinduced Electron Transfer in Solution: Exciplex and Radical Ion Pair Formation Free Enthalpies and their Solvent Dependence, *Z. Phys. Chem.* **1982**, *133*, 93-98.
- [32] Hartnett, P. E.; Dyar, S. M.; Margulies, E. A.; Shoer, L. E.; Cook, A. W.; Eaton, S. W.; Marks, T. J.; Wasielewski, M. R., Long-Lived Charge Carrier Generation in Ordered Films of a Covalent Perylenediimide-Diketopyrrolopyrrole-Perylenediimide Molecule, *Chem. Sci.* **2015**, *6*, 402-411.
- [33] Wu, Y.-L.; Brown, K. E.; Wasielewski, M. R., Extending Photoinduced Charge Separation Lifetimes by Using Supramolecular Design: Guanine-Perylenediimide G-Quadruplex, *J. Am. Chem. Soc.* **2013**, *135*, 13322-13325.
- [34] Scholes, G. D.; Ghiggino, K. P., Electronic Interactions and Interchromophore Excitation Transfer, *J. Phys. Chem.* **1994**, *98*, 4580-4590.
- [35] Förster, T., Zwischenmolekulare Energiewanderung und Fluoreszenz, *Ann. Phys. (Berlin)* **1948**, *437*, 55-75.
- [36] Braslavsky, S. E.; Fron, E.; Rodríguez, H. B.; Román, E. S.; Scholes, G. D.; Schweitzer, G.; Valeur, B.; Wirz, J., Pitfalls and limitations in the practical use of Förster's theory of resonance energy transfer, *Photochem. Photobiol. Sci.* **2008**, *7*, 1444-1448.
- [37] Kasha, M.; Rawls, H. R.; Ashraf El-Bayoumi, M., The exciton model in molecular spectroscopy, *Pure Appl. Chem.* **1965**, *11*, 371-392.
- [38] Kistler, K. A.; Pochas, C. M.; Yamagata, H.; Matsika, S.; Spano, F. C., Absorption, Circular Dichroism, and Photoluminescence in Perylene Diimide Bichromophores: Polarization-Dependent H- and J-Aggregate Behavior, *J. Phys. Chem. B* **2012**, *116*, 77-86.
- [39] Varghese, S.; Das, S., Role of Molecular Packing in Determining Solid-State Optical Properties of  $\pi$ -Conjugated Materials, *J. Phys. Chem. Lett.* **2011**, *2*, 863-873.
- [40] Kasha, M., Energy Transfer Mechanisms and the Molecular Exciton Model for Molecular Aggregates, *Radiation Research* **1963**, *20*, 55-70.
- [41] Austin, A.; Hestand, N. J.; McKendry, I. G.; Zhong, C.; Zhu, X.; Zdilla, M. J.; Spano, F. C.; Szarko, J. M., Enhanced Davydov Splitting in Crystals of a Perylene Diimide Derivative, *J. Phys. Chem. Lett.* **2017**, *8*, 1118-1123.
- [42] Hestand, N. J.; Spano, F. C., Expanded Theory of H- and J-Molecular Aggregates: The Effects of Vibronic Coupling and Intermolecular Charge Transfer, *Chem. Rev.* **2018**, *118*, 7069-7163.

- [43] Hinoue, T.; Shigenoi, Y.; Sugino, M.; Mizobe, Y.; Hisaki, I.; Miyata, M.; Tohnai, N., Regulation of  $\pi$ -Stacked Anthracene Arrangement for Fluorescence Modulation of Organic Solid from Monomer to Excited Oligomer Emission, *Chem. Eur. J.* **2012**, *18*, 4634-4643.
- [44] Lakowicz, J. R., *Principles of Fluorescence Spectroscopy*. 3rd ed.; Springer: 2007.
- [45] Smith, M. B.; Michl, J., Recent Advances in Singlet Fission, *Annu. Rev. Phys. Chem.* **2013**, *64*, 361-386.
- [46] Smith, M. B.; Michl, J., Singlet Fission, *Chem. Rev.* **2010**, *110*, 6891-6936.
- [47] van Grondelle, R., Excitation energy transfer, trapping and annihilation in photosynthetic systems, *Biochim. Biophys. Acta, Rev. Bioenerg.* **1985**, *811*, 147-195.
- [48] Fückel, B.; Hinze, G.; Nolde, F.; Müllen, K.; Basché, T., Quantification of the Singlet-Singlet Annihilation Times of Individual Bichromophoric Molecules by Photon Coincidence Measurements, *J. Phys. Chem. A* **2010**, *114*, 7671-7676.
- [49] Ciamician, G., The Photochemistry of the Future, *Science* **1912**, *36*, 385-394.
- [50] Fujishima, A.; Honda, K., Electrochemical Photolysis of Water at a Semiconductor Electrode, *Nature* **1972**, *238*, 37.
- [51] Akira, F.; Kenichi, H., Electrochemical Evidence for the Mechanism of the Primary Stage of Photosynthesis, *Bull. Chem. Soc. Jpn.* **1971**, *44*, 1148-1150.
- [52] Whang, D. R.; Apaydin, D. H., Artificial Photosynthesis: Learning from Nature, *ChemPhotoChem* **2018**, *2*, 148-160.
- [53] Inoue, T.; Fujishima, A.; Konishi, S.; Honda, K., Photoelectrocatalytic reduction of carbon dioxide in aqueous suspensions of semiconductor powders, *Nature* **1979**, *277*, 637.
- [54] Chen, S.; Takata, T.; Domen, K., Particulate photocatalysts for overall water splitting, *Nat. Rev. Mater.* **2017**, *2*, 17050.
- [55] Miseki, Y.; Sayama, K., Photocatalytic Water Splitting for Solar Hydrogen Production Using the Carbonate Effect and the Z-Scheme Reaction, *Adv. Energy Mater.* *0*, 1801294.
- [56] Takanabe, K., Photocatalytic Water Splitting: Quantitative Approaches toward Photocatalyst by Design, *ACS Catalysis* **2017**, *7*, 8006-8022.
- [57] Liu, C.; Colón, B. C.; Ziesack, M.; Silver, P. A.; Nocera, D. G., Water splitting-biosynthetic system with CO<sub>2</sub> reduction efficiencies exceeding photosynthesis, *Science* **2016**, *352*, 1210-1213.
- [58] Nocera, D. G., Solar Fuels and Solar Chemicals Industry, *Acc. Chem. Res.* **2017**, *50*, 616-619.
- [59] Goto, Y.; Hisatomi, T.; Wang, Q.; Higashi, T.; Ishikiriya, K.; Maeda, T.; Sakata, Y.; Okunaka, S.; Tokudome, H.; Katayama, M.; Akiyama, S.; Nishiyama, H.; Inoue, Y.;

- Takewaki, T.; Setoyama, T.; Minegishi, T.; Takata, T.; Yamada, T.; Domen, K., A Particulate Photocatalyst Water-Splitting Panel for Large-Scale Solar Hydrogen Generation, *Joule* **2018**, *2*, 509-520.
- [60] Hedley, G. J.; Ruseckas, A.; Samuel, I. D. W., Light Harvesting for Organic Photovoltaics, *Chem. Rev.* **2017**, *117*, 796-837.
- [61] Tang, C. W., Two-layer organic photovoltaic cell, *Appl. Phys. Lett.* **1986**, *48*, 183-185.
- [62] Kumaresan, P.; Vegiraju, S.; Ezhumalai, Y.; Yau, S.; Kim, C.; Lee, W.-H.; Chen, M.-C., Fused-Thiophene Based Materials for Organic Photovoltaics and Dye-Sensitized Solar Cells, *Polymers* **2014**, *6*, 2645.
- [63] Mallia, A. R.; Salini, P. S.; Hariharan, M., Nonparallel Stacks of Donor and Acceptor Chromophores Evade Geminate Charge Recombination, *J. Am. Chem. Soc.* **2015**, *137*, 15604-15607.
- [64] Ley, D.; Guzman, C. X.; Adolfsson, K. H.; Scott, A. M.; Braunschweig, A. B., Cooperatively Assembling Donor-Acceptor Superstructures Direct Energy Into an Emergent Charge Separated State, *J. Am. Chem. Soc.* **2014**, *136*, 7809-7812.
- [65] Wang, M.; Wudl, F., Top-Down Meets Bottom-Up: Organized Donor-Acceptor Heterojunctions for Organic Solar Cells, *J. Mater. Chem.* **2012**, *22*, 24297-24314.
- [66] Dössel, L. F.; Kamm, V.; Howard, I. A.; Laquai, F.; Pisula, W.; Feng, X.; Li, C.; Takase, M.; Kudernac, T.; De Feyter, S.; Müllen, K., Synthesis and Controlled Self-Assembly of Covalently Linked Hexa-peri-hexabenzocoronene/Perylene Diimide Dyads as Models To Study Fundamental Energy and Electron Transfer Processes, *J. Am. Chem. Soc.* **2012**, *134*, 5876-5886.
- [67] Yamamoto, Y.; Fukushima, T.; Suna, Y.; Ishii, N.; Saeki, A.; Seki, S.; Tagawa, S.; Taniguchi, M.; Kawai, T.; Aida, T., Photoconductive Coaxial Nanotubes of Molecularly Connected Electron Donor and Acceptor Layers, *Science* **2006**, *314*, 1761-1764.
- [68] Zhang, W.; Jin, W.; Fukushima, T.; Saeki, A.; Seki, S.; Aida, T., Supramolecular Linear Heterojunction Composed of Graphite-Like Semiconducting Nanotubular Segments, *Science* **2011**, *334*, 340-343.
- [69] Idé, J.; Méreau, R.; Ducasse, L.; Castet, F.; Bock, H.; Olivier, Y.; Cornil, J.; Beljonne, D.; D'Avino, G.; Roscioni, O. M.; Muccioli, L.; Zannoni, C., Charge Dissociation at Interfaces between Discotic Liquid Crystals: The Surprising Role of Column Mismatch, *J. Am. Chem. Soc.* **2014**, *136*, 2911-2920.
- [70] Sinks, L. E.; Rybtchinski, B.; Iimura, M.; Jones, B. A.; Goshe, A. J.; Zuo, X.; Tiede, D. M.; Li, X.; Wasielewski, M. R., Self-Assembly of Photofunctional Cylindrical Nanostructures Based on Perylene-3,4:9,10-bis(dicarboximide), *Chem. Mater.* **2005**, *17*, 6295-6303.

- [71] Bill, N. L.; Ishida, M.; Kawashima, Y.; Ohkubo, K.; Sung, Y. M.; Lynch, V. M.; Lim, J. M.; Kim, D.; Sessler, J. L.; Fukuzumi, S., Long-lived charge-separated states produced in supramolecular complexes between anionic and cationic porphyrins, *Chem. Sci.* **2014**, *5*, 3888-3896.
- [72] Schenning, A. P. H. J.; v. Herrikhuyzen, J.; Jonkheijm, P.; Chen, Z.; Würthner, F.; Meijer, E. W., Photoinduced Electron Transfer in Hydrogen-Bonded Oligo(p-phenylene vinylene)-Perylene Bisimide Chiral Assemblies, *J. Am. Chem. Soc.* **2002**, *124*, 10252-10253.
- [73] Hayashi, H.; Nihashi, W.; Umeyama, T.; Matano, Y.; Seki, S.; Shimizu, Y.; Imahori, H., Segregated Donor-Acceptor Columns in Liquid Crystals That Exhibit Highly Efficient Ambipolar Charge Transport, *J. Am. Chem. Soc.* **2011**, *133*, 10736-10739.
- [74] Chu, C.-C.; Raffy, G.; Ray, D.; Guerso, A. D.; Kauffmann, B.; Wantz, G.; Hirsch, L.; Bassani, D. M., Self-Assembly of Supramolecular Fullerene Ribbons via Hydrogen-Bonding Interactions and Their Impact on Fullerene Electronic Interactions and Charge Carrier Mobility, *J. Am. Chem. Soc.* **2010**, *132*, 12717-12723.
- [75] García-Iglesias, M.; Peuntinger, K.; Kahnt, A.; Krausmann, J.; Vázquez, P.; González-Rodríguez, D.; Guldi, D. M.; Torres, T., Supramolecular Assembly of Multicomponent Photoactive Systems via Cooperatively Coupled Equilibria, *J. Am. Chem. Soc.* **2013**, *135*, 19311-19318.
- [76] Charvet, R.; Yamamoto, Y.; Sasaki, T.; Kim, J.; Kato, K.; Takata, M.; Saeki, A.; Seki, S.; Aida, T., Segregated and Alternately Stacked Donor/Acceptor Nanodomains in Tubular Morphology Tailored with Zinc Porphyrin-C60 Amphiphilic Dyads: Clear Geometrical Effects on Photoconduction, *J. Am. Chem. Soc.* **2012**, *134*, 2524-2527.
- [77] Sforazzini, G.; Orentas, E.; Bolag, A.; Sakai, N.; Matile, S., Toward Oriented Surface Architectures with Three Coaxial Charge-Transporting Pathways, *J. Am. Chem. Soc.* **2013**, *135*, 12082-12090.
- [78] Lefler, K. M.; Co, D. T.; Wasielewski, M. R., Self-Assembly-Induced Ultrafast Photodriven Charge Separation in Perylene-3,4-dicarboximide-Based Hydrogen-Bonded Foldamers, *J. Phys. Chem. Lett.* **2012**, *3*, 3798-3805.
- [79] Rieth, S.; Li, Z.; Hinkle, C. E.; Guzman, C. X.; Lee, J. J.; Nehme, S. I.; Braunschweig, A. B., Superstructures of Diketopyrrolopyrrole Donors and Perylenediimide Acceptors Formed by Hydrogen-Bonding and  $\pi\cdots\pi$  Stacking, *J. Phys. Chem. C* **2013**, *117*, 11347-11356.
- [80] Tovar, J. D., Supramolecular Construction of Optoelectronic Biomaterials, *Acc. Chem. Res.* **2013**, *46*, 1527-1537.

- [81] Sanders, A. M.; Magnanelli, T. J.; Bragg, A. E.; Tovar, J. D., Photoinduced Electron Transfer within Supramolecular Donor–Acceptor Peptide Nanostructures under Aqueous Conditions, *J. Am. Chem. Soc.* **2016**, *138*, 3362-3370.
- [82] Wu, Y.-L.; Brown, K. E.; Gardner, D. M.; Dyar, S. M.; Wasielewski, M. R., Photoinduced Hole Injection into a Self-Assembled  $\pi$ -Extended G-Quadruplex, *J. Am. Chem. Soc.* **2015**, *137*, 3981-3990.
- [83] Wu, Y.-L.; Horwitz, N. E.; Chen, K.-S.; Gomez-Gualdron, D. A.; Luu, N. S.; Ma, L.; Wang, T. C.; Hersam, M. C.; Hupp, J. T.; Farha, O. K.; Snurr, R. Q.; Wasielewski, M. R., G-Quadruplex Organic Frameworks, *Nat. Chem.* **2017**, *9*, 466-472.
- [84] Wu, Y.-L.; Bobbitt, N. S.; Logsdon, J. L.; Powers-Riggs, N. E.; Nelson, J. N.; Liu, X.; Wang, T. C.; Snurr, R. Q.; Hupp, J. T.; Farha, O. K.; Hersam, M. C.; Wasielewski, M. R., Tunable Crystallinity and Charge Transfer in Two-Dimensional G-Quadruplex Organic Frameworks, *Angew. Chem., Int. Ed.* **2018**, *57*, 3985-3989.
- [85] Yamamoto, Y.; Zhang, G.; Jin, W.; Fukushima, T.; Ishii, N.; Saeki, A.; Seki, S.; Tagawa, S.; Minari, T.; Tsukagoshi, K.; Aida, T., Ambipolar-Transporting Coaxial Nanotubes with a Tailored Molecular Graphene–Fullerene Heterojunction, *Proc. Natl. Acad. Sci. U. S. A.* **2009**, *106*, 21051-21056.
- [86] Anthony, J. E., Functionalized Acenes and Heteroacenes for Organic Electronics, *Chem. Rev.* **2006**, *106*, 5028-5048.
- [87] Park, S. K.; Kim, J. H.; Park, S. Y., Organic 2D Optoelectronic Crystals: Charge Transport, Emerging Functions, and Their Design Perspective, *Adv. Mater.* *0*, 1704759.
- [88] Ostroverkhova, O., Organic Optoelectronic Materials: Mechanisms and Applications, *Chem. Rev.* **2016**, *116*, 13279-13412.
- [89] Gierschner, J.; Park, S. Y., Luminescent distyrylbenzenes: tailoring molecular structure and crystalline morphology, *J. Mater. Chem. C* **2013**, *1*, 5818-5832.
- [90] Davydov, A. S., The theory of molecular excitons, *Usp. Fiz. Nauk* **1964**, *82*, 393-448.
- [91] de Halleux, V.; Calbert, J. P.; Brocorens, P.; Cornil, J.; Declercq, J. P.; Brédas, J. L.; Geerts, Y., 1,3,6,8-Tetraphenylpyrene Derivatives: Towards Fluorescent Liquid-Crystalline Columns?, *Adv. Funct. Mater.* **2004**, *14*, 649-659.
- [92] Spano, F. C., The Spectral Signatures of Frenkel Polarons in H- and J-Aggregates, *Acc. Chem. Res.* **2010**, *43*, 429-439.
- [93] Aragó, J.; Troisi, A., Dynamics of the Excitonic Coupling in Organic Crystals, *Physical Review Letters* **2015**, *114*, 026402.
- [94] Jelley, E. E., Spectral Absorption and Fluorescence of Dyes in the Molecular State, *Nature* **1936**, *138*, 1009-1010.

- [95] Scheibe, G.; Schöntag, A.; Katheder, F., Fluoreszenz und Energiefortleitung bei reversibel polymerisierten Farbstoffen, *Naturwissenschaften* **1939**, 29, 499-501.
- [96] Würthner, F.; Kaiser, T. E.; Saha-Möller, C. R., J-Aggregates: From Serendipitous Discovery to Supramolecular Engineering of Functional Dye Materials. In *Angew. Chem., Int. Ed.*, WILEY-VCH Verlag: 2011; Vol. 50, pp 3376-3410.
- [97] Xie, Z.; Yang, B.; Li, F.; Cheng, G.; Liu, L.; Yang, G.; Xu, H.; Ye, L.; Hanif, M.; Liu, S.; Ma, D.; Ma, Y., Cross Dipole Stacking in the Crystal of Distyrylbenzene Derivative: The Approach toward High Solid-State Luminescence Efficiency, *J. Am. Chem. Soc.* **2005**, 127, 14152-14153.
- [98] Lewis, F. D.; Yang, J.-S., Solid-State Fluorescence of Aromatic Dicarboxamides. Dependence upon Crystal Packing, *J. Phys. Chem. B* **1997**, 101, 1775-1781.
- [99] Scholes, G. D.; Rumbles, G., Excitons in nanoscale systems, *Nat. Mater.* **2006**, 5, 683-696.
- [100] Sundström, V.; Gillbro, T., Excited state dynamics and photophysics of aggregated dye chromophores in solution, *J. Chem. Phys.* **1985**, 83, 2733-2743.
- [101] Liu, H.; Yao, L.; Li, B.; Chen, X.; Gao, Y.; Zhang, S.; Li, W.; Lu, P.; Yang, B.; Ma, Y., Excimer-induced high-efficiency fluorescence due to pairwise anthracene stacking in a crystal with long lifetime, *Chem. Commun.* **2016**, 52, 7356-7359.
- [102] Atsushi, S.; Eisuke, O.; Yuichi, Y.; Mirai, T.; Yasunori, M.; Kazuhiko, M.; Hiroshi, I., New Fluorescence Domain "Excited Multimer" Formed upon Photoexcitation of Continuously Stacked Diaroylmethanoboron Difluoride Molecules with Fused  $\pi$ -Orbitals in Crystals, *Chem. Eur. J.* **2015**, 21, 18128-18137.
- [103] Rajagopal, S. K.; Philip, A. M.; Nagarajan, K.; Hariharan, M., Progressive Acylation of Pyrene Engineers Solid State Packing and Colour via C-H•••H-C, C-H•••O and p-p Interactions, *Chem. Commun.* **2014**, 50, 8644-8647.
- [104] Nagarajan, K.; Gopan, G.; Cheriya, R. T.; Hariharan, M., Long alkyl side-chains impede exciton interaction in organic light harvesting crystals, *Chem. Commun.* **2017**, 53, 7409-7411.
- [105] Nagarajan, K.; Rajagopal, S. K.; Hariharan, M., C-H•••H-C and C-H•••p contacts Aid Transformation of Dimeric to Monomeric Anthracene in the Solid State, *CrystEngComm* **2014**, 16, 8946-8949.
- [106] Birks, J. B.; Christophorou, L. G., Excimer Formation in Polycyclic Hydrocarbons and their Derivatives, *Nature* **1963**, 197, 1064-1065.
- [107] Jenekhe, S. A.; Osaheni, J. A., Excimers and Exciplexes of Conjugated Polymers, *Science* **1994**, 265, 765-768.

- [108] Luo, J.; Xie, Z.; Lam, J. W. Y.; Cheng, L.; Chen, H.; Qiu, C.; Kwok, H. S.; Zhan, X.; Liu, Y.; Zhu, D.; Tang, B. Z., Aggregation-induced emission of 1-methyl-1,2,3,4,5-pentaphenylsilole, *Chem. Commun.* **2001**, 1740-1741.
- [109] Son, M.; Park, K. H.; Shao, C.; Würthner, F.; Kim, D., Spectroscopic Demonstration of Exciton Dynamics and Excimer Formation in a Sterically Controlled Perylene Bisimide Dimer Aggregate, *J. Phys. Chem. Lett.* **2014**, *5*, 3601-3607.
- [110] Jagtap, S. P.; Mukhopadhyay, S.; Coropceanu, V.; Brizius, G. L.; Brédas, J.-L.; Collard, D. M., Closely Stacked Oligo(phenylene ethynylene)s: Effect of  $\pi$ -Stacking on the Electronic Properties of Conjugated Chromophores, *J. Am. Chem. Soc.* **2012**, *134*, 7176-7185.
- [111] Zhang, H. Y.; Zhang, Z. L.; Ye, K. Q.; Zhang, J. Y.; Wang, Y., Organic Crystals with Tunable Emission Colors Based on a Single Organic Molecule and Different Molecular Packing Structures, *Adv. Mater.* **2006**, *18*, 2369-2372.
- [112] Li, F.; Gao, N.; Xu, H.; Liu, W.; Shang, H.; Yang, W.; Zhang, M., Relationship between Molecular Stacking and Optical Properties of 9,10-Bis((4-N,N-dialkylamino)styryl) Anthracene Crystals: The Cooperation of Excitonic and Dipolar Coupling, *Chem. Eur. J.* **2014**, *20*, 9991-9997.
- [113] Hayashi, T.; Mataga, N.; Sakata, Y.; Misumi, S.; Morita, M.; Tanaka, J., Excimer fluorescence and photodimerization of anthracenophanes and 1,2-dianthrylethanes, *J. Am. Chem. Soc.* **1976**, *98*, 5910-5913.
- [114] Chen, J.; Neels, A.; Fromm, K. M., Excimer formation in crystalline and nanostructured coordination polymers, *Chem. Commun.* **2010**, *46*, 8282-8284.
- [115] Kaanumalle, L. S.; Gibb, C. L. D.; Gibb, B. C.; Ramamurthy, V., A Hydrophobic Nanocapsule Controls the Photophysics of Aromatic Molecules by Suppressing Their Favored Solution Pathways, *J. Am. Chem. Soc.* **2005**, *127*, 3674-3675.
- [116] Zhang, G.; Yang, G.; Wang, S.; Chen, Q.; Ma, J. S., A Highly Fluorescent Anthracene-Containing Hybrid Material Exhibiting Tunable Blue-Green Emission Based on the Formation of an Unusual "T-Shaped" Excimer, *Chem. Eur. J.* **2007**, *13*, 3630-3635.
- [117] Lekha, P. K.; Prasad, E., Aggregation-Controlled Excimer Emission from Anthracene-Containing Polyamidoamine Dendrimers, *Chem. Eur. J.* **2010**, *16*, 3699-3706.
- [118] Mizobe, Y.; Miyata, M.; Hisaki, I.; Hasegawa, Y.; Tohnai, N., Anomalous Anthracene Arrangement and Rare Excimer Emission in the Solid State: Transcription and Translation of Molecular Information, *Org. Lett.* **2006**, *8*, 4295-4298.
- [119] Olivier, J. H.; Camerel, F.; Barberá, J.; Retailleau, P.; Ziessel, R., Ionic Liquid Crystals Formed by Self-Assembly around an Anionic Anthracene Core, *Chem. Eur. J.* **2009**, *15*, 8163-8174.

- [120] Cheriya, R. T.; Nagarajan, K.; Hariharan, M., Single-Component Organic Light-Harvesting Red Luminescent Crystal, *J. Phys. Chem. C* **2013**, *117*, 3240-3248.
- [121] Philip, A. M.; Mallia, A. R.; Hariharan, M., Prolonged Charge Separated States in Twisted Stacks of All-Carbon Donor and Acceptor Chromophores, *J. Phys. Chem. Lett.* **2016**, *7*, 4751-4756.
- [122] Philip, A. M.; Kuriakose, F.; Hariharan, M., Unsolicited Photoexcited-State Pathways Relegate the Long-Lived Charge Separation in Self-Assembled Nucleobase-Arene Conjugate, *J. Phys. Chem. C* **2017**, *121*, 23259-23267.
- [123] Friedel, C.; Crafts, J. M., Sur une nouvelle méthode générale de synthèse d'hydrocarbures, d'acétones, etc., *Compt. Rend.* **1877**, *84*, 1392-1395.
- [124] Bader, R. F. W., *Atoms in Molecules: A Quantum Theory*. Clarendon Press: 1994.
- [125] Spackman, M. A.; Jayatilaka, D., Hirshfeld Surface Analysis, *CrystEngComm* **2009**, *11*, 19-32.
- [126] Loots, L.; Barbour, L. J., A Simple and Robust Method for the Identification of p-p Packing Motifs of Aromatic Compounds, *CrystEngComm* **2012**, *14*, 300-304.
- [127] Curtis, M. D.; Cao, J.; Kampf, J. W., Solid-State Packing of Conjugated Oligomers: From  $\pi$ -Stacks to the Herringbone Structure, *J. Am. Chem. Soc.* **2004**, *126*, 4318-4328.
- [128] Rajagopal, S. K.; Mallia, A. R.; Hariharan, M., Enhanced intersystem crossing in carbonylpyrenes, *Phys. Chem. Chem. Phys.* **2017**, *19*, 28225-28231.
- [129] v. Berlepsch, H.; Böttcher, C., H-Aggregates of an Indocyanine Cy5 Dye: Transition from Strong to Weak Molecular Coupling, *J. Phys. Chem. B* **2015**, *119*, 11900-11909.
- [130] Cheriya, R. T.; Joy, J.; Alex, A. P.; Shaji, A.; Hariharan, M., Energy Transfer in Near-Orthogonally Arranged Chromophores Separated through a Single Bond, *J. Phys. Chem. C* **2012**, *116*, 12489-12498.
- [131] Krueger, B. P.; Scholes, G. D.; Fleming, G. R., Calculation of Couplings and Energy-Transfer Pathways between the Pigments of LH2 by the ab Initio Transition Density Cube Method, *J. Phys. Chem. B* **1998**, *102*, 5378-5386.
- [132] Chaikin, P. M.; Lubensky, T. C., *Principles of Condensed Matter Physics*. Cambridge University Press: 2000.
- [133] *Variation in the rotational angle dependent transport property in crystalline PTE-Br<sub>4</sub> is due to the large longitudinal and transverse slips in the slip-stacked molecular assembly. For comparing with PTE-Br<sub>2</sub>, molecular centroids of the two molecules of PTE-Br<sub>4</sub> were collimated via nullifying the longitudinal and the transverse slips (see Table S10, Figure S21, SI).*
- [134] Frisch, M. J.; Trucks, G. W.; Schlegel, H. B.; Scuseria, G. E.; Robb, M. A.; Cheeseman, J. R.; Scalmani, G.; Barone, V.; Mennucci, B.; Petersson, G. A.; Nakatsuji, H.; Caricato, M.; Li, X.; Hratchian, H. P.; Izmaylov, A. F.; Bloino, J.; Zheng, G.; Sonnenberg, J. L.;

- Hada, M.; Ehara, M.; Toyota, K.; Fukuda, R.; Hasegawa, J.; Ishida, M.; Nakajima, T.; Honda, Y.; Kitao, O.; Nakai, H.; Vreven, T.; Montgomery Jr., J. A.; Peralta, J. E.; Ogliaro, F.; Bearpark, M. J.; Heyd, J.; Brothers, E. N.; Kudin, K. N.; Staroverov, V. N.; Kobayashi, R.; Normand, J.; Raghavachari, K.; Rendell, A. P.; Burant, J. C.; Iyengar, S. S.; Tomasi, J.; Cossi, M.; Rega, N.; Millam, N. J.; Klene, M.; Knox, J. E.; Cross, J. B.; Bakken, V.; Adamo, C.; Jaramillo, J.; Gomperts, R.; Stratmann, R. E.; Yazyev, O.; Austin, A. J.; Cammi, R.; Pomelli, C.; Ochterski, J. W.; Martin, R. L.; Morokuma, K.; Zakrzewski, V. G.; Voth, G. A.; Salvador, P.; Dannenberg, J. J.; Dapprich, S.; Daniels, A. D.; Farkas, Ö.; Foresman, J. B.; Ortiz, J. V.; Cioslowski, J.; Fox, D. J. *Gaussian 09 Rev. A.02*, Gaussian, Inc.: Wallingford CT, USA, 2009.
- [135] Sheldrick, G., A Short History of SHELX, *Acta Cryst. A* **2008**, *64*, 112-122.
- [136] Farrugia, L., WinGX Suite for Small-Molecule Single-Crystal Crystallography, *J. Appl. Cryst.* **1999**, *32*, 837-838.
- [137] Bruno, I. J.; Cole, J. C.; Edgington, P. R.; Kessler, M.; Macrae, C. F.; McCabe, P.; Pearson, J.; Taylor, R., New Software for Searching the Cambridge Structural Database and Visualizing Crystal Structures, *Acta Cryst. B* **2002**, *58*, 389-397.
- [138] Macrae, C. F.; Bruno, I. J.; Chisholm, J. A.; Edgington, P. R.; McCabe, P.; Pidcock, E.; Rodriguez-Monge, L.; Taylor, R.; van de Streek, J.; Wood, P. A., Mercury CSD 2.0 - New Features for the Visualization and Investigation of Crystal Structures, *J. Appl. Cryst.* **2008**, *41*, 466-470.
- [139] Mallia, A. R.; Philip, A. M.; Bhat, V.; Hariharan, M., Persistent Charge-Separated States in Self-Assembled Twisted Nonsymmetric Donor-Acceptor Triads, *J. Phys. Chem. C* **2017**, *121*, 4765-4777.
- [140] Cölle, M.; Gmeiner, J.; Milius, W.; Hillebrecht, H.; Brütting, W., Preparation and Characterization of Blue-Luminescent Tris(8-hydroxyquinoline)-aluminum (Alq3), *Adv. Funct. Mater.* **2003**, *13*, 108-112.
- [141] Snellenburg, J. J.; Laptinok, S. P.; Seger, R.; Mullen, K. M.; van Stokkum, I. H. M., Glotaran: A Java-Based Graphical User Interface for the R-package TIMP, *J. Stat. Softw.* **2012**, *49*, 1-22.
- [142] van Stokkum, I. H. M.; Larsen, D. S.; van Grondelle, R., Global and Target Analysis of Time-Resolved Spectra, *Biochim. Biophys. Acta - Bioenerg.* **2004**, *1657*, 82-104.
- [143] Wolff, S. K.; Grimwood, D. J.; McKinnon, J. J.; Turner, M. J.; Jayatilaka, D.; Spackman, M. A. *CrystalExplorer (Version 3.1)*, University of Western Australia, 2012.
- [144] Gust, D.; Moore, T. A.; Moore, A. L., Solar Fuels via Artificial Photosynthesis, *Acc. Chem. Res.* **2009**, *42*, 1890-1898.

- [145] Yang, L.; Brazier, J. B.; Hubbard, T. A.; Rogers, D. M.; Cockroft, S. L., Can Dispersion Forces Govern Aromatic Stacking in an Organic Solvent?, *Angew. Chem., Int. Ed.* **2016**, *55*, 912-916.
- [146] Jin, S.; Supur, M.; Addicoat, M.; Furukawa, K.; Chen, L.; Nakamura, T.; Fukuzumi, S.; Irle, S.; Jiang, D., Creation of Superheterojunction Polymers via Direct Polycondensation: Segregated and Bicontinuous Donor-Acceptor  $\pi$ -Columnar Arrays in Covalent Organic Frameworks for Long-Lived Charge Separation, *J. Am. Chem. Soc.* **2015**, *137*, 7817-7827.
- [147] Middleton, C. T.; de La Harpe, K.; Su, C.; Law, Y. K.; Crespo-Hernández, C. E.; Bern, K., DNA Excited-State Dynamics: From Single Bases to the Double Helix, *Annu. Rev. Phys. Chem.* **2009**, *60*, 217-239.
- [148] Kawai, K.; Majima, T., Hole Transfer Kinetics of DNA, *Acc. Chem. Res.* **2013**, *46*, 2616-2625.
- [149] Schuster, G. B., Long-Range Charge Transfer in DNA: Transient Structural Distortions Control the Distance Dependence, *Acc. Chem. Res.* **2000**, *33*, 253-260.
- [150] Harris, M. A.; Mishra, A. K.; Young, R. M.; Brown, K. E.; Wasielewski, M. R.; Lewis, F. D., Direct Observation of the Hole Carriers in DNA Photoinduced Charge Transport, *J. Am. Chem. Soc.* **2016**, *138*, 5491-5494.
- [151] Schreier, W. J.; Schrader, T. E.; Koller, F. O.; Gilch, P.; Crespo-Hernández, C. E.; Swaminathan, V. N.; Carell, T.; Zinth, W.; Kohler, B., Thymine Dimerization in DNA is an Ultrafast Photoreaction, *Science* **2007**, *315*, 625-629.
- [152] Hariharan, M.; Lewis, F. D., Context-Dependent Photodimerization in Isolated Thymine-Thymine Steps in DNA, *J. Am. Chem. Soc.* **2008**, *130*, 11870-11871.
- [153] Sinha, R. P.; Hader, D.-P., UV-Induced DNA Damage and Repair: A Review, *Photochem. Photobiol. Sci.* **2002**, *1*, 225-236.
- [154] Cheriya, R. T.; Mallia, A. R.; Hariharan, M., Light Harvesting Vesicular Donor-Acceptor Scaffold Limits the Rate of Charge Recombination in the Presence of an Electron Donor, *Energy Environ. Sci.* **2014**, *7*, 1661-1669.
- [155] Cheriya, R. T.; Joy, J.; Rajagopal, S. K.; Nagarajan, K.; Hariharan, M., DNA-Enforced Conformational Restriction of an Atropisomer, *J. Phys. Chem. C* **2012**, *116*, 22631-22636.
- [156] Qiao, J. X.; Lam, P. Y. S., Copper-Promoted Carbon-Heteroatom Bond Cross-Coupling with Boronic Acids and Derivatives, *Synthesis* **2011**, *6*, 829-856.
- [157] Yue, Y.; Zheng, Z.-G.; Wu, B.; Xia, C.-Q.; Yu, X.-Q., Copper-Catalyzed Cross-Coupling Reactions of Nucleobases with Arylboronic Acids: An Efficient Access to N-Arylnucleobases, *Eur. J. Org. Chem.* **2005**, *2005*, 5154-5157.
- [158] Kuhlemeier, C., Phyllotaxis, *Trends Plant Sci.* **2007**, *12*, 143-150.

- [159] Fraind, A. M.; Sini, G.; Risko, C.; Ryzhkov, L. R.; Brédas, J.-L.; Tovar, J. D., Charge Delocalization through Benzene, Naphthalene, and Anthracene Bridges in  $\pi$ -Conjugated Oligomers: An Experimental and Quantum Chemical Study, *J. Phys. Chem. B* **2013**, *117*, 6304-6317.
- [160] Kucheryavy, P.; Li, G.; Vyas, S.; Hadad, C.; Glusac, K. D., Electronic Properties of 4-Substituted Naphthalimides, *J. Phys. Chem. A* **2009**, *113*, 6453-6461.
- [161] Lauer, A.; Dobryakov, A. L.; Kovalenko, S. A.; Fidler, H.; Heyne, K., Dual photochemistry of anthracene-9,10-endoperoxide studied by femtosecond spectroscopy, *Phys. Chem. Chem. Phys.* **2011**, *13*, 8723-8732.
- [162] Bebelaar, D., Time Resolved Molecular Spectroscopy Using High Power Solid State Lasers in Pulse Transmission Mode. A Re-Examination of the  $S_n \leftarrow S_1$  Spectra of Naphthalene and Anthracene, *Chem. Phys.* **1974**, *3*, 205-216.
- [163] Liu, A.; Sauer, M. C.; Loffredo, D. M.; Trifunac, A. D., Transient Absorption Spectra of Aromatic Radical Cations in Hydrocarbon Solutions, *J. Photochem. Photobiol. A* **1992**, *67*, 197-208.
- [164] Banyasz, A.; Ketola, T.-M.; Muñoz-Losa, A.; Rishi, S.; Adhikary, A.; Sevilla, M. D.; Martinez-Fernandez, L.; Improta, R.; Markovitsi, D., UV-Induced Adenine Radicals Induced in DNA A-Tracts: Spectral and Dynamical Characterization, *J. Phys. Chem. Lett.* **2016**, *7*, 3949-3953.
- [165] Shida, T.; Iwata, S., Electronic Spectra of Ion Radicals and Their Molecular Orbital Interpretation. III. Aromatic Hydrocarbons, *J. Am. Chem. Soc.* **1973**, *95*, 3473-3483.
- [166] Shida, T.; Iwata, S., Absorption Spectra of Dianthracene Anion Radical and Anthracene Dimer Anion, *J. Chem. Phys.* **1972**, *56*, 2858-2864.
- [167] Roest, M. R.; Verhoeven, J. W.; Schuddeboom, W.; Warman, J. M.; Lawson, J. M.; Paddon-Row, M. N., Solvent and Distance Dependent Charge Separation in Rigid Trichromophoric Systems, *J. Am. Chem. Soc.* **1996**, *118*, 1762-1768.
- [168] Imahori, H.; El-Khouly, M. E.; Fujitsuka, M.; Ito, O.; Sakata, Y.; Fukuzumi, S., Solvent Dependence of Charge Separation and Charge Recombination Rates in Porphyrin-Fullerene Dyad, *J. Phys. Chem. A* **2001**, *105*, 325-332.
- [169] Fukuzumi, S.; Ohkubo, K.; Imahori, H.; Guldi, D. M., Driving Force Dependence of Intermolecular Electron-Transfer Reactions of Fullerenes, *Chem. Eur. J.* **2003**, *9*, 1585-1593.
- [170] Martin, M. M.; Plaza, P.; Changenet-Barret, P.; Siemiarczuk, A., UV-Vis Subpicosecond Spectroscopy of 4-(9-Anthryl)-N,N'-dimethylaniline in Polar and Nonpolar Solvents: A Two-Dimensional View of the Photodynamics, *J. Phys. Chem. A* **2002**, *106*, 2351-2358.

- [171] Zweig, A.; Maurer, A. H.; Roberts, B. G., Oxidation, Reduction, and Electrochemiluminescence of Donor-Substituted Polycyclic Aromatic Hydrocarbons, *J. Org. Chem.* **1967**, *32*, 1322-1329.
- [172] Banyasz, A.; Martinez-Fernandez, L.; Ketola, T.-M.; Muñoz-Losa, A.; Esposito, L.; Markovitsi, D.; Improta, R., Excited State Pathways Leading to Formation of Adenine Dimers, *J. Phys. Chem. Lett.* **2016**, *7*, 2020-2023.
- [173] Spek, A., PLATON SQUEEZE: A Tool for the Calculation of the Disordered Solvent Contribution to the Calculated Structure Factors, *Acta Cryst. C* **2015**, *71*, 9-18.
- [174] Spek, A., Single-Crystal Structure Validation with the Program PLATON, *J. Appl. Cryst.* **2003**, *36*, 7-13.
- [175] Berlman, I. B., in *Handbook of Fluorescence Spectra of Aromatic Molecules* (2<sup>nd</sup> Ed.), Berlman, I. B., Ed. Academic Press: 1971; 1-473.
- [176] van Stokkum, I. H. M.; Larsen, D. S.; van Grondelle, R., Erratum to "Global and Target Analysis of Time-Resolved Spectra" [Biochimica et Biophysica Acta 1658/2-3 (2004) 82-104], *Biochim. Biophys. Acta - Bioenerg.* **2004**, *1658*, 262.
- [177] Deng, P.; Liu, L.; Ren, S.; Li, H.; Zhang, Q., N-Acylation: An Effective Method for Reducing the LUMO Energy Levels of Conjugated Polymers Containing Five-Membered Lactam Units, *Chem. Commun.* **2012**, *48*, 6960-6962.
- [178] Wen, X.-L.; Zhang, J.; Liu, Z.-L.; Han, Z.-X.; Rieker, A., Micellar Effects on the Oxidative Electrochemistry of Lipophilic Vitamin C Derivatives, *J. Chem. Soc., Perkin Trans. 2* **1998**, 905-910.
- [179] Kamamoto, Y.; Nitta, Y.; Kubo, K.; Mizuta, T.; Kume, S., Selection of Two Optional Covalent Bonds by Electric Stimuli: Dual Catalytic Switching of Redox-Active Copper, *Chem. Commun.* **2016**, *52*, 10486-10489.
- [180] Seidel, C. A. M.; Schulz, A.; Sauer, M. H. M., Nucleobase-Specific Quenching of Fluorescent Dyes. 1. Nucleobase One-Electron Redox Potentials and Their Correlation with Static and Dynamic Quenching Efficiencies, *J. Phys. Chem.* **1996**, *100*, 5541-5553.
- [181] Serrano-Andrés, L.; Merchán, M.; Borin, A. C., Adenine and 2-Aminopurine: Paradigms of Modern Theoretical Photochemistry, *Proc. Natl. Acad. Sci. U. S. A.* **2006**, *103*, 8691-8696.
- [182] Peng, L. W.; Keelan, B. W.; Semmes, D. H.; Zewail, A. H., Dynamics of Intramolecular Vibrational Energy Redistribution in Deuteriated Anthracenes: Rotational Band Contour Analysis and Time-Resolved Measurements, *J. Phys. Chem.* **1988**, *92*, 5540-5549.
- [183] Zilberg, S.; Haas, Y.; Shaik, S., Electronic Spectrum of Anthracene: An ab-Initio Molecular Orbital Calculation Combined with a Valence Bond Interpretation, *J. Phys. Chem.* **1995**, *99*, 16558-16565.

- [184] Avila Ferrer, F. J.; Cerezo, J.; Stendardo, E.; Improta, R.; Santoro, F., Insights for an Accurate Comparison of Computational Data to Experimental Absorption and Emission Spectra: Beyond the Vertical Transition Approximation, *J. Chem. Theory Comput.* **2013**, *9*, 2072-2082.
- [185] Bochevarov, A. D.; Harder, E.; Hughes, T. F.; Greenwood, J. R.; Braden, D. A.; Philipp, D. M.; Rinaldo, D.; Halls, M. D.; Zhang, J.; Friesner, R. A., Jaguar: A High-Performance Quantum Chemistry Software Program with Strengths in Life and Materials Sciences, *Int. J. Quantum Chem.* **2013**, *113*, 2110-2142.
- [186] Georgakilas, V.; Perman, J. A.; Tucek, J.; Zboril, R., Broad Family of Carbon Nanoallotropes: Classification, Chemistry, and Applications of Fullerenes, Carbon Dots, Nanotubes, Graphene, Nanodiamonds, and Combined Superstructures, *Chem. Rev.* **2015**, *115*, 4744-4822.
- [187] Saito, S., Carbon Nanotubes for Next-Generation Electronics Devices, *Science* **1997**, *278*, 77-78.
- [188] Umeyama, T.; Imahori, H., Photofunctional Hybrid Nanocarbon Materials, *J. Phys. Chem. C* **2013**, *117*, 3195-3209.
- [189] Umeyama, T.; Imahori, H., Carbon Nanotube-Modified Electrodes for Solar Energy Conversion, *Energy Environ. Sci.* **2008**, *1*, 120-133.
- [190] Guldi, D. M., Fullerene-Porphyrin Architectures; Photosynthetic Antenna and Reaction Center Models, *Chem. Soc. Rev.* **2002**, *31*, 22-36.
- [191] Liu, T.; Troisi, A., What Makes Fullerene Acceptors Special as Electron Acceptors in Organic Solar Cells and How to Replace Them, *Adv. Mater.* **2013**, *25*, 1038-1041.
- [192] D'Souza, F.; Chitta, R.; Sandanayaka, A. S. D.; Subbaiyan, N. K.; D'Souza, L.; Araki, Y.; Ito, O., Supramolecular Carbon Nanotube-Fullerene Donor-Acceptor Hybrids for Photoinduced Electron Transfer, *J. Am. Chem. Soc.* **2007**, *129*, 15865-15871.
- [193] Vizueté, M.; Gomez-Escalonilla, M. J.; Fierro, J. L. G.; Ohkubo, K.; Fukuzumi, S.; Yudasaka, M.; Iijima, S.; Nierengarten, J.-F.; Langa, F., Photoinduced Electron Transfer in a Carbon Nanohorn-C<sub>60</sub> Conjugate, *Chem. Sci.* **2014**, *5*, 2072-2080.
- [194] Tung, V. C.; Huang, J.-H.; Tevis, I.; Kim, F.; Kim, J.; Chu, C.-W.; Stupp, S. I.; Huang, J., Surfactant-Free Water-Processable Photoconductive All-Carbon Composite, *J. Am. Chem. Soc.* **2011**, *133*, 4940-4947.
- [195] Kennedy, R. D.; Ayzner, A. L.; Wanger, D. D.; Day, C. T.; Halim, M.; Khan, S. I.; Tolbert, S. H.; Schwartz, B. J.; Rubin, Y., Self-Assembling Fullerenes for Improved Bulk-Heterojunction Photovoltaic Devices, *J. Am. Chem. Soc.* **2008**, *130*, 17290-17292.
- [196] Heumueller, T.; Mateker, W. R.; Distler, A.; Fritze, U. F.; Cheacharoen, R.; Nguyen, W. H.; Biele, M.; Salvador, M.; von Delius, M.; Egelhaaf, H.-J.; McGehee, M. D.; Brabec, C.

- J., Morphological and Electrical Control of Fullerene Dimerization Determines Organic Photovoltaic Stability, *Energy Environ. Sci.* **2016**, *9*, 247-256.
- [197] Nielsen, C. B.; Holliday, S.; Chen, H.-Y.; Cryer, S. J.; McCulloch, I., Non-Fullerene Electron Acceptors for Use in Organic Solar Cells, *Acc. Chem. Res.* **2015**, *48*, 2803-2812.
- [198] Sauvé, G.; Fernando, R., Beyond Fullerenes: Designing Alternative Molecular Electron Acceptors for Solution-Processable Bulk Heterojunction Organic Photovoltaics, *J. Phys. Chem. Lett.* **2015**, *6*, 3770-3780.
- [199] Dang, H.; Garcia-Garibay, M. A., Palladium-Catalyzed Formation of Aceanthrylenes: A Simple Method for Peri-Cyclopentenelation of Aromatic Compounds, *J. Am. Chem. Soc.* **2001**, *123*, 355-356.
- [200] Dang, H.; Levitus, M.; Garcia-Garibay, M. A., One Step Pd(0)-Catalyzed Synthesis, X-ray Analysis, and Photophysical Properties of Cyclopent[*hi*]aceanthrylene: Fullerene-Like Properties in a Nonalternant Cyclopentafused Aromatic Hydrocarbon, *J. Am. Chem. Soc.* **2002**, *124*, 136-143.
- [201] Jellison, J. L.; Lee, C.-H.; Zhu, X.; Wood, J. D.; Plunkett, K. N., Electron Acceptors Based on an All-Carbon Donor-Acceptor Copolymer, *Angew. Chem., Int. Ed.* **2012**, *51*, 12321-12324.
- [202] Wakamiya, A.; Nishimura, H.; Fukushima, T.; Suzuki, F.; Saeki, A.; Seki, S.; Osaka, I.; Sasamori, T.; Murata, M.; Murata, Y.; Kaji, H., On-Top  $\pi$ -Stacking of Quasiplanar Molecules in Hole-Transporting Materials: Inducing Anisotropic Carrier Mobility in Amorphous Films, *Angew. Chem., Int. Ed.* **2014**, *53*, 5800-5804.
- [203] Xia, H.; Liu, D.; Xu, X.; Miao, Q., Ambipolar Organic Semiconductors from Electron-Accepting Cyclopenta-Fused Anthracene, *Chem. Commun.* **2013**, *49*, 4301-4303.
- [204] Gu, X.; Xu, X.; Li, H.; Liu, Z.; Miao, Q., Synthesis, Molecular Packing, and Thin Film Transistors of Dibenzo[*a,m*]rubicenes, *J. Am. Chem. Soc.* **2015**, *137*, 16203-16208.
- [205] Winters, M. U.; Dahlstedt, E.; Blades, H. E.; Wilson, C. J.; Frampton, M. J.; Anderson, H. L.; Albinsson, B., Probing the Efficiency of Electron Transfer through Porphyrin-Based Molecular Wires, *J. Am. Chem. Soc.* **2007**, *129*, 4291-4297.
- [206] Weidemaier, K.; Tavernier, H. L.; Swallen, S. F.; Fayer, M. D., Photoinduced Electron Transfer and Geminate Recombination in Liquids, *J. Phys. Chem. A* **1997**, *101*, 1887-1902.
- [207] Higashino, T.; Yamada, T.; Yamamoto, M.; Furube, A.; Tkachenko, N. V.; Miura, T.; Kobori, Y.; Jono, R.; Yamashita, K.; Imahori, H., Remarkable Dependence of the Final Charge Separation Efficiency on the Donor-Acceptor Interaction in Photoinduced Electron Transfer, *Angew. Chem., Int. Ed.* **2016**, *55*, 629-633.
- [208] Miura, T.; Tao, R.; Shibata, S.; Umeyama, T.; Tachikawa, T.; Imahori, H.; Kobori, Y., Geometries, Electronic Couplings, and Hole Dissociation Dynamics of Photoinduced

- Electron–Hole Pairs in Polyhexylthiophene–Fullerene Dyads Rigidly Linked by Oligophenylenes, *J. Am. Chem. Soc.* **2016**, *138*, 5879–5885.
- [209] Kilså, K.; Kajanus, J.; Macpherson, A. N.; Mårtensson, J.; Albinsson, B., Bridge-Dependent Electron Transfer in Porphyrin-Based Donor–Bridge–Acceptor Systems, *J. Am. Chem. Soc.* **2001**, *123*, 3069–3080.
- [210] Wiberg, J.; Guo, L.; Pettersson, K.; Nilsson, D.; Ljungdahl, T.; Mårtensson, J.; Albinsson, B., Charge Recombination versus Charge Separation in Donor–Bridge–Acceptor Systems, *J. Am. Chem. Soc.* **2007**, *129*, 155–163.
- [211] Pettersson, K.; Wiberg, J.; Ljungdahl, T.; Mårtensson, J.; Albinsson, B., Interplay between Barrier Width and Height in Electron Tunneling: Photoinduced Electron Transfer in Porphyrin-Based Donor–Bridge–Acceptor Systems, *J. Phys. Chem. A* **2006**, *110*, 319–326.
- [212] Talipov, M. R.; Navale, T. S.; Rathore, R., The HOMO Nodal Arrangement in Polychromophoric Molecules and Assemblies Controls the Interchromophoric Electronic Coupling, *Angew. Chem., Int. Ed.* **2015**, *54*, 14468–14472.
- [213] Kaiser, C.; Schmiedel, A.; Holzapfel, M.; Lambert, C., Long-Lived Singlet and Triplet Charge Separated States in Small Cyclophane-Bridged Triarylamine-Naphthalene Diimide Dyads, *J. Phys. Chem. C* **2012**, *116*, 15265–15280.
- [214] Davis, W. B.; Svec, W. A.; Ratner, M. A.; Wasielewski, M. R., Molecular-wire behaviour in p -phenylenevinylene oligomers, *Nature* **1998**, *396*, 60.
- [215] Sukegawa, J.; Schubert, C.; Zhu, X.; Tsuji, H.; Guldi, D. M.; Nakamura, E., Electron transfer through rigid organic molecular wires enhanced by electronic and electron–vibration coupling, *Nat. Chem.* **2014**, *6*, 899.
- [216] Natali, M.; Campagna, S.; Scandola, F., Photoinduced electron transfer across molecular bridges: electron- and hole-transfer superexchange pathways, *Chem. Soc. Rev.* **2014**, *43*, 4005–4018.
- [217] Thomas, K. G.; Biju, V.; Kamat, P. V.; George, M. V.; Guldi, D. M., Dynamics of Photoinduced Electron-Transfer Processes in Fullerene-Based Dyads: Effects of Varying the Donor Strength, *ChemPhysChem* **2003**, *4*, 1299–1307.
- [218] Goldsmith, R. H.; Sinks, L. E.; Kelley, R. F.; Betzen, L. J.; Liu, W.; Weiss, E. A.; Ratner, M. A.; Wasielewski, M. R., Wire-like charge transport at near constant bridge energy through fluorene oligomers, *Proc. Natl. Acad. Sci. U. S. A.* **2005**, *102*, 3540–3545.
- [219] Gélinas, S.; Rao, A.; Kumar, A.; Smith, S. L.; Chin, A. W.; Clark, J.; van der Poll, T. S.; Bazan, G. C.; Friend, R. H., Ultrafast Long-Range Charge Separation in Organic Semiconductor Photovoltaic Diodes, *Science* **2014**, *343*, 512–516.
- [220] Calik, M.; Auras, F.; Salonen, L. M.; Bader, K.; Grill, I.; Handloser, M.; Medina, D. D.; Dogru, M.; Löbermann, F.; Trauner, D.; Hartschuh, A.; Bein, T., Extraction of

- Photogenerated Electrons and Holes from a Covalent Organic Framework Integrated Heterojunction, *J. Am. Chem. Soc.* **2014**, *136*, 17802-17807.
- [221] Mallia, A. R.; Hariharan, M., Self-Assembled Donor–Acceptor Trefoils: Long-Lived Charge Separated State through Aggregation, *J. Phys. Chem. C* **2017**, *121*, 4778-4788.
- [222] Radenkovic, S.; Durdevic, J.; Bultinck, P., Local Aromaticity of the Five-Membered Rings in Acenaphthylene Derivatives, *Phys. Chem. Chem. Phys.* **2012**, *14*, 14067-14078.
- [223] Wood, J. D.; Jellison, J. L.; Finke, A. D.; Wang, L.; Plunkett, K. N., Electron Acceptors Based on Functionalizable Cyclopenta[hi]aceanthrylenes and Dicyclopenta[de,mn]tetracenes, *J. Am. Chem. Soc.* **2012**, *134*, 15783-15789.
- [224] Plummer, B. F.; Singleton, S. F., An Analysis of the Electronic States of Aceanthrylene, *J. Phys. Chem.* **1990**, *94*, 7363-7366.
- [225] Neti, V. S. P. K.; Ceron, M. R.; Duarte-Ruiz, A.; Olmstead, M. M.; Balch, A. L.; Echegoyen, L., High-Yield, Regiospecific Bis-Functionalization of C<sub>70</sub> Using a Diels-Alder Reaction in Molten Anthracene, *Chem. Commun.* **2014**, *50*, 10584-10587.
- [226] Lai, R. Y.; Fleming, J. J.; Merner, B. L.; Vermeij, R. J.; Bodwell, G. J.; Bard, A. J., Electrogenerated Chemiluminescence. 74. Photophysical, Electrochemical, and Electrogenerated Chemiluminescent Studies of Selected Nonplanar Pyrenophanes, *J. Phys. Chem. A* **2004**, *108*, 376-383.
- [227] Guha, S.; Goodson, F. S.; Corson, L. J.; Saha, S., Boundaries of Anion/Naphthalenediimide Interactions: From Anion- $\pi$  Interactions to Anion-Induced Charge-Transfer and Electron-Transfer Phenomena, *J. Am. Chem. Soc.* **2012**, *134*, 13679-13691.
- [228] Stoll, S.; Schweiger, A., Easyspin, A Comprehensive Software Package for Spectral Simulation and Analysis in EPR, *J. Magn. Reson.* **2006**, *178*, 42-55.
- [229] Ruoff, R. S.; Kadish, K. M.; Boulas, P.; Chen, E. C. M., Relationship between the Electron Affinities and Half-Wave Reduction Potentials of Fullerenes, Aromatic Hydrocarbons, and Metal Complexes, *J. Phys. Chem.* **1995**, *99*, 8843-8850.
- [230] Trasatti, S., The Absolute Electrode Potential: An Explanatory Note (Recommendations 1986), *Pure Appl. Chem.* **1986**, *58*, 955-966.
- [231] Bockris, J. O. M.; Reddy, A. K. N., *Modern Electrochemistry: Ionics*. Springer US, 1998; Vol. 1.
- [232] Schleyer, P. v. R.; Maerker, C.; Dransfeld, A.; Jiao, H.; Hommes, N. J. R. v. E., Nucleus-Independent Chemical Shifts: A Simple and Efficient Aromaticity Probe, *J. Am. Chem. Soc.* **1996**, *118*, 6317-6318.
- [233] Deng, W.-Q.; Goddard, W. A., Predictions of Hole Mobilities in Oligoacene Organic Semiconductors from Quantum Mechanical Calculations, *J. Phys. Chem. B* **2004**, *108*, 8614-8621.

## 6. List of Publications

### Journal Articles

- 11 *Carbonylation of Pyrene: Crystal Engineering  $\pi$ -ways for Charge Transport.*  
Rajagopal, S. K.; John, A. P.; Roy, A.; **Philip, A. M.**; Bhat, V.; Thalukulam, M.\*; and Hariharan, M.\*  
(To be communicated)
- 10 *Decoding the Curious Tale of Atypical Excited State Dynamics in Regioisomeric Acetylanthracenes*  
**Philip, A. M.**; Gudem, M.; Sebastian, E.; and Hariharan, M.\*  
(To be communicated)
- 09 *Null Exciton Splitting in Chromophoric Greek Cross (+) Aggregate*  
Sebastian, E.;<sup>+</sup> **Philip, A. M.**; <sup>+</sup> Benny, A.; Hariharan, M.\*  
Angew. Chem. Int. Ed. **2018**, 57, 15696-15701 (+ - contributed equally)
- 08 *Concerted Interplay of Excimer and Dipole Coupling Governs the Exciton Relaxation Dynamics in Crystalline Anthracenes*  
**Philip, A. M.**; Manikandan, S.; Shaji, A.\*; and Hariharan, M.\*  
Chem. Eur. J. **2018**, 24, 18089-18096
- 07 *Viable Access to the Triplet Excited State in Peryleneimide Based Palladium Complex*  
**Philip, A. M.**; Sebastian, E.; Gopan, G.; Ramakrishnan, R. and Hariharan, M.\*  
J. Chem. Sci. **2018**, 130, 137
- 06 *Unsolicited Photoexcited State Pathways Relegate the Long-Lived Charge Separation in Self-Assembled Nucleobase-Arene Conjugate*  
**Philip, A. M.**; Kuriakose, F.; and Hariharan, M.\*  
J. Phys. Chem. C **2017**, 121, 23259-23267 (Outside Frontispiece)
- 05 *Persistent Charge-Separated States in Self-Assembled Twisted Nonsymmetric Donor-Acceptor Triads*  
Mallia, A. R.; **Philip, A. M.**; Bhat, V.; and Hariharan, M.\*  
J. Phys. Chem. C, **2017**, 121, 4765-4777 (Outside Frontispiece)
- 04 *Prolonged Charge Separated States in Twisted Stacks of All-Carbon Donor and Acceptor Chromophores*  
**Philip, A. M.**; Mallia, A. R.; and Hariharan, M.\*  
J. Phys. Chem. Lett. **2016**, 7, 4751-4756 (Highlighted as ACS Liveslides)
- 03 *On the Origin of Multiexponential Fluorescence Decays from 2-Aminopurine-Labeled Dinucleotides*  
Remington, J. M.; **Philip, A. M.**; Hariharan, M.; and Kohler, B.\*  
J. Chem. Phys. **2016**, 145, 155101

- 02 *Progressive Acylation of Pyrene Engineers Solid State Packing and Colour via C-H•••H-C, C-H•••O and  $\pi$ - $\pi$  Interactions*

Rajagopal, S. K.; **Philip, A. M.**; Nagarajan, K.; and Hariharan, M.\*

Chem. Commun. **2014**, 50, 8644-8647 (Inside Frontispiece)

**Book Chapter**

- 01 *Excited State Dynamics in Chromophore Appended Nucleic Acids*

**Philip, A. M.**; Bhat, V.; and Hariharan, M.\*

Templated DNA Nanotechnology: Functional DNA Nanoarchitectonics (Editor: T. Govindaraju), Pan Stanford Publications, Singapore: **2018** (In Press)

## 7. Internship, Workshop and Conferences

- 08 Invited Lightning Talk and Poster Presentation at "*Faraday Discussions (2018): Photoinduced Processes in Nucleic Acids and Proteins*" (January 11-13, 2018) held at Thiruvananthapuram, Kerala, India.
- 07 Visited **South Dakota State University, United States** (August-December, 2017) under the Prestigious "*Bhaskara Advanced Solar Energy (BASE) Fellowship*" program supported by the Indo-U.S. Science and Technology Forum (IUSSTF) and the Department of Science and Technology (DST), Govt. of India.  
Research Topic: Exploration of Novel Nonfullerene Acceptors for Organic Photovoltaic Applications. (Host: Prof. Qiquan Qiao, SDSU).
- 06 Invited Short Talk in "*Inter-IISER Chemistry Meet 2017 (IICM 2017)*" (January 19-22, 2017) held at IISER-Bhopal, Madhya Pradesh, India.
- 05 Poster Presentation in "*12<sup>th</sup> JNC Research Conference on "Chemistry of Materials"*" (September 23-25, 2016) held at Thiruvananthapuram, Kerala, India. (Best Poster Presentation Prize)
- 04 Participated in *Inter-IISER Chemistry Meet 2016 (IICM 2016)* (December 11-13, 2015) held at IISER-TVM, Thiruvananthapuram, Kerala, India.
- 03 Participated in "*8<sup>th</sup> Asian Photochemistry Conference (APC-2014)*" (November 10-13) held at Kovalam, Thiruvananthapuram, Kerala, India.
- 02 Participated in *DAE-BRNS conference on "Organic Device: A Future Ahead (ODeFA-2014)"* (March 03-06, 2014) held at Bhabha Atomic Research Centre (BARC), Mumbai, India.
- 01 Participated in "*ACS on Campus Workshop*" an initiative from American Chemical Society (November 29, 2013) held at National Institute for Interdisciplinary Science and Technology (NIIST), Thiruvananthapuram, Kerala, India.

---

## 8. Copyrights and Permissions



RightsLink®

Home

Account Info

Help



**SPRINGER NATURE**

**Title:** Photosynthetic Light Harvesting

**Author:** Tihana Mirkovic, Gregory D. Scholes

**Publication:** Springer eBook

**Publisher:** Springer Nature

**Date:** Jan 1, 2015

Copyright © 2015, Springer Science Business Media  
New York

Logged in as:

Abbey Philip  
Indian Institute of Science  
Education and Research,  
Thiruvananthapuram (IISER-  
TVM)

Account #:  
3001089150

LOGOUT

### Order Completed

Thank you for your order.

This Agreement between Indian Institute of Science Education and Research, Thiruvananthapuram (IISER-TVM) -- Abbey Philip ("You") and Springer Nature ("Springer Nature") consists of your license details and the terms and conditions provided by Springer Nature and Copyright Clearance Center.

Your confirmation email will contain your order number for future reference.

### [printable details](#)

License Number	4434641100386
License date	Sep 23, 2018
Licensed Content Publisher	Springer Nature
Licensed Content Publication	Springer eBook
Licensed Content Title	Photosynthetic Light Harvesting
Licensed Content Author	Tihana Mirkovic, Gregory D. Scholes
Licensed Content Date	Jan 1, 2015
Type of Use	Thesis/Dissertation
Requestor type	non-commercial (non-profit)
Format	print and electronic
Portion	figures/tables/illustrations
Number of figures/tables/illustrations	1
Will you be translating?	no
Circulation/distribution	2,001 to 5,000
Author of this Springer Nature content	no
Title	Moderation the Photogenerated Exciton and Charge Transfer Dynamics in Molecular Aggregates
Instructor name	Dr. Mahesh Hariharan
Institution name	Indian Institute of Science Education and Research Thiruvananthapuram (IISER-TVM)
Expected presentation date	Dec 2018
Portions	Fig. 17.3, Page 234
Requestor Location	Indian Institute of Science Education and Research, Thiruvananthapuram (IISER-TVM) PhD Student, IISER-TVM CET Campus Sreekaryam Trivandrum, Kerala 695016 India Attn: Abbey M. Philip
Billing Type	Invoice
Billing address	Indian Institute of Science Education and Research, Thiruvananthapuram (IISER-TVM) PhD Student, IISER-TVM CET Campus Sreekaryam Trivandrum, India 695016 Attn: Abbey M. Philip
Total	0.00 USD

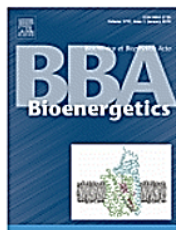


RightsLink®

Home

Account  
Info

Help



**Title:** Charge separation in Photosystem II: A comparative and evolutionary overview

**Author:** Tanai Cardona, Arezki Sedoud, Nicholas Cox, A. William Rutherford

**Publication:** Biochimica et Biophysica Acta (BBA) - Bioenergetics

**Publisher:** Elsevier

**Date:** January 2012

Logged in as:  
Abbey Philip  
Indian Institute of Science  
Education and Research,  
Thiruvananthapuram (IISER-  
TVM)

Account #:  
3001089150

LOGOUT

Copyright © 2011 Elsevier B.V. All rights reserved.

### Order Completed

Thank you for your order.

This Agreement between Indian Institute of Science Education and Research, Thiruvananthapuram (IISER-TVM) -- Abbey Philip ("You") and Elsevier ("Elsevier") consists of your license details and the terms and conditions provided by Elsevier and Copyright Clearance Center.

Your confirmation email will contain your order number for future reference.

#### [printable details](#)

License Number	4450390320220
License date	Oct 15, 2018
Licensed Content Publisher	Elsevier
Licensed Content Publication	Biochimica et Biophysica Acta (BBA) - Bioenergetics
Licensed Content Title	Charge separation in Photosystem II: A comparative and evolutionary overview
Licensed Content Author	Tanai Cardona, Arezki Sedoud, Nicholas Cox, A. William Rutherford
Licensed Content Date	Jan 1, 2012
Licensed Content Volume	1817
Licensed Content Issue	1
Licensed Content Pages	18
Type of Use	reuse in a thesis/dissertation
Portion	figures/tables/illustrations
Number of figures/tables/illustrations	1
Format	both print and electronic
Are you the author of this Elsevier article?	No
Will you be translating?	No
Original figure numbers	Figure 1B
Title of your thesis/dissertation	Moderation of the Photogenerated Exciton Dynamics in Molecular Aggregates
Publisher of new work	Indian Institute of Science Education and Research Thiruvananthapuram (IISER-TVM)
Author of new work	Dr. Mahesh Hariharan
Expected completion date	Dec 2018
Estimated size (number of pages)	1
Requestor Location	Indian Institute of Science Education and Research, Thiruvananthapuram (IISER-TVM) PhD Student, IISER-TVM CET Campus Sreekaryam Trivandrum, Kerala 695016 India Attn: Abbey M. Philip
Publisher Tax ID	GB 494 6272 12
Total	0.00 USD



RightsLink®

Home

Account  
Info

Help

**SPRINGER NATURE****Title:** Introduction to Fluorescence**Publication:** Springer eBook**Publisher:** Springer Nature**Date:** Jan 1, 2006

Copyright © 2006, Springer Science Business Media, LLC

Logged in as:

Abbey Philip  
Indian Institute of Science  
Education and Research,  
Thiruvananthapuram (IISER-  
TVM)Account #:  
3001089150

LOGOUT

**Order Completed**

Thank you for your order.

This Agreement between Indian Institute of Science Education and Research, Thiruvananthapuram (IISER-TVM) -- Abbey Philip ("You") and Springer Nature ("Springer Nature") consists of your license details and the terms and conditions provided by Springer Nature and Copyright Clearance Center.

Your confirmation email will contain your order number for future reference.

printable details

License Number	4438160364013
License date	Sep 29, 2018
Licensed Content Publisher	Springer Nature
Licensed Content Publication	Springer eBook
Licensed Content Title	Introduction to Fluorescence
Licensed Content Date	Jan 1, 2006
Type of Use	Thesis/Dissertation
Requestor type	academic/university or research institute
Format	print and electronic
Portion	figures/tables/illustrations
Number of figures/tables/illustrations	2
Will you be translating?	no
Circulation/distribution	<501
Author of this Springer Nature content	no
Title	Moderation the Photogenerated Exciton Dynamics in Molecular Aggregates
Instructor name	Dr. Mahesh Hariharan
Institution name	Indian Institute of Science Education and Research Thiruvananthapuram (IISER-TVM)
Expected presentation date	Dec 2018
Portions	Chapter 1, Figures 1.10 and 1.11, Page 9
Requestor Location	Indian Institute of Science Education and Research, Thiruvananthapuram (IISER-TVM) PhD Student, IISER-TVM CET Campus Sreekaryam Trivandrum, Kerala 695016 India Attn: Abbey M. Philip
Billing Type	Invoice
Billing address	Indian Institute of Science Education and Research, Thiruvananthapuram (IISER-TVM) PhD Student, IISER-TVM CET Campus Sreekaryam Trivandrum, India 695016 Attn: Abbey M. Philip
Total	0.00 USD

[ORDER MORE](#)[CLOSE WINDOW](#)

This page is available in the following languages:



## Creative Commons License Deed

Attribution 4.0 International (CC BY 4.0)



This is a human-readable summary of (and not a substitute for) the license.

### You are free to:

**Share** — copy and redistribute the material in any medium or format

**Adapt** — remix, transform, and build upon the material

for any purpose, even commercially.

The licensor cannot revoke these freedoms as long as you follow the license terms.

### Under the following terms:

**Attribution** — You must give appropriate credit, provide a link to the license, and indicate if changes were made. You may do so in any reasonable manner, but not in any way that suggests the licensor endorses you or your use.

**No additional restrictions** — You may not apply legal terms or technological measures that legally restrict others from doing anything the license permits.

### Notices:

You do not have to comply with the license for elements of the material in the public domain or where your use is permitted by an applicable exception or limitation.

No warranties are given. The license may not give you all of the permissions necessary for your intended use. For example, other rights such as publicity, privacy, or moral rights may limit how you use the material.



RightsLink®

[Home](#)

[Account Info](#)

[Help](#)



**Title:** Self-Assembly-Induced Ultrafast Photodriven Charge Separation in Perylene-3,4-dicarboximide-Based Hydrogen-Bonded Foldamers

**Author:** Kelly M. Lefler, Dick T. Co, Michael R. Wasielewski

**Publication:** Journal of Physical Chemistry Letters

**Publisher:** American Chemical Society

**Date:** Dec 1, 2012

Copyright © 2012, American Chemical Society

Logged in as:  
Abbey Philip  
Indian Institute of Science  
Education and Research,  
Thiruvananthapuram (IISER-  
TVM)

Account #:  
3001089150

[LOGOUT](#)

#### PERMISSION/LICENSE IS GRANTED FOR YOUR ORDER AT NO CHARGE

This type of permission/license, instead of the standard Terms & Conditions, is sent to you because no fee is being charged for your order. Please note the following:

- Permission is granted for your request in both print and electronic formats, and translations.
- If figures and/or tables were requested, they may be adapted or used in part.
- Please print this page for your records and send a copy of it to your publisher/graduate school.
- Appropriate credit for the requested material should be given as follows: "Reprinted (adapted) with permission from (COMPLETE REFERENCE CITATION). Copyright (YEAR) American Chemical Society." Insert appropriate information in place of the capitalized words.
- One-time permission is granted only for the use specified in your request. No additional uses are granted (such as derivative works or other editions). For any other uses, please submit a new request.

If credit is given to another source for the material you requested, permission must be obtained from that source.



RightsLink®

[Home](#) [Account Info](#) [Help](#)



**ACS Publications**  
Most Trusted. Most Cited. Most Read.

**Title:** Cooperatively Assembling Donor–Acceptor Superstructures Direct Energy Into an Emergent Charge Separated State  
**Author:** David Ley, Carmen X. Guzman, Karin H. Adolfsen, et al  
**Publication:** Journal of the American Chemical Society  
**Publisher:** American Chemical Society  
**Date:** Jun 1, 2014

Logged in as:  
Abbey Philip  
Indian Institute of Science  
Education and Research,  
Thiruvananthapuram (IISER-  
TVM)

Account #:  
3001089150

[LOGOUT](#)

Copyright © 2014, American Chemical Society

#### PERMISSION/LICENSE IS GRANTED FOR YOUR ORDER AT NO CHARGE

This type of permission/license, instead of the standard Terms & Conditions, is sent to you because no fee is being charged for your order. Please note the following:

- Permission is granted for your request in both print and electronic formats, and translations.
- If figures and/or tables were requested, they may be adapted or used in part.
- Please print this page for your records and send a copy of it to your publisher/graduate school.
- Appropriate credit for the requested material should be given as follows: "Reprinted (adapted) with permission from (COMPLETE REFERENCE CITATION). Copyright (YEAR) American Chemical Society." Insert appropriate information in place of the capitalized words.
- One-time permission is granted only for the use specified in your request. No additional uses are granted (such as derivative works or other editions). For any other uses, please submit a new request.

If credit is given to another source for the material you requested, permission must be obtained from that source.



RightsLink®

Home

Account Info

Help



**Title:** Photoinduced Electron Transfer within Supramolecular Donor-Acceptor Peptide Nanostructures under Aqueous Conditions

**Author:** Allix M. Sanders, Timothy J. Magnanelli, Arthur E. Bragg, et al

**Publication:** Journal of the American Chemical Society

**Publisher:** American Chemical Society

**Date:** Mar 1, 2016

Copyright © 2016, American Chemical Society

Logged in as:  
Abbey Philip  
Indian Institute of Science  
Education and Research,  
Thiruvananthapuram (IISER-  
TVM)

Account #:  
3001089150

LOGOUT

#### PERMISSION/LICENSE IS GRANTED FOR YOUR ORDER AT NO CHARGE

This type of permission/license, instead of the standard Terms & Conditions, is sent to you because no fee is being charged for your order. Please note the following:

- Permission is granted for your request in both print and electronic formats, and translations.
- If figures and/or tables were requested, they may be adapted or used in part.
- Please print this page for your records and send a copy of it to your publisher/graduate school.
- Appropriate credit for the requested material should be given as follows: "Reprinted (adapted) with permission from (COMPLETE REFERENCE CITATION). Copyright (YEAR) American Chemical Society." Insert appropriate information in place of the capitalized words.
- One-time permission is granted only for the use specified in your request. No additional uses are granted (such as derivative works or other editions). For any other uses, please submit a new request.

If credit is given to another source for the material you requested, permission must be obtained from that source.



RightsLink®

[Home](#)

[Account Info](#)

[Help](#)



**Title:** Extending Photoinduced Charge Separation Lifetimes by Using Supramolecular Design: Guanine–Peryleneimide G-Quadruplex

**Author:** Yi-Lin Wu, Kristen E. Brown, Michael R. Wasielewski

**Publication:** Journal of the American Chemical Society

**Publisher:** American Chemical Society

**Date:** Sep 1, 2013

Copyright © 2013, American Chemical Society

Logged in as:  
Abbey Philip  
Indian Institute of Science  
Education and Research,  
Thiruvananthapuram (IISER-  
TVM)

Account #:  
3001089150

[LOGOUT](#)

#### PERMISSION/LICENSE IS GRANTED FOR YOUR ORDER AT NO CHARGE

This type of permission/license, instead of the standard Terms & Conditions, is sent to you because no fee is being charged for your order. Please note the following:

- Permission is granted for your request in both print and electronic formats, and translations.
- If figures and/or tables were requested, they may be adapted or used in part.
- Please print this page for your records and send a copy of it to your publisher/graduate school.
- Appropriate credit for the requested material should be given as follows: "Reprinted (adapted) with permission from (COMPLETE REFERENCE CITATION). Copyright (YEAR) American Chemical Society." Insert appropriate information in place of the capitalized words.
- One-time permission is granted only for the use specified in your request. No additional uses are granted (such as derivative works or other editions). For any other uses, please submit a new request.

If credit is given to another source for the material you requested, permission must be obtained from that source.



RightsLink®

Home

Account Info

Help



ACS Publications  
Most Trusted. Most Cited. Most Read.

**Title:** Segregated and Alternately Stacked Donor/Acceptor Nanodomains in Tubular Morphology Tailored with Zinc Porphyrin-C60 Amphiphilic Dyads: Clear Geometrical Effects on Photoconduction

**Author:** Richard Charvet, Yohei Yamamoto, Takayuki Sasaki, et al

**Publication:** Journal of the American Chemical Society

**Publisher:** American Chemical Society

**Date:** Feb 1, 2012

Copyright © 2012, American Chemical Society

Logged in as:

Abbey Philip  
Indian Institute of Science  
Education and Research,  
Thiruvananthapuram (IISER-TVM)

Account #:  
3001089150

LOGOUT

#### PERMISSION/LICENSE IS GRANTED FOR YOUR ORDER AT NO CHARGE

This type of permission/license, instead of the standard Terms & Conditions, is sent to you because no fee is being charged for your order. Please note the following:

- Permission is granted for your request in both print and electronic formats, and translations.
- If figures and/or tables were requested, they may be adapted or used in part.
- Please print this page for your records and send a copy of it to your publisher/graduate school.
- Appropriate credit for the requested material should be given as follows: "Reprinted (adapted) with permission from (COMPLETE REFERENCE CITATION). Copyright (YEAR) American Chemical Society." Insert appropriate information in place of the capitalized words.
- One-time permission is granted only for the use specified in your request. No additional uses are granted (such as derivative works or other editions). For any other uses, please submit a new request.

If credit is given to another source for the material you requested, permission must be obtained from that source.